INTERVAL FINITE ELEMENT APPROACH FOR INVERSE PROBLEM UNDER UNCERTAINTY

A Thesis
Presented to
The Academic Faculty

by

Naijia Xiao

In Partial Fulfillment
of the Requirements for the Degree
Doctor of Philosophy in the
School of Civil and Enviromental Engineering

Georgia Institute of Technology
December 2015

INTERVAL FINITE ELEMENT APPROACH FOR INVERSE PROBLEM UNDER UNCERTAINTY

Approved by:

Dr. Rafi L. Muhanna,
Committee Chair, Advisor
School of Civil and Enviromental
Engineering
Georgia Institute of Technology

Dr. Francesco Fedele, Advisor
School of Civil and Enviromental
Engineering
Georgia Institute of Technology

Dr. Donald W. White
School of Civil and Enviromental
Engineering
Georgia Institute of Technology

Dr. Abdul-Hamid Zureick
School of Civil and Enviromental
Engineering
Georgia Institute of Technology

Dr. George Kardomateas
School of Aerospace Engineering
Georgia Institute of Technology

Date Approved: 6 July 2015

To my parents,

and to Yixuan Sun.

ACKNOWLEDGEMENTS

First and foremost, I would like to express my deep gratitude to my advisors, Dr. Rafi Muhanna and Dr. Francesco Fedele, for the many hours of excellent guidance, for providing me with excellent facilities, and for providing financial support during my Ph.D. studies. It is their support that have been the key to my academic and personal growth over the past four years. I am grateful for their contributions, not just to this thesis, but also to making me a better researcher and a better person.

I also wish to thank the other faculty of Georgia Institute of Technology, most notably my committee members, Dr. Donald White, Dr. Abdul-Hamid Zureick and Dr. George Kardomateas, for their suggestions on my thesis and valuable time serving as my advisory committee. I would also like to thank Dr. Robert Mullen in University of South Carolina for his help during my research.

Finally, I would like to thank my parents and fiancée for their help and encouragement through all these years. I dedicate my work to them.

TABLE OF CONTENTS

LIST OF TABLES

LIST OF FIGURES

xiii

LIST OF SYMBOLS

$\mathbf{A}$ Cross section area for trusses and frames.

A Matrix in the decomposition of $\mathbf{K}$.

A_h Deterministic matrix in a linear inverse problem.

A_k Transfer matrix in the system equation of Kalman filtering.

A_m Matrix in the decomposition of $\mathbf{M}$.

A_s Matrix in the decomposition of $\mathbf{S}$.

A^C Matrix in the decomposition of $\mathbf{K}^C$ in dynamic inverse problems.

A_m^C Matrix in the decomposition of $\mathbf{M}^C$ in dynamic inverse problems.

A_g^F Matrix in the decomposition of $\mathbf{F}_g$ in dynamic inverse problems.

$\mathbf{a}$ Nodal acceleration vector due to ground motion.

B Generalized strain-displacement matrix.

B_f Matrix in the decomposition of $\mathbf{f}$ due to ground motion.

B^C Matrix in the decomposition of $\mathbf{K}^C$ in dynamic inverse problems.

B_m^C Matrix in the decomposition of $\mathbf{M}^C$ in dynamic inverse problems.

B_g^F Matrix in the decomposition of $\mathbf{F}_g$ in dynamic inverse problems.

$\mathbf{C}$ Damping matrix.

C Constraint matrix for compatibility and boundary conditions.

c Objective vector used in nonlinear programming.

$\mathbf{D}$ Interval diagonal matrix in the decomposition of $\mathbf{K}$.

$\mathbf{d}_t$ Load uncertainty time-history vector in dynamic problems.

d Descending direction in the adjoint optimization.

d_{u0} Equivalent load time-history vector due to initial displacement.

d_{v0} Equivalent load time-history vector due to initial velocity.

$\mathbf{E}$ Young's modulus.

$\mathbf{E}_e$ Constitutive matrix at given points.

F Matrix in the decomposition of $\mathbf{f}$.

$\mathbf{f}$ Nodal equivalent load vector.

$\mathbf{f}_j$ Concentrated, line, face, and body load distributions,

or the j-th order natural frequency.

f_{eq} Equality constraints in nonlinear programming.

f_{inv} Inverse function in SVD-based pseudo-inverse approach.

f_{mea} Nonlinear measurement equation in Kalman filtering.

f_{sys} Nonlinear system equation in Kalman filtering.

G Inverse of generalized stiffness matrix.

G_t Matrix used in the pseudo-inverse approach.

G_u Inverse matrix for $\Delta\mathbf{u}$ in the generalized eigenvalue problems.

G_α Newton-Raphson inverse in adjoint optimization.

G_ω Inverse matrix for $\Delta\boldsymbol{\omega}^2$ in the generalized eigenvalue problems.

g Gradient of the objective functional.

$\mathbf{H}_{ij}$ Entries of the effective flexibility matrix in dynamic problems.

H Measurement-displacement matrix used in inverse problems.

H_k Hessian matrix in Newton-Raphson iteration.

H_α Partial derivative of measurement with respect to parameter vector.

$\mathbf{I}$ Moment of inertia for beams.

I Identity matrix.

i Imaginary unit.

J Determinant of the Jacobian matrix.

$\mathbf{K}$ Stiffness matrix.

$\mathbf{K}^C$ Extended stiffness matrix in dynamic problems.

K_k Optimal Kalman gain in Kalman filtering.

$\mathbf{K}_{\text{eff}}$ Effective stiffness matrix.

L Element length for trusses and beams.

L_R	Finite difference matrix in regularization method.
L_j	Load distribution matrix for different load types.
L_α	Interpolation matrices for material parameter vector.
L_δ	Interpolation matrices for equivalent load vector.
$\mathbf{M}$	Mass matrix, or bending moment.
$\mathbf{M}^C$	Extended mass matrix in dynamic problems.
$\mathbf{N}$	Axial forces for trusses and frames.
N	Total length of the signal in discrete Fourier transform.
N_e	Element shape function matrix.
$\mathbf{P}$	Concentrated forces.
$\mathbf{P}_\eta^C$	Equivalent load mapping matrix in dynamic inverse problems.
$\mathbf{P}_{\eta\rho}^C$	Equivalent load mapping matrix due to magnitude measurement.
$\mathbf{P}_{\eta\varphi}^C$	Equivalent load mapping matrix due to phase measurement.
$P_{k|k-1}$	Covariance of prior state estimate in Kalman filtering.
$P_{k|k}$	Covariance of posterior state estimate in Kalman filtering.
P_r	Matrix relating stress to internal forces inside an element.
P_{xy}	Covariance between state estimate and predicted measurement.
P_y	Covariance of predicted measurement in Kalman filtering.
$\mathbf{p}$	Axial distributed load.
Q_k	Covariance of process noise w_k in Kalman filtering.
$\mathbf{q}$	Lateral distributed load.
q	Vector relating nodal acceleration to ground motion.
R	Regularization matrix.
R_k	Covariance of measurement noise v_k in Kalman filtering.
$\mathbf{r}$	Internal forces inside an element.
r_j	Coefficient in descending direction updates.
$\mathbf{S}$	Generalized stress-displacement matrix.

S_k Covariance of measurement residue in Kalman filtering.

s_j Step size in parameter vector updating.

T Total time of a signal in discrete Fourier transform.

T_0 Time of an unpadded signal in discrete Fourier transform.

T_b Block matrix in static inverse problems.

T_e Interpolation matrix between local and global coordinate systems.

T_p Time of zero-padding in discrete Fourier transform.

T_w Auxiliary matrix in original and adjoint systems.

$T\langle \mathbf{x} \rangle$ Influence matrix for the stiffness parameter vector $\boldsymbol{\alpha}$.

$T_m\langle \mathbf{x} \rangle$ Influence matrix for the mass parameter vector $\boldsymbol{\alpha}_m$.

$\mathbf{t}$ Thickness in plane stress/strain problems.

t Time in time-domain dynamic analysis.

U_h Matrix in the singular value decomposition (SVD) of A_h.

$\mathbf{u}$ Nodal displacement vector, or axial displacement.

$\dot{\mathbf{u}}$, $\ddot{\mathbf{u}}$ Nodal velocity and acceleration.

$\mathbf{u}_0$ Interval initial displacement vector.

u_j Singular vector in the singular value decomposition (SVD) of A_h.

u_k Input vector in the system equation of Kalman filtering.

V_h Matrix in the singular value decomposition (SVD) of A_h.

$\mathbf{v}_0$ Interval initial velocity vector.

$\mathbf{v}_g$ Auxiliary variables in iterative enclosure method.

$\mathbf{v}_g^F$ Auxiliary variable in the decomposition of $\mathbf{F}_g$.

v_j Singular vector in the singular value decomposition (SVD) of A_h, or interpolation weights.

v_k Measurement noise in Kalman filtering.

W Diagonal weight matrix for measurements.

W_η^C Modification matrix in Newton-Raphson iteration.

$W^C_{\eta\rho}$	Modification matrix due to magnitude measurement.
$W^C_{\eta\varphi}$	Modification matrix due to phase measurement.
$\mathbf{w}$	Lagrangian multiplier used in the adjoint method.
$\dot{\mathbf{w}}, \ddot{\mathbf{w}}$	First and second derivatives of $\mathbf{w}$ with respect to time.
w_j	Weights for the numerical integration points.
w_k	Process noise in Kalman filtering.
x	Unknown vector in nonlinear programming.
x_k	State vector in Kalman filtering.
$\hat{x}_{k|k-1}$	Prior state estimate in Kalman filtering.
$\hat{x}_{k|k}$	Posterior state estimate in Kalman filtering.
y_k	Measurement vector in Kalman filtering.
$\tilde{y}_k$	Innovation vector in Kalman filtering.
$\boldsymbol{\alpha}$	Interval stiffness parameter vector.
$\boldsymbol{\alpha}_m$	Interval mass parameter vector.
α_d	Rayleigh damping coefficient.
$\boldsymbol{\beta}$	Intervals with zero midpoints.
β	Uncertainty level of an interval.
β_d	Rayleigh damping coefficient.
$\boldsymbol{\Gamma}$	Objective functional in adjoint optimization.
γ	Regularization weight.
Δ	Deviation with respect to reference vector.
$\boldsymbol{\delta}$	Load uncertainty vector.
$\boldsymbol{\delta}_t$	Time-varying load uncertainty vector in dynamic problems.
δ	Variation of a variable.
δ_η	Measurement device tolerance.
$\boldsymbol{\varepsilon}$	Generalized strain vector, or axial strain.
ζ	Effective damping ratio.

$\boldsymbol{\eta}$	Interval measurement vector.
$\boldsymbol{\eta}_\rho$	Measurements containing magnitude information.
$\boldsymbol{\eta}_\varphi$	Measurements containing phase information.
$\boldsymbol{\Theta}(\mathbf{x})$	Quadratic mapping of an interval vector.
$\boldsymbol{\theta}$	Rotation angle.
$\boldsymbol{\kappa}$	Curvature or bending strain.
Λ	Matrix in the decomposition of $\mathbf{K}$.
Λ_m	Matrix in the decomposition of $\mathbf{M}$.
Λ_s	Matrix in the decomposition of $\mathbf{S}$.
Λ^C	Matrix in the decomposition of $\mathbf{K}^C$ in dynamic inverse problems.
Λ_m^C	Matrix in the decomposition of $\mathbf{M}^C$ in dynamic inverse problems.
Λ_g^F	Matrix in the decomposition of $\mathbf{F}^C$ in dynamic inverse problems.
$\boldsymbol{\lambda}$	Lagrangian multiplier denoting internal forces and support reactions.
$\boldsymbol{\mu}_1$	Lagrangian multiplier for generalized strains.
$\boldsymbol{\mu}_2$	Lagrangian multiplier for generalized stresses.
ν	Poisson's ratio.
ξ_j	Coordinates for the numerical integration points.
$\boldsymbol{\Pi}$	Energy functional for equilibrium.
$\boldsymbol{\rho}$	Mass density.
Σ_h	Diagonal matrix in the singular value decomposition (SVD) of A_h.
$\boldsymbol{\sigma}$	Generalized stress vector, or normal stress.
σ_j	Singular value in the singular value decomposition (SVD) of A_h.
τ	Error tolerance for stopping criterion in iterative methods.
τ_1, τ_2	Constants in inexact line search.
τ_{err}	Error tolerance in determining zero-padding length.
Φ_e	Matrix in the decomposition of $\mathbf{E}_e$.
Φ_s	Matrix in the decomposition of $\mathbf{S}$.

φ_e	Vector in the decomposition of $\mathbf{E}_e$.
Ω	Objective function for nonlinear programming.
$\boldsymbol{\omega}$	Angular frequency in dynamic problems.
bold	Interval variables.
italic	Deterministic variables.
$*$	Convolution of two signals.
$\circ$	Element-by-element vector product.
$\otimes$	Fundamental arithmetic operations $+$, $-$, $\times$, or $/$.
$\underline{\cup}$	Interval hull of two intervals.
$\lvert\ \rvert$	Absolute values for vectors and matrices.
$\underline{a},\ \overline{a}$	Lower and upper bounds.
arg( )	Argument of a complex number.
atan2( )	Two-dimension arctangent function.
diag( )	Mapping a vector to a diagonal matrix.
mid( )	Midpoint value of an interval.
rad( )	Radius of an interval.
$\mathcal{F}_t( )$	Fourier transform of a signal.
$\mathcal{F}_t^{-1}( )$	Inverse Fourier transform of a signal.
$*$	Conjugate of a complex variable.
C	Realization of a complex variable.
PI	Pseudo-inverse of a matrix.
R	Real part of a complex variable.
I	Imaginary part of a complex variable.
T	Transpose of a vector or a matrix.
inn	Interval inner enclosure.
out	Interval outer enclosure.
0	Reference variables, or midpoint of interval variables.

$_b$ Block vectors and matrices in iterative enclosure method.

$_c$ Concentrated loads.

$_d$ Distributed loads.

$_e$ Element vectors and matrices.

$_g$ Generalized variables in iterative enclosure method.

$_n$ Variables related to common nodes.

$_\text{eff}$ Variables related to the effective stiffness.

$_{mid}$ Midpoint value of an interval.

$_{rad}$ Radius of an interval.

SUMMARY

In this dissertation, for the first time a novel Interval Finite Element approach is formulated for the solution of inverse problems under uncertainty. Inverse problems include many structural problems of practical importance, such as structural health monitoring and structural damage detection, in which material properties of the structure are predicted based on measurement data collected from measuring devices. Due to the inevitable errors in data acquisition process, predicted material properties contain uncertainties. In this work, elastic structures with uncertain load, geometric, and material properties are studied. All uncertain parameters are modeled by intervals, and interval algorithms are developed to track propagation of the uncertainties. The goal is to obtain an interval enclosure of the exact solution set, with the least overestimation possible.

In the static analysis, the static response of the structure is considered. To obtain guaranteed interval enclosure of the exact solutions and reduce overestimation due to interval dependency, a new decomposition strategy for interval matrices is presented in the interval forward solver. In addition, derived quantities are solved simultaneously as primary quantities. New element assembly strategies and a new variant of iterative enclosure method are proposed. To solve interval inverse problems with static measurements, a two-stage algorithm is proposed. The algorithm is based on an adjoint-based optimization technique. To obtain a guaranteed interval enclosure of the unknown parameters, governing equations are reintroduced into a fixed-point form that facilitates the implementation of iterative enclosure method.

In the dynamic analysis, the structure is studied in the frequency domain, the modal space, and the time domain. In the forward solver, the proposed matrix

decomposition is extended to account for uncertain inertial properties and different excitation forms. In the frequency-domain analysis, complex interval variables are handled successfully. In the modal analysis, Interval Generalized Eigenvalue Problems (IGEP) are solved. In the time-domain analysis, Discrete Fourier Transform (DFT) and its inverse are incorporated into the interval solver. For the interval inverse solver with dynamic measurements, the proposed method allows a diverse forms of measurements: real and imaginary parts of the response, magnitudes, or the phase angles. Guaranteed interval bounds that enclose the exact solution set is obtained from the proposed new variant of iterative enclosure method.

In summary, this study successfully solves structural inverse problems under uncertainty for the first time, using a novel Interval Finite Element Method. The presented method provides guaranteed sharp bounds on the exact solution sets, at low computational cost when compared with other available methods. Overestimation due to interval dependency is successfully handled, and the proposed method provides a useful tool in the analysis of structural forward and inverse problems under uncertainty.

CHAPTER I

INTRODUCTION

Many structural problems of practical importance can be classified as inverse problems. For instance, in structural health monitoring [1, 22, 57, 111, 149], material properties of the structure are predicted by collecting measurement data from the structure under prescribed loading conditions. In structural damage detection [14, 35, 39, 84, 142, 156, 163], available measurement data is used to estimate the location and severity of the damages in the structure.

Inevitably, the collected data contains errors or uncertainties caused by measurement device or unfriendly environmental conditions during data acquisition. Such uncertainties causes inconsistencies between the estimated and actual system properties [48]. Thus uncertainty analysis is necessary for the evaluation of the accuracy of the yielded solution. Conventional treatment of uncertainties involves the probability theory [92, 144], in which all the uncertainties are modeled as random variables. There are extensive researches on the parameter identification [3, 133] and damage detection [145, 161] of a stochastic system. In particular, Kalman filtering [71, 131, 151] provides error estimate on the modal parameters based on noisy measurements of the response of a time-evolving system.

However, there are limitations for probabilistic approaches, since they require a prior knowledge on the nature of the uncertainties. In real life situations, there are often not enough measurements to reliably assess the statistical nature of the associated uncertainties. Instead, only partial information about its probabilities is available. Under such circumstances, the validity of the probability approach is under debate [98, 160], as the obtained solution depends heavily on the assumed nature of

the probability distribution.

As an alternative, one can turn to other non-probabilistic approaches, such as Bayesian networks [67, 132, 138], fuzzy sets [2, 33, 43, 75], evidence theory [13, 34, 70, 126], and intervals [28, 37, 69, 104]. In this dissertation, it is assumed that the only information available is the uncertainty bounds, and intervals are used to model all the uncertainties involved. The obtained solution is guaranteed to enclose the exact solution, regardless of the actual nature of the uncertainties under consideration. The results are useful in the analysis of low-probability but high-consequence events.

In the following sections, discussions on structural inverse problems are made, followed by a brief introduction on the optimization approach that is used in the study, as well as a review of other alternative approaches that are available in the literature. Then the interval arithmetic is presented, which is used as the cornerstone in the modeling and analysis of uncertainties. Basic concepts on intervals are introduced, as well as recent developments that is relevant to the current study. In addition, discussions are made regarding other non-interval approaches which are usually used as comparison. Finally, the objectives of the research are stated.

1.1 Structural Inverse Problems

A structure can be viewed as a parametrized system with external excitations as input and various forms of structural responses as output [38, 52, 80, 153]. External excitations include different types of loads on the structure. Structural responses include internal forces, deflections and strains at certain locations. The system is parameterized by structural geometric and material properties such as the geometry, stiffness, mass, and strength of each member [4, 12, 15, 97].

Sometimes the forward problem is encountered, in which both the excitations and system properties are given, and the goal is to predict the resulting structural responses, as shown in Figure 1.1. In the figure, the excitation, system properties, and
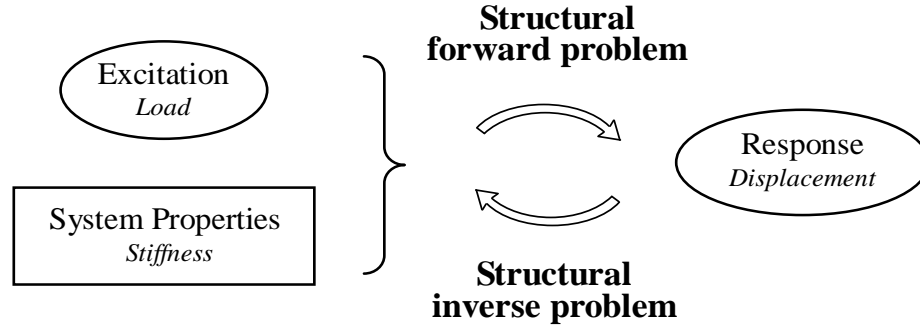
Figure 1.1: Comparison between structural forward and inverse problems.

responses are realized as load, stiffness, and displacement, respectively. In contrast, for the inverse problem, either the excitations or system properties are unknown, and the goal is to predict the unknown excitations or system properties based on the available measurements of the responses. The comparison between structural forward and inverse problems is displayed in the figure [62].

Unlike their forward counterparts, inverse problems are usually ill-conditioned and require regularization to stabilize the algorithm. In addition, the forward solver is usually an integral part of the corresponding inverse solver. Thus in the following subsections, discussions are made regarding the ill-conditioning of inverse problems and the commonly used regularization methods, followed by the introduction of three commonly used inverse methods, viz. the optimization method, the Kalman filter, and the pseudo-inverse method.

1.1.1 Regularization methods

Inverse problems are usually ill-conditioned (or equivalently ill-posed) when compared with the corresponding forward problems, in the sense that they bear one or more of the following characters [62]:

Non-existence: The problem may not have a solution at all. Usually the non-existence is caused by inconsistent measurement data due to random noise

induced during the data acquisition process or round-off error introduced later in the data-processing stage.

Non-uniqueness: There may be more than one feasible solution to the problem. Non-uniqueness can be caused by the inherent nonlinearity, or more frequently, by the under-determined nature of the problem, viz. the measurements are not sufficient to determine all the unknown parameters.

Instability: The solution does not depend continuously on the data. As a result, small perturbations in the given data may cause significant changes in the solution, rendering the yielded solution highly unreliable.

To overcome the drawbacks of the ill-conditioning of inverse problem, various types of regularization methods are used. The goal is to stabilize the algorithm and improve the conditioning of the problem.

To implement the regularization, one fundamental but computationally costly approach is the Truncated Singular Value Decomposition (TSVD), which is based on the Singular Value Decomposition (SVD) [62]. For instance, this approach is applied to solving the following linear system

$$A_h x_h = b_h, \tag{1.1}$$

where the matrix A_h and the right-hand side b_h are given, and x_h is the unknown solution vector. Then for any matrix A_h, its SVD takes the form

$$A_h = U_h \Sigma_h V_h^T = \sum_{j=1}^{n} \sigma_j \left(u_j v_j^T \right), \tag{1.2}$$

where U_h and V_h are square unitary matrices with *singular vectors* u_j and v_j as their columns, respectively, and Σ_h is a rectangular diagonal matrix with non-negative *singular value* σ_j in a descending order, viz. $\sigma_1 \geq \sigma_2 \geq \ldots \geq \sigma_n \geq 0$. Then a "naïve"

solution to Eq. (1.1) is given by

$$x_h = \sum_{j=1}^{n} \frac{u_j^T b_h}{\sigma_j} v_j. \tag{1.3}$$

This solution is "naïve" in the sense that it does not distinguish components corresponding to larger σ_j, which mainly contains effective data, and components corresponding to smaller σ_j, which mainly contains random noise. To reduce this undesirable effects, the TSVD only uses the first k-terms of the summation in Eq. (1.3),

$$x_h = \sum_{j=1}^{k} \frac{u_j^T b_h}{\sigma_j} v_j, \tag{1.4}$$

where $\sigma_{k+1} \leq \gamma \leq \sigma_k$, and γ is the threshold that is used as a controlling parameter. The method is computationally costly, as the singular vectors and singular values are explicitly computed. However, it is theoretically important, as it gives insights about the difference between effective data and random noise.

As an alternative, the Tikhonov regularization [47, 87] is computationally efficient and widely applicable. The regularization is realized as adding a penalizing term $\frac{1}{2}\gamma \left(\alpha^T R \alpha\right)$ to the objective function associated, where γ is the regularization weight, α is the unknown parameter vector, and R is the regularization matrix. The weight γ serves as the controlling parameter in the algorithm. If γ is too large, the solution is completely determined by the regularization; if γ is too small, the problem is still ill-conditioned and the regularization is not working. The matrix R is constructed by its associated matrix L_R, where $R = L_R^T L_R$. For a 1-D problem, popular choices for L_R include identity matrix $L_R = I$, first-order finite difference matrix

$$L_R = \left\{ \begin{matrix} 1 & -1 & & & \\ & 1 & -1 & & \\ & & \ddots & \ddots & \\ & & & 1 & -1 \end{matrix} \right\}, \tag{1.5}$$

and second-order finite difference matrix

$$L_R = \left\{ \begin{matrix} -1 & 2 & -1 & & & \\ & -1 & 2 & -1 & & \\ & & \ddots & \ddots & \ddots & \\ & & & -1 & 2 & -1 \end{matrix} \right\}. \tag{1.6}$$

The idea can be easily extended to higher-order finite difference matrices and higher dimensions.

1.1.2 Optimization approach

In the optimization approach, an inverse problem is solved by minimizing the differences between the predicted structural responses and the measured data. Throughout the entire process, equilibrium and boundary conditions are treated as additional constraints that must be satisfied. The algorithm starts from an initial guess α_0 of the parameter vector. Then the parameter vector α_j is updated iteratively,

$$\alpha_{j+1} = \alpha_j + s_j d_j, \tag{1.7}$$

where the subscripts denote the iteration steps, s_j and d_j are the step size and the descending direction at the j-th step, respectively. In the current work, conjugate gradient method [50] and Newton-Raphson method are used to determine the descending direction d_j that decreases the objective function. In addition, an inexact line search algorithm is implemented to find the optimal search step s_j. During the process, the adjoint method is exploited to compute the gradient of the objective function. The algorithm stops when the gradient g and the update on α are both small enough, that is

$$\frac{\|\alpha_{j+1} - \alpha_j\|}{\|\alpha_j\|} \leq \tau, \quad \frac{\|g_{j+1}\|}{\|g_1\|} \leq \tau. \tag{1.8}$$

where τ is the error tolerance. Each part of the optimization process is detailed in the following discussions.

The adjoint method [56, 94] aims to provide a computationally efficient approach to compute gradient (or equivalently, derivative) of a function subject to prescribed constraints. For instance, let the primary variable $\alpha \in \mathbb{R}^{n_\alpha}$ and the secondary variable $u \in \mathbb{R}^{n_u}$. Consider the function

$$\Gamma(u, \alpha) : \ \mathbb{R}^{n_u} \times \mathbb{R}^{n_\alpha} \to \mathbb{R}^{n_\gamma}, \tag{1.9}$$

subject to the following constraint

$$f_{eq}(u, \alpha) = 0, \qquad f_{eq} \in \mathbb{R}^{n_u}. \tag{1.10}$$

Note that the number of constraints equals the dimension of u, as in the cases of structural problems.

To compute the gradient of Γ with respect to α, u is treated as an implicit function of α via the constraint equation $f_{eq}(u, \alpha) = 0$. Then according to the chain rule of partial derivatives,

$$\frac{d\Gamma}{d\alpha} = \frac{d\Gamma(u(\alpha), \alpha)}{d\alpha} = \frac{\partial\Gamma}{\partial\alpha} + \frac{\partial\Gamma}{\partial u}\frac{\partial u}{\partial\alpha}. \tag{1.11}$$

Since the constraint Eq. (1.10) is zero everywhere, so is its total derivative. Thus applying the chain rule again yields

$$\frac{\partial f_{eq}}{\partial u}\frac{\partial u}{\partial\alpha} + \frac{\partial f_{eq}}{\partial\alpha} = 0. \tag{1.12}$$

By assuming that $\dfrac{\partial f_{eq}}{\partial u}$ is everywhere non-singular, Eq. (1.12) can be used to eliminate the term $\dfrac{\partial u}{\partial\alpha}$ in Eq. (1.11). Thus

$$\frac{d\Gamma}{d\alpha} = \frac{\partial\Gamma}{\partial\alpha} - \frac{\partial\Gamma}{\partial u}\left(\frac{\partial f_{eq}}{\partial u}\right)^{-1}\frac{\partial f_{eq}}{\partial\alpha}. \tag{1.13}$$

The expression $-\dfrac{\partial\Gamma}{\partial u}\left(\dfrac{\partial f_{eq}}{\partial u}\right)^{-1}$ can be understood as the solution vector w to the following linear system

$$\left(\frac{\partial f_{eq}}{\partial u}\right)^T w = -\left(\frac{\partial\Gamma}{\partial u}\right)^T, \tag{1.14}$$

where superscript T denotes matrix transpose. The matrix transpose is also called the matrix *adjoint*. Subsequently the vector w is called the *adjoint variable*, and the linear Eq. (1.14) is called the *adjoint equation*. As a result,

$$\frac{d\Gamma}{d\alpha} = \frac{\partial\Gamma}{\partial\alpha} + w^T\frac{\partial f_{eq}}{\partial\alpha}. \tag{1.15}$$

The adjoint approach needs to solve the original system in Eq. (1.10), and the linear adjoint system in Eq. (1.14).

1.1.2.2   Conjugate gradient method

The conjugate gradient method [76, 143, 158] determines the descending direction d_j at the j-th iteration step from a recursive rule. The natural choice for the initial trial d_1 is the steepest direction (opposite of the gradient)

$$d_1 = -g_1 = \left.\frac{\partial\Gamma}{\partial\alpha}\right|_1, \tag{1.16}$$

which guarantees a decrease in the objective function for a sufficiently small step size. Then in the next iteration step, d_{j+1} is determined by

$$d_{j+1} = -g_{j+1} + r_j d_j, \tag{1.17}$$

where the choice of r_j differentiates versions of the conjugate gradient method. Popular choices for r_j include

Fletcher-Reeves [49]:

$$r_j^{FR} = \frac{g_{j+1}^T g_{j+1}}{g_j^T g_j}; \tag{1.18}$$

Polak-Ribière-Polyak [116, 117]:

$$r_j^{PRP} = \frac{g_{j+1}^T(g_{j+1} - g_j)}{g_j^T g_j}; \tag{1.19}$$

Hestenses-Stiefel [64]:

$$r_j^{HS} = \frac{g_{j+1}^T(g_{j+1} - g_j)}{d_j^T(g_{j+1} - g_j)}; \tag{1.20}$$

Dai-Yuan [29]:

$$r_j^{DY} = \frac{g_{j+1}^T g_{j+1}}{d_j^T (g_{j+1} - g_j)}. \tag{1.21}$$

The descending directions lose conjugacy subsequently for a nonlinear problem. Thus it is preferable to reset the descending direction to the steepest direction if progress stops, viz. $d_{j+1} = -g_{j+1}$.

1.1.2.3 Newton-Raphson method

The Newton-Raphson method is an iterative method used to solve differentiable nonlinear equations [18]. In optimization, the method is applied to the derivative of a twice-differentiable objective function to find its stationary point, where the first derivative (gradient) is zero. To reach the stationary point $g_{j+1} = 0$ in the next step,

$$g_{j+1} \approx g_j + H_j (\alpha_{j+1} - \alpha_j) = 0, \tag{1.22}$$

where H_j is the Hessian matrix (second-order derivative) at the j-th step

$$H_j = \left. \frac{\partial^2 \Gamma}{\partial \alpha^2} \right|_j = \left. \frac{\partial g}{\partial \alpha} \right|_j. \tag{1.23}$$

The descending direction d_j, as well as the step size s_j, is obtained from

$$s_j d_j = \alpha_{j+1} - \alpha_j = -H_j^{-1} g_j. \tag{1.24}$$

However, due to the underlying nonlinearity of the problem, usually it is still necessary to implement a line search algorithm to obtain an optimal step size s_j that minimizes the objective function along the descending direction d_j.

Newton-Raphson method computes the Hessian in addition to the gradient of the objective function. Thus it tends to converge in fewer iterations than the conjugate gradient method, but requiring more computations in each iteration. It is also more prone to fail if the starting initial guess is far away from the final solution.

The inexact line search [7, 127, 128, 162] is implemented to find a suitable step size s_j at each iteration after the descending direction d_j is determined. Compared with the exact line search, the inexact line search does not exactly satisfy the optimization condition $g_{j+1}^T d_j = 0$ at each step. As a result, the implementation is easier and the computation is less time-consuming. In particular, the inexact line search only requires that the accepted step size s_j is large enough to yield a significant decrease in Γ, while not too large to deviate too far from the optimal point. In particular, the weak Wolfe line search [61, 147, 148, 157] requires

$$\tau_1 \leq \frac{\Gamma_{j+1} - \Gamma_j}{s_j g_j^T d_j}, \qquad \frac{g_{j+1}^T d_j}{g_j^T d_j} \leq \tau_2, \tag{1.25}$$

where $0 < \tau_1 < \tau_2 < 1$. Other available choices include the strong Wolfe line search

$$\tau_1 \leq \frac{\Gamma_{j+1} - \Gamma_j}{s_j g_j^T d_j}, \qquad \left| \frac{g_{j+1}^T d_j}{g_j^T d_j} \right| \leq \tau_2, \tag{1.26}$$

and the Goldstein-Armijo line search [9]

$$\tau_1 \leq \frac{\Gamma_{j+1} - \Gamma_j}{s_j g_j^T d_j} \leq \tau_2. \tag{1.27}$$

The trial step sizes s_k are determined from a backtracking [41, 58], a bisection [20], a golden section [10, 74], or an interpolation search [8, 146] algorithm.

1.1.3 Kalman filtering

In the Kalman filter, the dynamic of a time-varying system is considered. Internal state of a process is estimated based on a sequence of noisy observations [136]. The yielded estimate contains information about the accuracy about the estimate itself, in the form of a covariance matrix. Different versions of Kalman filters are developed, which are applicable to linear and nonlinear problems. In the following discussions, various types of discrete Kalman filters are presented. Further discussions can be found in Simon's book [131].

In this subsection, the linear discrete Kalman filter is considered. The state of the system evolves according to the following *system equation*

$$x_{k+1} = A_k x_k + B_k u_k + w_k, \tag{1.28}$$

where subscripts $_k$ denote quantities at the k-th step, x_k is the unknown state parameter to be estimated, u_k represents some given input parameters that is known prior to the analysis, w_k models unknown random process noise, A_k and B_k are given matrices. The measurement data is linearly related to x_k and corrupted with random measurement noise, according to the following *measurement equation*

$$y_k = C_k x_k + v_k, \tag{1.29}$$

where y_k is the measurement vector, and v_k is the measurement noise. Usually w_k and v_k are assumed as white, zero-mean, Gaussian random noise, whose probability characteristics are known as a prior.

The linear discrete Kalman filter provides an optimal estimate for the state parameter x as well as its error covariance matrix P, by minimizing the covariance of the estimation. The process starts from the initial guess $\hat{x}_0$ for the state x and P_0 for the covariance P. Then an prior state estimate $\hat{x}_{k|k-1}$ and its covariance $P_{k|k-1}$ at the current step is made based on the process equation (1.28)

$$\hat{x}_{k|k-1} = A_{k-1}\hat{x}_{k-1|k-1} + B_{k-1}u_{k-1}; \tag{1.30}$$

$$P_{k|k-1} = A_{k-1}P_{k-1|k-1}A_{k-1}^T + Q_{k-1},$$

where $\hat{x}_{k-1|k-1}$ and $P_{k-1|k-1}$ are respectively the posterior state estimate and its covariance at the previous step, and Q_{k-1} is the given covariance matrix for the process noise w_{k-1}.

According to the measurement Eq. (1.29), the innovation vector (measurement residue) $\tilde{y}_k$ and its covariance S_k are given by

$$\tilde{y}_k = y_k - C_k \hat{x}_{k|k-1}; \tag{1.31}$$

$$S_k = C_k P_{k|k-1} C_k^T + R_k,$$

where R_k is the given covariance matrix for the measurement noise v_k. Then the posterior state estimate $\hat{x}_{k|k}$ and its covariance $P_{k|k}$ are given by

$$\hat{x}_{k|k} = \hat{x}_{k|k-1} + K_k \tilde{y}_k; \tag{1.32}$$

$$P_{k|k} = (I - K_k C_k) P_{k|k-1},$$

where K_k is the optimal Kalman gain given by

$$K_k = P_{k|k-1} C_k S_k^{-1}. \tag{1.33}$$

The Kalman gain above is optimal in the sense that the yielded posterior covariance $P_{k|k}$ is minimal. Note that $P_{k|k}$ is symmetric, and the second equation in (1.32) is a simplified version of

$$P_{k|k} = (I - K_k C_k) P_{k|k-1} (I - K_k C_k)^T + K_k R_k K_k^T, \tag{1.34}$$

which is also known as the "Joseph form" [131] of the posterior estimate equation.

1.1.3.2 Extended Kalman filter

The extended Kalman filter (EKF) [120, 131] is one version of nonlinear Kalman filter that can be applied to nonlinear systems. The nonlinear system equation is given by

$$x_{k+1} = f_{sys}(x_k, u_k) + w_k, \tag{1.35}$$

where f_{sys} is a nonlinear function. The nonlinear measurement equation that links measurement data y_k and state parameter vector x_k is given by

$$y_k = f_{mea}(x_k) + v_k. \tag{1.36}$$

12

Again, the probability characteristics of the random process noise w_k and measurement noise v_k are known in prior.

The algorithm starts from the initial guess $\hat{x}_0$ for the state x and P_0 for the covariance P. By defining the following partial derivative matrices associated with the system Eq. (1.35)

$$A_{k-1} = \left. \frac{\partial f_{sys}}{\partial x_{k-1}} \right|_{\hat{x}_{k-1|k-1}}, \tag{1.37}$$

the prior state estimate $\hat{x}_{k|k-1}$ and its covariance $P_{k|k-1}$ are given by

$$\hat{x}_{k|k-1} = f_{sys}\left(\hat{x}_{k-1|k-1}, u_{k-1}\right); \tag{1.38}$$

$$P_{k|k-1} = A_{k-1}P_{k-1|k-1}A_{k-1}^T + Q_{k-1}.$$

where Q_{k-1} is the covariance matrix for the process noise w_{k-1}.

Similarly, by defining the following partial derivative matrices associated with the measurement Eq. (1.36)

$$C_k = \left. \frac{\partial f_{mea}}{\partial x_k} \right|_{\hat{x}_{k|k-1}}, \tag{1.39}$$

the innovation vector (measurement residue) $\tilde{y}_k$ and its covariance S_k are given by

$$\tilde{y}_k = y_k - f_{mea}\left(\hat{x}_{k|k-1}\right); \tag{1.40}$$

$$S_k = C_k P_{k|k-1} C_k^T + R_k,$$

where R_k is the covariance matrix for the measurement noise v_k. Then the posterior state estimate $\hat{x}_{k|k}$ and its covariance $P_{k|k}$, as well as the optimal Kalman gain K_k, are exactly the same as in Eqs. (1.32) and (1.33), viz.

$$\hat{x}_{k|k} = \hat{x}_{k|k-1} + K_k \tilde{y}_k;$$

$$P_{k|k} = \left(I - K_k C_k\right) P_{k|k-1}; \tag{1.41}$$

$$K_k = P_{k|k-1} C_k S_k^{-1}.$$

The EKF is a widely applied nonlinear Kalman filter. However, it can be difficult to tune and often yields unreliable results if the nonlinearities in the system are severe. This is because the EKF relies on the linearization of the system and measurement equations at the estimation points. Thus in the following discussion, another version of Kalman filter is presented, which directly propagate the mean and covariance of the state without linearization.

1.1.3.3 Unscented Kalman filter

The unscented Kalman filter (UKF) [131, 135] uses unscented transformation to propagate the mean and covariance of the state parameters for a nonlinear dynamic system. The probability characteristics of the random variables are represented by a set of deterministic vectors called the σ-points, whose ensemble mean and covariance are equal to the state parameter x and its error covariance P. For given state $x \in \mathbb{R}^n$ and covariance $P \in \mathbb{R}^{n \times n}$, the ensemble of $2n$ σ-points are given by

$$
\begin{aligned}
x^{(j)} &= x + \tilde{x}^{(j)}, & j &= 1, \ldots, 2n; \\
\tilde{x}^{(j)} &= \left(\sqrt{nP}\right)_j^T, & j &= 1, \ldots, n; \\
\tilde{x}^{(n+j)} &= -\left(\sqrt{nP}\right)_j^T, & j &= 1, \ldots, n,
\end{aligned}
\tag{1.42}
$$

where $\sqrt{nP}$ is the matrix square root of nP such that $\left(\sqrt{nP}\right)^T \sqrt{nP} = nP$, and $\left(\sqrt{nP}\right)_j$ is the j-th row of $\sqrt{nP}$.

For the nonlinear system given in Eqs. (1.35) and (1.36), the UKF starts from the initial guess $\hat{x}_0$ for the state estimate and P_0 for its covariance. For each step, the σ-points $x_{k-1|k-1}^{(j)}$ are sought for the posterior estimates $\hat{x}_{k-1|k-1}$ and $P_{k-1|k-1}$ at the previous step. Then the system Eq. (1.35) is used to propagate the σ-points $x_{k-1|k-1}^{(j)}$ to the k-th time step

$$
\hat{x}_{k|k-1}^{(j)} = f_{sys}\left(x_{k-1|k-1}^{(j)}, u_k\right).
\tag{1.43}
$$

14

Then the prior state estimate $\hat{x}_{k|k-1}$ and its covariance $P_{k|k-1}$ are given by

$$\hat{x}_{k|k-1} = \frac{1}{2n} \sum_{j=1}^{2n} \hat{x}_{k|k-1}^{(j)}; \tag{1.44}$$

$$P_{k|k-1} = \frac{1}{2n} \sum_{j=1}^{2n} \left(\hat{x}_{k|k-1}^{(j)} - \hat{x}_{k|k-1} \right) \left(\hat{x}_{k|k-1}^{(j)} - \hat{x}_{k|k-1} \right)^T + Q_{k-1}.$$

Note that Q_{k-1} is added to the equation to account for the process noise w_{k-1}.

For the measurement update, the σ-points $x_{k|k-1}^{(j)}$ are sought for the prior esti-
mates $\hat{x}_{k|k-1}$ and $P_{k|k-1}$ from Eq. (1.44). Then by using the σ-points $x_{k|k-1}^{(j)}$ and the
measurement Eq. (1.36), viz.

$$\hat{y}_k^{(j)} = f_{mea} \left(x_{k|k-1}^{(j)} \right), \tag{1.45}$$

the predicted measurements $\hat{y}_k$ and its covariance P_y are obtained as

$$\hat{y}_k = \frac{1}{2n} \sum_{j=1}^{2n} \hat{y}_k^{(j)}; \tag{1.46}$$

$$P_y = \frac{1}{2n} \sum_{j=1}^{2n} \left(\hat{y}_k^{(j)} - \hat{y}_k \right) \left(\hat{y}_k^{(j)} - \hat{y}_k \right)^T + R_k,$$

in which R_k is added to the equation to account for the measurement noise v_k. In
addition, the cross covariance P_{xy} between $\hat{x}_{k|k-1}$ and $\hat{y}_k$ is estimated from

$$P_{xy} = \frac{1}{2n} \sum_{j=1}^{2n} \left(\hat{x}_{k|k-1}^{(j)} - \hat{x}_{k|k-1} \right) \left(\hat{y}_k^{(j)} - \hat{y}_k \right)^T. \tag{1.47}$$

Then the posterior state estimate $\hat{x}_{k|k}$ and its covariance $P_{k|k}$ are given by

$$\hat{x}_{k|k} = \hat{x}_{k|k-1} + K_k \left(y_k - \hat{y}_k \right);$$

$$P_{k|k} = P_{k|k-1} - K_k P_y K_k^T, \tag{1.48}$$

where K_k is the optimal Kalman gain given by

$$K_k = P_{xy} P_y^{-1}. \tag{1.49}$$

From the above discussion, it is observed that the UKF neither use the lineariza-
tion of the governing equations nor require the computation of the Jacobian (partial

derivative matrix) as in the EKF. Thus it is widely applied to problems with severe nonlinearity or without easy analytical expressions for the Jacobian.

1.1.4 Pseudo-inverse approach

When the inverse problem is linear, or when the nonlinearity is not significant, the measurement data b_h is assumed to be related to the unknown parameter vector x_h via the matrix A_h, as stated before in Eq. (1.1), viz. $A_h x_h = b_h$. The pseudo-inverse approach [62, 73] aims at finding a pseudo-inverse for A_h such that

$$x_h^{PI} = A_h^{PI} b_h \tag{1.50}$$

is an approximate solution to the original linear inverse problem.

The Singular Value Decomposition (SVD) approach uses the SVD of A_h, which is given by Eq. (1.2). The corresponding pseudo-inverse is given in terms of the singular vectors u_j, v_j, and the singular values σ_j,

$$A_h^{PI} = \sum_{j=1}^{n} f_{inv}\left(\sigma_j, \gamma\right)\left(u_j v_j^T\right) \tag{1.51}$$

where $f_{inv}\left(x, \gamma\right)$ denotes the inverse function parameterized by a controlling parameter γ. For the "naïve" inversion in Eq. (1.3), the corresponding inverse function

$$f_{inv}\left(x, \gamma\right) = \frac{1}{x}. \tag{1.52}$$

For the TSVD solution in Eq. (1.4),

$$f_{inv}\left(x, \gamma\right) = \begin{cases} 1/x, & x \geq \gamma; \\ 0, & x < \gamma. \end{cases} \tag{1.53}$$

Other available choices include the following function proposed by Sun *et al.* [134]

$$f_{inv}\left(x, \gamma\right) = \frac{1}{x}\left\{1 - \frac{4}{\pi} \arctan\left(e^{-x/\alpha}\right)\right\}. \tag{1.54}$$

The above inverse functions with different values of γ are plotted in Figure 1.2. Observe that the function is continuous everywhere. The function is approximately constant when $x < \gamma$, and very close to $1/x$ when $x > \gamma$.
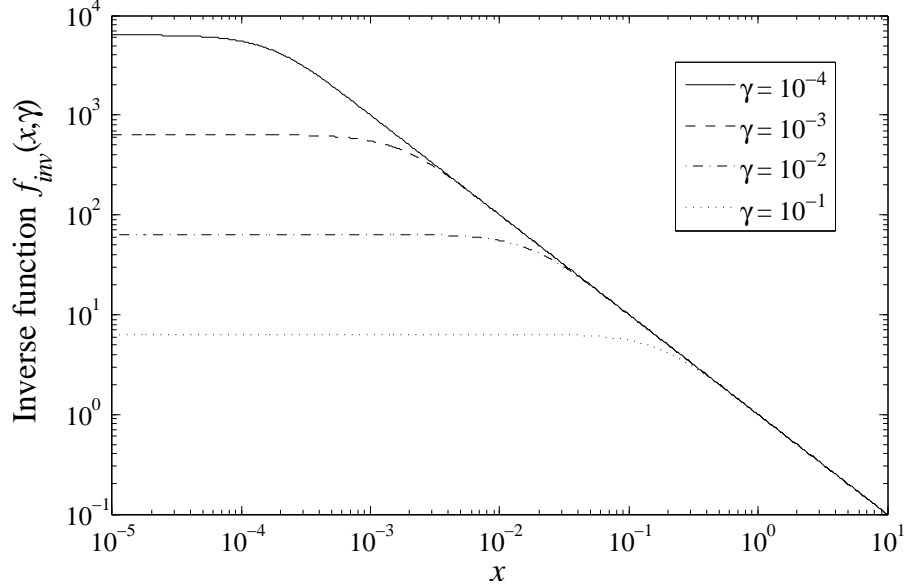
Figure 1.2: Inverse functions with different values of controlling parameter, used in the Singular Value Decomposition approach.

The SVD approach outlined above gives insight into the inversion process, yet it is inefficient because SVD is a computational expensive process. As an alternative, the Moore-Penrose pseudo inverse [100, 114] can be used. Let $A_h \in \mathbb{R}^{n \times m}$. When $n > m$, viz. the rows in A_h is more than the columns, the left inverse

$$A_h^{PI} = \left(A_h^T A_h + \gamma R\right)^{-1} A_h^T, \tag{1.55}$$

where γ is the regularization weight and R is the regularization matrix to ensure the inverse can be performed accurately and stably. When $n < m$, viz. the rows in A_h is less than the columns, the right inverse

$$A_h^{PI} = A_h \left(A_h A_h^T + \gamma R\right)^{-1}. \tag{1.56}$$

In essence, Eq. (1.55) yields a least-square solution, while Eq. (1.56) yields a minimal-norm solution. The regularization term γR widens the application of Eqs. (1.55) and (1.56). Both approaches can be very good approximations to Eq. (1.51) when appropriate regularization weights are chosen.
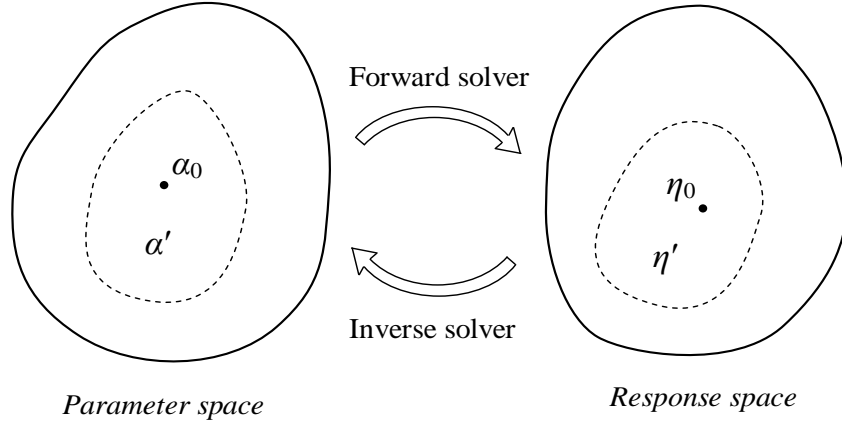
Figure 1.3: Differences between deterministic and uncertainty analyses.

1.2 Uncertainty Analysis with Intervals

The uncertainty analysis of a physical system models and tracks the propagation of the system uncertainties. The goal is to provide information regarding the reliability of the yielded solution. Compared with its deterministic counterpart, the uncertainty analysis handles variables representing sets of numbers.

As an example, consider the structural forward and inverse problems discussed previously. The system properties are described by points in the parameter space, while the measurable responses are described by points in the response space. The parameter and response spaces are denoted by solid lines in Figure 1.3. Then the deterministic forward and inverse solvers represent mappings between the single point α_0 in the parameter space and the single point η_0 in the response space, denoted by solid dots in the figure. In contrast, the uncertain forward and inverse solvers represent mappings between the subset including α_0 and its neighborhood α' and the subset including η_0 and its neighborhood η', denoted by dashed lines in the figure.

In this study, intervals are used to model uncertainties in the structural system, whose propagation is tracked by the interval arithmetic. The obtained solution guarantees to enclose the exact solution to the problem, regardless of the probability characteristics of the uncertainties under consideration. The results are especially

useful in the analysis of low-probability but high-consequence events. In the following subsections, various topics about the interval-based uncertainty analysis are discussed.

1.2.1 Preliminaries on intervals

In the current work, intervals are used to model uncertain variables encountered. Algorithms based on interval arithmetic are proposed to obtain an interval solution to the problem. Introductions on intervals and interval arithmetic, as well as the nature of the interval solutions and the Taylor expansion of nonlinear interval functions, are presented. Additional discussions on intervals can be found in [5, 79, 101].

1.2.1.1 Interval arithmetic

Intervals are extension of real numbers. Instead of representing one single real number, an interval denotes a continuous sets of real numbers, which are most suitably denoted by their *lower and upper bounds (endpoints)*,

$$\mathbf{x} = [\underline{x}, \overline{x}] = \{x \,|\, \underline{x} \leq x \leq \overline{x}, \, x \in \mathbb{R}\}, \tag{1.57}$$

where $\mathbf{x}$ denotes the interval, $\underline{x}$ and $\overline{x}$ denote its lower and upper bounds, respectively. *Hereafter, boldface font will be used to denote interval quantities.*

Alternatively, an interval can be described by its *midpoint* $x_{\mathrm{mid}} = \frac{1}{2} \left(\underline{x} + \overline{x} \right)$ and *radius* $x_{\mathrm{rad}} = \frac{1}{2} \left(\overline{x} - \underline{x} \right)$. The *width* of an interval is defined as $x_{\mathrm{wid}} = \left(\overline{x} - \underline{x} \right) = 2 x_{\mathrm{rad}}$. Intervals with zero-width is also referred to as *degenerated intervals*. For intervals with non-zero midpoint values, they can be brought into the form

$$\mathbf{x} = x_{\mathrm{mid}} \left(1 + \boldsymbol{\beta} \right) = x_{\mathrm{mid}} \left[1 - \left| \frac{x_{\mathrm{rad}}}{x_{\mathrm{mid}}} \right|, \ 1 + \left| \frac{x_{\mathrm{rad}}}{x_{\mathrm{mid}}} \right| \right], \tag{1.58}$$

where $|\ |$ denotes the absolute value. The width of $\boldsymbol{\beta}$, measured in percentage, is referred to as the *uncertainty level* of $\mathbf{x}$.

As intervals are sets of numbers, ordinary set operations on intervals, such as the *intersection* $\cap$ and the *union* $\cup$, can be defined in the conventional sense without

difficulty for two intersecting intervals $\mathbf{x}$ and $\mathbf{y}$,

$$\mathbf{x} \cap \mathbf{y} = \left[\max\{\underline{x}, \underline{y}\}, \ \min\{\overline{x}, \overline{y}\}\right];$$
$$\mathbf{x} \cup \mathbf{y} = \left[\min\{\underline{x}, \underline{y}\}, \ \max\{\overline{x}, \overline{y}\}\right]. \tag{1.59}$$

When the two intervals are not intersecting, viz. $\min\{\overline{x}, \overline{y}\} < \max\{\underline{x}, \underline{y}\}$, neither the intersection nor the union of $\mathbf{x}$ and $\mathbf{y}$ yields another interval. However, the corresponding *interval hull* $\mathbf{x} \ \underline{\cup} \ \mathbf{y}$ always exists,

$$\mathbf{x} \ \underline{\cup} \ \mathbf{y} = \left[\min\{\underline{x}, \underline{y}\}, \ \max\{\overline{x}, \overline{y}\}\right]. \tag{1.60}$$

Fundamental arithmetic operations on intervals can be defined as,

$$\mathbf{x} \otimes \mathbf{y} = \{x \otimes y \mid x \in \mathbf{x}, \ y \in \mathbf{y}\}. \tag{1.61}$$

where $\otimes$ denote any of the fundamental arithmetic operations $+$, $-$, $\times$, $/$, and the denominator in division cannot contain zero. For example, consider the interval addition $\mathbf{x} + \mathbf{y}$ and subtraction $\mathbf{x} - \mathbf{y}$, which can be expressed in an endpoint form

$$\mathbf{x} + \mathbf{y} = \left[\underline{x} + \underline{y}, \ \overline{x} + \overline{y}\right];$$
$$\mathbf{x} - \mathbf{y} = \left[\underline{x} - \overline{y}, \ \overline{x} - \underline{y}\right]. \tag{1.62}$$

Commutative and associative laws holds for interval addition and multiplication, but the distributive law fails to hold. Instead, there is a sub-distributive law:

$$\mathbf{x}(\mathbf{y} + \mathbf{z}) \subseteq \mathbf{x}\mathbf{y} + \mathbf{x}\mathbf{z}. \tag{1.63}$$

Additive inverse and multiplicative inverse only exist for degenerated intervals.

According to Eq. (1.61), the interval arithmetic operations yield results that are considered "conservative": the obtained solution guarantees to enclose the exact lower and upper bounds. This feature is referred to as the *isotonic inclusion* of interval arithmetic operations. It also causes overestimation in the solution when there are dependencies between the intervals, yielding wide enclosures that are practically useless. This is the main obstacle in any interval implementation.
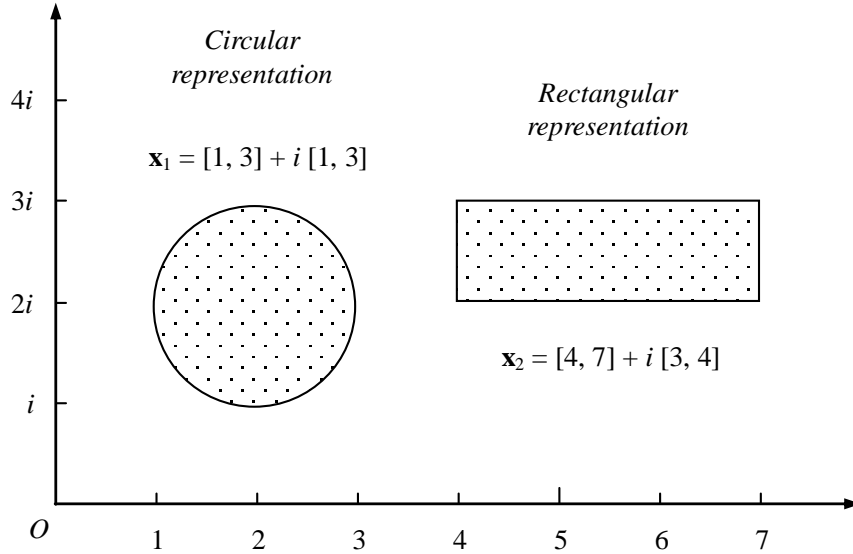
Figure 1.4: Circular and rectangular representations of complex interval numbers.

1.2.1.2 Interval complex numbers

The concept of intervals can be extended to complex numbers. There are two popular choices to model a complex interval number [17, 63, 115]: the circular representation that denotes a circle in the complex plane, and the rectangular representation that denotes a rectangle, as shown in Figure 1.4.

In the circular representation, a complex interval $\mathbf{z}$ is represented by its midpoint z_{mid} (a complex number) and radius z_{rad} (a positive real number). Let the real and imaginary parts of the midpoint z_{mid} be respectively $\mathrm{Re}\,(z_{\mathrm{mid}})$ and $\mathrm{Im}\,(z_{\mathrm{mid}})$. Then $\mathbf{z}$ can be expressed in the following endpoint form

$$\mathbf{z} = \Big[\mathrm{Re}\,(z_{\mathrm{mid}}) - z_{\mathrm{rad}},\ \mathrm{Re}\,(z_{\mathrm{mid}}) + z_{\mathrm{rad}}\Big] \tag{1.64}$$
$$+ i\,\Big[\mathrm{Im}\,(z_{\mathrm{mid}}) - z_{\mathrm{rad}},\ \mathrm{Im}\,(z_{\mathrm{mid}}) + z_{\mathrm{rad}}\Big],$$

where $i = \sqrt{-1}$ is the imaginary unit. Note that the real and imaginary parts of $\mathbf{z}$ have the same width in the circular representation.

In the rectangular representation, a complex interval $\mathbf{z}$ is represented by its real part $\mathrm{Re}\,(\mathbf{z})$ and its imaginary part $\mathrm{Im}\,(\mathbf{z})$, which are both ordinary real intervals.

21
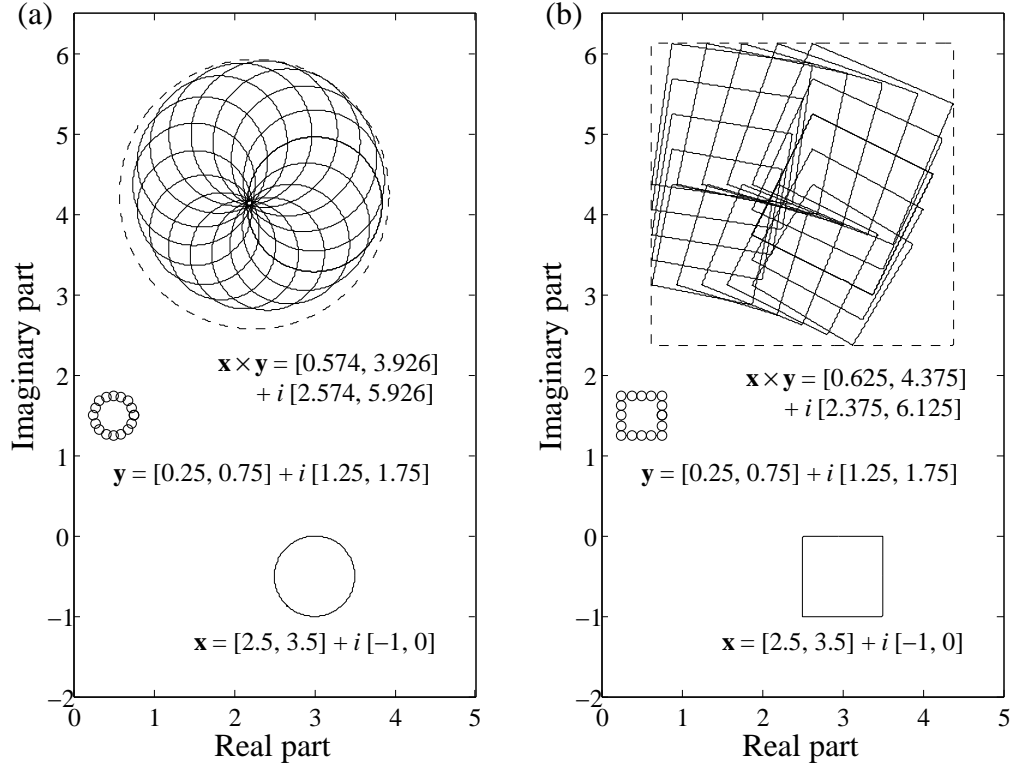
Figure 1.5: Interval multiplication of two complex intervals with circular and rectangular representations.

Thus $\mathbf{z}$ is expressed as

$$\mathbf{z} = \operatorname{Re}(\mathbf{z}) + i\operatorname{Im}(\mathbf{z}). \tag{1.65}$$

Note that, unlike the circular representation, the width of the real part $\operatorname{Re}(\mathbf{z})$ and the imaginary part $\operatorname{Im}(\mathbf{z})$ can be different. Thus the rectangular representation is useful when the uncertainty levels for the real and imaginary parts of a complex interval variable are different.

For the circular representation, the corresponding arithmetic operations exploit the midpoint and radius form. For instance, given two complex intervals $\mathbf{x}$ and $\mathbf{y}$, the midpoint and radius of the multiplication $\mathbf{z} = \mathbf{x} \times \mathbf{y}$ are given by

$$z_{\mathrm{mid}} = x_{\mathrm{mid}} y_{\mathrm{mid}}; \tag{1.66}$$

$$z_{\mathrm{rad}} = |x_{\mathrm{mid}}| y_{\mathrm{rad}} + |y_{\mathrm{mid}}| x_{\mathrm{rad}} + x_{\mathrm{rad}} y_{\mathrm{rad}}.$$

For the rectangular representation, the real and imaginary parts are treated as independent intervals. Thus the multiplication $\mathbf{z} = \mathbf{x} \times \mathbf{y}$ yields

$$\operatorname{Re}(\mathbf{z}) = \operatorname{Re}(\mathbf{x})\operatorname{Re}(\mathbf{y}) - \operatorname{Im}(\mathbf{x})\operatorname{Im}(\mathbf{y}); \quad (1.67)$$

$$\operatorname{Im}(\mathbf{z}) = \operatorname{Re}(\mathbf{x})\operatorname{Im}(\mathbf{y}) + \operatorname{Im}(\mathbf{x})\operatorname{Re}(\mathbf{y}).$$

Figure 1.5 compares the products of two complex intervals $\mathbf{x} = [2.5,\ 3.5] + i\,[-1,\ 0]$ and $\mathbf{y} = [0.25,\ 0.75] + i\,[1.25,\ 1.75]$, using the circular (subplot a) and rectangular representations (subplot b), respectively. The boundary of $\mathbf{x}$ is denoted by solid lines, while the boundary of $\mathbf{y}$ is denoted by white circular markers. The boundaries of the yielded products $\mathbf{x} \times \mathbf{y}$ are plotted as dashed circle and rectangle, respectively. To obtain the exact solution set, 16 equally spaced points y_j on the boundary of $\mathbf{y}$ are selected, denoted by white markers. Then the boundaries of $y_j\mathbf{x}$ are plotted as circles and rectangles in solid lines in the figure. The ensemble of these circles and rectangles represent the exact solution set. Thus the overestimation is realized as the white space inside the dashed circle and rectangle in the figure. Apparently, in general, the overestimation level is much smaller for the circular representation, because there is implicit dependency between the real and imaginary parts for the rectangular representation.

1.2.1.3 Interval linear system

The exact solution set to an interval system, even for a linear one, may be a very complicated set and its computation is an NP-hard problem in general [78]. For instance, consider the following interval linear system [72, 101]

$$\left\{ \begin{matrix} [2,\ 4] & [-2,\ 1] \\ [-1,\ 2] & [2,\ 4] \end{matrix} \right\} \left\{ \begin{matrix} \mathbf{x}_1 \\ \mathbf{x}_2 \end{matrix} \right\} = \left\{ \begin{matrix} [-2,\ 2] \\ [-2,\ 2] \end{matrix} \right\}, \quad (1.68)$$

in which each interval is assumed to vary independently. The exact solution set is displayed in Figure 1.6, which is shaded and bounded by solid lines. In practice, this
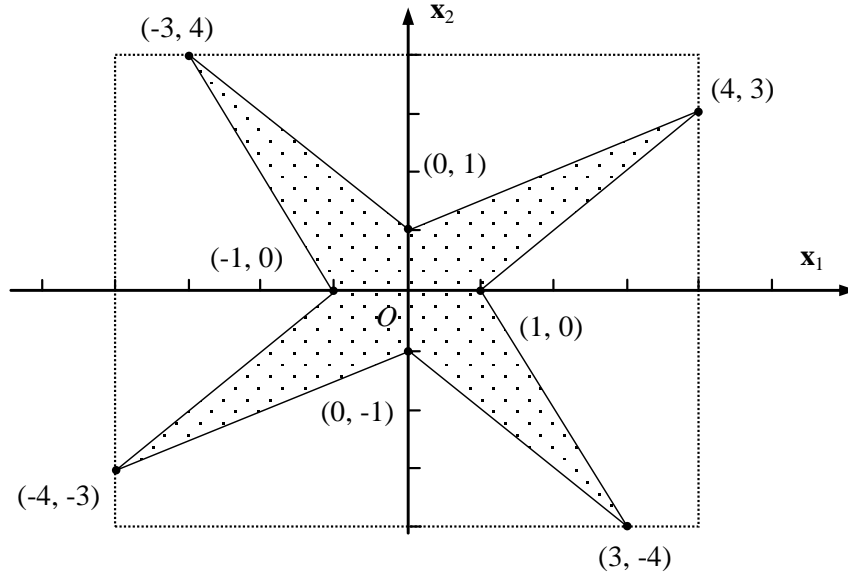
Figure 1.6: Exact solution set and its interval enclosure to the interval linear system in Eq. (1.68).

exact solution set is too complicated to be useful in the computation. Instead its interval enclosure is preferred

$$\left\{\begin{matrix} \mathbf{x}_1 \\ \mathbf{x}_2 \end{matrix}\right\} = \left\{\begin{matrix} [-4,\, 4] \\ [-4,\, 4] \end{matrix}\right\}, \tag{1.69}$$

whose boundary is denoted by dotted lines in the figure.

From the figure, it is observed that the interval enclosure contains the exact solution set, as well as points that are not a solution to the original system in Eq. (1.68). Information about the dependency between the components $\mathbf{x}_1$ and $\mathbf{x}_2$ is completely lost. Thus direct use of interval enclosure is not recommended.

1.2.1.4   Interval Taylor's theorem

Another important application of interval arithmetic is to evaluate nonlinear functions over a given interval [101, 124]. The Taylor's theorem states that, for a given second-order differentiable function $y(x)$ and an arbitrary reference point x_0,

$$y(x) = y(x_0) + y'(x_0)(x - x_0) + \frac{1}{2}y''(\xi)(x - x_0)^2, \tag{1.70}$$

24

where $y'(x)$ and $y''(x)$ denote the first- and second-order derivatives of $y(x)$ with respect to x, respectively, and ξ is bounded by x and x_0. Let x be substituted by an interval $\mathbf{x}$ that contains x_0, viz. $x_0 \in \mathbf{x}$. By noting that $\xi \in \mathbf{x}$, the following second-order Taylor's expansion for an interval function $\mathbf{y}(\mathbf{x})$ is obtained

$$\mathbf{y}(\mathbf{x}) \subseteq y(x_0) + y'(x_0)(\mathbf{x} - x_0) + \frac{1}{2}\mathbf{y}''(\mathbf{x})(\mathbf{x} - x_0)^2, \tag{1.71}$$

where $\mathbf{y}''(\mathbf{x})$ is the interval extension of the second-order derivative $y''(x)$. Due to the dependency between $\mathbf{y}''(\mathbf{x})$ and $(\mathbf{x} - x_0)^2$, the right-hand side of Eq. (1.71) is wider than the exact interval enclosure $\mathbf{y}(\mathbf{x})$. Apparently, Eq. (1.71) can be easily extended to higher-order Taylor expansions, at the cost of computing the higher-order $\mathbf{y}^{(n)}(\mathbf{x})$.

1.2.2 Interval finite element method

The Interval Finite Element Method (IFEM) [90, 103, 119] incorporates interval arithmetic into conventional Finite Element Method (FEM) formulations. Uncertain parameters about the load, geometry, and material of the structure are modeled by intervals. The goal is to obtain interval solutions that guarantee to enclose the exact solutions to the problem.

To obtain a tight enclosure and reduce the overestimation due to interval dependency, which is the main challenge in any interval computations, matrix decomposition strategies were proposed for the IFEM matrices, such as the nodal equivalent load vector [105] and the stiffness matrix [110]. The goal is to reduce the multiple occurrences of the same interval variable to the minimum [32]. Then special iterative schemes were proposed to solve the associated governing equations, taking advantage of the interval matrix decomposition mentioned earlier. In addition, Muhanna and Mullen [102] proposed a non-iterative strategy to solve the inner solution that bounds the exact solution from inside, which can be used to check the quality of the bounds obtained. Developments on these topics are introduced below.

1.2.2.1 Decomposition of $\mathbf{f}$ and $\mathbf{K}$

The decomposition of the nodal equivalent load $\mathbf{f}$ was first proposed by Mullen and Muhanna [105], in which $\mathbf{f}$ is decomposed into the product of a deterministic matrix F that contains information about the load distribution and a load uncertainty vector $\boldsymbol{\delta}$ that contains all the uncertainties in the load, viz.

$$\mathbf{f} = F\boldsymbol{\delta}. \tag{1.72}$$

The decomposition can be conducted as follows: after obtaining the nodal equivalent load $\mathbf{f}$ by following the conventional FEM procedure, all the uncertain parameters involved are collected into the load uncertainty vector $\boldsymbol{\delta}$. Then the deterministic matrix F is obtained by comparing $\mathbf{f}$ with $\boldsymbol{\delta}$.

Compared with the equivalent load decomposition, the idea of decomposing the stiffness matrix $\mathbf{K}$ is relatively new in IFEM. Early researchers [24, 102] on IFEM focus on simple structures such as trusses and frames, whose stiffness matrix have a simple matrix structure that does not require decomposition. Researchers can also handle the dependency issue following a non-decomposition strategy [23, 36, 106], in which the stiffness matrix is expressed as

$$\mathbf{K} = K_0 + \sum_j \frac{\partial K}{\partial \alpha_j} \left(\boldsymbol{\alpha}_j - \alpha_{j0} \right), \tag{1.73}$$

where K_0 is the midpoint of $\mathbf{K}$, $\boldsymbol{\alpha}_j$ are the parameters describing stiffness uncertainties of the structure, and α_{j0} are corresponding midpoint values.

Then in the work of Impollonia [68], the following stiffness matrix decomposition is proposed for a number of elements, such as truss element, frame element, and 2D constant strain element, in which

$$\mathbf{K}(\boldsymbol{\alpha}) = A\mathbf{D}(\boldsymbol{\alpha})A^T, \tag{1.74}$$

Here $\boldsymbol{\alpha}$ is the uncertain stiffness parameter vector, A is a deterministic matrix, and $\mathbf{D}$ is a diagonal matrix whose diagonal is just $\boldsymbol{\alpha}$, viz. $\mathbf{D} = \text{diag}(\boldsymbol{\alpha})$. The idea can

be tracked back to Rong and Lü [121]. The decomposition is applicable for simple elements, and the geometric and material uncertainties in each element are assumed to vary independently. The same decomposition can also be found in Neumaier and Pownuk [110] and Gao [53].

1.2.2.2 Iterative enclosure method

The iterative enclosure method, developed by Neumaier and Pownuk [110], aims at solving an interval linear system of the form

$$(C + A\mathbf{D}B)\,\mathbf{u} = a + F\boldsymbol{\delta}, \tag{1.75}$$

with uncertainties in $\mathbf{D}$ and $\boldsymbol{\delta}$. Note that the interval terms in Eq. (1.75) resemble the decomposition of $\mathbf{K}$ and $\mathbf{f}$ in Eqs. (1.74) and (1.72), respectively.

The iterative enclosure method assumes that there exists D_0 such that the matrix $(C + AD_0B)$ is invertible, and defines

$$G = (C + AD_0B)^{-1}, \tag{1.76}$$

which can be interpreted as the flexibility matrix for the structure. Then the solution $\mathbf{u}$ to Eq. (1.75) is related to the auxiliary variables $\mathbf{v} = B\mathbf{u}$ and $\mathbf{d} = (D_0 - \mathbf{D})\,\mathbf{v}$ via

$$\mathbf{u} = (Ga) + (GF)\boldsymbol{\delta} + (GA)\mathbf{d}; \tag{1.77}$$

$$\mathbf{v} = (BGa) + (BGF)\boldsymbol{\delta} + (BGA)\mathbf{d}.$$

For trusses, $\mathbf{v}$ denotes the uncertain strains, and $\mathbf{d}$ denote uncertainties in the stresses, both of which are caused by the uncertain deformation of the structure.

To obtain the interval solution $\mathbf{u}$, the method starts from the initial guess

$$\mathbf{d}_0 = [-\alpha w, \ \alpha w], \qquad \alpha = \max_j \frac{w_j''}{w_j'}, \tag{1.78}$$

in which the vectors $w \geq 0$, $w' > 0$, and

$$w' \leq w - |D_0 - \mathbf{D}|\,|BGA|\,w; \tag{1.79}$$

$$w'' \geq |D_0 - \mathbf{D}|\,|(BGa) + (BGF)\boldsymbol{\delta}|.$$

Then the following iterative scheme is used to obtain guaranteed interval enclosures of the auxiliary variables $\mathbf{v}$ and $\mathbf{d}$,

$$\mathbf{v}_j = \{(BGa) + (BGF)\boldsymbol{\delta} + (BGA)\mathbf{d}_{j-1}\} \cap \mathbf{v}_{j-1}; \tag{1.80}$$

$$\mathbf{d}_j = \{(D_0 - \mathbf{D})\mathbf{v}_j\} \cap \mathbf{d}_{j-1}.$$

The iteration stops when there is no improvement in $\mathbf{v}_j$ and $\mathbf{d}_j$ for two consecutive steps, and the converged solution is denoted as $\mathbf{v}^{out}$ and $\mathbf{d}^{out}$. Then a guaranteed interval solution $\mathbf{u}^{out}$ for the original linear system is obtained by substituting $\mathbf{d}$ with the converged $\mathbf{d}^{out}$ in Eq. (1.77).

1.2.2.3 Interval inner solution

The exact enclosure $\mathbf{u}^{enc}$, which is the tightest enclosure that contains the exact solution set, is usually difficult to compute and only available under very rare circumstances. More often only the interval outer solution $\mathbf{u}^{out}$ is available, which guarantees to enclose the exact enclosure $\mathbf{u}^{enc}$, viz. $\mathbf{u}^{out} \supseteq \mathbf{u}^{enc}$. Due to the isotonic inclusion of interval arithmetic operation, usually $\mathbf{u}^{out}$ overestimates $\mathbf{u}^{enc}$. Thus in order to reliably judge the overestimation level of $\mathbf{u}^{out}$ without explicitly computing $\mathbf{u}^{enc}$, the interval inner solution $\mathbf{u}^{inn}$ is sought, which satisfies $\mathbf{u}^{inn} \subseteq \mathbf{u}^{enc}$. If the overestimation in $\mathbf{u}^{out}$ is approximately the same as the underestimation in $\mathbf{u}^{inn}$, the difference between $\mathbf{u}^{out}$ and $\mathbf{u}^{inn}$ is used to evaluate the overestimation level.

In this work, a non-iterative interval approach is pursued to compute $\mathbf{u}^{inn}$, which was first proposed by Muhanna and Mullen [102]. The yielded inner solution has approximately the same overestimation level as the outer solution. For the converged outer solution $\mathbf{v}^{out}$ as in Eq. (1.80), the following equation holds

$$\mathbf{u} + (GA)(D_0 - \mathbf{D})(v_0 - \mathbf{v}) \tag{1.81}$$

$$= (Ga) + (GF)\mathbf{b} + (GA)(D_0 - \mathbf{D})v_0,$$

where v_0 is a reference vector such that $v_0 \in \mathbf{v}^{out}$, and preferably $v_0 = \text{mid } \mathbf{v}^{out}$. By noting that the right-hand side of Eq. (1.81) can be evaluated without overestimation (all interval variables appear only once) and defining the following auxiliary variables

$$\mathbf{P}_c = (Ga) + (GF)\mathbf{b} + (GA)(D_0 - \mathbf{D})v_0; \tag{1.82}$$

$$\mathbf{Q}_c = (GA)(D_0 - \mathbf{D})(v_0 - \mathbf{v}),$$

the inner solution $\mathbf{u}^{inn}$ is obtained as

$$\mathbf{u}^{inn} = \left[\underline{P}_c - \underline{Q}_c, \ \overline{P}_c - \overline{Q}_c \right] \tag{1.83}$$

where $\underline{a}$ and $\overline{a}$ denote the lower and upper bounds of an interval $\mathbf{a}$, respectively.

1.2.3 Alternative approaches

Besides the non-iterative interval approach outlined above, there are other non-interval approaches to obtain the inner solution $\mathbf{u}^{inn}$, which include nonlinear programming technique [16, 91], Monte Carlo simulation [110], sensitivity analysis [77], and endpoint combination method [109]. In general, these methods are computationally expensive and inefficient, and the results often underestimate the exact enclosure. However, when the situation permits, these methods can yield high-quality results, or even sometimes the exact enclosure. As an example, the structural forward problem is considered. Thus the structural parameter vector $\boldsymbol{\alpha}$ is given, and the goal is to predict the structural response $\mathbf{u}$. Apparently, the idea can be extended to account structural inverse problems.

1.2.3.1 Nonlinear programming approach

The nonlinear programming approach [16, 91] provides the exact solution set whenever convergence is reached. Both the parameter vector α and the response vector u are included in the solution vector x. The problem is formulated as a series of constrained minimization problems. To compute the lower or upper bound for the

j-th component in u, the objective function Γ to be minimized is given by

$$\Gamma = \pm u_j = \pm c_j^T u, \tag{1.84}$$

where $\pm$ corresponds to the lower and upper bounds, respectively, and c_j extracts the j-th component u_j from the response vector u. Equality constraints usually include the equilibrium condition of the structure, such as $Ku = f$, as well as essential boundary conditions. The interval condition $\alpha \in \boldsymbol{\alpha}$ can be interpreted as the corresponding inequality constraints,

$$\alpha \geq \underline{\alpha}, \qquad -\alpha \geq -\overline{\alpha}, \tag{1.85}$$

where $\underline{\alpha}$ and $\overline{\alpha}$ are the lower and upper bounds of $\boldsymbol{\alpha}$, respectively. Then standard nonlinear programming techniques are implemented to find the lower and upper bounds of u_j, starting from a deterministic solution that satisfies all the constraints, using the midpoint values for the parameter vector $\alpha_0 = \text{mid } \boldsymbol{\alpha}$.

The nonlinear programming approach is able to give exact bounds whenever convergence is attained and local minimums are avoided. However, it is computationally costly because one has to solve one constrained optimization problem for each component in the response vector u. Thus it is not applicable to large-scale problems. In addition, there is no guarantee of convergence prior to the analysis.

1.2.3.2 Monte Carlo simulation

In the Monte Carlo simulation approach [110], the corresponding deterministic solver is run multiple times, using randomly generated vectors $\alpha_k \in \boldsymbol{\alpha}$. Then the final interval solution $\mathbf{u}$ is obtained by combining all the deterministic solutions u_k,

$$\mathbf{u} = \left[\min_k u_k, \ \max_k u_k \right]. \tag{1.86}$$

The Monte Carlo simulation approach is flexible and non-intrusive, since it can use existing deterministic solvers without any adaptation. However, the method is very

slow. Usually thousands of simulations are required for a meaningful solution. The quality of the obtained solution often depends on the assumed probability distribution used to generate the parameter vector α_k in each simulation. In addition, the yielded results underestimate the uncertainty in the solution, and thus are non-conservative.

1.2.3.3 Sensitivity analysis

The sensitivity analysis also yields underestimated results and uses the deterministic solver. One version of the sensitivity analysis [77] can be conducted as follows:

1. A reference response vector u_0 is obtained using the midpoint values for the parameter vector $\alpha_0 = \text{mid } \boldsymbol{\alpha}$.

2. The same midpoint values are used for the parameter vector, except for the j-th component α_j, which is set as its lower or upper bound. The corresponding response vector is obtained as u_j. By comparing u_j with the reference vector u_0, the sign of $\partial u / \partial \alpha_j$ is obtained. Repeat for every component in $\boldsymbol{\alpha}$.

3. The lower (upper) bound of $\mathbf{u}$ is computed using deterministic vector α^- (α^+), whose j-th component is given by

   - $\alpha_j^- = \underline{\boldsymbol{\alpha}}_j$ and $\alpha_j^+ = \overline{\boldsymbol{\alpha}}_j$, for $\boldsymbol{\alpha}_j$ with positive $\partial u / \partial \alpha_j$;
   - $\alpha_j^- = \overline{\boldsymbol{\alpha}}_j$ and $\alpha_j^+ = \underline{\boldsymbol{\alpha}}_j$, for $\boldsymbol{\alpha}_j$ with negative $\partial u / \partial \alpha_j$.

This approach is also flexible and non-intrusive. However, it requires that the structural response vector $\mathbf{u}$ to vary monotonically within the interval ranges of the parameters. Thus it is not applicable to problems with severe nonlinearity and high uncertainty levels. In addition, the computation is still very costly, especially for large-scale problems.

1.2.3.4 Endpoint combination

The endpoint combination approach [109] uses the deterministic solver with all possible combinations of the lower and upper bounds of the parameter vector $\boldsymbol{\alpha}$. Then the

final solution **u** is combined from the corresponding deterministic solutions u_k from each run, using the same Eq. (1.86) as in the Monte Carlo simulation.

The method is also non-intrusive and easy to implement. However, as the number of combinations increases exponentially as the number of interval parameters increase, it is only applicable to structures with very few interval parameters. In addition, the method requires monotonicity to yield the exact enclosure. Thus it is usually used to provide a reference solution when the structure is simple and there are very few interval variables involved.

1.3   Research Objectives

In this dissertation, structural forward and inverse problems are studied, with uncertainties in load, geometry, and material. Intervals are used to model uncertainties in the structure, and Interval Finite Element Method (IFEM) is used as the cornerstone in the formulation. The structure is assumed to be subject to small deformations, so the strain-displacement relationship and the constitutive law are assumed linear. The formulation is implemented for trusses, frames, and plane stress/strain problems, and can be extended to other structural forms. The goal of the research is to obtain guaranteed interval enclosures on the exact solutions to the following problems:

a) Structural *static forward* problems. The structure is governed by the following equilibrium equation formulated by IFEM,

$$\mathbf{Ku} = \mathbf{f}, \tag{1.87}$$

where **K** is the stiffness matrix, **u** is the unknown nodal displacement vector, and **f** is the nodal equivalent load vector. The goal is to solve for the primary variable **u**, as well as derived variables such as the generalized strain $\boldsymbol{\varepsilon}$ and the generalized stress $\boldsymbol{\sigma}$ given by

$$\boldsymbol{\varepsilon} = B\mathbf{u}, \qquad \boldsymbol{\sigma} = \mathbf{Su}, \tag{1.88}$$

where B is the deterministic generalized strain-displacement matrix, and $\mathbf{S}$ is the interval generalized stress-displacement matrix.

b) Structural *static inverse* problems. The governing equations include the equilibrium and the measurement equation for the structure, viz.

$$\mathbf{Ku} = \mathbf{f}, \qquad \boldsymbol{\eta} = H\mathbf{u}, \tag{1.89}$$

where $\boldsymbol{\eta}$ is the measurement vector that is approximated by a linear function of the nodal displacement $\mathbf{u}$. The goal is to reliably estimate the interval stiffness parameter vector $\boldsymbol{\alpha}$, which parameterizes the stiffness matrix $\mathbf{K}$, based on the available measurement data stored in the measurement vector $\boldsymbol{\eta}$.

c) Structural *dynamic forward* problems. The research includes three different topics. In the *frequency response* analysis, the structure is analyzed in the frequency domain, which is governed by

$$\left(-\omega^2 \mathbf{M} + i\omega \mathbf{C} + \mathbf{K}\right) \mathbf{u} = \mathbf{f}, \tag{1.90}$$

where ω is the angular frequency of interest, $\mathbf{M}$ and $\mathbf{C}$ are the mass and damping matrix, respectively. In the *natural frequency* and *modal shape* analysis, the following Interval Generalized Eigenvalue Problem (IGEP) is solved

$$\left(-\boldsymbol{\omega}^2 \mathbf{M} + \mathbf{K}\right) \mathbf{u} = 0, \tag{1.91}$$

where $\boldsymbol{\omega}$ is the required natural frequency and $\mathbf{u}$ is the corresponding modal shape. In the *transient response* analysis, the structure is analyzed in the time domain, which is governed by

$$\mathbf{M}\ddot{\mathbf{u}} + \mathbf{C}\dot{\mathbf{u}} + \mathbf{Ku} = \mathbf{f}, \tag{1.92}$$

where $\dot{\mathbf{u}}$ and $\ddot{\mathbf{u}}$ are the nodal velocity and acceleration, respectively.

d) Structural *dynamic inverse* problems. Measurement data is processed and transformed into the frequency domain prior to the analysis. So the governing equations include the equilibrium and measurement equations as follows

$$\left(-\omega^2 \mathbf{M} + i\omega \mathbf{C} + \mathbf{K}\right) \mathbf{u} = \mathbf{f}, \qquad \boldsymbol{\eta} = H\mathbf{u}. \tag{1.93}$$

The measurement vector $\boldsymbol{\eta}$ can be strain or acceleration signals. The goal is to reliably estimate the interval stiffness parameter vector $\boldsymbol{\alpha}$ based on the interval measurement data stored in $\boldsymbol{\eta}$.

The proposed study includes structural forward problems, as well as structural inverse problems. This is because the innovative techniques in the proposed structural forward solvers are also essential in solving structural inverse problems. For instance, consider the static forward and inverse problems in Chapter 2 and 3. The deterministic forward solver is an integral part of the deterministic inverse solver. In addition, the interval inverse solver also utilizes the matrix decomposition strategy and essential boundary condition enforcement, which originates from the interval forward solver. Finally, the interval inverse solver is based on a variant of iterative enclosure method, which is originally developed to solve interval forward problems. As a result, the proposed study contains both the forward and inverse problems.

1.4 *Summary*

In this chapter, background information regarding the proposed research is introduced, which include discussions on structural inverse problems and the interval-based uncertainty modeling and analysis. Specifically, ill-conditioning and regularization of inverse problems are included, followed by the introductions on the optimization method, the Kalman filters, and the pseudo-inverse method. Then preliminaries on interval arithmetic and Interval Finite Element Method (IFEM) are presented in detail, followed by a review of non-interval approaches that are commonly used for comparison. Finally, the objectives of the proposed research is stated.

CHAPTER II

UNCERTAINTY ANALYSIS OF STRUCTURAL STATIC PROBLEMS BY INTERVALS

In this chapter, interval forward solvers are developed for structural static problems with uncertainties in load, geometry and material. The system uncertainties are modeled by interval variables, and Interval Finite Element Method (IFEM) [24, 54, 68, 159] is implemented. Thus the structural equilibrium condition can be described by the following interval linear system

$$\mathbf{Ku} = \mathbf{f}, \tag{2.1}$$

where $\mathbf{K}$ is the stiffness matrix, $\mathbf{u}$ is the nodal displacement vector, and $\mathbf{f}$ is the nodal equivalent load vector. Then the proposed solver aims to obtain guaranteed interval enclosures for the primary unknown variable $\mathbf{u}$, as well as the following derived variables

$$\boldsymbol{\varepsilon} = B\mathbf{u}, \qquad \boldsymbol{\sigma} = \mathbf{Su}, \tag{2.2}$$

where $\boldsymbol{\varepsilon}$ and $\boldsymbol{\sigma}$ represent the generalized strain and stress vector, respectively, B and $\mathbf{S}$ are corresponding generalized strain- and stress-displacement matrix.

In the following sections, the proposed interval forward solver is introduced in detail. In addition, the nonlinear programming approach is implemented to provide reference solutions. Then the performance of the proposed method, the nonlinear programming approach and other available methods outlined in Section 1.2.3 is tested in a couple of numerical examples. The results show that the proposed method gives guaranteed enclosure of the exact solution at low computational cost, and the yielded solution is the tightest among the available methods in the literature.

35

2.1 Interval Finite Element Formulation

To solve the interval linear system with the least overestimation possible, new decomposition strategies are proposed for the IFEM variables encountered. The matrix decompositions avoid multiple occurrences of the same interval variables, and consequently reduce the overestimation due to interval dependency [101]. In particular, the stiffness matrix $\mathbf{K}$ and the nodal equivalent load $\mathbf{f}$ are decomposed into

$$\mathbf{K} = A\text{diag}(\Lambda\boldsymbol{\alpha})A^T, \quad \mathbf{f} = F\boldsymbol{\delta}, \tag{2.3}$$

where A, Λ, F are deterministic matrices, $\boldsymbol{\alpha}$ is the interval stiffness parameter vector that accounts for the geometric and material uncertainties in $\mathbf{K}$, and $\boldsymbol{\delta}$ is the load uncertainty vector that accounts for the load uncertainty in $\mathbf{f}$.

The derived variables are solved simultaneously as the primary variable, by introducing Lagrangian multipliers into the energy functional of the problem [119]. Thus any unnecessary interval intermediate steps are avoided and overestimation due to interval dependency is reduced. In addition, as the generalized stress-displacement matrix $\mathbf{S}$ is linearly dependent on the material properties, it is decomposed into

$$\mathbf{S} = \Phi_s\text{diag}(\Lambda_s\boldsymbol{\alpha})A_s^T, \tag{2.4}$$

where Φ_s, Λ_s, and A_s are deterministic matrices.

In practice, the decompositions in Eqs. (2.3) and (2.4) are performed at the element level before assembly. First the element stiffness matrix $\mathbf{K}_e$ and the element nodal equivalent load vector $\mathbf{f}_e$ are computed. Their decompositions yield the element matrices A_e, Λ_e, F_e, $\boldsymbol{\alpha}_e$ and $\boldsymbol{\delta}_e$. These are further assembled into their global counterparts A, Λ, F, $\boldsymbol{\alpha}$ and $\boldsymbol{\delta}$. During the assembly, either the Element-by-Element (EBE) assembly strategy or the conventional strategy is adopted. In the following subsections, details on the aforementioned topics are discussed.

2.1.1 Element matrix decomposition

In this subsection, decompositions for the element stiffness matrix $\mathbf{K}_e$, the element nodal equivalent load $\mathbf{f}_e$, and the element generalized stress-displacement matrix $\mathbf{S}_e$ are presented.

2.1.1.1 Decomposition of $\mathbf{K}_e$

According to Eq. (2.3), the element stiffness matrix $\mathbf{K}_e$ is decomposed into

$$\mathbf{K}_e = A_e \mathrm{diag}(\Lambda_e \boldsymbol{\alpha}_e) A_e^T, \tag{2.5}$$

where A_e and Λ_e are deterministic matrices, and $\boldsymbol{\alpha}_e$ accounts for the geometric and material uncertainties in $\mathbf{K}_e$. In the following discussion, plane truss, plane frame, and plane stress/strain elements are used, but the idea is applicable to other elements.

For the standard two-node plane truss elements, because there are uncertainties in the geometry and material property, the cross section area $\mathbf{A}$ and the Young's modulus $\mathbf{E}$ are modeled as intervals. The corresponding element stiffness matrix $\mathbf{K}_e$ in the local coordinate system is given by

$$\mathbf{K}_e = \left\{ \begin{matrix} \dfrac{\mathbf{EA}}{L} & 0 & -\dfrac{\mathbf{EA}}{L} & 0 \\ 0 & 0 & 0 & 0 \\ -\dfrac{\mathbf{EA}}{L} & 0 & \dfrac{\mathbf{EA}}{L} & 0 \\ 0 & 0 & 0 & 0 \end{matrix} \right\}. \tag{2.6}$$

where L is the element length. Then $\boldsymbol{\alpha}_e$ contains the only interval variables $\mathbf{EA}$ in the element, and the corresponding deterministic matrices A_e and Λ_e are given by

$$A_e = \left\{ \begin{matrix} -1 & 0 & 1 & 0 \end{matrix} \right\}^T, \qquad \Lambda_e = \left\{ 1/L \right\}, \qquad \boldsymbol{\alpha}_e = \left\{ \mathbf{EA} \right\}. \tag{2.7}$$

For the standard two-node Euler-Bernoulli beam elements, the cross section area $\mathbf{A}$, the moment of inertia $\mathbf{I}$, and the Young's modulus $\mathbf{E}$ are modeled as intervals.

Considering the axial and bending deformation, the corresponding $\mathbf{K}_e$ in the local coordinate system is given by

$$\mathbf{K}_e = \left\{ \begin{array}{cccccc} \dfrac{\mathbf{EA}}{L} & 0 & 0 & -\dfrac{\mathbf{EA}}{L} & 0 & 0 \\[2mm] 0 & \dfrac{12\mathbf{EI}}{L^3} & \dfrac{6\mathbf{EI}}{L^2} & 0 & -\dfrac{12\mathbf{EI}}{L^3} & \dfrac{6\mathbf{EI}}{L^2} \\[2mm] 0 & \dfrac{6\mathbf{EI}}{L^2} & \dfrac{4\mathbf{EI}}{L} & 0 & -\dfrac{6\mathbf{EI}}{L^2} & \dfrac{2\mathbf{EI}}{L} \\[2mm] -\dfrac{\mathbf{EA}}{L} & 0 & 0 & \dfrac{\mathbf{EA}}{L} & 0 & 0 \\[2mm] 0 & -\dfrac{12\mathbf{EI}}{L^3} & -\dfrac{6\mathbf{EI}}{L^2} & 0 & \dfrac{12\mathbf{EI}}{L^3} & -\dfrac{6\mathbf{EI}}{L^2} \\[2mm] 0 & \dfrac{6\mathbf{EI}}{L^2} & \dfrac{2\mathbf{EI}}{L} & 0 & -\dfrac{6\mathbf{EI}}{L^2} & \dfrac{2\mathbf{EI}}{L} \end{array} \right\}, \tag{2.8}$$

where L is the element length. Then $\boldsymbol{\alpha}_e$ contains the element axial stiffness $\mathbf{EA}$ and the element bending stiffness $\mathbf{EI}$. The corresponding A_e is a 6×3 matrix, whose columns are the eigenvectors of $\mathbf{K}_e$, and Λ_e is a 3×2 matrix,

$$A_e = \left\{ \begin{array}{ccc} 1 & 0 & 0 \\ 0 & 0 & 2 \\ 0 & 1 & L \\ -1 & 0 & 0 \\ 0 & 0 & -2 \\ 0 & -1 & L \end{array} \right\}, \qquad \Lambda_e = \left\{ \begin{array}{cc} \dfrac{2}{L} & 0 \\[2mm] 0 & \dfrac{2}{L^3} \\[2mm] 0 & \dfrac{3}{L^3} \end{array} \right\}, \qquad \boldsymbol{\alpha}_e = \left\{ \begin{array}{c} \mathbf{EA} \\ \mathbf{EI} \end{array} \right\}. \tag{2.9}$$

Note that the above decompositions in Eqs. (2.7) and (2.9) are not unique. This approach requires the analytical expression for $\mathbf{K}_e$, which is usually not available for most finite elements. Thus in the following discussion, a different approach based on numerical integration is presented, using plane stress/strain elements as illustration. This approach can be extended to a wide range of elements.

For the standard 8-node rectangular isoparametric elements in plane stress/strain problem, the element Young's modulus $\mathbf{E}$ is modeled as intervals. Then the corresponding $\mathbf{K}_e$ is given by

$$\mathbf{K}_e = \int_\Omega B_e^T(\xi) \mathbf{E}_e(\xi) B_e(\xi) t(\xi) d\Omega, \tag{2.10}$$

38

where the integration domain Ω is just the entire element, t is the thickness, and B_e is the strain-displacement matrix. For isotropic material with Poisson's ratio ν, the interval constitutive matrix $\mathbf{E}_e$ for plane stress state is given by

$$\mathbf{E}_e = \frac{\mathbf{E}}{1-\nu^2} \begin{Bmatrix} 1 & \nu & 0 \\ \nu & 1 & 0 \\ 0 & 0 & \dfrac{1-\nu}{2} \end{Bmatrix}. \tag{2.11}$$

and for plane strain state,

$$\mathbf{E}_e = \frac{\mathbf{E}}{(1-2\nu)(1+\nu)} \begin{Bmatrix} 1-\nu & \nu & 0 \\ \nu & 1-\nu & 0 \\ 0 & 0 & \dfrac{1-2\nu}{2} \end{Bmatrix}. \tag{2.12}$$

The double integral in Eq. (2.10) can be evaluated numerically by using a 3×3 Gaussian integration rule, that is

$$\mathbf{K}_e = \sum_{j=1}^{9} B_e^T(\xi_j)\mathbf{E}_e(\xi_j)B_e(\xi_j)w_j J(\xi_j)t(\xi_j), \tag{2.13}$$

where the coordinates ξ_j and weights w_j for all the integration points in the standard domain $[-1, 1] \times [-1, 1]$ are given, and J is the determinant of the Jacobian of the coordinate transformation between the local and global reference system. Note that the use of numerical integration has the effect of changing the modulus from a spatial function bounded by interval values to a function described by interval coefficients. Thus the discretization by the finite element methods results in additional smoothness in the spatial variation of the modulus field.

In Eq. (2.13), the only interval term $\mathbf{E}$ can be factored out, viz. $\mathbf{K}_e = P_e\mathbf{E}$, where P_e is a deterministic matrix. This can be decomposed as $P_e = A_e\mathrm{diag}(\Lambda_e)A_e^T$, where Λ_e is the eigenvalue matrix and the columns of A_e are the corresponding eigenvectors. Note that Λ_e includes three zero eigenvalues, which correspond to rigid body motion of translation and rotation. They are dropped and Eq. (2.13) is rewritten as

$$\mathbf{K}_e = A_e\mathrm{diag}(\Lambda_e)A_e^T\boldsymbol{\alpha}_e = A_e\mathrm{diag}(\Lambda_e\boldsymbol{\alpha}_e)A_e^T, \tag{2.14}$$

where $\boldsymbol{\alpha}_e = \{\mathbf{E}\}$ is the only interval quantity. One can also use an LDL decomposition of P_e. As a result, A_e is a lower unitriangular matrix, and Λ_e is also different.

In the above decomposition strategy, P_e is explicitly computed in order to obtain A_e and Λ_e. In addition, the Young's modulus $\mathbf{E}$ is assumed to be constant inside the element. Alternatively, the B-matrix approach outlined below can be adopted, in which P_e is never explicitly computed and the element stiffness parameter vector $\boldsymbol{\alpha}_e$ contains $\mathbf{E}_j$ at all the numerical integration points.

The B-matrix approach first decompose the constitutive matrix $\mathbf{E}_e(\xi_j)$ into

$$\mathbf{E}_e(\xi_j) = \Phi_e \mathrm{diag}\{\phi_e \mathbf{E}_j\} \Phi_e^T. \tag{2.15}$$

where Φ_e is a 3×3 deterministic matrix and ϕ_e is a 3×1 deterministic vector, both depending on the Poisson's ratio ν. And $\mathbf{E}_j$ denotes the Young's modulus at the j-th integration point ξ_j. Then, from Eq. (2.13)

$$
\begin{aligned}
\mathbf{K}_e &= \sum_{j=1}^{9} B_e^T(\xi_j) \Phi_e \mathrm{diag}\{\phi_e \mathbf{E}_j\} \Phi_e^T B_e(\xi_j) w_j J_j t_j \\
&= \left\{ B_e^T(\xi_1)\Phi_e \quad \cdots \quad B_e^T(\xi_9)\Phi_e \right\} \\
&\quad \left\{ \begin{matrix} (w_1 J_1 t_1)\mathrm{diag}(\phi_e)\mathbf{E}_1 & & \\ & \ddots & \\ & & (w_9 J_9 t_9)\mathrm{diag}(\phi_e)\mathbf{E}_9 \end{matrix} \right\} \left\{ \begin{matrix} \Phi_e^T B_e(\xi_1) \\ \vdots \\ \Phi_e^T B_e(\xi_9) \end{matrix} \right\},
\end{aligned}
\tag{2.16}
$$

where the subscripts $_j$ denotes variables evaluated at the j-th integration point. Then the deterministic matrices A_e and Λ_e are obtained as

$$A_e = \left\{ B_e^T(\xi_1)\Phi_e \quad \cdots \quad B_e^T(\xi_9)\Phi_e \right\};$$

$$\Lambda_e = \left\{ \begin{matrix} w_1 J_1 t_1 \phi_e & & \\ & \ddots & \\ & & w_9 J_9 t_9 \phi_e \end{matrix} \right\}, \qquad \boldsymbol{\alpha}_e = \left\{ \begin{matrix} \mathbf{E}_1 \\ \vdots \\ \mathbf{E}_9 \end{matrix} \right\}. \tag{2.17}$$

The B-matrix approach yields A_e and Λ_e directly from B_e and $\mathbf{E}_e$, but matrices are larger than those from the eigen- or LDL-decomposition. Indeed, in the eigen- or

LDL-decomposition, a 16×16 matrix $\mathbf{K}_e$ is decomposed, and A_e is 16×13 and Λ_e is 13×1. In the B-matrix approach, a 3×3 matrix $\mathbf{E}_e$ is decomposed, and A_e is 16×27 and Λ_e is 27×9. Clearly, the B-matrix approach saves time in the decomposition process, but it is more time-consuming in later computation. Comparisons between the performance of these decomposition strategies are presented in the numerical examples section.

Finally, note that the decomposition of diagonal matrix $\text{diag}(\Lambda_e \boldsymbol{\alpha}_e)$ is novel in the current method, when compared with others in the literature [53, 68, 110]. The decomposition reduces multiple occurrences of interval terms to the minimum. In later discussions on iterative enclosure method, this decomposition plays an important role.

2.1.1.2 Decomposition of $\mathbf{f}_e$

The element nodal equivalent load vector $\mathbf{f}_e$ is decomposed into the following form using the M-$\boldsymbol{\delta}$ method [105],

$$\mathbf{f}_e = F_e \boldsymbol{\delta}_e. \tag{2.18}$$

Thus the interval terms in the element load uncertainty vector $\boldsymbol{\delta}_e$ is completely separated from the deterministic part F_e of the equivalent load. For an arbitrary element, its nodal equivalent load vector is given by

$$\mathbf{f}_e = \sum_j N^T(\xi_j)\mathbf{f}_0(\xi_j) + \int_{\Omega_1} N^T(\xi)\mathbf{f}_1(\xi)d\Omega_1 \tag{2.19}$$
$$+ \int_{\Omega_2} N^T(\xi)\mathbf{f}_2(\xi)d\Omega_2 + \int_{\Omega_3} N^T(\xi)\mathbf{f}_3(\xi)d\Omega_3,$$

where $N(\xi)$ is the shape function matrix, ξ is the local coordinate of the element, ξ_j are coordinates where concentrated load is applied, $\mathbf{f}_0(\xi_j)$ are the concentrated loads under consideration, Ω_1, Ω_2, Ω_3 are the integration domains in which line load $\mathbf{f}_1$, surface load $\mathbf{f}_2$, volume load $\mathbf{f}_3$ are non-zero.

By rewriting $\mathbf{f}_j(\xi) = L_j(\xi)\boldsymbol{\delta}_e$ $(j = 0, 1, 2, 3)$, the interval element load uncertainty
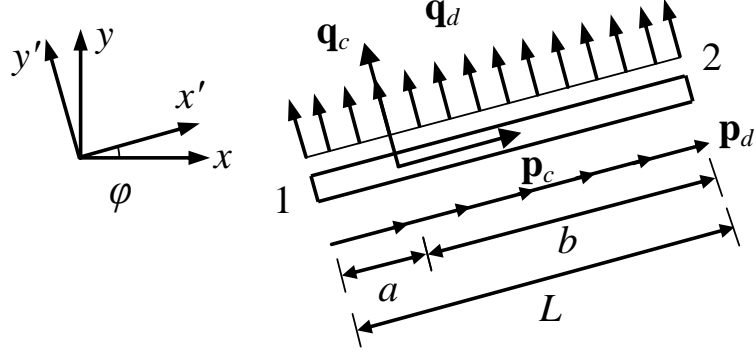
Figure 2.1: Distributed and concentrated loads acting on a two-node Euler-Bernoulli beam element.

vector $\boldsymbol{\delta}_e$ can be separated from the deterministic part of $\mathbf{f}_e$. Then

$$F_e = \sum_j N^T(\xi_j)L_0(\xi_j) + \int_{\Omega_1} N^T(\xi)L_1(\xi)d\Omega_1 \tag{2.20}$$

$$+ \int_{\Omega_2} N^T(\xi)L_2(\xi)d\Omega_2 + \int_{\Omega_3} N^T(\xi)L_3(\xi)d\Omega_3,$$

As a first example, consider the Euler-Bernoulli beam element of length L shown in Figure 2.1. The element is subject to concentrated loads $\mathbf{p}_c$ and $\mathbf{q}_c$ applied at distance a from node 1, as well as transverse uniform load $\mathbf{q}_d$ and axial uniform load $\mathbf{p}_d$ along the element. Then the element nodal equivalent load vector $\mathbf{f}_e$ and its decomposition are given by

$$\mathbf{f} = \left\{ \begin{array}{c} \dfrac{b}{L}\mathbf{p}_c + \dfrac{L}{2}\mathbf{p}_d \\[2mm] \dfrac{b}{L}\mathbf{q}_c + \dfrac{L}{2}\mathbf{q}_d \\[2mm] \dfrac{L^2}{12}\mathbf{q}_d \\[2mm] \dfrac{a}{L}\mathbf{p}_c + \dfrac{L}{2}\mathbf{p}_d \\[2mm] \dfrac{a}{L}\mathbf{q}_c + \dfrac{L}{2}\mathbf{q}_d \\[2mm] \dfrac{L^2}{12}\mathbf{q}_d \end{array} \right\} = \left\{ \begin{array}{cccc} \dfrac{b}{L} & 0 & \dfrac{L}{2} & 0 \\[2mm] 0 & \dfrac{b}{L} & 0 & \dfrac{L}{2} \\[2mm] 0 & 0 & 0 & \dfrac{L^2}{12} \\[2mm] \dfrac{b}{L} & 0 & \dfrac{L}{2} & 0 \\[2mm] 0 & \dfrac{a}{L} & 0 & \dfrac{L}{2} \\[2mm] 0 & 0 & 0 & \dfrac{L^2}{12} \end{array} \right\} \left\{ \begin{array}{c} \mathbf{p}_c \\[2mm] \mathbf{q}_c \\[2mm] \mathbf{p}_d \\[2mm] \mathbf{q}_d \end{array} \right\} = F_e\boldsymbol{\delta}_e, \tag{2.21}$$

where the load uncertainty vector $\boldsymbol{\delta}_e$ contains the four intervals in $\mathbf{f}_e$, and each column of F_e corresponds to one of them.
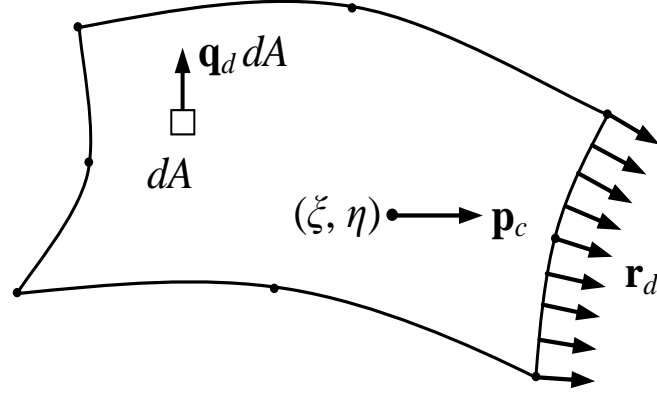
Figure 2.2: Concentrated, body and line loads acting on an 8-node rectangular isoparametric element.

As a second example, consider the 8-node rectangular isoparametric element in Figure 2.2. The element is subject to a concentrated load $\mathbf{p}_c$ in the x-direction at (ξ, η), a uniform body load $\mathbf{q}_d$ in the y-direction, and a uniform line load $\mathbf{r}_d$ outwards on the right edge. Then $\boldsymbol{\delta}_e = \{\mathbf{p}_c\ \mathbf{q}_d\ \mathbf{r}_d\}^T$ and F_e is given by

$$
F_e = \left\{
\begin{array}{ccc}
N_1(\xi, \eta) & 0 & \int_{x=0}^{L} N_1 J_{11} dl \\
0 & \iint_A N_1(\xi, \eta) dA & \int_{x=0}^{L} N_1 J_{21} dl \\
\vdots & \vdots & \vdots \\
N_8(\xi, \eta) & 0 & \int_{x=0}^{L} N_8 J_{11} dl \\
0 & \iint_A N_8(\xi, \eta) dA & \int_{x=0}^{L} N_8 J_{21} dl
\end{array}
\right\},
\tag{2.22}
$$

where N_j is the shape function with respect to the j-th node, L is the length of the right edge, and $\{J_{11}\ J_{21}\}^T$ is the first column of the Jacobian, accounting for the uniform load $\mathbf{r}_d$ acting on the right edge. The formulation can be easily extended to cases when the loads are non-uniform or defined in the local coordinate system.

2.1.1.3 Decomposition of $\mathbf{S}_e$

The element stress-displacement matrix $\mathbf{S}_e$, which is linearly dependent on the element stiffness parameter vector $\boldsymbol{\alpha}_e$, is decomposed into a similar form as $\mathbf{K}_e$

$$
\mathbf{S}_e = \Phi_{se} \text{diag}(\Lambda_{se}\boldsymbol{\alpha}_e) A_{se}^T.
\tag{2.23}
$$

For illustration, consider the standard 8-node rectangular isoparametric element discussed on Page 40. Then the stress $\boldsymbol{\sigma}_e$ at given location is interpolated/extrapolated from stresses at the numerical integration points,

$$\boldsymbol{\sigma}_e = \sum_{j=1}^{9} v_j \boldsymbol{\sigma}_e(\xi_j) = \sum_{j=1}^{9} v_j \mathbf{E}_e(\xi_j) B_e(\xi_j) \mathbf{u}_e, \tag{2.24}$$

where ξ_j are the coordinate of the integration points, and v_j are the corresponding interpolation/extrapolation weights. Factoring out $\mathbf{u}_e$, the element stress-displacement matrix

$$\mathbf{S}_e = \sum_{j=1}^{9} v_j \mathbf{E}_e(\xi_j) B_e(\xi_j). \tag{2.25}$$

Substituting $\mathbf{E}_e(\xi_j) = \Phi_e \mathrm{diag}\{\phi_e \mathbf{E}_j\} \Phi_e^T$ in Eq. (2.15) into the above equation yields

$$\mathbf{S}_e = \sum_{j=1}^{9} v_j \Phi_e \mathrm{diag}\{\phi_e \mathbf{E}_j\} \Phi_e^T B_e(\xi_j)$$

$$= \left\{ \Phi_e \quad \cdots \quad \Phi_e \right\} \left\{ \begin{matrix} v_1 \mathrm{diag}(\phi_e) \mathbf{E}_1 & & \\ & \ddots & \\ & & v_9 \mathrm{diag}(\phi_e) \mathbf{E}_9 \end{matrix} \right\} \left\{ \begin{matrix} \Phi_e^T B_e(\xi_1) \\ \vdots \\ \Phi_e^T B_e(\xi_9) \end{matrix} \right\}. \tag{2.26}$$

Then the deterministic matrices Φ_{se}, Λ_{se}, and A_{se} are obtained as

$$\Phi_{se} = \left\{ \Phi_e \quad \cdots \quad \Phi_e \right\}, \quad \Lambda_{se} = \left\{ \begin{matrix} v_1 \phi_e & & \\ & \ddots & \\ & & v_9 \phi_e \end{matrix} \right\};$$

$$A_{se} = \left\{ B_e^T(\xi_1) \Phi_e \quad \cdots \quad B_e^T(\xi_9) \Phi_e \right\}. \tag{2.27}$$

The idea can be easily extended to other type of elements.

2.1.2 Element assembly strategies

In this subsection, $\mathbf{K}_e$, $\mathbf{f}_e$, $\mathbf{S}_e$, and B_e are assembled into their global counterparts $\mathbf{K}$, $\mathbf{f}$, $\mathbf{S}$, and B. At the same time, the assembly rule for the decomposed matrices are presented. Two assembly strategies are introduced here: one is the Element-by-Element approach, which assembles the matrices block-by-block; the other is the conventional FEM assembly strategy.

2.1.2.1 Element-by-Element assembly

In the Element-by-Element approach, the structure is modeled by separated elements and common nodes that connect the elements. As a result, the structural nodal displacement vector $\mathbf{u}$ is a collection of all the element nodal displacement vectors $\mathbf{u}_e$, and the nodal displacement vector $\mathbf{u}_n$ of the common nodes. Then the global stiffness matrix $\mathbf{K}$ and nodal equivalent load $\mathbf{f}$ are assembled from their element counterparts

$$\mathbf{u} = \begin{Bmatrix} \mathbf{u}_e \\ \vdots \\ \mathbf{u}_e \\ \mathbf{u}_n \end{Bmatrix}, \qquad \mathbf{K} = \begin{Bmatrix} \mathbf{K}_e & & \\ & \ddots & \\ & & \mathbf{K}_e \\ & & & 0 \end{Bmatrix}, \qquad \mathbf{f} = \begin{Bmatrix} \mathbf{f}_e \\ \vdots \\ \mathbf{f}_e \\ \mathbf{f}_n \end{Bmatrix}, \qquad (2.28)$$

where $\mathbf{f}_n$ denotes concentrated forces applied directly on the common nodes. In contrast to the standard FEM assembly, $\mathbf{K}$ and $\mathbf{f}$ are assembled block by block from the individual element stiffness $\mathbf{K}_e$ and individual element load $\mathbf{f}_e$, respectively [119]. Note that $\mathbf{K}$ is a singular matrix.

To reduce overestimation due to dependency of multiple occurrences of the same variable, $\mathbf{K}$ and $\mathbf{f}$ are further decomposed as in Eq. (2.3), viz. $\mathbf{K} = A\mathrm{diag}(\Lambda\boldsymbol{\alpha})A^T$ and $\mathbf{f} = F\boldsymbol{\delta}$. The element vectors $\boldsymbol{\alpha}_e$ and $\boldsymbol{\delta}_e$ can be selected components of the global interval vectors $\boldsymbol{\alpha}$ and $\boldsymbol{\delta}$, or they can be interpolated from $\boldsymbol{\alpha}$ and $\boldsymbol{\delta}$. In either way, they can be brought into the following form,

$$\boldsymbol{\alpha}_e = L_\alpha\boldsymbol{\alpha}, \quad \boldsymbol{\delta}_e = L_\delta\boldsymbol{\delta}. \qquad (2.29)$$

The corresponding assembly rule for A, Λ, and F is quite similar to the assembly rule for $\mathbf{K}$ and $\mathbf{f}$. Indeed, they are all assembled block by block,

$$A = \begin{Bmatrix} A_e & & \\ & \ddots & \\ & & A_e \\ 0 & \cdots & 0 \end{Bmatrix}, \qquad \Lambda = \begin{Bmatrix} \Lambda_e L_\alpha \\ \vdots \\ \Lambda_e L_\alpha \end{Bmatrix}, \qquad F = \begin{Bmatrix} F_e L_\delta \\ \vdots \\ F_e L_\delta \\ F_n \end{Bmatrix}. \qquad (2.30)$$

where $\mathbf{f}_n = F_n \boldsymbol{\delta}$ is the decomposition of $\mathbf{f}_n$. In the derivation, it is assumed that each interval component in $\boldsymbol{\alpha}$ and $\boldsymbol{\delta}$ varies independently. If two or more components in $\boldsymbol{\alpha}$ or $\boldsymbol{\delta}$ represent the same variable, corresponding columns in Λ or F should be added together. If certain entries in $\boldsymbol{\delta}$ were equal to zero, the corresponding columns in F should be deleted.

The structural strain vector $\boldsymbol{\varepsilon}$ combines all the element strain vectors $\boldsymbol{\varepsilon}_e$ of interest to the analysis, while the corresponding strain-displacement matrix B is assembled block by block from B_e,

$$\boldsymbol{\varepsilon} = \left\{ \begin{array}{c} \boldsymbol{\varepsilon}_e \\ \vdots \\ \boldsymbol{\varepsilon}_e \end{array} \right\}, \qquad B = \left\{ \begin{array}{ccc} B_e & & 0 \\ & \ddots & \vdots \\ & & B_e \quad 0 \end{array} \right\}. \tag{2.31}$$

The assembly rules for the stress vector $\boldsymbol{\sigma}$ and the stress-displacement matrix $\mathbf{S}$ are the same as those for $\boldsymbol{\varepsilon}$ and B, respectively

$$\boldsymbol{\sigma} = \left\{ \begin{array}{c} \boldsymbol{\sigma}_e \\ \vdots \\ \boldsymbol{\sigma}_e \end{array} \right\}, \qquad \mathbf{S} = \left\{ \begin{array}{ccc} \mathbf{S}_e & & 0 \\ & \ddots & \vdots \\ & & \mathbf{S}_e \quad 0 \end{array} \right\}. \tag{2.32}$$

The assembly rule for deterministic matrices Φ_s, Λ_s, and A_s are given by

$$\Phi_s = \left\{ \begin{array}{ccc} \Phi_{se} & & \\ & \ddots & \\ & & \Phi_{se} \end{array} \right\}, \qquad \Lambda_s = \left\{ \begin{array}{c} \Lambda_{se} L_\alpha \\ \vdots \\ \Lambda_{se} L_\alpha \end{array} \right\}, \qquad A_s = \left\{ \begin{array}{cccc} A_{se} & & & \\ & \ddots & & \\ & & A_{se} & \\ 0 & \cdots & & 0 \end{array} \right\}. \tag{2.33}$$

2.1.2.2 Conventional assembly

The conventional assembly strategy provides smaller stiffness matrix and is more efficient for large scale problems. In this case, the global nodal displacement vector $\mathbf{u}$ contains only displacement vector $\mathbf{u}_n$ of the common nodes. The global stiffness matrix and nodal equivalent load vector are given by

$$\mathbf{K} = \sum_e T_e^T \mathbf{K}_e T_e, \qquad \mathbf{f} = \sum_e T_e^T \mathbf{f}_e + \mathbf{f}_n, \tag{2.34}$$

where T_e is the transformation matrix between the global and local nodal displacement vector $\mathbf{u}$ and $\mathbf{u}_e$. By inserting $\mathbf{K}_e = A_e \mathrm{diag}(\Lambda_e \boldsymbol{\alpha}_e) A_e^T$ of Eq. (2.5) into Eq. (2.34), the decomposition rule for $\mathbf{K}$ follows as

$$\mathbf{K} = \sum_e T_e^T A_e \mathrm{diag}(\Lambda_e \boldsymbol{\alpha}_e) A_e^T T_e \tag{2.35}$$

$$= \left\{ T_e^T A_e \quad \cdots \quad T_e^T A_e \right\} \mathrm{diag} \left\{ \begin{matrix} \Lambda_e \boldsymbol{\alpha}_e \\ \vdots \\ \Lambda_e \boldsymbol{\alpha}_e \end{matrix} \right\} \left\{ \begin{matrix} A_e^T T_e \\ \vdots \\ A_e^T T_e \end{matrix} \right\}.$$

The assembly rules for A and Λ are given by

$$A = \left\{ T_e^T A_e \quad \cdots \quad T_e^T A_e \right\}, \qquad \Lambda = \left\{ \begin{matrix} \Lambda_e L_\alpha \\ \vdots \\ \Lambda_e L_\alpha \end{matrix} \right\}. \tag{2.36}$$

Similarly, using the decompositions $\mathbf{f}_e = F_e \boldsymbol{\delta}_e$ and $\mathbf{f}_n = F_n \boldsymbol{\delta}_n$, the nodal equivalent load $\mathbf{f}$ in Eq. (2.34) can be written as

$$\mathbf{f} = \sum_e T_e^T F_e \boldsymbol{\delta}_e + F_n \boldsymbol{\delta}_n. \tag{2.37}$$

The assembly rule for F is given by

$$F = \sum_e T_e^T F_e L_\delta + F_n. \tag{2.38}$$

Finally, the global B and $\mathbf{S}$ are obtained from

$$B = \left\{ \begin{matrix} B_e T_e \\ \vdots \\ B_e T_e \end{matrix} \right\}, \qquad \mathbf{S} = \left\{ \begin{matrix} \mathbf{S}_e T_e \\ \vdots \\ \mathbf{S}_e T_e \end{matrix} \right\}. \tag{2.39}$$

The assembly rules for Φ_s and Λ_s are exactly the same as in Eq. (2.33), and the assembly rule for A_s is given by

$$A_s = \left\{ T_e^T A_{se} \quad \cdots \quad T_e^T A_{se} \right\}. \tag{2.40}$$

2.1.3   Calculation of derived variables

In this subsection, derived variables are solved simultaneously as the primary variable $\mathbf{u}$ via the introduction of Lagrangian multipliers into the energy functional of the structure. In the indirect approach, internal forces and support reactions can be obtained as a by-product during the enforcement of compatibility and essential boundary conditions. In contrast, in the direct approach, derived variables such as $\boldsymbol{\sigma}$ and $\boldsymbol{\varepsilon}$ are obtained by directly enforcing $\boldsymbol{\sigma} = \mathbf{S}\mathbf{u}$ and $\boldsymbol{\varepsilon} = B\mathbf{u}$, respectively.

2.1.3.1   The indirect approach

The obtained stiffness matrix $\mathbf{K}$ from the earlier EBE assembly strategies is singular, because there is no connection between elements and common nodes, and essential boundary conditions are not applied yet. To eliminate this singularity, compatibility requirements and essential boundary conditions are enforced, which are collected into the matrix constraint equation $C\mathbf{u} = 0$. For instance, consider the two-node Euler-Bernoulli element discussed earlier. To enforce compatibility between one element node (with three DOF) and the connecting common node, the corresponding three rows of C take the following simple form,

$$
C = \begin{Bmatrix}
\cdots & \cdots & \cdots & \cdots & \cdots & \cdots & \cdots & \cdots & \cdots \\
\cdots & 1 & 0 & 0 & \cdots & -\cos\varphi & -\sin\varphi & 0 & \cdots \\
\cdots & 0 & 1 & 0 & \cdots & \sin\varphi & -\cos\varphi & 0 & \cdots \\
\cdots & 0 & 0 & 1 & \cdots & 0 & 0 & -1 & \cdots \\
\cdots & \cdots & \cdots & \cdots & \cdots & \cdots & \cdots & \cdots & \cdots
\end{Bmatrix}
\qquad (2.41)
$$

$$\overbrace{}^{\text{element node DOF}} \qquad \overbrace{}^{\text{common node DOF}}$$

where φ is the rotational angle between the local and global coordinate systems for each element, $\mathbf{u}_e$ for the element nodes is given in the local coordinate system, $\mathbf{u}_n$ for the common nodes is given in the global coordinate system, and the rest entries

of these three rows are zeros. For the 8-node rectangular isoparametric element (two DOF at each node), the corresponding two rows of C are given by

$$\text{element node DOF} \quad \text{common node DOF}$$

$$C = \begin{Bmatrix} \cdots & \cdots & \cdots & \cdots & \cdots & \cdots & \cdots \\ \cdots & 1 & 0 & \cdots & -1 & 0 & \cdots \\ \cdots & 0 & 1 & \cdots & 0 & -1 & \cdots \\ \cdots & \cdots & \cdots & \cdots & \cdots & \cdots & \cdots \end{Bmatrix}. \tag{2.42}$$

Essential boundary conditions are applied by setting corresponding entries in C to 1 and leaving the rest of the row zero.

To impose compatibility and equilibrium, Lagrangian multiplier $\boldsymbol{\lambda}$ is introduced to enforce the constraint $C\mathbf{u} = 0$. The energy functional $\boldsymbol{\Pi}$ of the system is

$$\boldsymbol{\Pi} = \frac{1}{2}\mathbf{u}^T\mathbf{K}\mathbf{u} - \mathbf{u}^T\mathbf{f} + \boldsymbol{\lambda}^T C\mathbf{u}. \tag{2.43}$$

Minimizing $\boldsymbol{\Pi}$ with respect to $\mathbf{u}$ and $\boldsymbol{\lambda}$ yields the interval governing equations

$$\begin{Bmatrix} \mathbf{K} & C^T \\ C & 0 \end{Bmatrix} \begin{Bmatrix} \mathbf{u} \\ \boldsymbol{\lambda} \end{Bmatrix} = \begin{Bmatrix} \mathbf{f} \\ \mathbf{0} \end{Bmatrix}. \tag{2.44}$$

To reduce overestimation, $\mathbf{K}$ and $\mathbf{f}$ are decomposed as in Eq. (2.3). Thus

$$\left(\begin{Bmatrix} A \\ 0 \end{Bmatrix} \text{diag}(\Lambda\Delta\boldsymbol{\alpha}) \begin{Bmatrix} A^T & 0 \end{Bmatrix} + \begin{Bmatrix} K_0 & C^T \\ C & 0 \end{Bmatrix} \right) \begin{Bmatrix} \mathbf{u} \\ \boldsymbol{\lambda} \end{Bmatrix} = \begin{Bmatrix} F \\ 0 \end{Bmatrix} \boldsymbol{\delta}, \tag{2.45}$$

where $\Delta\boldsymbol{\alpha}$ is the difference between interval vector $\boldsymbol{\alpha}$ and its reference vector α_0, viz. $\Delta\boldsymbol{\alpha} = \boldsymbol{\alpha} - \alpha_0$, and $K_0 = A\text{diag}(\Lambda\alpha_0)A^T$. Preferably, $\alpha_0 = \text{mid } \boldsymbol{\alpha}$.

The Lagrangian multiplier $\boldsymbol{\lambda}$ denotes negative internal forces between element nodes and common nodes, when the constraint is a compatibility condition; $\boldsymbol{\lambda}$ denotes reactions at the supports, when the constraint is an essential boundary condition. Thus internal forces and support reactions are obtained as a by-product as the Lagrangian multiplier $\boldsymbol{\lambda}$ enforcing the constraint equation $C\mathbf{u} = 0$.

49

To compute other types of derived variables, such as and the generalized strain ε and the generalized stress $\boldsymbol{\sigma}$ in Eq. (2.2), the direct approach is adopted. To avoid interval intermediate steps and reduce overestimation, ε, $\boldsymbol{\sigma}$ and $\mathbf{u}$ are solved simultaneously, by introducing the Lagrangian multipliers $\boldsymbol{\mu}_1$ and $\boldsymbol{\mu}_2$ associated with $\varepsilon = B\mathbf{u}$ and $\boldsymbol{\sigma} = \mathbf{S}\mathbf{u}$, respectively. Thus the energy functional

$$\Pi = \frac{1}{2}\mathbf{u}^T\mathbf{K}\mathbf{u} - \mathbf{u}^T\mathbf{f} + \boldsymbol{\lambda}^T C\mathbf{u} \tag{2.46}$$
$$+ \boldsymbol{\mu}_1^T(\varepsilon - B\mathbf{u}) + \boldsymbol{\mu}_2^T(\boldsymbol{\sigma} - \mathbf{S}\mathbf{u}),$$

where $\mathbf{u}$, $\boldsymbol{\lambda}$, $\boldsymbol{\mu}_1$, $\boldsymbol{\mu}_2$, ε and $\boldsymbol{\sigma}$ are the six unknowns of the problem. The first variation of the energy functional Π yields

$$\begin{Bmatrix} \begin{bmatrix} \mathbf{K} & C^T & B^T & \mathbf{S}^T & 0 & 0 \\ C & 0 & 0 & 0 & 0 & 0 \\ B & 0 & 0 & 0 & -I & 0 \\ \mathbf{S} & 0 & 0 & 0 & 0 & -I \\ 0 & 0 & -I & 0 & 0 & 0 \\ 0 & 0 & 0 & -I & 0 & 0 \end{bmatrix} \end{Bmatrix} \begin{Bmatrix} \mathbf{u} \\ \boldsymbol{\lambda} \\ \boldsymbol{\mu}_1 \\ \boldsymbol{\mu}_2 \\ \varepsilon \\ \boldsymbol{\sigma} \end{Bmatrix} = \begin{Bmatrix} \mathbf{f} \\ 0 \\ 0 \\ 0 \\ 0 \\ 0 \end{Bmatrix}. \tag{2.47}$$

According to the last two rows of Eq. (2.47), $\boldsymbol{\mu}_1 = 0$ and $\boldsymbol{\mu}_2 = 0$. Substituting the trivial solutions $\boldsymbol{\mu}_1 = 0$ and $\boldsymbol{\mu}_2 = 0$ into Eq. (2.47), the governing equation takes the following asymmetric form,

$$\begin{Bmatrix} \begin{bmatrix} \mathbf{K} & C^T & 0 & 0 \\ C & 0 & 0 & 0 \\ B & 0 & -I & 0 \\ \mathbf{S} & 0 & 0 & -I \end{bmatrix} \end{Bmatrix} \begin{Bmatrix} \mathbf{u} \\ \boldsymbol{\lambda} \\ \varepsilon \\ \boldsymbol{\sigma} \end{Bmatrix} = \begin{Bmatrix} \mathbf{f} \\ 0 \\ 0 \\ 0 \end{Bmatrix}. \tag{2.48}$$

The resulting stiffness matrix is smaller, but it is not symmetric as that based on the indirect approach. Taking into account the decomposition of $\mathbf{K}$ and $\mathbf{f}$ in Eq. (2.3),

Eq. (2.48) is rewritten into the following decomposed form

$$
\left(\left\{ \begin{bmatrix} A & 0 \\ 0 & 0 \\ 0 & 0 \\ 0 & \Phi_s \end{bmatrix} \right\} \mathrm{diag} \left(\left\{ \begin{matrix} \Lambda \\ \Lambda_s \end{matrix} \right\} \Delta\boldsymbol{\alpha} \right) \left\{ \begin{matrix} A^T & 0 & 0 & 0 \\ A_s^T & 0 & 0 & 0 \end{matrix} \right\} \right.
$$

$$
\left. + \left\{ \begin{bmatrix} K_0 & C^T & 0 & 0 \\ C & 0 & 0 & 0 \\ B & 0 & -I & 0 \\ S_0 & 0 & 0 & -I \end{bmatrix} \right\} \right) \left\{ \begin{matrix} \mathbf{u} \\ \boldsymbol{\lambda} \\ \boldsymbol{\varepsilon} \\ \boldsymbol{\sigma} \end{matrix} \right\} = \left\{ \begin{matrix} F \\ 0 \\ 0 \\ 0 \end{matrix} \right\} \boldsymbol{\delta},
$$

(2.49)

where $\Delta\boldsymbol{\alpha}$, K_0 are defined earlier in Eq. (2.45), and $S_0 = \Phi_s\mathrm{diag}(\Lambda_s\alpha_0)A_s^T$. The procedure described above also applies to derived quantities that can be brought into the form of $\mathbf{r} = P_r\boldsymbol{\lambda}$, where P_r is a deterministic matrix and $\mathbf{r}$ is the derived quantity associated with internal forces $\boldsymbol{\lambda}$.

2.2   Iterative Enclosure Method

The equilibrium equations to be solved for elastic structures with interval uncertainties in load, material, and geometry are given in Eqs. (2.45) and (2.49). These are special cases of the general interval equation

$$
\left\{ A_g\mathrm{diag}(\Lambda_g\Delta\boldsymbol{\alpha})B_g + K_g \right\}\mathbf{u}_g = F_g\boldsymbol{\delta},
$$

(2.50)

where A_g, Λ_g, B_g, K_g, F_g are given deterministic matrices, $\Delta\boldsymbol{\alpha}$ and $\boldsymbol{\delta}$ are given interval vectors. Any interval solver can be used to solve for Eq. (2.50). In the current study, a new variant of the iterative enclosure method [110] is proposed, which incorporates the new decomposition of $\mathbf{K}$ given in Eq. (2.3). In addition, the new method follows an expanding strategy and starts the iteration from a very simple initial guess. The goal is to find a guaranteed outer enclosure $\mathbf{u}_g^{out}$ for the exact enclosure $\mathbf{u}_g$ such that $\mathbf{u}_g^{out} \supseteq \mathbf{u}_g$ is guaranteed.

2.2.1 The expanding strategy

To compute the outer solution $\mathbf{u}_g^{out}$, $A_g \mathrm{diag}\{\Lambda_g \Delta \boldsymbol{\alpha}\} B_g \mathbf{u}_g$ in Eq. (2.50) is moved to the right-hand side, leaving $\mathbf{u}_g$ the only interval term on the left-hand side, viz.

$$K_g \mathbf{u}_g = F_g \boldsymbol{\delta} - A_g \mathrm{diag}(\Lambda_g \Delta \boldsymbol{\alpha}) B_g \mathbf{u}_g. \tag{2.51}$$

Now define $G = K_g^{-1}$ as the flexibility matrix of the structure. Then $\mathbf{u}_g$ satisfies the following fixed-point equation

$$\mathbf{u}_g = (GF_g)\boldsymbol{\delta} - (GA_g)\mathrm{diag}(B_g \mathbf{u}_g)\Lambda_g \Delta \boldsymbol{\alpha}, \tag{2.52}$$

where the following identities has been used

$$\mathrm{diag}(\Lambda_g \Delta \boldsymbol{\alpha})B_g \mathbf{u}_g = (\Lambda_g \Delta \boldsymbol{\alpha}) \circ (B_g \mathbf{u}_g) = \mathrm{diag}(B_g \mathbf{u}_g)\Lambda_g \Delta \boldsymbol{\alpha}. \tag{2.53}$$

Here $a \circ b$ denotes the element-by-element Hadamard product of two vectors a and b. The fixed-point Eq. (2.52) is the basis for the iterative enclosure method.

To solve for $\mathbf{u}_g$, one can directly iterate Eq. (2.52) to find its fixed point until convergence is attained. However, $B_g \mathbf{u}_g$ is computed after each iteration, causing unnecessary overestimation. To avoid that, an alternative approach follows from the work by Neumaier and Pownuk [110]. In particular, from Eq. (2.52), the auxiliary variable $\mathbf{v}_g = B_g \mathbf{u}_g$ is introduced, which satisfies

$$\mathbf{v}_g = B_g \mathbf{u}_g = (B_g GF_g)\boldsymbol{\delta} - (B_g GA_g)\mathrm{diag}(\mathbf{v}_g)\Lambda_g \Delta \boldsymbol{\alpha}. \tag{2.54}$$

To find $\mathbf{v}_g$, the fixed-point of Eq. (2.54), the following iterative scheme is used,

$$\mathbf{v}_g^{j+1} = (B_g GF_g)\boldsymbol{\delta} - (B_g GA_g)\mathrm{diag}(\mathbf{v}_g^j)\Lambda_g \Delta \boldsymbol{\alpha}, \tag{2.55}$$

where the trivial initial guess $\mathbf{v}_g^1 = (B_g GF_g)\boldsymbol{\delta}$ is used to start the iteration.

Iterating Eq. (2.55) does not yield any additional overestimation since there is no pre-multiplication of $\mathbf{v}_g$ by any interval quantity as in Eq. (2.52). The iterations are

stopped when there is no improvement in two successive iterations, viz. $\mathbf{v}_g^n = \mathbf{v}_g^{n-1}$.
Due to the isotonic inclusion of interval operations [101], the converged $\mathbf{v}_g^n$ guarantees
to enclose the exact fixed-point $\mathbf{v}_g$. The outer solution $\mathbf{u}_g^{out}$ is obtained by substituting
$B_g \mathbf{u}_g$ in Eq. (2.55) with the converged $\mathbf{v}_g^n$, viz.

$$\mathbf{u}_g^{out} = (GF_g)\boldsymbol{\delta} - (GA_g)\mathrm{diag}(\mathbf{v}_g^n)\Lambda_g \Delta\boldsymbol{\alpha}, \tag{2.56}$$

In addition, following the discussion in Section 1.2.2.3, the inner enclosure $\mathbf{u}_g^{inn}$ is
obtained using the following interval equality

$$\mathbf{u}_g^{inn} + (GA_g)\mathrm{diag}(\mathbf{v}_g^n - v_{g0})\Lambda_g \Delta\boldsymbol{\alpha} \tag{2.57}$$
$$= (GF_g)\boldsymbol{\delta} - (GA_g)\mathrm{diag}(v_{g0})\Lambda_g \Delta\boldsymbol{\alpha},$$

where v_{g0} is the reference vector for $\mathbf{v}_g^n$, and preferrably $v_{g0} = \mathrm{mid}\,\mathbf{v}_g^n$. As mentioned
before, the inner enclosure $\mathbf{u}_g^{inn} \subseteq \mathbf{u}_g$. Combined with the outer enclosure $\mathbf{u}_g^{out}$, it can
be used to judge the overestimation level of interval solutions.

2.2.2 Computational details

Note that during the computation, matrices (GF_g), $(B_g GF_g)$, $(GA_g)\mathrm{diag}(\mathbf{v}_g)\Lambda$, and
$(B_g GA_g)\mathrm{diag}(\mathbf{v}_g)\Lambda$ are computed before multiplied by $\boldsymbol{\delta}$ and $\Delta\boldsymbol{\alpha}$, respectively. For
the sake of efficiency, the block structure of these matrices are taken into account
during the computation. For instance, consider the governing equation (2.49). The
block matrices K_b, S_b, and F_b are defined as

$$K_b = \left\{ \begin{matrix} K_0 & C^T \\ C & 0 \end{matrix} \right\}, \qquad S_b = \left\{ \begin{matrix} B & 0 \\ S_0 & 0 \end{matrix} \right\}, \qquad F_b = \left\{ \begin{matrix} F \\ 0 \end{matrix} \right\}. \tag{2.58}$$

Then the scalar matrix GF_g is given by

$$GF_g = \left\{ \begin{matrix} K_b & 0 \\ S_b & -I \end{matrix} \right\}^{-1} \left\{ \begin{matrix} F_b \\ 0 \end{matrix} \right\} = \left\{ \begin{matrix} K_b^{-1}F_b \\ S_b K_b^{-1}F_b \end{matrix} \right\}, \tag{2.59}$$

53

Similarly, block matrices A_b, Φ_b, and A_{sb} are defined as

$$A_b = \left\{ \begin{matrix} A \\ 0 \end{matrix} \right\}, \qquad \Phi_b = \left\{ \begin{matrix} 0 \\ \Phi_s \end{matrix} \right\}, \qquad A_{sb} = \left\{ \begin{matrix} A_s \\ 0 \end{matrix} \right\}. \qquad (2.60)$$

Then the scalar matrix GA_g is given by

$$GA_g = \left\{ \begin{matrix} K_b & 0 \\ S_b & -I \end{matrix} \right\}^{-1} \left\{ \begin{matrix} A_b & 0 \\ 0 & \Phi_b \end{matrix} \right\} = \left\{ \begin{matrix} K_b^{-1}A_b & 0 \\ S_b K_b^{-1} A_b & -\Phi_b \end{matrix} \right\}, \qquad (2.61)$$

and the scalar matrices $B_g GF_g$ and $B_g GA_g$ are obtained from

$$B_g GF_g = \left\{ \begin{matrix} A_b^T K_b^{-1} F_b \\ A_{sb}^T K_b^{-1} F_b \end{matrix} \right\}, \qquad B_g GA_g = \left\{ \begin{matrix} A_b^T K_b^{-1} A_b & 0 \\ A_{sb}^T K_b^{-1} A_b & 0 \end{matrix} \right\}. \qquad (2.62)$$

Apparently the computational efficiency is enhanced, because now the only time-consuming step is to compute the block stiffness matrices $K_b^{-1} F_b$ and $K_b^{-1} A_b$, which can be performed efficiently from Gaussian elimination.

2.3   Nonlinear Programming Approach

In this section, nonlinear programming techniques are implemented to solve the uncertain structural forward problem as a constrained optimization problem. Real ordinary numbers are exclusively used, i.e. no interval variables are involved in the computation. Two different approaches, the direct approach and the adjoint approach, are introduced in the following discussion. The corresponding solutions, which will be compared with the proposed interval solutions in later numerical simulations, are computed using the optimization toolbox in MATLAB.

2.3.1   The direct approach

In the direct approach, the solution vector x contains the load uncertainty vector δ, the stiffness parameter vector α, the nodal displacement vector u, and the Lagrangian multiplier λ (denoting internal forces and support reactions):

$$x = \left\{ \delta^T \quad \alpha^T \quad u^T \quad \lambda^T \right\}^T. \qquad (2.63)$$

To compute the lower (or upper) bound of the j-th component of the nodal displacement vector u_j, the objective functional Ω has the following form

$$\Omega = cu, \quad \text{or} \quad -cu, \tag{2.64}$$

where c is a row vector, whose only non-zero component is unity at the j-th component. For the j-th component of the generalized strain or stress vector, the objective functional Ω has the same form as in Eq. (2.64), with $c = B_j$ or S_j being the j-th row of the strain- or stress-displacement matrices B or S, respectively.

Equality constraints f_{eq} include equilibrium condition, compatibility requirements and essential boundary conditions, which are given by

$$\begin{cases} K(\alpha)u + C^T\lambda - F\delta = 0; \\ Cu = 0. \end{cases} \tag{2.65}$$

Further, the inequality constraints require that the load uncertainty vector δ and the stiffness parameter vectors α vary within their respective interval bounds:

$$\begin{cases} \underline{\delta} \leq \delta \leq \overline{\delta}; \\ \underline{\alpha} \leq \alpha \leq \overline{\alpha}, \end{cases} \tag{2.66}$$

where $\underline{a}$ and $\overline{a}$ denote the lower and upper bounds of an interval $\mathbf{a}$, respectively.

To accelerate the optimization algorithm, the gradient of the objective function Ω and the equality constraint equation f_{eq} are provided. When the nodal displacement or the generalized strain is considered and c does not depend on α, the gradient of the objective functional Ω with respect to x is given by

$$\frac{\partial \Omega}{\partial x} = \left\{ 0 \quad 0 \quad c \quad 0 \right\}. \tag{2.67}$$

When the generalized stress is considered and $c = S_j = \Phi_{sj}\text{diag}(\Lambda_s\alpha)A_s^T$,

$$\frac{\partial \Omega}{\partial x} = \left\{ 0 \quad \Phi_{s,j}\text{diag}(A_s^Tu)\Lambda_s \quad S_j \quad 0 \right\}. \tag{2.68}$$

In addition, the gradient of the equality constraints f_{eq} with respect to x is given by

$$\frac{\partial f_{eq}}{\partial x} = \begin{Bmatrix} -F & A\text{diag}(A^T u)\Lambda & K & C^T \\ 0 & 0 & C & 0 \end{Bmatrix}. \tag{2.69}$$

The direct approach directly use equilibrium, compatibility, and essential boundary conditions in the formulation. Thus the implementation is straight-forward and easy, at the cost of a higher memory consumption. As an alternative, in the following discussion, the adjoint approach is presented.

2.3.2 The adjoint approach

In the adjoint approach, the unknown variable x only contains the load uncertainty vector δ and the stiffness parameter vector α,

$$x = \left\{ \delta^T \ \alpha^T \right\}^T. \tag{2.70}$$

A Lagrangian multiplier w is introduced into the system to enforce the equilibrium constraint $Ku - F\delta$. As a result, the objective functional

$$\Omega = cu + w^T(Ku - F\delta). \tag{2.71}$$

The governing equations for the original and adjoint systems are obtained from taking partial derivatives of Ω with respect to w and u

$$\begin{Bmatrix} K & 0 \\ 0 & K \end{Bmatrix} \begin{Bmatrix} u \\ w \end{Bmatrix} = \begin{Bmatrix} F\delta \\ c^T \end{Bmatrix}. \tag{2.72}$$

The system does not include any equality constraints. The corresponding inequality constraint is exact the same as in Eq. (2.66).

When the nodal displacement or the generalized strain is considered and c does not depend on α, the gradient of Ω with respect to x is given by

$$\frac{\partial \Omega}{\partial x} = \left\{ -w^T F \quad w^T A\text{diag}(A^T u)\Lambda \right\}. \tag{2.73}$$

When the generalized stress is considered and $c = S_j = \Phi_{s,j}\mathrm{diag}(\Lambda_s\alpha)A_s^T$,

$$\frac{\partial\Omega}{\partial x} = \left\{-w^T F \quad w^T A\mathrm{diag}(A^T u)\Lambda + \Phi_{s,j}\mathrm{diag}(A_s^T u)\Lambda_s\right\}. \tag{2.74}$$

2.4 Numerical Examples

The proposed IFEM algorithm for trusses, frames and plane stress/strain problems is implemented using the interval MATLAB toolbox INTLAB (developed by Rump [122]). Several numerical test cases are presented to illustrate the performance and efficiency of the method: i) a simply supported truss, ii) a two-span continuous beam, iii) a two-bay two-story frame, iv) a rectangular plate, and v) a plate with a circular cutoff. The interval outer and inner solutions (OS and IS) obtained from the proposed method are compared with i) the nonlinear programming approach (NLP), ii) the endpoint combination method (EC), iii) the sensitivity analysis (SA), and iv) the Monte Carlo (MC) predictions, whenever appropriate. The computations are carried out on a PC with Intel Core2 Duo CPU E8400 3GHz with 4GB RAM under Windows 7. The results show that the proposed IFEM algorithm gives guaranteed enclosures of the exact structural response. Furthermore, it provides the sharpest interval enclosure in comparison to that from other known interval solvers, and it is computationally efficient and cheap.
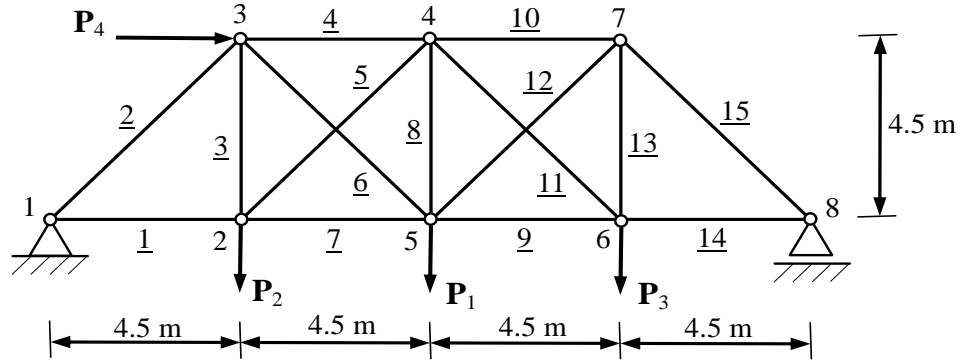
Figure 2.3: A simply supported 8-joint 15-bar truss subject to point loads.

2.4.1 Simply supported truss

The first example is a simply supported symmetric truss composed of 15 bars, as shown in Figure 2.3. The joints are labeled from 1 to 8, and the bars are labeled from $\underline{1}$ to $\underline{15}$. Point loads $\mathbf{P}_1$, $\mathbf{P}_2$, $\mathbf{P}_3$, and $\mathbf{P}_4$ are applied at joints 5, 2, 6, and 3, respectively, with midpoint values $P_1 = 200$ kN, $P_2 = P_3 = 100$ kN, and $P_4 = 90$ kN. Bars $\underline{1}$ to $\underline{3}$, $\underline{13}$ to $\underline{15}$ have the same cross section area $A = 1.0 \times 10^{-3}$ m^2, and all other bars, viz. bars $\underline{4}$ to $\underline{12}$, have a smaller cross section area $A = 6.0 \times 10^{-4}$ m^2. All the bars are made of steel and have interval Young's moduli $\mathbf{E}$ with midpoint value $E = 200$ GPa.

Fifteen plane truss elements are used to model the truss in Figure 2.3, one for each bar. The point loads $\mathbf{P}_j$ and element Young's moduli $\mathbf{E}$ are assumed to vary

Table 2.1: Horizontal and vertical displacements $\mathbf{u}_5$ and $\mathbf{v}_5$, axial forces $\mathbf{N}_2$ and $\mathbf{N}_8$ for the simple truss of Figure 2.3 with 10% uncertainties in load and material.

	Horizontal displ. $\mathbf{u}_5$ (m)				Horizontal displ. $\mathbf{v}_5$ (m)			
	Lower Bound	Uncertainty (%)	Upper Bound	Uncertainty (%)	Lower Bound	Uncertainty (%)	Upper Bound	Uncertainty (%)
Outer Solution (OS)	0.02987	-1.372	0.03749	0.114	-0.13143	-0.111	-0.10613	1.243
Reference (EC)	0.03029	---	0.03744	---	-0.13129	---	-0.10747	---
Inner Solution (IS)	0.03035	0.202	0.03701	-1.159	-0.12989	1.063	-0.10767	-0.191
Monte Carlo (MC)	0.03082	1.758	0.03670	-1.973	-0.12680	3.416	-0.11095	-3.240

	Axial force $\mathbf{N}_2$ (kN)				Axial force $\mathbf{N}_8$ (kN)			
	Lower Bound	Uncertainty (%)	Upper Bound	Uncertainty (%)	Lower Bound	Uncertainty (%)	Upper Bound	Uncertainty (%)
Outer Solution (OS)	-266.76	0.000	-235.29	0.000	47.069	-4.002	78.834	1.658
Reference (EC)	-266.76	---	-235.29	---	49.031	---	77.548	---
Inner Solution (IS)	-266.76	0.000	-235.29	0.000	50.414	2.819	75.490	-2.655
Monte Carlo (MC)	-265.90	0.321	-235.93	-0.271	53.061	8.219	73.278	-5.507

independently. Thus 19 interval variables are used to model the load and material uncertainties in the truss. Then horizontal and vertical displacements $\mathbf{u}_5$ and $\mathbf{v}_5$ at joint 5, the axial forces $\mathbf{N}_2$ and $\mathbf{N}_8$ in bar $\underline{2}$ and $\underline{8}$ are selected for comparison among the various methods mentioned previously.

In a first scenario, 10% uncertainties are assigned to the loads $\mathbf{P}_j$ and the Young's moduli $\mathbf{E}$, i.e. the width of each interval is 10% of its midpoint value. Table 2.1 compares the outer and inner solutions (OS and IS) from the proposed method and
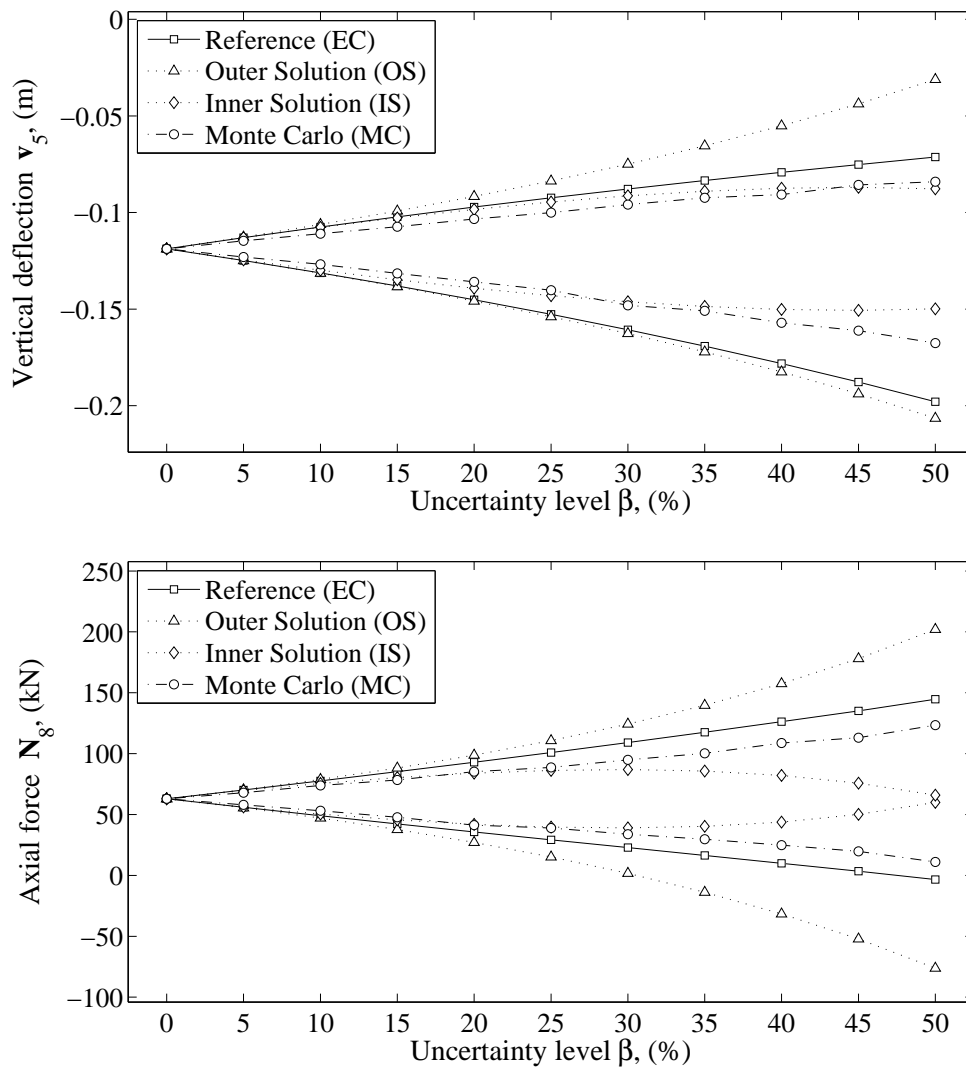
Figure 2.4: Vertical displacement $\mathbf{v}_5$ and axial force $\mathbf{N}_8$ for the simply supported truss of Figure 2.3 under up to 50% uncertainties in load and material. The Monte Carlo prediction (MC) is obtained from an ensemble of 100,000 simulations.

the Monte Carlo (MC) predictions from an ensemble of 100,000 simulations against the reference solution obtained from the endpoint combination method (EC). Observe that the OS (IS) contains (is contained by) the reference solution EC. Further, $\mathbf{N}_2$ is obtained without overestimation since the axial force in bar $\underline{2}$ is independent of material properties, which indicates how the present formulation captures the structural property of statically determinate structures.

Then in a second scenario, the lower and upper bounds of $\mathbf{v}_5$ and $\mathbf{N}_8$ obtained from the proposed method are displayed in Figure 2.4 as functions of the uncertainty level β (up to 50% uncertainties assigned to $\mathbf{P}_j$ and $\mathbf{E}_j$). The MC prediction and the EC reference solution are also shown in the same figure. Note that as the uncertainty level increases, so does overestimation. Further, the OS provides a guaranteed enclosure and the IS is close to MC predictions for levels of uncertainties up to 25%.
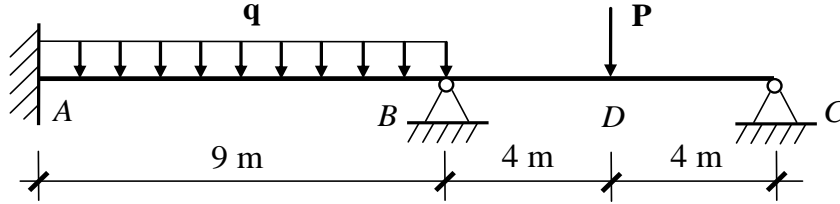
Figure 2.5: A two-span continuous beam subject to vertical loads.

2.4.2 Two-span continuous beam

The second example is a two-span continuous beam with uniformly distributed load q applied on the left span and concentrated load $\mathbf{P}$ acting in the middle of the right span, as given in Figure 2.5. In order to compare results with Zhang [160], distributed load $\mathbf{q} = [3, 4.5]$ kN/m and concentrated load $\mathbf{P} = [30, 40]$ kN are used, which represent 40% and 28.6% uncertainties, respectively. Uncertainties in the Young's modulus is 2% , viz. $\mathbf{E} = [198, 202]$ GPa. The cross section areas A_{AB}, A_{BC} and moments of inertia I_{AB}, I_{BC} are deterministic, and $A_{AB} = 6 \times 10^{-2}$ m^2, $I_{AB} = 1.2 \times 10^{-4}$ m^4,

Table 2.2: Selected results for the continuous beam with of Figure 2.5 load and material uncertainties. $\mathbf{q}$ = [3, 4.5] kN/m, $\mathbf{P}$ = [30, 40] kN and $\mathbf{E}$ = [198, 200] GPa (40%, 28.6% and 2% uncertainties respectively).

	Vertical displ. $\mathbf{v}_D$ (10^{-3} m)				Rotation angle $\boldsymbol{\theta}_C$ (10^{-3} rad)			
	Lower Bound	Uncer- tainty (%)	Upper Bound	Uncer- tainty (%)	Lower Bound	Uncer- tainty (%)	Upper Bound	Uncer- tainty (%)
Zhang [160]	-13.949	-0.115	-8.877	0.792	3.682	-0.915	5.655	0.230
Outer Solution (OS)	-13.934	-0.008	-8.8969	0.569	3.6942	-0.586	5.6445	0.045
Reference (EC)	-13.933	---	-8.9479	---	3.7160	---	5.6420	---
Inner Solution (IS)	-13.882	0.369	-8.9495	-0.018	3.7188	0.073	5.6200	-0.390
Monte Carlo (MC)	-13.802	0.938	-9.0532	-1.177	3.7558	1.070	5.5902	-0.918

	Bending moment $\mathbf{M}_B$ (kN·m)				Bending moment $\mathbf{M}_D$ (kN·m)			
	Lower Bound	Uncer- tainty (%)	Upper Bound	Uncer- tainty (%)	Lower Bound	Uncer- tainty (%)	Upper Bound	Uncer- tainty (%)
Zhang [160]	-48.756	-0.133	-35.157	0.346	40.204	-0.169	57.814	0.294
Outer Solution (OS)	-48.741	-0.104	-35.185	0.268	40.223	-0.122	57.814	0.029
Reference (EC)	-48.691	---	-35.279	---	40.272	---	57.797	---
Inner Solution (IS)	-48.596	0.195	-35.331	-0.145	40.295	0.059	57.741	-0.091
Monte Carlo (MC)	-48.410	0.577	-35.467	-0.530	40.389	0.290	57.566	-0.401

	Curvature $\boldsymbol{\kappa}_B$ (10^{-3} m^{-1})				Curvature $\boldsymbol{\kappa}_D$ (10^{-3} m^{-1})			
	Lower Bound	Uncer- tainty (%)	Upper Bound	Uncer- tainty (%)	Lower Bound	Uncer- tainty (%)	Upper Bound	Uncer- tainty (%)
Outer Solution (OS)	-2.7327	-0.079	-1.9299	0.582	2.2071	-0.516	3.2393	0.028
Reference (EC)	-2.7306	---	-1.9412	---	2.2186	---	3.2384	---
Inner Solution (IS)	-2.7193	0.417	-1.9434	-0.115	2.2199	0.061	3.2265	-0.367
Monte Carlo (MC)	-2.6940	1.338	-1.9624	-1.096	2.2302	0.521	3.2186	-0.614
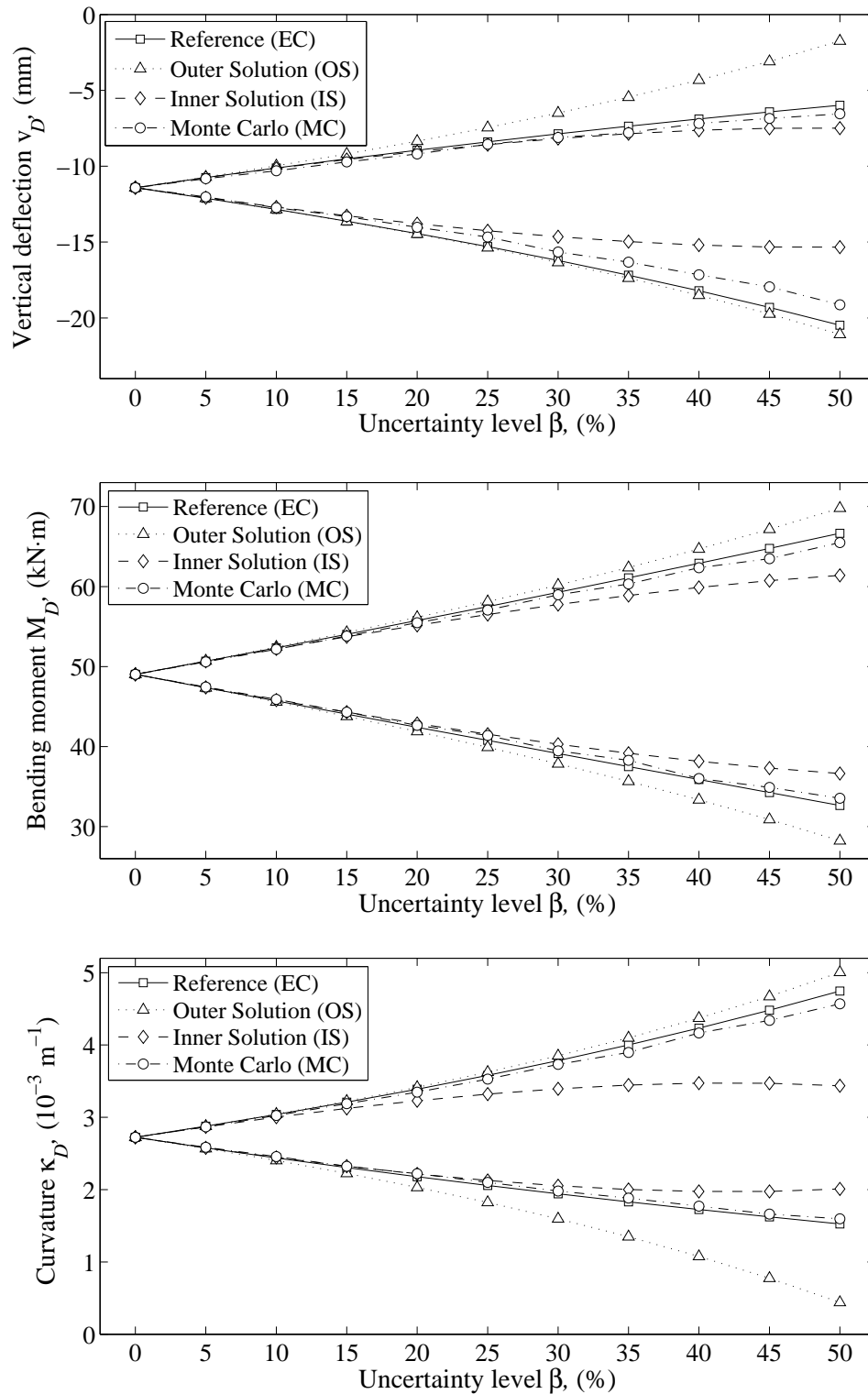
Figure 2.6: Selected results for the continuous beam of Figure 2.5 under up to 50% uncertainties in load and material. The Monte Carlo prediction (MC) is obtained from an ensemble of 100,000 simulations.

$A_{BC} = 4 \times 10^{-2}$ m^2, $I_{BC} = 0.9 \times 10^{-4}$ m^4. The problem is modeled by three beam elements (AB, BD and DC). The element Young's moduli are assumed to vary independently, while the uniform load $\mathbf{q}$ and the concentrated load $\mathbf{P}$ are modeled by two intervals. Thus, there are 5 interval variables.

Table 2.2 reports the interval solutions for the nodal deflection $\mathbf{v}_D$ at point D, rotational angle $\boldsymbol{\theta}_C$ at point C, bending moment $\mathbf{M}_B$, $\mathbf{M}_D$ at points B and D, curvature $\boldsymbol{\kappa}_B$ at point B obtained from element BD, and curvature $\boldsymbol{\kappa}_D$ at point D obtained from element DC. The endpoint combination (EC) solution is used as the reference, and results from Zhang [160], the proposed method (OS and IS) and Monte Carlo (MC) predictions with 100,000 simulations are compared in Table 2.2. As the structure is statically indeterminate, internal forces depend on material properties and overestimation in $\mathbf{M}_B$ and $\mathbf{M}_D$ is observed. Derived quantities $\mathbf{M}_B$, $\mathbf{M}_D$, $\boldsymbol{\kappa}_B$, $\boldsymbol{\kappa}_D$ and primary quantities $\mathbf{v}_D$, $\boldsymbol{\theta}_C$ are obtained with the same accuracy.

The performance of the solution with increasing uncertainty up to 50% in $\mathbf{q}$, $\mathbf{P}$, and $\mathbf{E}$ is studied. All interval variables have the following midpoint values, $q = 3.75$ kN/m, $P = 35$ kN, $E = 200$ GPa, and the same uncertainty level is applied to $\mathbf{q}$, $\mathbf{P}$, and $\mathbf{E}$. Nodal deflection $\mathbf{v}_D$, bending moment $\mathbf{M}_D$ and curvature $\boldsymbol{\kappa}_D$ of element DC, calculated using different method, are compared and displayed in Figure 2.6. Observe that MC gives tighter inner bounds than IS, when uncertainty level is high. This is not surprising, as 100,000 simulations are used for just 5 interval variables.

2.4.3 Two-bay two-story frame

The third example is a two-bay two-story frame adopted from Buonopane, *et al.* [19], subject to distributed loads acting on each floor as shown in Figure 2.7. Columns are labeled from C1 to C6, beams from B1 to B4, and nodes from 1 to 9. Nodes 1 to 3 are hinged to the ground. Distributed loads are modeled by four independent intervals, i.e. $\mathbf{q}_1 = [105.8, 113.1]$ kN/m (6.67% uncertainty), $\mathbf{q}_2 = [105.8, 113.1]$
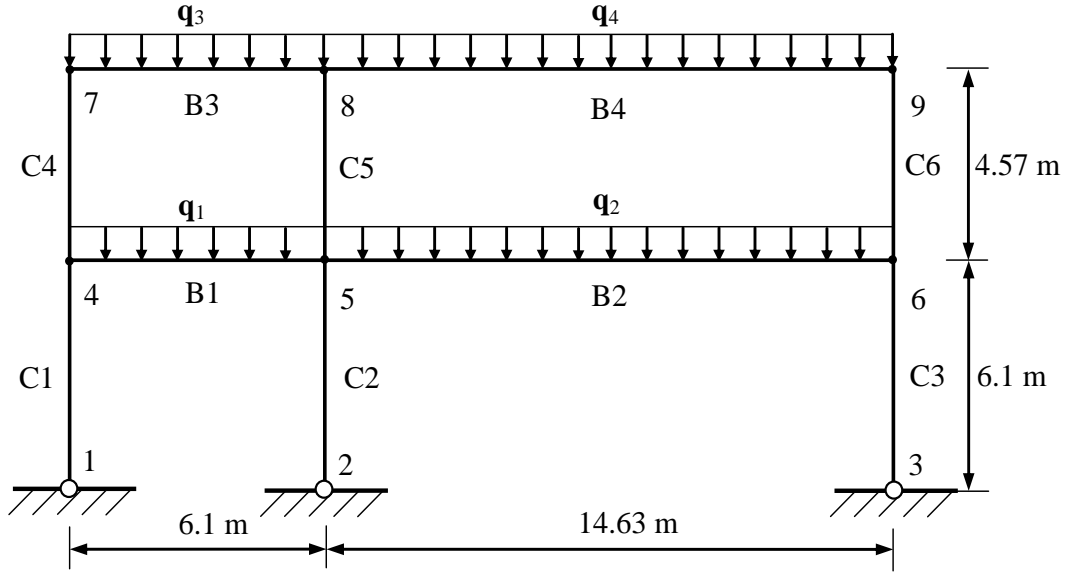
Figure 2.7: A two-bay two-story frame subject to distributed loads..

kN/m (6.67% uncertainty), $\mathbf{q}_3 = [49.255, 52.905]$ kN/m (7.15% uncertainty), and $\mathbf{q}_4 = [49.255, 52.905]$ kN/m (7.15% uncertainty). In addition, the geometric and material uncertainties are accounted. Young's modulus $\mathbf{E}$, cross section area $\mathbf{A}$, and moment of inertia $\mathbf{I}$ of each member are modeled by intervals, and given in Table 2.3.

The proposed method is now compared with the work by Muhanna and Zhang [103], assuming $\mathbf{E}$, $\mathbf{A}$, and $\mathbf{I}$ to vary independently with 1% uncertainty. Numerical simulations also show that the proposed method works just as well for uncertainty levels up to 30%. One beam element is used to model each frame member; so there are 10 elements and 34 independent interval variables.

Vertical displacements $\mathbf{v}_5$ and $\mathbf{v}_9$ at nodes 5 and 9 are given in the upper half of Table 2.4, while bending moments $\mathbf{M}_{B2l}$ and $\mathbf{M}_{C5b}$ at the left end of beam B2 and the bottom end of column C5 are included in the lower half of the table, where subscript $_{B2l}$ denotes the left node of B2 and $_{C5b}$ the bottom node of C5.

The solution from the sensitivity analysis (SA) method serves as a reference, because the endpoint combination method requires $2^{34} \approx 1.72 \times 10^{10}$ combinations,

64

Table 2.3: Geometric and material properties for the two-bay two-story frame of Figure 2.7 (1% uncertainty for **E**, **A** and **I**).

	Shape	**E** (GPa)	**A** (10^{-4} m²)	**I** (10^{-8} m⁴)
C1	W12×19	[199, 201]	[35.76, 36.12]	[5383.95, 5438.06]
C2	W14×132	[199, 201]	[249.0, 251.57]	[63364.99, 64001.83]
C3	W14×109	[199, 201]	[205.42, 207.48]	[51354.63, 51870.76]
C4	W10×12	[199, 201]	[22.72, 22.95]	[2228.13, 2250.52]
C5	W14×109	[199, 201]	[205.42, 207.48]	[51354.63, 51870.76]
C6	W14×109	[199, 201]	[205.42, 207.48]	[51354.63, 51870.76]
B1	W27×84	[199, 201]	[159.20, 160.80]	[118032.83, 119219.09]
B2	W36×135	[199, 201]	[254.85, 257.41]	[323037.21, 326283.81]
B3	W18×40	[199, 201]	[75.75, 76.51]	[25346.00, 25600.73]
B4	W27×94	[199, 201]	[177.82, 179.60]	[135427.14, 136788.21]

which is infeasible. SA assumes that the system response monotonically varies within the interval ranges of the parameters, and it gives good inner bounds when the uncertainty levels are low (see Section 1.2.3.3). Table 2.4 shows that the proposed IFEM method gives solutions for the upper and lower bounds that contain the reference SA solution with relative error less than 0.2%.

In the standard implementation of the iterative enclosure method, reference vectors α_0 and v_{g0} in Eqs. (2.45), (2.49) and (2.57) can be chosen arbitrarily. To compute the outer solution, only α_0 is needed; for the inner solution, both α_0 and v_{g0} are needed. If the midpoint values $\alpha_0 = \text{mid } \boldsymbol{\alpha}$ and $v_{g0} = \text{mid } \mathbf{v}_g^n$ are chosen, the proposed IFEM algorithm yields one outer and one inner estimate, hereafter referred to as the midpoint approach. Moreover, if the endpoints $\alpha_0 = \underline{\alpha}$ and $\overline{\alpha}$, $v_{g0} = \underline{v_g^n}$ and $\overline{v_g^n}$ are chosen, IFEM provides two outer and four inner estimates. By taking the intersection (interval hull) of these outer (inner) estimates, different outer and inner

Table 2.4: Vertical displacements at nodes 5 and 9, Bending moments at the left node of B2 and the bottom node of C5 for the frame of Figure 2.7 with given load uncertainty and 1% uncertainties in geometry and material.

	Vertical displ. $\mathbf{v}_5$ (10^{-3} m)				Vertical displ. $\mathbf{v}_9$ (10^{-3} m)			
	Lower Bound	Uncertainty (%)	Upper Bound	Uncertainty (%)	Lower Bound	Uncertainty (%)	Upper Bound	Uncertainty (%)
Muhanna & Zhang [105]	-2.4778	-0.012	-2.2610	0.128	-2.1009	-0.100	-1.9064	0.204
Outer Solution (OS)	-2.4777	-0.008	-2.2614	0.111	-2.0990	-0.006	-1.9083	0.107
Reference (SA)	-2.4775	---	-2.2639	---	-2.0988	---	-1.9103	---
Inner Solution (IS)	-2.4749	0.102	-2.2641	-0.010	-2.0968	0.098	-1.9105	-0.008
Monte Carlo (MC)	-2.4588	0.755	-2.2800	-0.713	-2.0886	0.488	-1.9156	-0.279

	Moment $\mathbf{M}_{B2l}$ (kN·m)				Moment $\mathbf{M}_{C5b}$ (kN·m)			
	Lower Bound	Uncertainty (%)	Upper Bound	Uncertainty (%)	Lower Bound	Uncertainty (%)	Upper Bound	Uncertainty (%)
Muhanna & Zhang [105]	1839.0	-0.071	1982.6	0.020	-688.02	-0.157	-614.90	0.274
Outer Solution (OS)	1839.3	-0.054	1982.8	0.031	-687.31	-0.055	-615.69	0.147
Reference (SA)	1840.3	---	1982.2	---	-686.94	---	-616.59	---
Inner Solution (IS)	1841.0	0.034	1981.2	-0.050	-686.03	0.132	-616.97	-0.061
Monte Carlo (MC)	1847.3	0.381	1976.6	-0.281	-680.14	0.990	-622.54	-0.965

solutions are obtained, hereafter referred to the endpoint approach.

In Table 2.5 the inner solutions obtained from the midpoint and endpoint approaches are compared against the reference SA (not listed in the table) for the nodal displacements $\mathbf{u}_5$, $\mathbf{v}_5$, $\boldsymbol{\theta}_5$ at node 5 and internal forces $\mathbf{N}_{B2l}$, $\mathbf{V}_{B2l}$, $\mathbf{M}_{B2l}$ at the left end of beam B2. Here $\mathbf{u}$, $\mathbf{v}$, $\boldsymbol{\theta}$ denote nodal displacements and rotation angle, and $\mathbf{N}$, $\mathbf{V}$, $\mathbf{M}$ denote axial force, shear force, and bending moment, respectively. Note that the midpoint solution is always slightly tighter than endpoint solution. This confirms that midpoints are usually the optimal choice for a deterministic reference value.

Table 2.5: Comparison of different choices of reference point for the inner estimation with given load uncertainty and 1% uncertainties in geometry and material.

	Lower Bounds				Upper Bounds			
	Mid-point	Uncer-tainty (%)	End-point	Uncer-tainty (%)	Mid-point	Uncer-tainty (%)	End-point	Uncer-tainty (%)
$\mathbf{u}_5$ (10^{-3} m)	-7.7828	0.796	-7.7714	0.942	-6.3930	-0.217	-6.4045	-0.397
$\mathbf{v}_5$ (10^{-3} m)	-2.4749	0.102	-2.4748	0.109	-2.2641	-0.010	-2.2642	-0.017
$\boldsymbol{\theta}_5$ (10^{-3} rad)	-4.1508	0.202	-4.1481	0.267	-3.4985	-0.078	-3.5012	-0.155
$\mathbf{N}_{B2l}$ (kN)	217.16	0.057	217.30	0.122	241.81	-0.137	241.68	-0.195
$\mathbf{V}_{B2l}$ (kN)	833.21	0.006	833.21	0.007	892.30	-0.010	892.30	-0.011
$\mathbf{M}_{B2l}$ (kN·m)	1841.0	0.034	1841.2	0.046	1981.2	-0.050	1981.0	-0.062
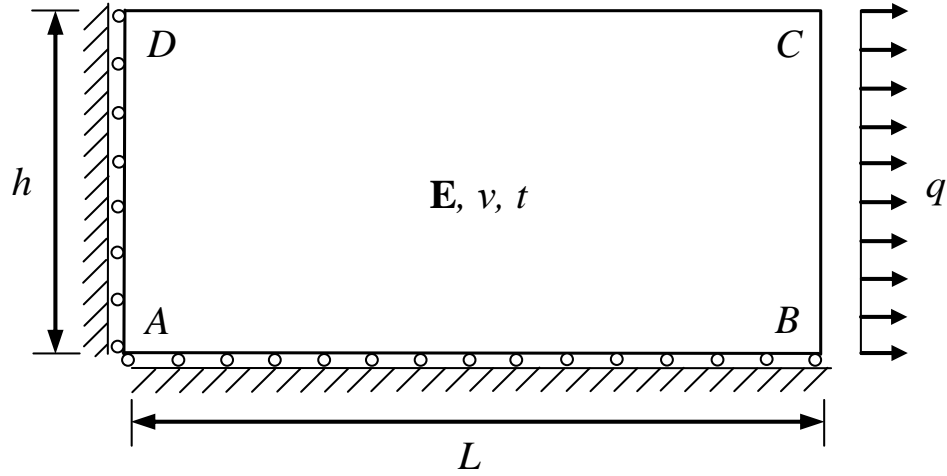
Figure 2.8: A rectangular plate subject to uniform distributed load.

2.4.4 Rectangular plate

The fourth example is a rectangular plate subject to uniformly distributed load $q = 100$ kN/m, as shown in Figure 2.8. The plate is constrained by rollers at the left and bottom edges. The length, height, and thickness of the plate are $L = 0.1$ m, $h = 0.05$ m and $t = 0.005$ m, respectively. The Poisson's ratio is $\nu = 0.3$. Consider 5%

uncertainty in the element Young's modulus, i.e. $\mathbf{E} = [195, 205]$ GPa.

A 6×8 finite element mesh is used to model the plate, as shown in Figure 2.9. Again, the endpoint combination is infeasible, because there are 48 independent interval Young's modulus $\mathbf{E}$ and $2^{48} \approx 2.81 \times 10^{14}$ combinations are required for endpoint combination method (EC). Thus the sensitivity analysis (SA) is adopted to provide a reference solution.

Table 2.6 lists outer and inner solutions (OS and IS) of the nodal displacements $\mathbf{u}_C$ and $\mathbf{v}_C$ computed using the proposed method, along with SA solution and MC predictions with 10,000 simulations. Three decomposition strategies are used, i.e. eigen, LDL and B-matrix decomposition approaches. Note that different decompositions have a small impact on OS and IS. In addition, IS is always better than MC.

To study the efficiency of the proposed method and other competing methods, the corresponding computational time are recorded as a function of the finite element mesh size. The MC predictions are obtained from an ensemble of 10,000 simulations.
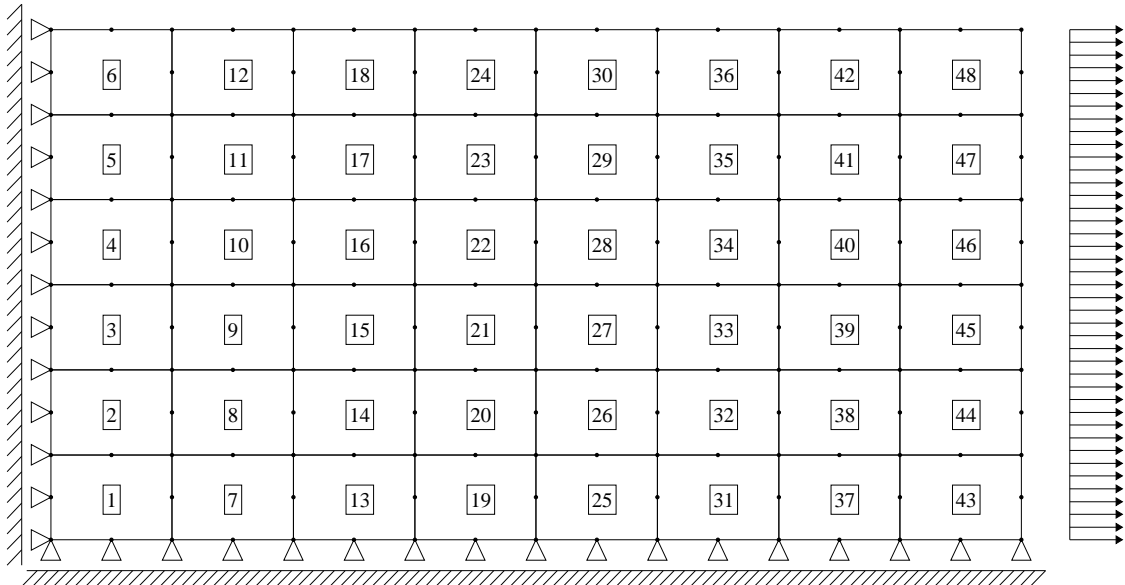
Figure 2.9: A 6×8 finite element mesh with 8-node rectangular isoparametric elements to model the plate of Figure 2.8.

Table 2.6: Horizontal displacement $\mathbf{u}_C$ and vertical displacement $\mathbf{v}_C$ at the upper right corner C of the plate of Figure 2.8 obtained from different methods and different decomposition strategies, with $\mathbf{E} = [195, 205]$ GPa (5% uncertainty).

		Horizontal displ. $\mathbf{u}_C$ (10^{-6} m)				Vertical displ. $\mathbf{v}_C$ (10^{-6} m)			
		Lower Bound	Uncertainty (%)	Upper Bound	Uncertainty (%)	Lower Bound	Uncertainty (%)	Upper Bound	Uncertainty (%)
Outer Solution (OS)	Eigen	9.7318	-0.244	10.2682	0.110	-1.6150	-0.679	-1.3850	0.948
	LDL	9.7312	-0.250	10.2688	0.116	-1.6146	-0.652	-1.3854	0.917
	B-matrix	9.7307	-0.256	10.2694	0.121	-1.6162	-0.753	-1.3838	1.033
Reference (SA)		9.7556	---	10.2569	---	-1.6041	---	-1.3982	---
Inner Solution (IS)	Eigen	9.7672	0.119	10.2328	-0.235	-1.5908	0.833	-1.4092	-0.786
	LDL	9.7678	0.125	10.2322	-0.241	-1.5912	0.805	-1.4088	-0.755
	B-matrix	9.7683	0.130	10.2317	-0.246	-1.5896	0.907	-1.4104	-0.871
Monte Carlo (MC)		9.8993	1.473	10.1021	-1.510	-1.5466	3.584	-1.4580	-4.272
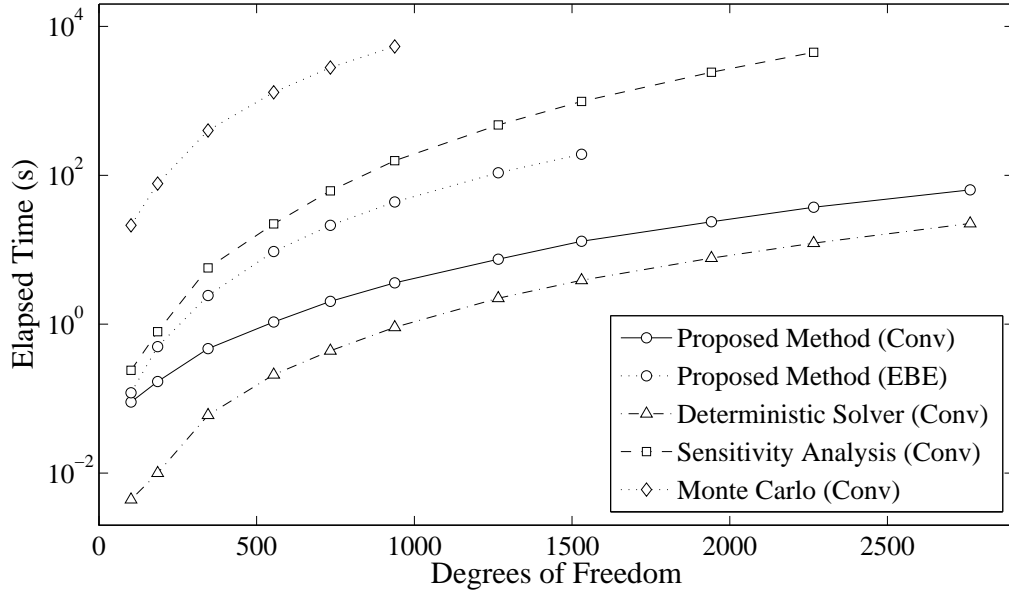
Figure 2.10: Efficiency study of the rectangular plate in Figure 2.8, under 5% uncertainty in the Young's modulus $\mathbf{E}$.

Table 2.7: Computational time required for the static analysis of the rectangular plate of Figure 2.8 using different methods (5% uncertainty in material properties, $\mathbf{E} = [195, 205]$ GPa).

Mesh	Element	DOF	Monte Carlo (MC, s)	Sensitivity Analysis (SA, s)	Deter-ministic (DS, s)	Current EBE (s)	Conv (s)
3×4	12	102	21.32	0.24	0.00	0.12	0.09
4×6	24	186	77.38	0.79	0.01	0.50	0.17
6×8	48	346	400.21	5.70	0.06	2.43	0.47
8×10	80	554	1299.76	22.27	0.21	9.45	1.07
9×12	108	734	2801.68	61.77	0.44	21.29	2.03
10×14	140	938	5375.86	156.88	0.91	43.85	3.59
12×16	192	1266	---	474.90	2.23	108.09	7.47
13×18	234	1530	---	982.34	3.89	191.26	12.98
15×20	300	1942	---	2423.76	7.73	---	23.73
16×22	352	2266	---	4476.31	12.28	---	37.15
18×24	432	2762	---	---	22.49	---	63.59

Table 2.7 lists the corresponding element numbers and total number of Degrees Of Freedom (DOF) for each mesh, as well as the computational time for each method. Figure 2.10 visualizes the comparison in the table via a semi-log plot. The computational time for the deterministic solver (DS) is also included, enabling to extend the estimate for cases when the SA and MC solutions are computationally unfeasible. For instance, for a 15×20 mesh, it is estimated that MC from an ensemble of 10,000 simulations requires $7.73 \times 10,000 = 7.73 \times 10^4$ seconds, or 21.5 hours. Both the Element-by-Element (EBE) and the conventional (Conv) assembly are included

Table 2.8: Computational time required for the static analysis of the rectangular plate of Figure 2.8 using different assembly strategies (5% uncertainty in material properties, $\mathbf{E} = [195, 205]$ GPa).

Mesh	Element Number	Dimen. of G	EBE Assembly				Dimen. of G	Conv. Assembly			
			Assembly (s)	Inversion (s)	Iteration (s)	Total (s)		Assembly (s)	Inversion (s)	Iteration (s)	Total (s)
3×4	12	502	0.03	0.03	0.06	0.12	118	0.00	0.00	0.09	0.09
4×6	24	976	0.06	0.28	0.16	0.50	208	0.00	0.05	0.12	0.17
6×8	48	1912	0.31	1.84	0.28	2.43	376	0.05	0.08	0.34	0.47
8×10	80	3152	1.15	7.69	0.61	9.45	592	0.19	0.27	0.61	1.07
9×12	108	4234	2.64	17.64	1.01	21.29	778	0.44	0.69	0.90	2.03
10×14	140	5468	5.35	37.22	1.28	43.85	988	0.83	1.34	1.42	3.59
12×16	192	7468	13.18	92.63	2.28	108.09	1324	2.07	2.95	2.45	7.47
13×18	234	9082	23.62	163.94	3.70	191.26	1594	3.62	5.30	4.06	12.98
15×20	300	---	---	---	---	---	2014	7.33	10.39	6.01	23.73
16×22	352	---	---	---	---	---	2344	11.64	16.54	8.97	37.15
18×24	432	---	---	---	---	---	2848	21.18	29.03	13.38	63.59

in the proposed method. However, SA, MC, and DS only use the conventional assembly. It is observed that MC is the most time-consuming, whereas the proposed method is the fastest when conventional assembly is used.

Table 2.8 compares the two element assembly strategies in detail. The algorithm is divided into three consecutive steps:

1) *Assembling* generalized stiffness matrix K_g from the deterministic matrices K_0, C, B, and S_0, as in Eqs. (2.45) and (2.49);

2) Computing GM_g and GA_g either by direct matrix *inversion* or by Gaussian elimination;

3) *Iterating* Eq. (2.55) to obtain the interval outer enclosure $\mathbf{u}_g^{out}$.

The computational time at each step, as well as the total time, is listed in Table 2.8. In addition, the dimension of G is included. Observe that the inversion is by far the most time-consuming component in the Element-by-Element assembly approach. This is because the dimension of G is much larger than its counterpart from the conventional assembly. Indeed, in the latter, the three steps require comparable time. Thus, the conventional assembly is preferred when efficiency is the primary concern.
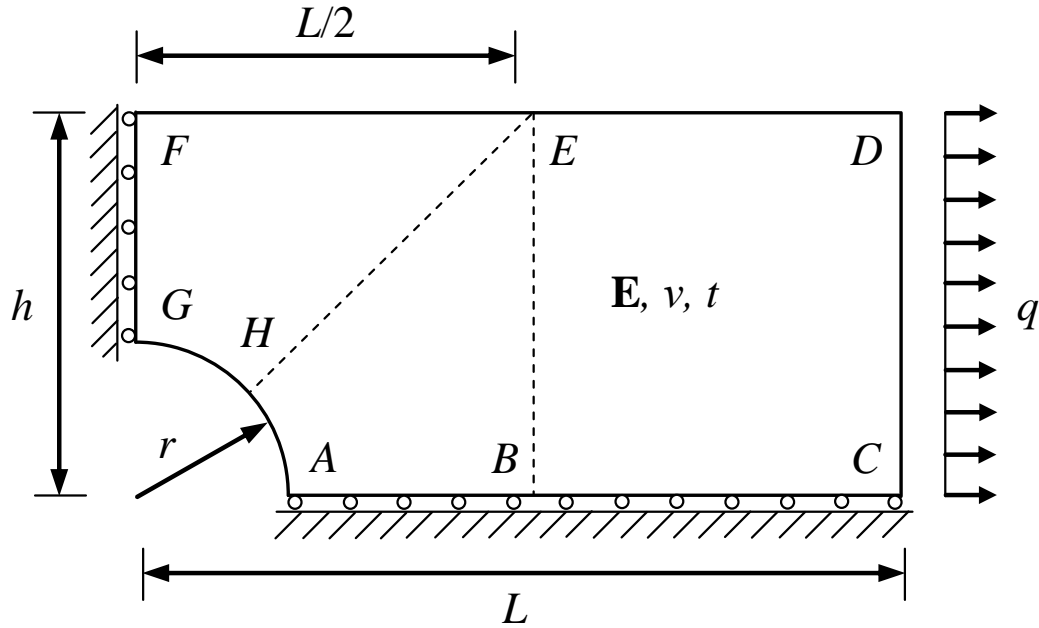
Figure 2.11: A rectangular plate with a circular cutoff subject to uniformly distributed line load.

2.4.5 Plate with a circular cutoff

The fifth example is a rectangular plate with a circular cutoff subject to uniformly distributed load $q = 100$ kN/m, as shown in Figure 2.11. The left and bottom edges of the plate are restrained by rollers. The length, height, and thickness of the plate are $L = 0.1$ m, $h = 0.05$ m, $t = 0.005$ m. The radius of the circular cutoff is $r = 0.02$ m, and the Poisson's ratio is $\nu = 0.3$. Element Young's moduli are modeled by intervals, i.e. $\mathbf{E} = [199, 201]$ GPa, and each $\mathbf{E}$ is assumed to vary independently. To compare results with Zhang [160], 1% uncertainty in $\mathbf{E}$ is used.

The finite element mesh of the plate is shown in Figure 2.12. This is generated by dividing the plate into three curvilinear quadrilaterals, *EFGH*, *ABEH* and *BCDE*, as shown in Figure 2.11. Each macro quadrilateral element is divided into $n \times n$ smaller curvilinear quadrilaterals, which are modeled by one 8-node rectangular element or two 6-node triangular elements. The generated mesh is characterized by n. For instance, Figure 2.12 shows a triangular element mesh with $n = 6$.

Table 2.9 compares nodal displacement $\mathbf{u}_C$ at point C and normal stress $\boldsymbol{\sigma}_{xx}$ at point G obtained from different methods, using 6-node triangular elements and 8-node rectangular elements. The nonlinear programming approach is implemented to provide the reference solution (NLP). The Monte Carlo prediction (MC, obtained from 10,000 simulations) as well as that reported by Zhang [160] is compared against the interval outer and inner solutions (OS and IS) obtained from the proposed method. Results in column 2 to 5 (6 to 9) are obtained using a mesh with 6-node triangular (8-node rectangular) elements. Observe that OS and IS provide the tightest bounds
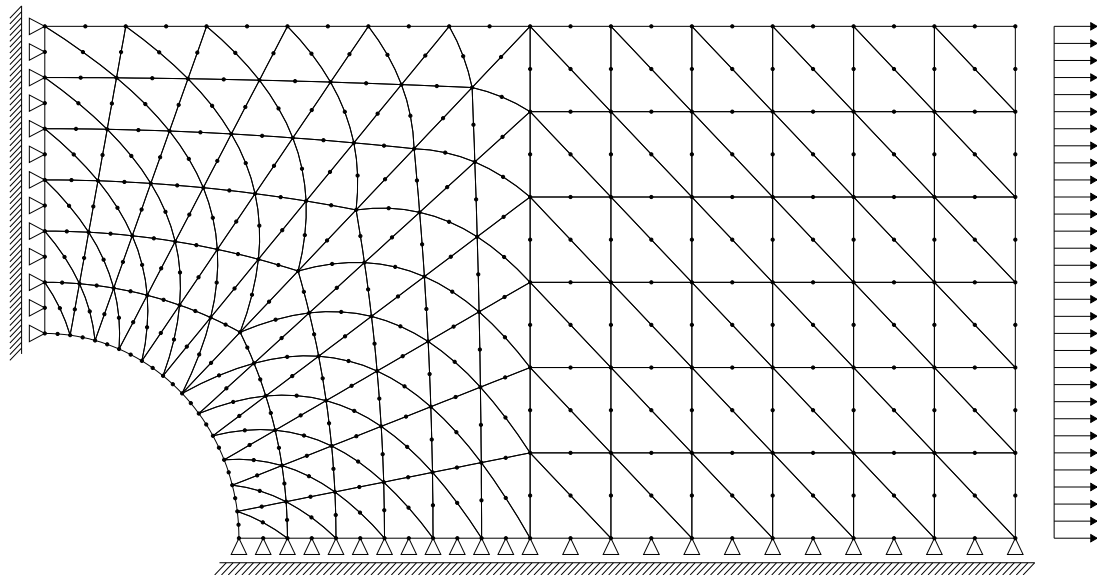
Figure 2.12: Finite element model used in the analysis of the plate with circular cutoff of Figure 2.11 (6-node triangular elements are used).

Table 2.9: Horizontal displacement $\mathbf{u}_C$ at point C and normal stress $\boldsymbol{\sigma}_{xx}$ at point G of the plate of Figure 2.11, obtained from different methods and different elements, with $\mathbf{E} = [199, 201]$ GPa (1% uncertainty).

Horizontal displacement $\mathbf{u}_C$ (10^{-6} m)	6-node triangular element				8-node rectangular element			
	Lower Bound	Uncer-tainty (%)	Upper Bound	Uncer-tainty (%)	Lower Bound	Uncer-tainty (%)	Upper Bound	Uncer-tainty (%)
Zhang (2005)	11.8768	-0.197	12.0387	0.144	---	---	---	---
Outer Solution (OS)	11.8989	-0.011	12.0221	0.006	11.9003	-0.010	12.0233	0.005
Reference (NLP)	11.9002	---	12.0214	---	11.9015	---	12.0227	---
Inner Solution (IS)	11.9009	0.006	12.0201	-0.011	11.9021	0.005	12.0214	-0.011
Monte Carlo (MC)	11.9457	0.382	11.9752	-0.384	11.9429	0.348	11.9784	-0.368
Normal stress $\boldsymbol{\sigma}_{xx}$ at point G (MPa)	6-node triangular element				8-node rectangular element			
	Lower Bound	Uncer-tainty (%)	Upper Bound	Uncer-tainty (%)	Lower Bound	Uncer-tainty (%)	Upper Bound	Uncer-tainty (%)
Outer Solution (OS)	75.0310	-0.055	76.6051	0.046	75.1558	-0.058	76.5105	0.053
Reference (NLP)	75.0726	---	76.5696	---	75.1996	---	76.4701	---
Inner Solution (IS)	75.1082	0.047	76.5280	-0.054	75.2400	0.054	76.4263	-0.057
Monte Carlo (MC)	75.4938	0.561	76.1068	-0.604	75.5849	0.512	76.1147	-0.465

of NLP, and they are respectively tighter than MC and Zhang's solutions.

To study the performance of proposed method under refinement of FE meshes, a series of meshes of the plate with coarse-to-fine discretization are considered. Six-node triangular elements are used in the modeling. Table 2.10 lists the total DOF, element numbers and dimension of the generalized flexibility matrix G for each mesh. Here, 5% material uncertainty is considered and $\mathbf{E} = [195, 205]$ GPa. Nodal displacements $\mathbf{u}_C$ at point C and normal stress $\boldsymbol{\sigma}_{xx}$ at point G computed from different methods are displayed in Figure 2.13. The NLP solution (solid lines with circular markers) is set as a reference, which is compared against MC solution (dashed lines with diamond

markers) and the interval OS (dotted lines with triangular markers). NLP and MC can only be computed for coarse meshes.

From Figure 2.13, it is observed that, when the mesh is refined, the overall widths of the interval solutions do not change, and the difference between OS and NLP remains unchanged. This means that overestimation in the proposed method, if any, does not depend on specific finite element mesh or problem scale.
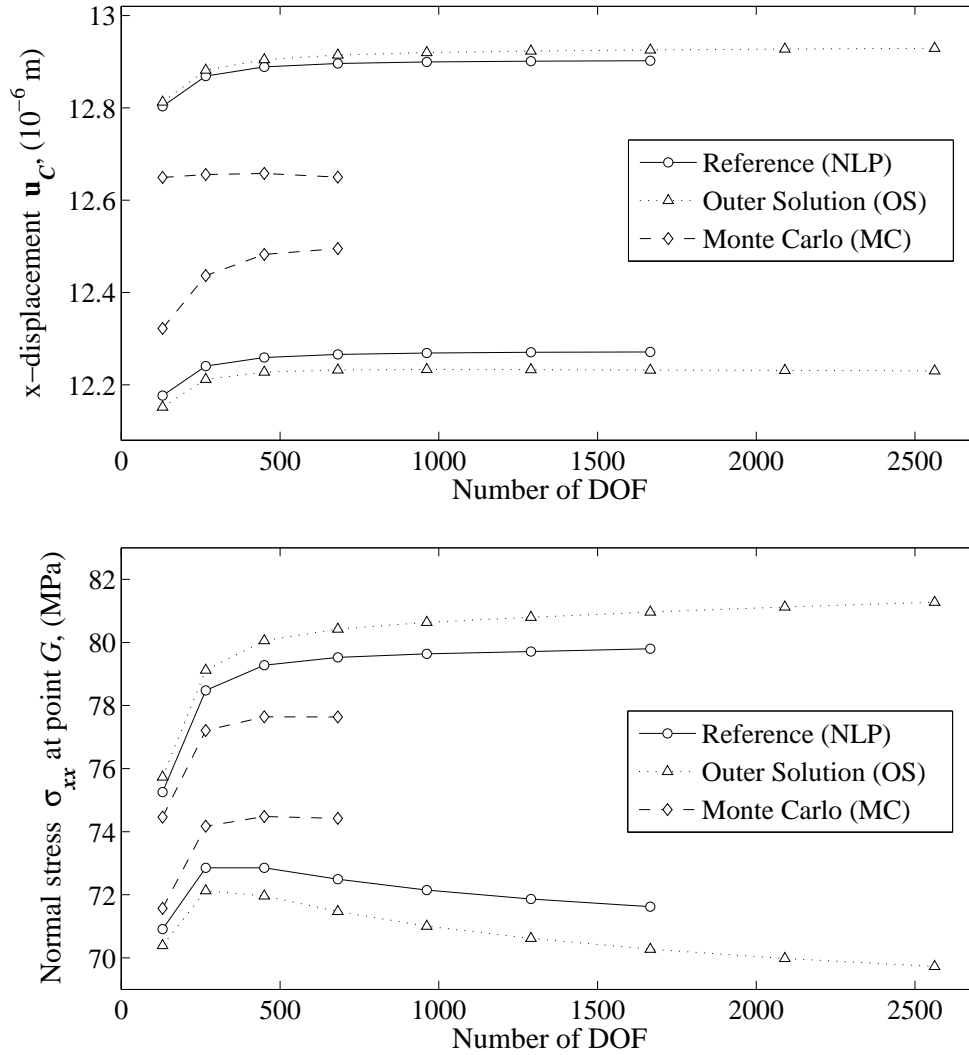
Figure 2.13: Horizontal displacement $\mathbf{u}_C$ at point C and normal stress $\boldsymbol{\sigma}_{xx}$ at point G of the plate of Figure 2.11, obtained from different methods, with $\mathbf{E} = [195, 205]$ GPa (5% uncertainty). The Monte Carlo prediction (MC) is obtained from an ensemble of 10,000 simulations.

Table 2.10: Finite element meshes used in the analysis of the plate of Figure 2.11: DOF, number of elements, and size of G for 6-node triangular elements.

Mesh	DOF	Element	Dimen.	Mesh	DOF	Element	Dimen.
2×2	130	24	144	7×7	1290	294	1334
3×3	266	54	286	8×8	1666	384	1716
4×4	450	96	476	9×9	2090	486	2146
5×5	682	150	714	10×10	2562	600	2624
6×6	962	216	1000				

2.5 Summary

In this chapter, a new interval-based formulation for the structural static analysis of trusses, frames, and plane stress/strain problems under uncertainty is presented. The presented work uses intervals to model uncertainties in the load, geometry and material of the structure. It is the basis for the interval inverse solver for structural static problems, which is presented in Chapter 3. The method is based on a new decomposition strategy of the stiffness matrix and a new variant of the iterative enclosure method, which is specially redesigned to incorporate the new decomposition strategy. The fixed-point form is the key to the development of the iterative scheme.

Numerical examples prove that the presented method is robust, efficient, and gives guaranteed tight enclosures on the exact solution. In particular, the presented method works stably under excessively large uncertainty levels; its computational time is negligible when compared with other methods such as nonlinear programming, Monte Carlo simulation, sensitivity analysis, and endpoint combination method; its outer solution always encloses the exact solution, and its inner solution is always enclosed by the exact solution; the obtained outer and inner encloses are the tightest in comparison with other competing methods in the literature.

CHAPTER III

INTERVAL PARAMETER IDENTIFICATION OF
STRUCTURAL STATIC PROBLEMS

In this chapter, interval-based parameter identification algorithm is developed for structural static problems with uncertainties in load, material, and measurement data. The uncertain parameters are modeled by intervals, and Interval Finite Element Method (IFEM) is used as the cornerstone of the proposed method. The goal is to provide a reliable estimate of the interval stiffness parameter vector $\boldsymbol{\alpha}$, based on the available measurement data $\boldsymbol{\eta}$ corrupted with noise [21, 43, 44, 52, 59]. The structural *equilibrium equation* is given by the following interval linear system

$$\mathbf{K}\mathbf{u} = \mathbf{f}, \tag{3.1}$$

where $\mathbf{K}$ is the stiffness matrix, $\mathbf{u}$ is the nodal displacement vector, and $\mathbf{f}$ is the nodal equivalent load vector. Here $\mathbf{K}$ is parameterized by the stiffness parameter vector $\boldsymbol{\alpha}$ to be identified. Further, the relationship between the measurement data $\boldsymbol{\eta}$ and the nodal displacement $\mathbf{u}$ is assumed linear. Thus $\boldsymbol{\eta}$ and $\mathbf{u}$ satisfy the following *measurement equation*

$$\boldsymbol{\eta} = H\mathbf{u}, \tag{3.2}$$

where H is a deterministic matrix. The above Eq. (3.2) means that the interval enclosure of the predicted response $H\mathbf{u}$ cannot exceed the interval bounds of $\boldsymbol{\eta}$.

In the following sections, the proposed interval inverse solver is introduced in detail. The solver is composed of a deterministic stage and an interval stage. In the deterministic stage, the inverse algorithm is formulated using the adjoint optimization method. Then the algorithm is extended to intervals. Alternative approaches based

on the pseudo-inverse method, the Kalman filtering, and the nonlinear programming technique are developed for comparion. Finally, several numerical examples are presented to validate the performance of the proposed method.

3.1 Deterministic Inverse Solver

In this section, a deterministic solution of the stiffness parameter vector α is sought, using the midpoint values of the interval load uncertainty vector $\boldsymbol{\delta}$ and the interval measurement vector $\boldsymbol{\eta}$. The proposed algorithm is derived using the adjoint-based optimization [26, 42, 45], and it exploits conjugate gradient or Newton-Raphson type methods to find the optimal estimate of the unknown parameters. At first, the measurement data is collected under a single load condition. Then the algorithm is extended to cases when mutiple load conditions are considered.

3.1.1 Conjugate gradient approach

The proposed inverse solver aims at minimizing the difference between the predicted response Hu and the midpoint measurement vector η, under the equilibrium constraint $Ku = f$. Thus the objective functional to be minimized is given by

$$\Gamma = \frac{1}{2}(Hu - \eta)^T W(Hu - \eta) \tag{3.3}$$
$$+ \frac{1}{2}\gamma(\alpha^T R\alpha) + w^T(Ku - f),$$

where W is a diagonal matrix defining the weight for each measurement, $\frac{1}{2}\gamma(\alpha^T R\alpha)$ provides regularization for the problem if necessary, and w is the Lagrangian multiplier to enforce equilibrium [46]. Here, γ is the regularizer weight and R is the regularization matrix associated with the second-order finite difference [62, 123].

From the decomposition of Eq. (2.3), the first variation of Γ

$$\delta\Gamma = \delta u^T H^T W(Hu - \eta) + \delta\alpha^T(\gamma R)\alpha \tag{3.4}$$
$$+ \delta u^T K^T w + \delta w^T(Ku - f) + w^T A\text{diag}(\Lambda\delta\alpha)A^T u$$

is null if

$$\begin{cases} Ku - f = 0; \\ Kw + (H^T W H)u - (H^T W)\eta = 0; \\ \Lambda^T (A^T u \circ A^T w) + (\gamma R)\alpha = 0, \end{cases} \qquad (3.5)$$

where $a \circ b$ denotes the element-by-element (Hadamard) product of two vectors a and b. To obtain Eq. (3.5) from Eq. (3.4), the following matrix symmetry

$$K = K^T = A \operatorname{diag}(\Lambda \alpha) A^T \qquad (3.6)$$

and the following chain of identities

$$w^T A \operatorname{diag}(\Lambda \delta \alpha) A^T u = w^T A (\Lambda \delta \alpha \circ A^T u) = \delta \alpha^T \Lambda^T (A^T u \circ A^T w). \qquad (3.7)$$

have been exploited. The three equations in Eq. (3.5) can be interpreted as: i) equilibrium condition of the original system with equivalent load f, ii) equilibrium condition for the adjoint system with equivalent load $H^T W(\eta - Hu)$, and iii) optimal condition that the gradient g of Γ with respect to α is zero at the solution point.

In the conjugate gradient approach, the first two equations in Eq. (3.5), viz. the equilibrium conditions for the original and adjoint systems, are recast in block form

$$\begin{Bmatrix} H^T W H & K \\ K & 0 \end{Bmatrix} \begin{Bmatrix} u \\ w \end{Bmatrix} = \begin{Bmatrix} H^T W \eta \\ f \end{Bmatrix}. \qquad (3.8)$$

The unknown vectors u and w follow as

$$\begin{Bmatrix} u \\ w \end{Bmatrix} = \begin{Bmatrix} 0 & K^{-1} \\ K^{-1} & T_w \end{Bmatrix} \begin{Bmatrix} H^T W \eta \\ f \end{Bmatrix}, \qquad (3.9)$$

where $T_w = -K^{-1} H^T W H K^{-1}$. The corresponding objective functional Γ and its gradient g with respect to α, viz. third equation in Eq. (3.5), can be rewritten as

$$\Gamma = \frac{1}{2}(Hu - \eta)^T W(Hu - \eta) + \frac{1}{2}\alpha^T (\gamma R)\alpha; \qquad (3.10)$$

$$g = \frac{\partial \Gamma}{\partial \alpha} = \Lambda^T (A^T u \circ A^T w) + (\gamma R)\alpha.$$

The conjugate gradient method is then exploited to iteratively solve for Eq. (3.5). During the computation, α serves as the "master" variable. The solution vectors u and w are solved from Eq. (3.9) after α is updated at each iteration.

3.1.2 Newton-Raphson approach

In the Newton-Raphson approach, in addition to the gradient g, second-order information such as the Hessian matrix is used to determine the descending direction. By noting the following approximations

$$\Delta(Ku) = K\Delta u + A\text{diag}(A^T u)\Lambda\Delta\alpha;$$

$$\Delta(Kw) = K\Delta w + A\text{diag}(A^T w)\Lambda\Delta\alpha; \tag{3.11}$$

$$\Delta\{\Lambda^T(A^T u \circ A^T w)\} = \Lambda^T\text{diag}(A^T u)A^T\Delta w + \Lambda^T\text{diag}(A^T w)A^T\Delta u,$$

the linearization of the governing Eq. (3.5) leads to

$$\begin{Bmatrix} \begin{matrix} H^T W H & K & T\langle A^T w\rangle^T \\ K & 0 & T\langle A^T u\rangle^T \\ T\langle A^T w\rangle & T\langle A^T u\rangle & \gamma R \end{matrix} \end{Bmatrix} \begin{Bmatrix} \Delta u \\ \Delta w \\ \Delta\alpha \end{Bmatrix} = \begin{Bmatrix} 0 \\ 0 \\ -g \end{Bmatrix}, \tag{3.12}$$

where $T\langle x\rangle$ maps a given vector x into the following matrix

$$T\langle x\rangle = \Lambda^T\text{diag}(x)A^T. \tag{3.13}$$

During the derivation, the following equalities have been used

$$(\Delta K)u = A\text{diag}(\Lambda\Delta\alpha)A^T u = A\text{diag}(A^T u)\Lambda\Delta\alpha; \tag{3.14}$$

$$(\Delta K)w = A\text{diag}(\Lambda\Delta\alpha)A^T w = A\text{diag}(A^T w)\Lambda\Delta\alpha.$$

Directly solving the linear system in Eq. (3.12) is inefficient, because one is only interested in the update in the stiffness parameter vector $\Delta\alpha$. Here the generlized stiffness matrix in Eq. (3.12) is divided into four blocks such that

$$K_b = \begin{Bmatrix} H^T W H & K \\ K & 0 \end{Bmatrix}, \qquad T_b = \begin{Bmatrix} T\langle A^T w\rangle & T\langle A^T u\rangle \end{Bmatrix} \tag{3.15}$$

The upper-left block K_b has already been inverted earlier in Eq. (3.9). Then the inverse of the generalized stiffness matrix is given by

$$\begin{Bmatrix} K_b & T_b^T \\ T_b & \gamma R \end{Bmatrix}^{-1} = \begin{Bmatrix} K_b^{-1} + K_b^{-1}T_b^T G_\alpha T_b K_b^{-1} & -K_b^{-1}T_b^T G_\alpha \\ -G_\alpha T_b K_b^{-1} & G_\alpha \end{Bmatrix}, \qquad (3.16)$$

where $G_\alpha = \left(\gamma R - T_b K_b^{-1} T_b^T\right)^{-1}$. Then the descending direction and the step size is determined simultaneously

$$\Delta\alpha = -G_\alpha g. \qquad (3.17)$$

The Newton-Raphson method converges faster than the aforementioned conjugate gradient method in the neighborhood of the optimal point, but it is not as robust as the conjugate gradient method elsewhere. Thus it is beneficial to switch between these methods to enhance the performance of the inverse algorithm.

3.1.3 Multiple load conditions

In the above discussion, the measurement data is assumed to be collected under a single load condition. To account for multiple load conditions, the objective functional Γ has the following form,

$$\Gamma = \sum_{j=1}^{m} \frac{1}{2}(Hu_j - \eta_j)^T W (Hu_j - \eta_j) \qquad (3.18)$$

$$+ \frac{m}{2}\alpha(\gamma R)\alpha + \sum_{j=1}^{m} w_j^T (Ku_j - f_j),$$

where m is the number of load conditions, and subscripts $_j$ denote variables associated with the j-th load condition. The corresponding optimal conditions are

$$\begin{cases} Ku_j - f_j = 0; \\ Kw_j + (H^T W H)u_j - (H^T W)\eta_j = 0; \\ \sum_{j=1}^{m} \Lambda^T (A^T u_j \circ A^T w_j) + m(\gamma R)\alpha = 0. \end{cases} \qquad (3.19)$$

The solution vectors u_j and w_j to the original and adjoint systems under each load condition are obtained from

$$
\left\{ \begin{array}{c} u_j \\ w_j \end{array} \right\} = \left\{ \begin{array}{cc} 0 & K^{-1} \\ K^{-1} & T_w \end{array} \right\} \left\{ \begin{array}{c} H^T W \eta_j \\ f_j \end{array} \right\}.
\tag{3.20}
$$

where $T_w = -K^{-1} H^T W H K^{-1}$. Then the objective functional Γ, as well as its gradient g with respect to α, is expressed in terms of u_j, w_j, and α as

$$
\Gamma = \sum_{j=1}^{m} \frac{1}{2} (Hu_j - \eta_j)^T W (Hu_j - \eta_j) + \frac{m}{2} \alpha^T (\gamma R) \alpha;
\tag{3.21}
$$

$$
g = \frac{\partial \Gamma}{\partial \alpha} = \sum_{j=1}^{m} \Lambda^T (A^T u_j \circ A^T w_j) + m (\gamma R) \alpha.
$$

The matrix G_α in the Newton-Raphson approach is given by

$$
G_\alpha = \left(m \gamma R - \sum_{j=1}^{m} T_{b,j} K_b^{-1} T_{b,j}^T \right)^{-1},
\tag{3.22}
$$

where $T_{b,j}$ is the block matrices associated with u_j and w_j

$$
T_{b,j} = \left\{ T \langle A^T w_j \rangle \quad T \langle A^T u_j \rangle \right\}.
\tag{3.23}
$$

Then either the conjugate gradient method or the Newton-Raphson method can be implemented to obtain the optimal estimate for the problem.

3.2 Interval Inverse Solver

The deterministic inverse solver outlined in the previous section obtains deterministic solutions u_0, w_0, and α_0. In the current section, by using these deterministic solutions as reference points, the corresponding interval governing equations are transformed into a fixed-point form. Then a special variant of the iterative enclosure method is implemented to solve for a guaranteed interval enclosure of the unknown stiffness parameter vector $\boldsymbol{\alpha}$. The current section develops the interval inverse solver for both single and multiple load conditions in detail.

3.2.1 Interval governing equations

When the measurement data is collected under a single load combination, the interval extension of Eq. (3.5) yields the following interval nonlinear governing equations

$$
\begin{cases}
\mathbf{K}(\boldsymbol{\alpha})\mathbf{u} - F\boldsymbol{\delta} = 0; \\
\mathbf{K}(\boldsymbol{\alpha})\mathbf{w} + (H^T W H)\mathbf{u} - (H^T W)\boldsymbol{\eta} = 0; \\
\Lambda^T (A^T \mathbf{u} \circ A^T \mathbf{w}) + (\gamma R)\boldsymbol{\alpha} = 0,
\end{cases}
\tag{3.24}
$$

where the decomposition $\mathbf{f} = F\boldsymbol{\delta}$ has been used, and $\mathbf{K}(\boldsymbol{\alpha})$ emphasizes the dependency of $\mathbf{K}$ on the unknown stiffness parameter $\boldsymbol{\alpha}$.

To transform Eq. (3.24) into a fixed-point form, the key step in implementing the iterative enclosure method, let δ_0 and η_0 be the midpoint values of $\boldsymbol{\delta}$ and $\boldsymbol{\eta}$, respectively. Now, introduce the auxiliary variables

$$
\begin{aligned}
\Delta\boldsymbol{\delta} = \boldsymbol{\delta} - \delta_0, \qquad & \Delta\boldsymbol{\eta} = \boldsymbol{\eta} - \eta_0; \\
\Delta\mathbf{u} = \mathbf{u} - u_0, \qquad \Delta\mathbf{w} = \mathbf{w} - w_0, \qquad & \Delta\boldsymbol{\alpha} = \boldsymbol{\alpha} - \alpha_0
\end{aligned}
\tag{3.25}
$$

to represent deviations of the interval vectors from the corresponding reference solutions, where u_0, w_0, and α_0 are the deterministic solutions obtained earlier. Note that δ_0, η_0, u_0, w_0, and α_0 satisfy Eq. (3.5). Then, the following equalities hold

$$
\begin{aligned}
\mathbf{Ku} &= K_0 u_0 + K_0 \Delta\mathbf{u} + \Delta\mathbf{K} u_0 + \Delta\mathbf{K}\Delta\mathbf{u}; \\
\mathbf{Kw} &= K_0 w_0 + K_0 \Delta\mathbf{w} + \Delta\mathbf{K} w_0 + \Delta\mathbf{K}\Delta\mathbf{w}; \\
A^T \mathbf{u} \circ A^T \mathbf{w} &= A^T u_0 \circ A^T w_0 + A^T u_0 \circ A^T \Delta\mathbf{w} \\
&\quad + A^T \Delta\mathbf{u} \circ A^T w_0 + A^T \Delta\mathbf{u} \circ A^T \Delta\mathbf{w}.
\end{aligned}
\tag{3.26}
$$

Eq. (3.24) is equivalent to

$$
\begin{Bmatrix}
H^T W H & K_0 & T\langle A^T w_0 \rangle^T \\
K_0 & 0 & T\langle A^T u_0 \rangle^T \\
T\langle A^T w_0 \rangle & T\langle A^T u_0 \rangle & \gamma R
\end{Bmatrix}
\begin{Bmatrix}
\Delta\mathbf{u} \\
\Delta\mathbf{w} \\
\Delta\boldsymbol{\alpha}
\end{Bmatrix}
=
$$

$$
\begin{Bmatrix}
0 & H^T W \\
F & 0 \\
0 & 0
\end{Bmatrix}
\begin{Bmatrix}
\Delta\boldsymbol{\delta} \\
\Delta\boldsymbol{\eta}
\end{Bmatrix}
-
\begin{Bmatrix}
A & 0 & 0 \\
0 & A & 0 \\
0 & 0 & \Lambda^T
\end{Bmatrix}
\begin{Bmatrix}
A^T \Delta\mathbf{w} \circ \Lambda\Delta\boldsymbol{\alpha} \\
A^T \Delta\mathbf{u} \circ \Lambda\Delta\boldsymbol{\alpha} \\
A^T \Delta\mathbf{u} \circ A^T \Delta\mathbf{w}
\end{Bmatrix},
\tag{3.27}
$$

by repeatedly using Eq. (3.26) and the following identities

$$\Delta \mathbf{K} \mathbf{x} = A\text{diag}(\Lambda \Delta \boldsymbol{\alpha})A^T \mathbf{x} = A\text{diag}(A^T \mathbf{x})\Lambda \Delta \boldsymbol{\alpha}; \tag{3.28}$$

$$A^T \mathbf{x} \circ A^T \mathbf{y} = \text{diag}(A^T \mathbf{x})A^T \mathbf{y} = \text{diag}(A^T \mathbf{y})A^T \mathbf{x},$$

where K_0 denotes stiffness matrix parameterized by α_0, viz. $K_0 = A\text{diag}(\Lambda \alpha_0)A^T$, $T\langle x \rangle$ has been defined earlier in Eq. (3.13), viz. $T\langle x \rangle = \Lambda^T \text{diag}(x)A^T$, $\mathbf{x}$ and $\mathbf{y}$ can be either $\Delta \mathbf{u}$ or $\Delta \mathbf{w}$ in Eq. (3.28).

3.2.2 Iterative enclosure method

The governing Eq. (3.27) can be recast into the compact form

$$K_g \Delta \mathbf{u}_g = F_g \Delta \boldsymbol{\delta}_g - A_g \boldsymbol{\Theta}(B_g \Delta \mathbf{u}_g), \tag{3.29}$$

which emphasizes the direct relationship between uncertainties of the given data $\Delta \boldsymbol{\delta}$, $\Delta \boldsymbol{\eta}$ (collectively denoted as $\Delta \boldsymbol{\delta}_g$) and those of the unknown vectors $\Delta \mathbf{u}$, $\Delta \mathbf{w}$, $\Delta \boldsymbol{\alpha}$ (collectively denoted as $\Delta \mathbf{u}_g$). Here, K_g, F_g, A_g are known scalar matrices, and $B_g \Delta \mathbf{u}_g$ is composed of the secondary unknown vectors $A^T \Delta \mathbf{u}$, $A^T \Delta \mathbf{w}$, and $\Lambda \Delta \boldsymbol{\alpha}$. The function $\boldsymbol{\Theta}(B_g \Delta \mathbf{u}_g)$ in Eq. (3.29) maps $B_g \Delta \mathbf{u}_g$ into the following interval vector

$$\boldsymbol{\Theta}(B_g \Delta \mathbf{u}_g) = \boldsymbol{\Theta}\left(\left\{ \begin{array}{c} A^T \Delta \mathbf{u} \\ A^T \Delta \mathbf{w} \\ \Lambda \Delta \boldsymbol{\alpha} \end{array} \right\} \right) = \left\{ \begin{array}{c} A^T \Delta \mathbf{w} \circ \Lambda \Delta \boldsymbol{\alpha} \\ A^T \Delta \mathbf{u} \circ \Lambda \Delta \boldsymbol{\alpha} \\ A^T \Delta \mathbf{u} \circ A^T \Delta \mathbf{w} \end{array} \right\}. \tag{3.30}$$

The generalized stiffness matrix K_g is invertible, as shown in Eq. (3.16). By defining $G = K_g^{-1}$, Eq. (3.29) is equivalent to the following fixed-point form

$$\Delta \mathbf{u}_g = (GF_g)\Delta \boldsymbol{\delta}_g - (GA_g)\boldsymbol{\Theta}(B_g \Delta \mathbf{u}_g), \tag{3.31}$$

Following the work by Neumaier and Pownuk [110], an auxiliary variable $\mathbf{v}_g = B_g \Delta \mathbf{u}_g$ is introduced, which satisfies

$$\mathbf{v}_g = B_g \Delta \mathbf{u}_g = (B_g GF_g)\Delta \boldsymbol{\delta}_g - (B_g GA_g)\boldsymbol{\Theta}(\mathbf{v}_g). \tag{3.32}$$

From this, the following iterative scheme is proposed to find a guaranteed interval enclosure for $\mathbf{v}_g$. The iteration starts from the trivial initial guess $\mathbf{v}_g^1 = (B_g G F_g)\Delta\boldsymbol{\delta}_g$ and proceeds in accord with

$$\mathbf{v}_g^{j+1} = (B_g G F_g)\Delta\boldsymbol{\delta}_g - (B_g G A_g)\boldsymbol{\Theta}(\mathbf{v}_g^j), \tag{3.33}$$

where the superscripts ^{j} denote the j-th iteration steps. The iteration stops when there is no change between $\mathbf{v}_g^n$ and $\mathbf{v}_g^{n-1}$ in two consecutive steps. Then a guaranteed outer enclosure $\Delta\mathbf{u}_g^{out}$ is obtained by substituting $B_g\Delta\mathbf{u}_g$ in Eq. (3.31) with the converged $\mathbf{v}_g^n$. The final interval enclosures $\mathbf{u}$, $\mathbf{w}$ and $\boldsymbol{\alpha}$ are obtained by adding u_0, w_0, and α_0 to the obtained $\Delta\mathbf{u}$, $\Delta\mathbf{w}$, $\Delta\boldsymbol{\alpha}$ in the outer enclosure $\Delta\mathbf{u}_g^{out}$, viz

$$\mathbf{u} = \Delta\mathbf{u} + u_0, \qquad \mathbf{w} = \Delta\mathbf{w} + w_0, \qquad \boldsymbol{\alpha} = \Delta\boldsymbol{\alpha} + \alpha_0. \tag{3.34}$$

To further reduce overestimation, the scalar matrices (GF_g), (GA_g) in Eq. (3.31) and $(B_g G F_g)$, $(B_g G A_g)$ in Eq. (3.32) are calculated before multiplication with the interval vectors $\Delta\boldsymbol{\delta}_g$ and $\boldsymbol{\Theta}(\mathbf{v}_g)$. To enhance computational efficiency, the matrix inversion is performed in a block form, as shown in Eqs. (3.9), (3.15), and (3.16).

3.2.3 Multiple load conditions

When measurement data is collected under multiple load conditions, the interval extension of the governing Eq. (3.19) is given by

$$\begin{cases} \mathbf{K}\mathbf{u}_j - F\boldsymbol{\delta}_j = 0; \\ \mathbf{K}\mathbf{w}_j + (H^T W H)\mathbf{u}_j - (H^T W)\boldsymbol{\eta}_j = 0; \\ \sum_{j=1}^m \Lambda^T (A^T \mathbf{u}_j \circ A^T \mathbf{w}_j) + m(\gamma R)\boldsymbol{\alpha} = 0. \end{cases} \tag{3.35}$$

where subscript $_j$ denotes the j-th load condition.

By using the same manipulations as in the previous discussion and defining

$$\Delta\boldsymbol{\delta}_j = \boldsymbol{\delta}_j - \delta_{j0}, \qquad \Delta\boldsymbol{\eta}_j = \boldsymbol{\eta}_j - \eta_{j0},$$
$$\Delta\mathbf{u}_j = \mathbf{u}_j - u_{j0}, \qquad \Delta\mathbf{w}_j = \mathbf{w}_j - w_{j0}, \qquad \Delta\boldsymbol{\alpha} = \boldsymbol{\alpha} - \alpha_0, \tag{3.36}$$

the governing Eq. (3.35) is equivalent to

$$
\begin{Bmatrix} H^T W H & K_0 \\ K_0 & 0 \end{Bmatrix} \begin{Bmatrix} \Delta \mathbf{u}_j \\ \Delta \mathbf{w}_j \end{Bmatrix} + \begin{Bmatrix} T \langle A^T w_{0j} \rangle^T \\ T \langle A^T u_{0j} \rangle^T \end{Bmatrix} \Delta \boldsymbol{\alpha} \tag{3.37}
$$

$$
= \begin{Bmatrix} 0 & H^T W \\ F & 0 \end{Bmatrix} \begin{Bmatrix} \Delta \boldsymbol{\delta}_j \\ \Delta \boldsymbol{\eta}_j \end{Bmatrix} - \begin{Bmatrix} A & 0 \\ 0 & A \end{Bmatrix} \begin{Bmatrix} A^T \Delta \mathbf{w}_j \circ \Lambda \Delta \boldsymbol{\alpha} \\ A^T \Delta \mathbf{u}_j \circ \Lambda \Delta \boldsymbol{\alpha} \end{Bmatrix} ;
$$

and

$$
\sum_{j=1}^{m} \begin{Bmatrix} T \langle A^T w_{0j} \rangle & T \langle A^T u_{0j} \rangle \end{Bmatrix} \begin{Bmatrix} \Delta \mathbf{u}_j \\ \Delta \mathbf{w}_j \end{Bmatrix} + m(\gamma R) \Delta \boldsymbol{\alpha} \tag{3.38}
$$

$$
= -\sum_{j=1}^{m} \Lambda^T \left(A^T \Delta \mathbf{u}_j \circ A^T \Delta \mathbf{w}_j \right).
$$

Then the iterative enclosure method can be implemented to solve for a guaranteed outer enclosure for the stiffness parameter vector $\boldsymbol{\alpha}$, as well as for the solution vectors $\mathbf{u}_j$ and $\mathbf{w}_j$ corresponding to each load condition.

3.3   Pseudo-Inverse Approach

In the pseudo-inverse approach, the algorithm is also divided into two stages. The deterministic pseudo-inverse solver starts from an initial guess for the unknown parameter α, and iteratively updates it to minimize the difference between the predicted system response Hu and the measurement data η, just the same as in the optimization approach. However, the update is obtained from a linearization of the relationship between the unknown stiffness parameters α and the measurements η.

In particular, the system is governed by the equilibrium condition and the measurement equation,

$$
Ku = f, \qquad Hu = \eta, \tag{3.39}
$$

which can be linearized into

$$
A \mathrm{diag}(A^T u) \Lambda \Delta \alpha + K \Delta u = 0, \qquad H \Delta u = \Delta \eta, \tag{3.40}
$$

86

where the identities $\Delta K u = A \mathrm{diag}(\Lambda \alpha) A^T u = A \mathrm{diag}(A^T u) \Lambda \alpha$ have been used. Thus a direct relationship between the increment $\Delta \alpha$ and $\Delta \eta$ is obtained as

$$H_\alpha \Delta \alpha = \Delta \eta, \tag{3.41}$$

where $H_\alpha = -HK^{-1}A\mathrm{diag}(A^T u)\Lambda$.

For given stiffness parameter vector α and measurement vector η, the update $\Delta \alpha$ aims at eliminating the difference between the predicted system response $Hu = HK^{-1}f$ and the measurement data η, viz.

$$\Delta \alpha = -H_\alpha^{PI}(\eta - HK^{-1}f), \tag{3.42}$$

where H_α^{PI} is the pseudo-inverse of H_α, which can be obtained from one or more approaches outlined in Section 1.1.4. Iteratively update of α using Eq. (3.42) yields the deterministic solution α_0 and u_0.

In the interval stage, the following interval extension of Eq. (3.39) is solved,

$$\mathbf{Ku} = F\boldsymbol{\delta}, \qquad H\mathbf{u} = \boldsymbol{\eta}. \tag{3.43}$$

By introducing the new auxiliary variables

$$\begin{aligned} \Delta\boldsymbol{\delta} &= \boldsymbol{\delta} - \delta_0, & \Delta\boldsymbol{\eta} &= \boldsymbol{\eta} - \eta_0, \\ \Delta\mathbf{u} &= \mathbf{u} - u_0, & \Delta\boldsymbol{\alpha} &= \boldsymbol{\alpha} - \alpha_0 \end{aligned} \tag{3.44}$$

the governing Eq. (3.43) is equivalent to

$$\begin{aligned} \begin{Bmatrix} K_0 & A\mathrm{diag}(A^T u_0)\Lambda \\ H & 0 \end{Bmatrix} \begin{Bmatrix} \Delta\mathbf{u} \\ \Delta\boldsymbol{\alpha} \end{Bmatrix} \\ = \begin{Bmatrix} F & 0 \\ 0 & I \end{Bmatrix} \begin{Bmatrix} \Delta\boldsymbol{\delta} \\ \Delta\boldsymbol{\eta} \end{Bmatrix} - \begin{Bmatrix} A \\ 0 \end{Bmatrix} \left(A^T \Delta\mathbf{u} \circ \Lambda\Delta\boldsymbol{\alpha} \right). \end{aligned} \tag{3.45}$$

The newly formulated governing Eq. (3.45) can be recast into the fixed-point form

$$\Delta\mathbf{u}_b = (GF_b)\Delta\boldsymbol{\delta}_b - (GA_b)\left(A^T \Delta\mathbf{u} \circ \Lambda\Delta\boldsymbol{\alpha}\right). \tag{3.46}$$

where the pseudo-inverse matrix G is given by

$$G = \left\{ \begin{array}{cc} K_0 & A\mathrm{diag}(A^T u_0)\Lambda \\ H & 0 \end{array} \right\}^{PI} = \left\{ \begin{array}{cc} K_0^{-1} + G_t H_\alpha^{PI} H K_0^{-1} & -G_t H_\alpha^{PI} \\ -H_\alpha^{PI} H K_0^{-1} & H_\alpha^{PI} \end{array} \right\}. \qquad (3.47)$$

where $G_t = K_0^{-1} A\mathrm{diag}(A^T u_0)\Lambda$. Then the iterative enclosure method can be implemented based on Eq. (3.46) to obtain a guaranteed outer enclosure on $\boldsymbol{\alpha}$. The method can be extended to cases when measurements are collected under multiple load conditions.

3.4   Nonlinear Kalman Filtering

For a structural static problem, the stiffness parameter vector α does not evolve in time. To solve the parameter identification problem using Kalman filters, a pseudo time t' is introduced. Then the stiffness parameter vector α is the state vector, which nominally evolves over the pseudo time t' without any noise:

$$\alpha_{k+1} = \alpha_k, \qquad (3.48)$$

where subscripts $_k$ denote the k-th time step. Then the k-th set of measurement data η_k is related to the stiffness parameter α_k via the measurement equation

$$\eta_k = HK(\alpha_k)^{-1} f_k + v_k, \qquad (3.49)$$

where v_k is the random measurement noise, whose probability characteristics are known as a prior. Thus a sequence of measurements η_k are processed systematically.

When the Extended Kalman Filter (EKF) is used (see Section 1.1.3.2 for detail), one only needs to know the system and measurement equations, which are given in Eqs. (3.48) and (3.49), and the derivative matrices A_{k-1} and C_k, which are given by

$$A_{k-1} = I, \qquad C_k = \frac{\partial \eta_k}{\partial \alpha_k} = H_{\alpha_k}, \qquad (3.50)$$

where $H_{\alpha_k} = -HK(\alpha_k)^{-1} A\mathrm{diag}(A^T u)\Lambda$ has been defined earlier in Eq. (3.41).

When the Unscented Kalman Filter (UKF) is used (see Section 1.1.3.3 for detail), one only needs to replace the measurement Eq. (1.45) with

$$\hat{\eta}_k^{(j)} = HK(\hat{\alpha}_{k|k-1}^{(j)})^{-1}f_k \qquad (3.51)$$

where $\hat{\alpha}_{k|k-1}^{(j)}$ and $\hat{\eta}_k^{(j)}$ are the σ-points for the prior estimate and the predicted measurement at the k-th step, respectively. Apparently, the UKF is non-intrusive and easy to implement.

3.5 *Nonlinear Programming Approach*

In this section, the uncertain parameter identification problem is formulated as a constrained optimization problem. Depending on how the solution vector x and the equality constraints f_{eq} are constructed, the nonlinear programming algorithms are classified into: i) the direct approach, ii) the explicit adjoint approach, and iii) the implicit adjoint approach. These approaches are implemented using the MATLAB optimization toolbox, and provide reference solutions in later numerical examples.

3.5.1 The direct approach

In the direct approach, the solution vector x includes the load uncertainty vector δ, the measurement vector η, the nodal displacement vector u, the Lagrangian multiplier λ, and the stiffness parameter vector α:

$$x = \left\{ \delta^T \ \ \eta^T \ \ u^T \ \ \lambda^T \ \ \alpha^T \right\}^T. \qquad (3.52)$$

The objective functional Ω has the following general form

$$\Omega = c\alpha, \quad \text{or} \quad -c\alpha, \qquad (3.53)$$

when the lower (or upper) bound of the j-th component of the stiffness parameter vector α is computed. Here c is a row vector, whose only non-zero component is unity at the j-th component.

Equality constraints include equilibrium conditions, compatibility requirements, essential boundary conditions, and measurement equation, collectively given by

$$
\begin{cases}
K(\alpha)u + C^T\lambda - F\delta = 0; \\
Cu = 0; \\
Hu = \eta.
\end{cases}
\tag{3.54}
$$

And the inequality constraints require that the load uncertainty vector δ and the measurement vector η vary within their respective interval bounds:

$$
\begin{cases}
\underline{\delta} \le \delta \le \overline{\delta}; \\
\underline{\eta} \le \eta \le \overline{\eta}.
\end{cases}
\tag{3.55}
$$

To accelerate the convergence, the gradient of the objective functional

$$
\frac{\partial\Omega}{\partial x} = \begin{Bmatrix} 0 & 0 & 0 & 0 & c \end{Bmatrix}
\tag{3.56}
$$

and the gradient of the equality constraint equations

$$
\frac{\partial f_{eq}}{\partial x} = \begin{Bmatrix}
-F & 0 & K & C^T & T\langle A^T u\rangle^T \\
0 & 0 & C & 0 & 0 \\
0 & -I & H & 0 & 0
\end{Bmatrix}
\tag{3.57}
$$

are computed, where $T\langle x\rangle = \Lambda^T \text{diag}(x)A^T$ as in Eq. (3.13).

3.5.2 Explicit adjoint approach

In the adjoint approach, the measurement equation $\eta = Hu$ is not directly used. Instead, the governing Eq. (3.5) is used, either explicitly or implicitly. In the explicit adjoint approach, the solution vector x is given by

$$
x = \begin{Bmatrix} \delta^T & \eta^T & u^T & \lambda^T & w^T & \lambda_w^T & \alpha^T \end{Bmatrix}^T,
\tag{3.58}
$$

where w is the adjoint solution, and λ_w is the corresponding Lagrangian multipliers. Then the objective functional Ω, its gradient $\partial\Omega/\partial x$, and the inequality constraints are the same as in the direct approach.

However, the equality constraints are given by

$$
\begin{cases}
K(\alpha)w + C^T\lambda_w + (H^TWH)u - (H^TW)\eta = 0, \quad Cw = 0; \\
K(\alpha)u + C^T\lambda - F\delta = 0, \quad Cu = 0; \\
\Lambda^T(A^Tu \circ A^Tw) + \gamma R\alpha = 0.
\end{cases}
\tag{3.59}
$$

The corresponding gradient is

$$
\frac{\partial f_{eq}}{\partial x} =
\begin{Bmatrix}
0 & -H^TW & H^TWH & 0 & K & C^T & T\langle A^Tw\rangle^T \\
0 & 0 & 0 & 0 & C & 0 & 0 \\
-F & 0 & K & C^T & 0 & 0 & T\langle A^Tu\rangle^T \\
0 & 0 & C & 0 & 0 & 0 & 0 \\
0 & 0 & T\langle A^Tw\rangle & 0 & T\langle A^Tu\rangle & 0 & \gamma R
\end{Bmatrix}.
\tag{3.60}
$$

3.5.3 Implicit adjoint approach

In the third approach, the adjoint equations are no longer explicitly included in the equality constraints. Instead, they are implicitly satisfied in the optimization process. As a result, the solution vector

$$
x = \left\{ \delta^T \ \ \eta^T \ \ \alpha^T \right\}^T,
\tag{3.61}
$$

And the equality constraint is just

$$
\Lambda^T(A^Tu \circ A^Tw) + \gamma R\alpha = 0,
\tag{3.62}
$$

where u and w are the solution vectors to the original and adjoint systems, viz.

$$
\begin{Bmatrix} H^TWH & K \\ K & 0 \end{Bmatrix}
\begin{Bmatrix} u \\ w \end{Bmatrix}
=
\begin{Bmatrix} 0 & H^TW \\ F & 0 \end{Bmatrix}
\begin{Bmatrix} \delta \\ \eta \end{Bmatrix}.
\tag{3.63}
$$

The corresponding gradient of the equality constraint is

$$
\frac{\partial f_{eq}}{\partial x} = \left\{ T_b K_b^{-1} F_b \quad \gamma R - T_b K_b^{-1} T_b^T \right\},
\tag{3.64}
$$

where K_b and T_b are introduced earlier in Eq. (3.15), and F_b is the anti-diagonal block matrix on the right-hand side of Eq. (3.63).

3.6 Numerical Examples

The proposed interval inverse algorithm is coded in INTLAB [122], which is an interval arithmetic extension package developed for the MATLAB environment. To test the performance of the method, uncertain parameter identification of the Young's moduli of i) a pin-roller bar, ii) a simply supported truss, iii) a simply supported beam, and iv) a two-bay two-story frame are considered. The numerical results show that the proposed method is able to provide a guaranteed interval enclosure of the exact parameters. The results are independent of the probability characteristics of the uncertainty, and the algorithm is computationally efficient.

To obtain an interval measurement vector $\boldsymbol{\eta}$ that guarantees to enclose the exact system response, the following procedure is adopted to generate $\boldsymbol{\eta}$.

1) Use a structural FEM model (not necessarily that used in the inversion) to generate the exact measurement data η_{ex}. The interval vector $\boldsymbol{\eta}_{ex}$ is obtained with midpoint value η_{ex} and radius equal to the device tolerance δ_η.

2) An ensemble of perturbed measurements η_j are generated by adding random noise to η_{ex}. The noise is smaller than the tolerance δ_η so that $\eta_j \in \boldsymbol{\eta}_{ex}$.

3) Perturbed interval measurement vectors $\boldsymbol{\eta}_j$ are generated using η_j as midpoint and device tolerance δ_η as radius. $\boldsymbol{\eta}_j$ guarantees to contain η_{ex}, i.e. $\eta_{ex} \in \boldsymbol{\eta}_j$.

4) The measurement vector $\boldsymbol{\eta}$ is obtained as the intersection of all the $\boldsymbol{\eta}_j$ in the ensemble. As a result, $\boldsymbol{\eta}$ contains a random perturbation in its midpoint values and it still guarantees to contain η_{ex}, i.e. $\eta_{ex} \in \boldsymbol{\eta}$.
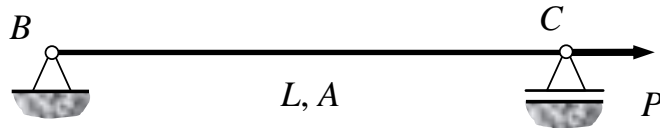
Figure 3.1: A pin-roller bar subject to concentrated traction at the other end.

3.6.1 Pin-roller bar

Consider a straight bar of length $L = 5$ m, as shown in Figure 3.1. The pin-roller bar is subject to concentrated force $P = 100$ kN at one end C. The cross section of the bar is uniform, with an area $A = 0.005$ m^2. Only axial deformations are allowed, and the bar is modeled by 10 equal-length planar truss elements with uniform material properties. For each element,

$$E = 115 + 10 \sin \left(\frac{x}{L} \right) - 5 \cos \left(\frac{x}{L} \right) \text{ GPa,} \tag{3.65}$$

where x is the coordinate of element centroid, and the values of E are given up to four significant digits. The same 10-element model is also used to generate measurement data. Axial displacements at 10 equally distributed nodes along the bar are collected

Table 3.1: Exact and perturbed measurement data for the pin-roller bar of Figure 3.1. The device tolerance is the same for all measurements, $\pm 2 \times 10^{-6}$ m, and 3 sets of perturbed measurements are sampled to define the perturbed data.

Node #	η_{ex} (10^{-3} m)	η (10^{-3} m) Lower Bound	Upper Bound	Difference (10^{-3} m) Lower Bound	Upper Bound	Uncertainty (%) Lower Bound	Upper Bound
1	0.09091	0.09042	0.09226	-0.00049	0.00135	-0.534	1.482
2	0.17281	0.17202	0.17570	-0.00079	0.00289	-0.458	1.671
3	0.24991	0.24789	0.25020	-0.00202	0.00029	-0.809	0.118
4	0.33208	0.33197	0.33265	-0.00011	0.00057	-0.032	0.171
5	0.41980	0.41975	0.42022	-0.00005	0.00042	-0.012	0.102
6	0.50713	0.50554	0.50771	-0.00159	0.00058	-0.315	0.114
7	0.59813	0.59800	0.60031	-0.00013	0.00218	-0.021	0.365
8	0.69694	0.69638	0.69975	-0.00056	0.00281	-0.080	0.403
9	0.79119	0.79014	0.79157	-0.00105	0.00038	-0.133	0.048
10	0.87466	0.87357	0.87555	-0.00109	0.00089	-0.125	0.101

into the exact measurement vector η_{ex}. The interval measurement vector $\boldsymbol{\eta}$ is obtained from 3 sets of perturbed measurements η_j with device tolerance $\pm 2 \times 10^{-6}$ m. The results are listed in Table 1. Note that $\boldsymbol{\eta}$ contains η_{ex}, and uncertainties in $\boldsymbol{\eta}$ range from 0.1% to 2%.

This problem has 10 measurements and 10 unknown element Young's moduli E_j, and it has an analytical solution. Since the bar is statically determined, axial forces in each element equal to the concentrated traction P at the free end. Then $\mathbf{E}_j$ depends upon the displacements $\mathbf{u}_j$, $\mathbf{u}_{j-1}$ of the neighboring nodes, viz.

$$N = \mathbf{E}_j A \frac{\mathbf{u}_j - \mathbf{u}_{j-1}}{L_e} \quad \Rightarrow \quad \mathbf{E}_j = \frac{NL_e}{A\left(\mathbf{u}_j - \mathbf{u}_{j-1}\right)}, \tag{3.66}$$

where $N = P = 100$ kN is the axial force, A is the cross section area, $L_e = L/10$ is the element length, and $\mathbf{u}_0 = 0$ denotes the boundary condition at the hinged end.

The problem is well-posed, so no regularization is required. The initial guess $E = 60$ GPa for all the elements. To reach convergence, 60 iterations are needed in
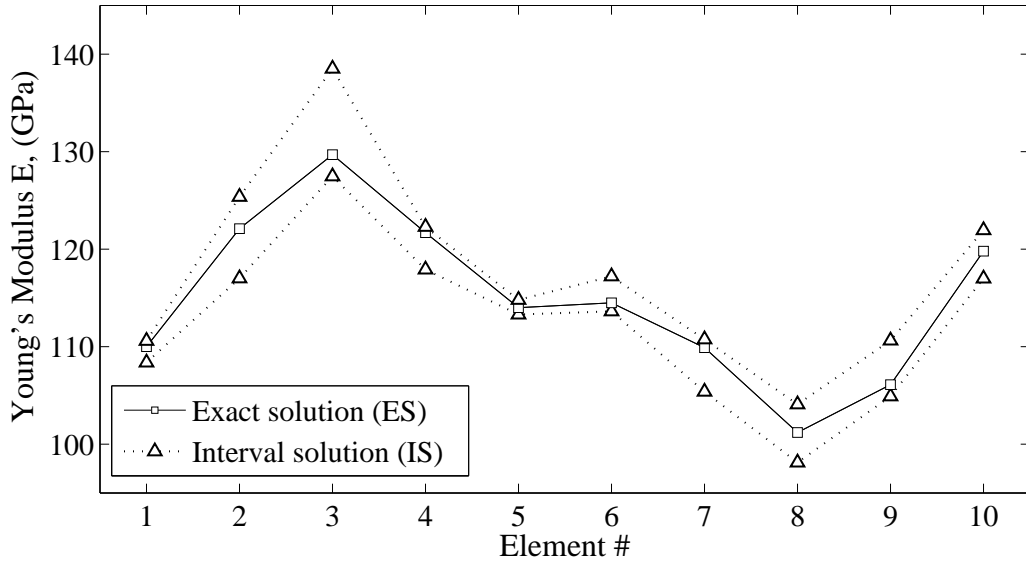
Figure 3.2: Interval-based identification of Young's moduli of the pin-roller bar of Figure 3.1: exact values (solid lines with squares) and interval solution (dashed lines with triangles), which is indistinguishable from the Monte Carlo predictions from an ensemble of 10,000 simulations (measurement uncertainty level 0.1-2%).

Table 3.2: Exact Young's moduli and predicted values for the pin-roller bar of Figure 3.1. Relative differences $(E_N - E_A)/E_A \times 100\%$ for the lower and upper bounds of the two interval solutions are also listed.

Element #	Exact (GPa)	$\mathbf{E}_N$ (GPa)		$\mathbf{E}_A$ (GPa)		Relative Diff. (%)	
		Lower Bound	Upper Bound	Lower Bound	Upper Bound	Lower Bound	Upper Bound
1	110.0	108.37	110.59	108.39	110.59	-0.020	0.000
2	122.1	117.00	125.37	117.27	125.37	-0.231	0.000
3	129.7	127.48	138.52	127.90	138.52	-0.332	0.000
4	121.7	117.91	122.30	117.98	122.30	-0.066	0.000
5	114.0	113.30	114.80	113.31	114.80	-0.009	0.000
6	114.5	113.63	117.22	113.68	117.22	-0.048	0.000
7	109.9	105.39	110.75	105.52	110.75	-0.120	0.000
8	101.2	98.12	104.08	98.28	104.08	-0.169	0.000
9	106.1	104.91	110.63	105.05	110.63	-0.137	0.000
10	119.8	116.99	121.95	117.09	121.95	-0.085	0.000

the deterministic stage, and 12 iterations in the interval stage. The estimated and exact solutions are plotted in Figure 3.2. In the figure, the lower and upper bounds of the estimated solution are the dashed lines with triangular markers, and the exact solution is the solid line with rectangular markers. Apparently, the exact values of the Young's moduli are contained by the interval bounds.

Table 3.2 compares the numerical solution $\mathbf{E}_N$ from the proposed method against the analytical solution $\mathbf{E}_A$ from Eq. (3.66). The upper bounds of the two solutions are identical, while the lower bounds of $\mathbf{E}_N$ are always smaller than the lower bounds of $\mathbf{E}_A$. In other words, $\mathbf{E}_N$ guarantees to enclose $\mathbf{E}_A$. Exact Young's moduli and relative differences $(E_N - E_A)/E_A \times 100\%$ for the lower and upper bounds of the two interval solutions are also included in the table.

Note that the row of GF_g corresponding to Young's modulus $\mathbf{E}_j$ of the j-th element has all of the entries close to zero, except those at columns corresponding to the measurements $\mathbf{u}_j$ and $\mathbf{u}_{j-1}$ at the neighboring nodes. In addition, the two entries have similar magnitude and opposite sign. This is in agreement with the analytical solution given in Eq. (3.66), that is: the modulus $\mathbf{E}_j$ of the j-th element is only a function of $\mathbf{u}_j$ and $\mathbf{u}_{j-1}$.
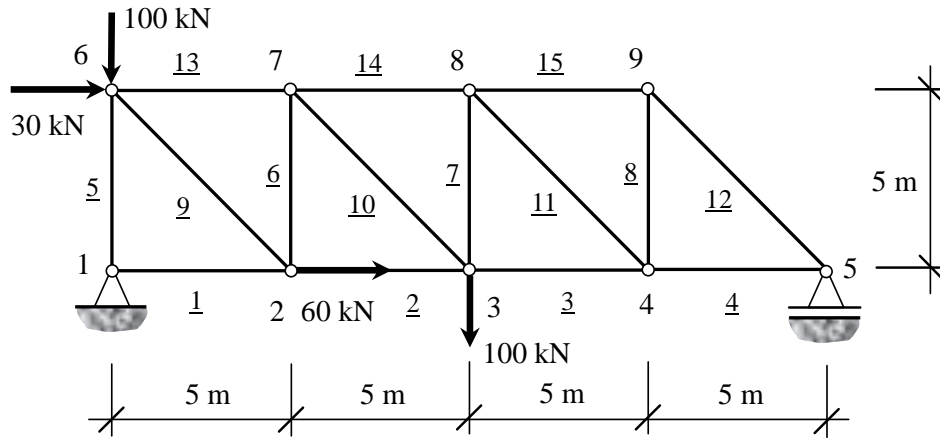
Figure 3.3: A simply supported truss subject to concentrated loads.

3.6.2 Simply supported truss

The second example is a simply supported 15-bar truss, subject to concentrated loads, as shown in Figure 3.3. Nodes of the truss are labeled from 1 to 9, and the bars are labeled from $\underline{1}$ to $\underline{15}$. Horizontal load 60 kN is applied at node 2, vertical load 100 kN at node 3, horizontal load 30 kN and vertical load 100 kN at node 6. The bars have uniform cross sections with area $A = 0.005$ m². Each bar is modeled by one planar truss element with constant material property, and the corresponding Young's modulus is denoted by short bars with circular markers in Figure 3.4. Here we assume that bar $\underline{3}$ and $\underline{13}$ have been damaged, and their effective Young's moduli are 80 GPa and 60 GPa, respectively.

The same finite element model is used to generate the exact measurement data.

Table 3.3: Exact and perturbed measurement data for the simply supported truss of Figure 3.3. The device tolerance is $\pm 1 \times 10^{-5}$ m for nodal displacements, and $\pm 1 \times 10^{-6}$ for strains. Three sets of perturbed measurements are sampled to yield the perturbed data.

	Exact (10^{-3} m)	Perturbed data (10^{-3} m)			
		Lower Bound	Uncer-tainty (%)	Upper Bound	Uncer-tainty (%)
$\mathbf{u}_2$	0.7557	0.7532	-0.321	0.7586	0.382
$\mathbf{v}_2$	-5.1714	-5.1732	-0.036	-5.1591	0.238
$\mathbf{u}_3$	1.3922	1.3871	-0.369	1.4021	0.711
$\mathbf{v}_3$	-7.6368	-7.6393	-0.032	-7.6349	0.025
$\mathbf{u}_4$	2.8297	2.8141	-0.551	2.8310	0.047
$\mathbf{v}_4$	-4.3003	-4.3045	-0.097	-4.2914	0.208
$\mathbf{u}_5$	3.2930	3.2924	-0.019	3.3089	0.482

	Exact (10^{-4})	Perturbed data (10^{-4})			
		Lower Bound	Uncer-tainty (%)	Upper Bound	Uncer-tainty (%)
$\boldsymbol{\varepsilon}_5$	-2.3246	-2.3306	-0.256	-2.3210	0.155
$\boldsymbol{\varepsilon}_6$	-0.6822	-0.6827	-0.078	-0.6674	2.161
$\boldsymbol{\varepsilon}_7$	0.9664	0.9661	-0.025	0.9777	1.167
$\boldsymbol{\varepsilon}_8$	1.0388	1.0309	-0.769	1.0456	0.648
$\boldsymbol{\varepsilon}_9$	1.1427	1.1387	-0.346	1.1457	0.265
$\boldsymbol{\varepsilon}_{10}$	1.1028	1.1000	-0.253	1.1043	0.133
$\boldsymbol{\varepsilon}_{11}$	-1.4241	-1.4354	-0.795	-1.4213	0.199
$\boldsymbol{\varepsilon}_{12}$	-1.3736	-1.3748	-0.088	-1.3591	1.058

To illustrate the performance of the current method under different forms of measurements, nodal displacements of bottom nodes 2 to 5, as well as strains of medium-height bars $\underline{5}$ to $\underline{12}$, are measured. The device tolerance is $\pm 1 \times 10^{-5}$ m for nodal displacement measurements, and $\pm 1 \times 10^{-6}$ for strain measurements. The measurement vector $\boldsymbol{\eta}$ is obtained from 3 sets of perturbed η_j, and the results are shown in Table 3.3. The uncertainties in $\boldsymbol{\eta}$ range from 0.06% to 2%, approximately.

This problem has 15 measurement and 15 unknowns. It is well-posed and no regularizer is needed. The initial guess $E = 60$ GPa is used. 465 iterations are run in the deterministic stage, and 12 iterations in the interval stage. In Figure 3.4, the obtained interval solution (IS) is compared against the exact solution (ES) and Monte Carlo (MC) predictions based on an ensemble of 10,000 simulations.

Clearly, both IS and MC predictions enclose the exact values of the Young's moduli, and IS contains MC. It is observed that the interval enclosures of IS are very tight for elements $\underline{5}$ to $\underline{12}$, and very wide for elements $\underline{13}$ to $\underline{15}$. This is caused by the
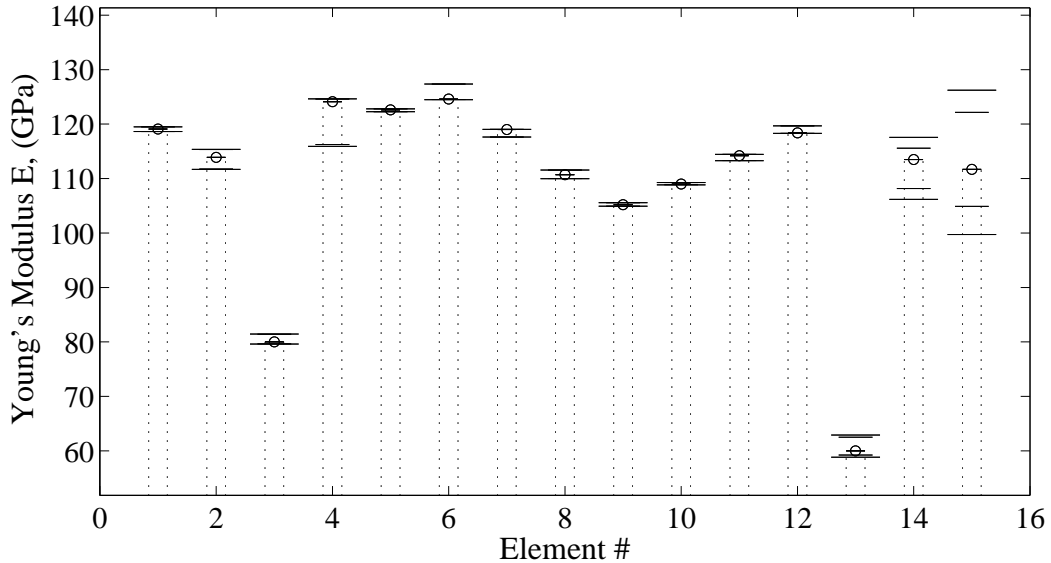
Figure 3.4: Interval-based identification of Young's moduli of a simply-supported truss of Figure 3.3: short bars with circular markers denote the exact values; the long bars denote interval prediction from the proposed method; median-length bars with circles denote Monte Carlo predictions from an ensemble of 10,000 simulations.

Table 3.4: Exact and predicted Young's modulus for the simply supported truss of Figure 3.3. Relative error of the interval solutions from the proposed method and Monte Carlo predictions from an ensemble of 10,000 simulations.

		Young's modulus $\mathbf{E}_3$ (GPa)				Young's modulus $\mathbf{E}_4$ (GPa)			
		Lower Bound	Uncertainty (%)	Upper Bound	Uncertainty (%)	Lower Bound	Uncertainty (%)	Upper Bound	Uncertainty (%)
Kalman Filters	EKF	80.08	0.056	81.69	-0.209	116.62	0.348	123.68	-0.758
	UKF	77.24	-3.497	85.14	4.007	116.01	-0.175	126.17	1.240
Proposed (IS)		80.02	-0.026	81.86	0.000	115.92	-0.253	124.63	0.000
NL Program. (NLP)		80.04	---	81.86	---	116.21	---	124.63	---
Monte Carlo (MC)		80.04	0.001	81.86	-0.001	116.22	0.003	124.62	-0.005
Exact Solution (ES)		80.40	0.453	80.40	-1.781	124.10	6.788	124.10	-0.424

		Young's modulus $\mathbf{E}_8$ (GPa)				Young's modulus $\mathbf{E}_9$ (GPa)			
		Lower Bound	Uncertainty (%)	Upper Bound	Uncertainty (%)	Lower Bound	Uncertainty (%)	Upper Bound	Uncertainty (%)
Kalman Filters	EKF	100.87	-8.288	121.69	9.080	96.71	-7.826	114.48	8.444
	UKF	101.79	-7.453	126.06	12.998	97.13	-7.430	119.34	13.048
Proposed (IS)		109.98	-0.010	111.56	0.000	104.92	-0.002	105.57	0.000
NL Program. (NLP)		109.99	---	111.56	---	104.92	---	105.57	---
Monte Carlo (MC)		109.99	0.000	111.56	0.000	104.92	0.000	105.57	0.000
Exact Solution (ES)		110.70	0.648	110.70	-0.769	105.20	0.265	105.20	-0.346

		Young's modulus $\mathbf{E}_{13}$ (GPa)				Young's modulus $\mathbf{E}_{14}$ (GPa)			
		Lower Bound	Uncertainty (%)	Upper Bound	Uncertainty (%)	Lower Bound	Uncertainty (%)	Upper Bound	Uncertainty (%)
Kalman Filters	EKF	53.27	-10.836	67.79	6.307	103.15	-3.316	129.39	10.055
	UKF	51.52	-13.765	77.09	20.885	91.92	-13.843	121.61	3.440
Proposed (IS)		59.61	-0.220	63.77	0.000	106.16	-0.495	117.57	0.000
NL Program. (NLP)		59.74	---	63.77	---	106.68	---	117.57	---
Monte Carlo (MC)		59.79	0.090	63.72	-0.082	106.93	0.227	117.18	-0.330
Exact Solution (ES)		60.80	1.776	60.80	-4.659	113.50	6.389	113.50	-3.458

distribution of measurements. The strains of element $\underline{5}$ to $\underline{12}$ and the displacements of the bottom nodes are directly measured. So the estimates on $\mathbf{E}_j$ $(j = 1, \ldots, 12)$, especially $\mathbf{E}_j$ $(j = 5, \ldots, 12)$, are more accurate than the estimates on $\mathbf{E}_j$ $(j = 13, \ldots, 15)$.

Table 3.4 compares the obtained estimates on the Young's modulus $\mathbf{E}_j$ in detail. In particular, $\mathbf{E}_3$, $\mathbf{E}_4$, $\mathbf{E}_8$, $\mathbf{E}_9$, $\mathbf{E}_{13}$, and $\mathbf{E}_{14}$ are chosen for display. Solutions obtained from the proposed method (IS), Extended Kalman Filter (EKF), Unscented Kalman Filter (UKF), and Monte Carlo prediction (MC) are compared against the reference solution obtained from the nonlinear programming approach (NLP). From the table, it is observed that:

1) The EKF does not guarantee to enclose the NLP. In contrast, the UKF guarantees to enclose the NLP, but the corresponding overesimation is large.

2) The proposed method guarantees to enclose the NLP with little overestimation. In addition, the upper bounds of the esimates are exactly the same as those obtained from NLP.

3) Different versions of NLP (the direct approach and explicit/implicit adjoint approach) give identical results. However, the implicit adjoint approach is the fastest, while the explicit adjoint approach is the slowest.

4) The Monte Carlo prediction obtained from an ensemble of 10,000 simulations is contained by the NLP, thus underestimates the uncertainties.

5) All these methods contains the exact values.
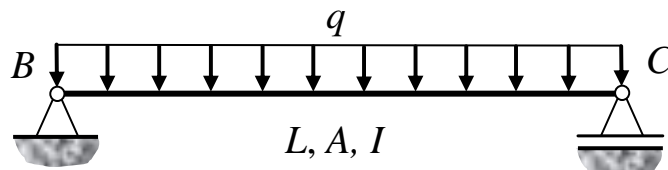
Figure 3.5: A simply supported beam subject to uniformly distributed load.

3.6.3 Simply supported beam

The third example is a simply-supported beam subject to uniformly distributed vertical load $q = 100$ kN/m, as shown in Figure 3.5. The beam has a length $L = 2$ m, and a 5 cm × 3 cm rectangular cross section (cross section area $A = 0.015$ m^2 and moment of inertia $I = 1.125 \times 10^{-4}$ m^4). The beam is subject to lateral deformation, and 20 two-node Euler-Bernoulli beam elements are used in the finite element mesh. The stiffness matrix is computed using the three-node Gaussian quadrature rule. In order to generated a continuous material field, Young's moduli at the quadrature nodes are linearly interpolated from those at the material mesh nodes

$$E = 220 + 10\sin\left(\frac{6x}{L}\right) - 5\cos\left(\frac{13x}{L}\right) \text{ GPa,} \tag{3.67}$$
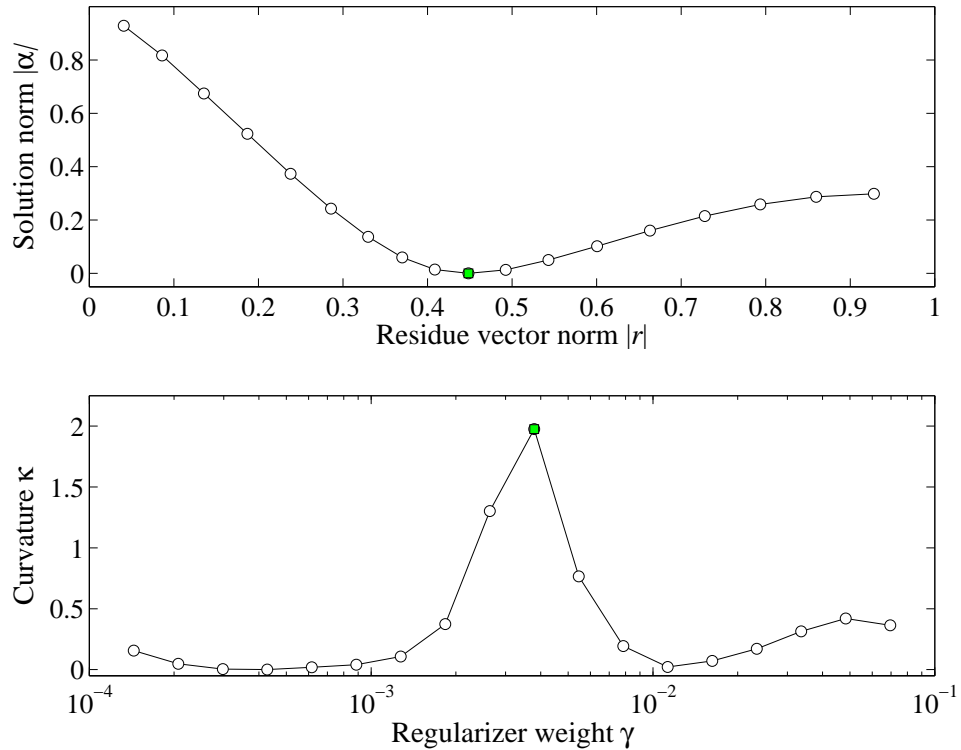
Figure 3.6: The L-curve used to find the optimal regularization weight γ: (top) normalized solution vector norm $|\alpha|$ vs. normalized residue vector norm $|r|$, (bottom) curvature κ of the curve in the top subplot vs. the regularization weight γ. Each circular marker corresponds a different weight γ, and the green rectangular marker denotes the optimal weight $\gamma \approx 2 \times 10^{-3}$.

where x is the nodal coordinate, and the values are given up to four significant digits. The stiffness parameter vector $\boldsymbol{\alpha}$ has 21 components, one for each mesh node.

In the first case, a finer 80-element finite element model is used to generate the measurement data. Young's moduli are linearly interpolated from the abovementioned 21-node material mesh. Further, 9 lateral deflections at equidistant points along the beam are collected as measurements. The measurement vector $\boldsymbol{\eta}$, which has 9 components, is obtained from 3 sets of perturbed data η_j with device tolerance $\pm 2 \times 10^{-6}$ m. The resulting $\boldsymbol{\eta}$ has uncertainties ranging from 0.1% to 1%, and contains the exact measurement data.

The problem is ill-posed, since only 9 measurements are available to estimate 21 unknown parameters. This requires regularization. The regularizer weight γ should be chosen with caution: it has to be large enough to avoid useless estimate or even divergence with unbounded intervals, but not that large, otherwise the solution will be over-smooth [62]. Here, a second-order regularization matrix R is used. To determine the optimal γ, the famous L-curve method is used, as shown in Figure 3.6. According to the figure, $\gamma = 2 \times 10^{-3}$ is chosen as the regularization weight.

Then for the proposed method, the initial guess $E = 160$ GPa for all components in $\boldsymbol{\alpha}$. Convergence is attained in 289 and 37 iterations in the deterministic and interval stages, respectively. The interval estimates are compared against the exact Young's moduli from Eq. (3.67) and Monte Carlo predictions from an ensemble of 100,000 simulations. Figure 3.7 shows the exact solution (ES, solid lines with rectangular markers), the interval solution (IS, dotted lines with triangular markers) and the Monte Carlo prediction (MC, dashed lines with diamond markers). Observe that IS indicates a high level of uncertainty near both ends, especially near the right end, which is attributed to the relatively small bending moment near the ends. In addition, both IS and MC guarantees to enclose ES everywhere, and IS contains MC.

In the second case, two opposing bending moments $M = 50$ kN·m are added to
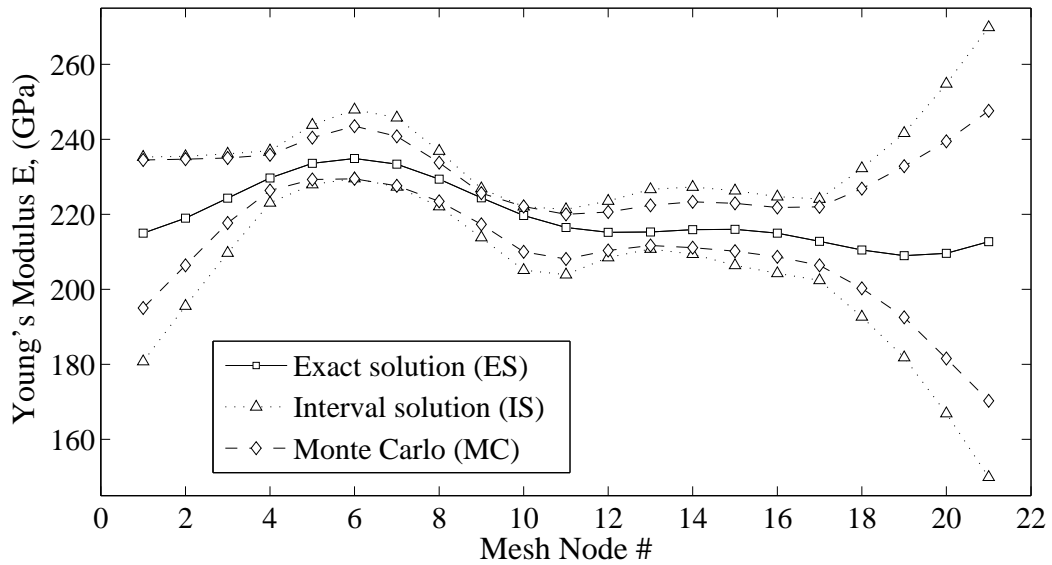
Figure 3.7: Interval-based identification of the Young's moduli of the simply supported beam of Figure 3.5 under uniformly distributed load: interval solution (IS), exact solution (ES) and Monte Carlo (MC) prediction from an ensemble of 100,000 simulations (measurement uncertainty level 0.1-1%).
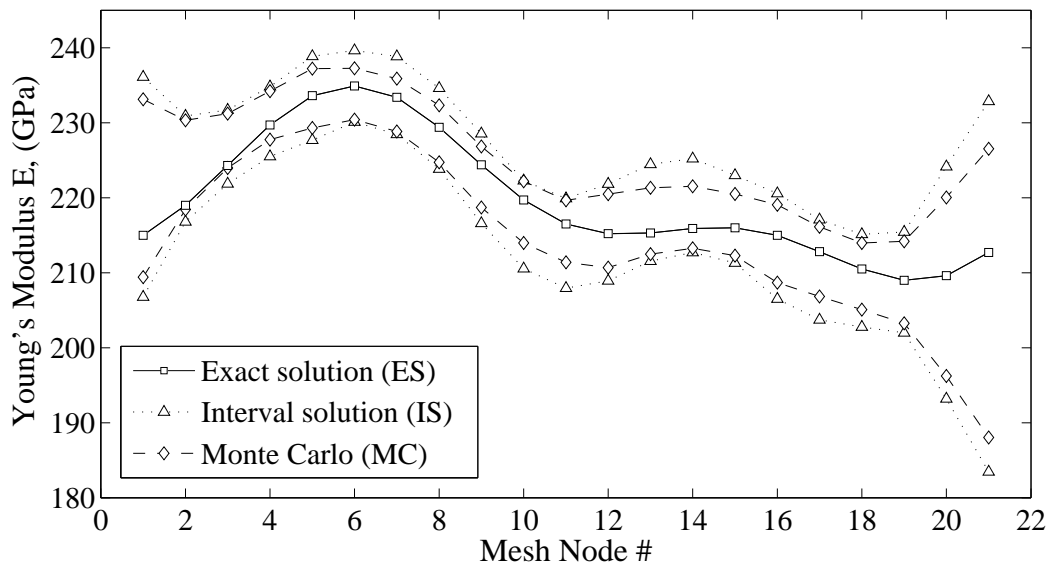
Figure 3.8: Interval-based identification of Young's moduli of the simply supported beam of Figure 3.5 under uniformly distributed load and bending moments at both ends: interval solution (IS), exact solution (ES) and Monte Carlo (MC) prediction from an ensemble of 100,000 simulations (measurement uncertainty level 0.1-1%).

the ends B and C, in order to create a more uniform bending moment diagram for the beam. In addition, rotation angles $\boldsymbol{\theta}_B$ and $\boldsymbol{\theta}_C$ at both ends are measured. The device tolerance is now $\pm 5 \times 10^{-6}$ m for deflections and $\pm 2 \times 10^{-5}$ rad for $\boldsymbol{\theta}_B$ and $\boldsymbol{\theta}_C$. As a result, the level of uncertainty in $\boldsymbol{\eta}$ ranges from 0.1% to 1%, roughly the same as in the first case. IS and MC predictions are compared against the exact values ES in Figure 3.8. Note that the level of uncertainty at the ends is reduced significantly. This is due to the additional bending moments at the ends and extra measurements $\boldsymbol{\theta}_B$ and $\boldsymbol{\theta}_C$. Indeed, the maximum level of uncertainty at the ends is approximately 13% on the left and 23% on the right. In the previous case of Figure 3.7, the uncertainty levels are much higher, approximately 25% on the left and 56% on the right. Near the mid-span, the level of uncertainty is slightly reduced from about 8% in Figure 3.7 to about 5% in Figure 3.8.
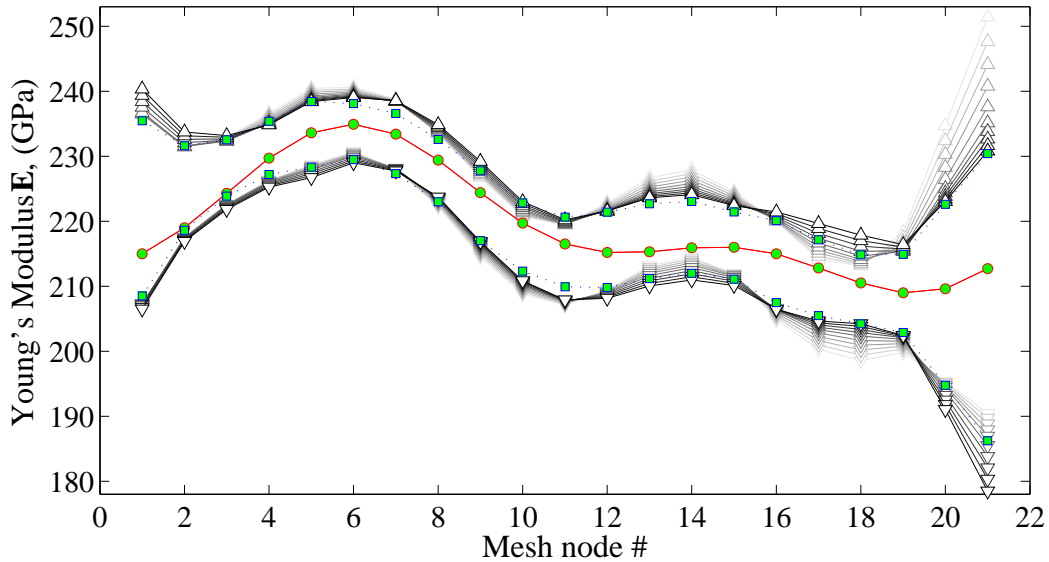
Figure 3.9: Influence of the reference measurement vector η_0 in the interval-based parameter identification of Young's moduli of the simply supported beam of Figure 3.5: exact solution (solid line with circular marker), Monte Carlo prediction from an ensemble of 100,000 simulations (dotted lines with square markers), lower and upper bounds of the interval solution (solid lines with triangular markers). The lightest lines correspond to the lower bound, viz. $\eta_0 = \inf \boldsymbol{\eta}$ and the darkest lines the upper bound, viz. $\eta_0 = \sup \boldsymbol{\eta}$.
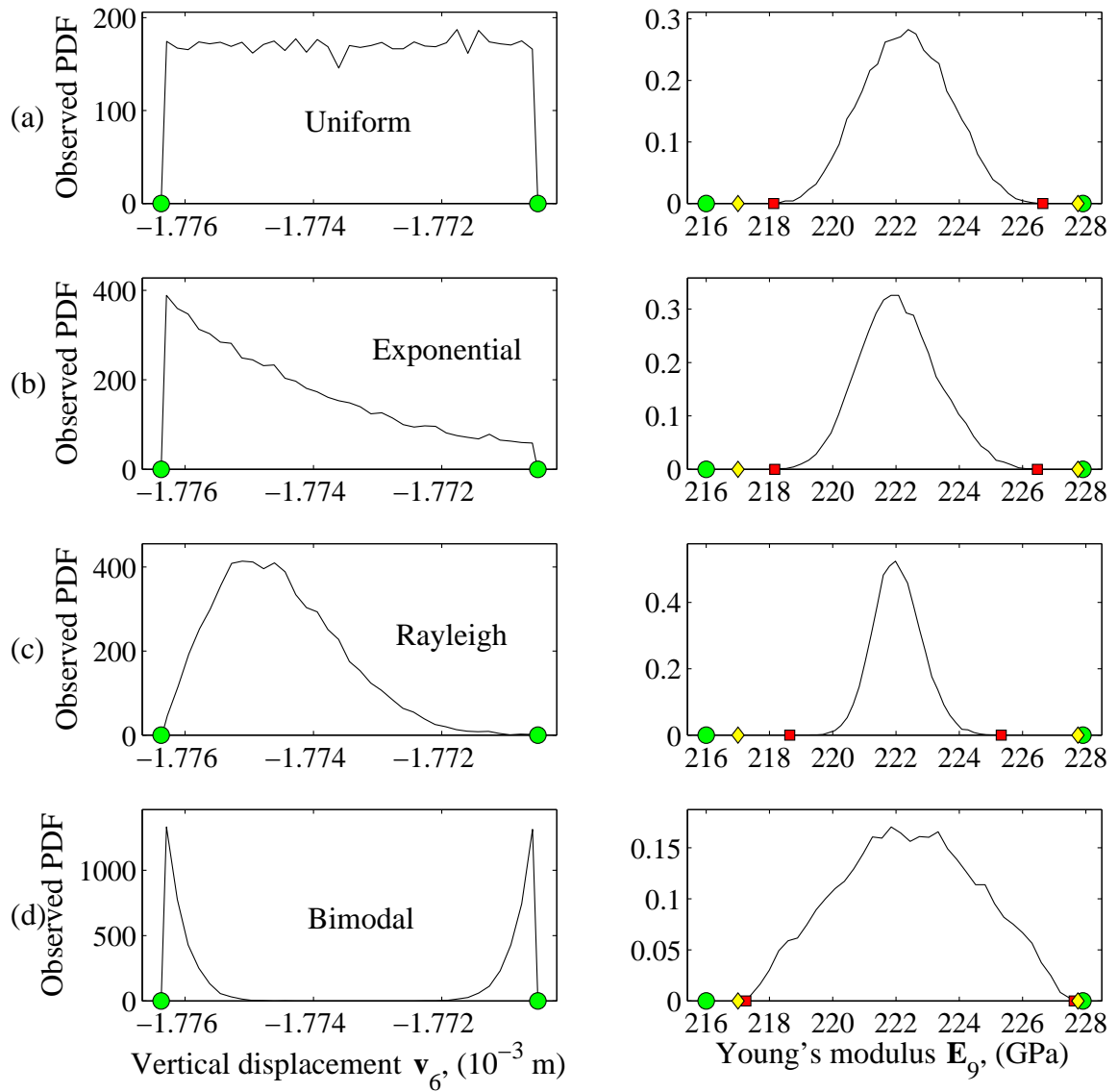
Figure 3.10: Comparison between the interval solution and Monte Carlo prediction of the Young's modulus $\mathbf{E}_9$ of the simply supported beam of Figure 3.5 from an ensemble of 100,000 simulations: (left) observed probability density function (PDF) of axial displacement measurement $\mathbf{v}_6$ sampled from (a) uniform, (b) truncated exponential, (c) truncated Rayleigh and (d) bimodal probability distributions (interval endpoints denoted by circular markers); (right) corresponding observed PDF of the Young's modulus $\mathbf{E}_9$, interval solution (endpoints denoted by circular markers), nonlinear programming solution (endpoints denoted by diamond markers), and Monte Carlo predicted interval $[\min(E_9)\ \max(E_9)]$ (square markers).

In the previous discussions, the deterministic reference vector η_0 is assumed to be the midpoint of the interval measurement vector $\boldsymbol{\eta}$. Figure 3.9 compares the interval solutions obtained from the proposed method with different choices of η_0, from the lower bound $\eta_0 = \inf \boldsymbol{\eta}$ to the upper bound $\eta_0 = \sup \boldsymbol{\eta}$. It is observed that the midpoint values $\eta_0 = \operatorname{mid} \boldsymbol{\eta}$ yields the tightest bounds in general.

Finally, note that interval solutions guarantee to enclose all possible predictions associated with different probabilistic distributions of the measurements, either symmetrical or not (see Figure 3.10).
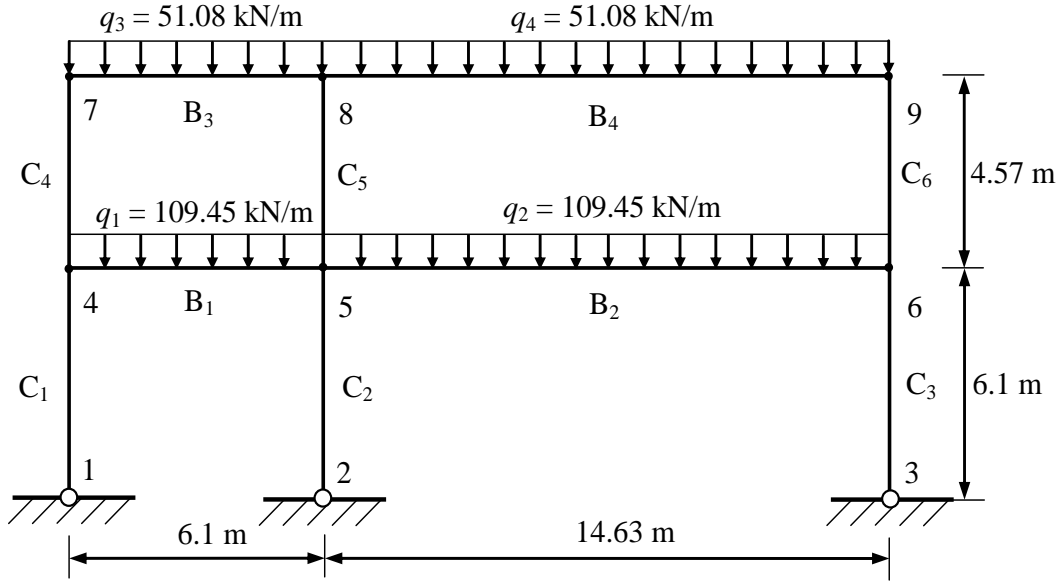
Figure 3.11: A two-bay two-story frame subject to uniformly distributed loads.

3.6.4 Two-bay two-story frame

The fourth example is a two-bay two-story planar frame hinged to the ground, subject to uniformly distributed vertical loads on each floor, as shown in Figure 3.11. The frame is composed of six columns and four beams, labeled as C_j $(j = 1, \ldots, 6)$ and B_j $(j = 1, \ldots, 4)$, respectively. Connecting joints and supports are labeled from 1 to 9. Uniformly distributed vertical loads q_j $(j = 1, \ldots, 4)$ are applied on B_j, where

Table 3.5: Geometric and material properties for the members of the two-bay two-story frame shown in Figure 3.11.

	Shape	A (10^{-4} m^2)	I (10^{-8} m^4)	E (GPa)		Shape	A (10^{-4} m^2)	I (10^{-8} m^4)	E (GPa)
C_1	W12×19	35.940	5411.00	210	B_1	W27×84	160.000	118625.96	205
C_2	W14×132	250.320	63683.41	214	B_2	W36×135	256.130	324660.51	208
C_3	W14×109	206.450	51612.70	205	B_3	W18×40	76.130	25473.36	215
C_4	W10×12	22.835	2239.32	201	B_4	W27×94	178.710	136107.68	214
C_5	W14×109	206.450	51612.70	204					
C_6	W14×109	206.450	51612.70	206					

$q_1 = q_2 = 109.45$ kN/m and $q_3 = q_4 = 51.08$ kN/m.

Each member of the frame has uniform cross section and material property. The corresponding cross section area A, moment of inertia I and Young's modulus E are listed in Table 3.5. Ten two-node Euler-Bernoulli beam elements are used to model the frame, one for each member.

Measurement data used in the inverse algorithm is generated from the same 10-element finite element model. Only nodal displacement $\mathbf{u}_j$, $\mathbf{v}_j$ and rotation angle $\boldsymbol{\theta}_j$ at nodes 4 to 9 ($i = 4, \ldots, 9$) are included in the measurement vector $\boldsymbol{\eta}$. $\boldsymbol{\eta}$ is obtained from 3 sets of perturbed measurements η_j, and the corresponding device tolerance is $\pm 2 \times 10^{-5}$ m for nodal displacements and $\pm 2 \times 10^{-5}$ rad for rotation angles. The level of uncertainty in $\boldsymbol{\eta}$ ranges from approximately 0.1% to 1%, with the exception of $\boldsymbol{\theta}_4 = [-1.2442, -0.9825] \times 10^{-4}$ rad (22.2% uncertainty).

In this benchmark case, 18 measurements (6 nodes × 3 DOF) are used to predict the Young's moduli E of the 10 members. The problem is well-posed and no regularizer is required. Initial guess $E = 160$ GPa is used. The results are compared with the exact values and the Monte Carlo prediction with 10,000 runs in Figure 3.12, following the same guidelines as in Figure 3.4 of the simply-supported truss.
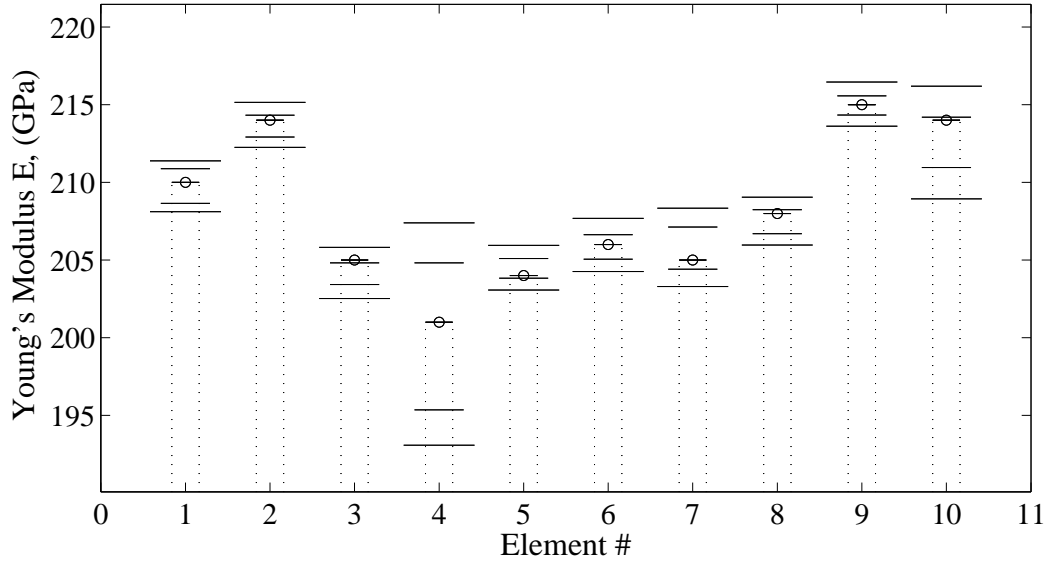
Figure 3.12: Interval-based identification of Young's moduli of the two-bay two-story frame in Figure 3.11: short bars with circular markers denote the exact values; long bars denote interval predictions from the proposed method; median-length bars denote the Monte Carlo predictions from an ensemble of 10,000 simulations (measurement uncertainty level 0.1-1%).
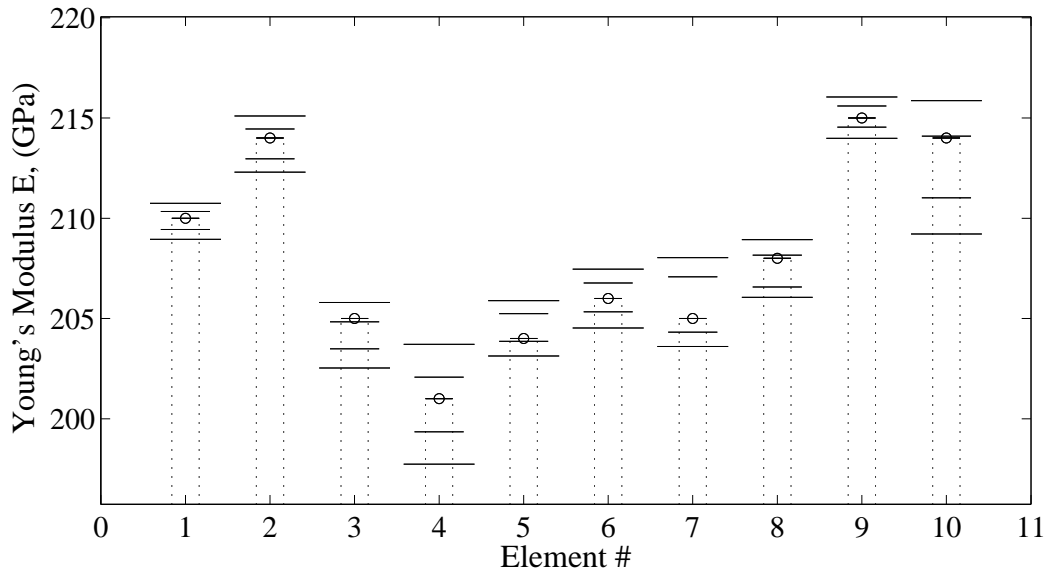
Figure 3.13: Interval-based identification of the Young's moduli of the two-bay two-story frame in Figure 3.11 using more accurate measurements in $\mathbf{v}_4$ and $\mathbf{v}_7$ than those used in Figure 3.12: short bars with circular markers denote the exact values; long bars denote interval prediction from the proposed method; median-length bars denote the Monte Carlo prediction from an ensemble of 10,000 simulations (measurement uncertainty level 0.1-1%).

Observe that the interval solution provides a guaranteed enclosure of both the exact and Monte Carlo solutions.

In Figure 3.12, note that the width of the interval estimate $\mathbf{E}_4$ for the Young's modulus of the left column C_4 on the upper floor, is much wider than other estimates. The wide enclosure is mainly caused by the lateral displacements $\mathbf{v}_4$ and $\mathbf{v}_7$ at nodes 4 and 7, viz. the vertical displacement of the column C_4. They are modeled by two intervals with about 1% uncertainty, i.e. $\mathbf{v}_4 = [-2.3599, -2.3399] \times 10^{-3}$ m and $\mathbf{v}_7 = [-3.4548, -3.4186] \times 10^{-3}$ m. In order to obtain a narrower interval prediction for $\mathbf{E}_4$, the accuracy of the measurements $\mathbf{v}_4$ and $\mathbf{v}_7$ is increased, and the level of uncertainty is reduced to about 0.2%, i.e. $\mathbf{v}_4 = [-2.3515, -2.3465] \times 10^{-3}$ m and $\mathbf{v}_7 = [-3.4378, -3.4288] \times 10^{-3}$ m. The results are depicted in Figure 3.13, showing a significant increase in the accuracy of the predicted value for $\mathbf{E}_4$. In particular, the previous estimate in Figure 3.12 is $\mathbf{E}_4 = [193.09, 207.39]$ GPa (7.1% uncertainty), and that in Figure 3.13 is $\mathbf{E}_4 = [197.72, 203.34]$ GPa (2.8% uncertainty).

3.7 Summary

In this chapter, for the first time structural inverse problems under uncertainty is solved using an interval-based inverse solver. Uncertainties in the system are modeled by intervals, and IFEM is exploited. The resulting inverse algorithm stems from an adjoint-based optimization formulation, and it provides an interval estimate of the unknown parameters (e.g. element Young's moduli). The associated nonlinear interval equations are solved by means of a new variant of the iterative enclosure method. In addition, overestimation is reduced by means of the decomposition of the IFEM matrices, which limits multiple occurrences of the same variable by separating deterministic and interval terms.

The interval solution from the current solver guarantees to enclose the exact parameters, as confirmed by several numerical benchmark problems. In addition, the

interval solution guarantees to enclose the reference solution obtained from the nonlinear programming approach and the Monte Carlo predictions, and the results are independent on the actual probability characteristics of the uncertainties used in the analysis. The performance of the current method is also superior to the nonlinear Kalman filters that are widely used in parameter identifications.

CHAPTER IV

FREQUENCY RESPONSE AND MODAL ANALYSIS OF STRUCTURAL DYNAMIC PROBLEMS BY INTERVALS

In this chapter, the interval forward solver outlined before is extended to structural dynamic problems. The frequency responses, natural frequencies and modal shapes of the structure with uncertain parameters are analyzed using Interval Finite Element Method (IFEM). In the frequency response analysis [31, 51, 99, 108, 124, 125, 155], the following complex interval linear system is solved

$$(-\omega^2 \mathbf{M} + i\omega \mathbf{C} + \mathbf{K})\mathbf{u} = \mathbf{f}, \tag{4.1}$$

where $i = \sqrt{-1}$ is the imaginary unit, ω is the angular frequency under consideration, $\mathbf{M}$, $\mathbf{C}$, and $\mathbf{K}$ are respectively the mass, damping, and stiffness matrix of the structure, $\mathbf{u}$ is the unknown nodal displacement vector, and $\mathbf{f}$ is the nodal equivalent load. Note that $\mathbf{u}$ and $\mathbf{f}$ are complex interval vectors. The goal is to compute an interval enclosure of the stationary response $\mathbf{u}$ at given frequency ω, as well as interval enclosures of derived quantities such as generalized strain $\boldsymbol{\varepsilon}$ and generalized stress $\boldsymbol{\sigma}$,

$$\boldsymbol{\varepsilon} = B\mathbf{u}, \quad \boldsymbol{\sigma} = \mathbf{S}\mathbf{u}, \tag{4.2}$$

where B and $\mathbf{S}$ are the generalized strain- and stress-displacement matrix.

In the modal analysis of the structure, the following Interval Generalized Eigenvalue Problem (IGEP) [65, 82, 83, 95, 96] is solved,

$$(\mathbf{K} - \boldsymbol{\omega}^2 \mathbf{M})\mathbf{u} = 0, \tag{4.3}$$

where $\boldsymbol{\omega}$ is the natural angular frequency measured in rad/s (with $\boldsymbol{\omega}^2$ being the generalized eigen-value of the system), $\mathbf{u}$ is the corresponding modal shape (or the corresponding generalized eigen-vector).

In the following sections, interval forward solvers are developed to provide guaranteed interval enclosures of the stationary responses at given frequencies, as well as the natural frequencies and modal shapes, for elastic structures with uncertainties in load and material. The proposed method is based on the new matrix decomposition outlined in Chapter 2 and new variants of iterative enclosure method specifically designed. In addition, the nonlinear programming techniques are implemented to provide reference solutions for comparison. Finally, several numerical examples are presented to illustrate the performance and computational efficiency of the proposed IFEM algorithm.

4.1 Frequency Response Analysis

In the interval-based frequency response analysis, the goal is to solve the complex interval linear system Eq. (4.1), and obtain guaranteed interval enclosures on the primary quantity $\mathbf{u}$, as well as derived quantities such as the strain vector $\boldsymbol{\varepsilon}$ and the stress vector $\boldsymbol{\sigma}$ [88]. For simplicity, the Rayleigh damping is adopted. Thus

$$\mathbf{C} = \alpha_d \mathbf{M} + \beta_d \mathbf{K}, \tag{4.4}$$

where α_d and β_d are the Rayleigh damping coefficients. More discussions on the Rayleigh damping can be found in Appendix B.

To reduce overestimation in the final solution, the matrix decomposition strategy is presented for IFEM interval vectors and matrices. Derived quantities are solved simultaneously as the primary variables $\mathbf{u}$ [119]. Then a new variant of the iterative enclosure method is presented, which provides guaranteed enclosures of the structural frequency response. The excitation can be either external loads or ground motion, and both the circular and rectangular representation of complex interval variables are considered. The final enclosures are expressed in either Cartesian (real and imaginary parts) or polar (amplitudes and phases) form. In the following subsections, these topics are discussed in detail.

4.1.1 Interval matrix decomposition

The matrix decomposition strategy aims at reducing overestimation when solving the complex interval linear system Eq. (4.1) by limiting multiple occurrences of the same interval variables. In particular, the stiffness matrix $\mathbf{K}$ and the stress-displacement matrix $\mathbf{S}$ are decomposed in accordance with Eqs. (2.3) and (2.4), viz.

$$\mathbf{K} = A\mathrm{diag}(\Lambda\boldsymbol{\alpha})A^T; \tag{4.5}$$

$$\mathbf{S} = \Phi_s\mathrm{diag}(\Lambda_s\boldsymbol{\alpha})A_s^T,$$

where A, Λ, Φ_s, Λ_s, and A_s are deterministic matrices, and $\boldsymbol{\alpha}$ is the interval stiffness parameter vector that accounts for the material uncertainties in the stiffness matrix $\mathbf{K}$. For the mass matrix $\mathbf{M}$, the decomposition is similar to that of $\mathbf{K}$, that is

$$\mathbf{M} = A_m\mathrm{diag}(\Lambda_m\boldsymbol{\alpha}_m)A_m^T, \tag{4.6}$$

where A_m and Λ_m are deterministic matrices, and $\boldsymbol{\alpha}_m$ is the mass parameter vector that accounts for the material uncertainties in $\mathbf{M}$. In practice, the decomposition of $\mathbf{M}$ is obtained from the same procedure as in the case of $\mathbf{K}$. First the element mass matrix $\mathbf{M}_e$ is computed. Its decomposition yields the element matrices A_{me}, Λ_{me}, and $\boldsymbol{\alpha}_{me}$. They are further assembled into their global counterparts A_m, Λ_m, and $\boldsymbol{\alpha}_m$.

For example, consider the decomposition of $\mathbf{M}_e$ for the standard 8-node rectangular isoparametric elements in plane stress/strain problem. Assume uncertainties in the mass density $\boldsymbol{\rho}$, and

$$\mathbf{M}_e = \int_\Omega \boldsymbol{\rho}(\xi)N_e^T(\xi)N_e(\xi)t(\xi)d\Omega, \tag{4.7}$$

where the integration domain Ω is just the entire element, N_e is the element shape function matrix, and t is the thickness of the element. The integral above is evaluated via a 3×3 numerical integration rule, that is

$$\mathbf{M}_e = \sum_{j=1}^{9} w_j J(\xi_j)\boldsymbol{\rho}(\xi_j)N_e^T(\xi_j)N_e(\xi_j)t(\xi_j), \tag{4.8}$$

113

where ξ_j are w_j are the coordinates and weights for all the integration points, and J is the determinant of the Jacobian of the coordinate transformation between the local and global reference systems. Following the same procedure adopted to decompose $\mathbf{K}_e$, the summation in Eq. (4.8) is rewritten into a matrix form

$$\mathbf{M}_e = \left\{ N_e^T(\xi_1) \quad \cdots \quad N_e^T(\xi_9) \right\} \tag{4.9}$$

$$\left\{ \begin{array}{ccc} (w_1 J_1 t_1) I_{2\times 2} \boldsymbol{\rho}_1 & & \\ & \ddots & \\ & & (w_9 J_9 t_9) I_{2\times 2} \boldsymbol{\rho}_9 \end{array} \right\} \left\{ \begin{array}{c} N_e(\xi_1) \\ \vdots \\ N_e(\xi_9) \end{array} \right\},$$

where the subscripts $_j$ denotes variables evaluated at the j-th integration point. Then the decomposition of $\mathbf{M}_e$ follows as

$$\mathbf{M}_e = A_{me} \mathrm{diag}(\Lambda_{me} \boldsymbol{\alpha}_{me}) A_{me}^T, \tag{4.10}$$

where deterministic matrices A_{me}, Λ_{me} and interval vector $\boldsymbol{\alpha}_{me}$ are given by

$$A_{me} = \left\{ N_e^T(\xi_1) \quad \cdots \quad N_e^T(\xi_9) \right\};$$

$$\Lambda_{me} = \left\{ \begin{array}{ccc} w_1 J_1 t_1 e_2 & & \\ & \ddots & \\ & & w_9 J_9 t_9 e_2 \end{array} \right\}, \qquad \boldsymbol{\alpha}_{me} = \left\{ \begin{array}{c} \boldsymbol{\rho}_1 \\ \vdots \\ \boldsymbol{\rho}_9 \end{array} \right\}. \tag{4.11}$$

Note that e_2 is an 2×1 vector with all entries set to 1. The length of the vector e_n equals the number of translational Degrees of Freedom (DOF) at each node.

For the nodal equivalent load vector $\mathbf{f}$, when the structure is excited by external loads, the decomposition is given in Eq. (2.3), viz.

$$\mathbf{f} = F\boldsymbol{\delta}, \tag{4.12}$$

where F is a deterministic matrix and $\boldsymbol{\delta}$ is the load uncertainty vector that accounts for the load uncertainty in $\mathbf{f}$. When the excitation is caused by ground motion, the corresponding nodal equivalent load

$$\mathbf{f} = -\mathbf{Ma} = -\mathbf{M}q\boldsymbol{\delta}, \tag{4.13}$$

where $\boldsymbol{\delta}$ denotes the ground acceleration, $\mathbf{a}$ represents the nodal acceleration of the structure caused by the ground acceleration, and q relates $\boldsymbol{\delta}$ to $\mathbf{a}$, viz. $\mathbf{a} = q\boldsymbol{\delta}$. Noting the decomposition of $\mathbf{M}$ in Eq. (4.6),

$$\mathbf{f} = -A_m \mathrm{diag}(\Lambda_m \boldsymbol{\alpha}_m) A_m^T q \boldsymbol{\delta} \tag{4.14}$$

$$= A_m \mathrm{diag}(\Lambda_m \boldsymbol{\alpha}_m) B_f \boldsymbol{\delta},$$

where $B_f = -A_m^T q$.

Then the complex interval linear system Eq. (4.1) is transformed into a fixed-point form using the matrix decompositions discussed above, and solved by a new variant of iterative enclosure method, as detailed in the following subsections.

4.1.2 Interval governing equations

According to Eq. (4.1), the effective stiffness matrix of the system is given by

$$\mathbf{K}_{\mathrm{eff}} = (-\omega^2 \mathbf{M} + i\omega \mathbf{C} + \mathbf{K}). \tag{4.15}$$

Since the Rayleigh damping is adopted,

$$\mathbf{K}_{\mathrm{eff}} = (-\omega^2 + i\alpha_d \omega)\mathbf{M} + (1 + i\beta_d \omega)\mathbf{K}. \tag{4.16}$$

This can be decomposed such as

$$\mathbf{K}_{\mathrm{eff}} = A_{\mathrm{eff}} \mathrm{diag}(\Lambda_{\mathrm{eff}} \boldsymbol{\alpha}_{\mathrm{eff}}) B_{\mathrm{eff}}, \tag{4.17}$$

where

$$A_{\mathrm{eff}} = \left\{ (1 + i\beta_d \omega)A \quad (-\omega^2 + i\alpha_d \omega)A_m \right\};$$

$$\Lambda_{\mathrm{eff}} = \begin{Bmatrix} \Lambda & 0 \\ 0 & \Lambda_m \end{Bmatrix}, \quad \boldsymbol{\alpha}_{\mathrm{eff}} = \begin{Bmatrix} \boldsymbol{\alpha} \\ \boldsymbol{\alpha}_m \end{Bmatrix}, \quad B_{\mathrm{eff}} = \begin{Bmatrix} A^T \\ A_m^T \end{Bmatrix}. \tag{4.18}$$

Note that the matrix decomposition in Eq. (4.17) is not symmetric since $B_{\mathrm{eff}} \neq A_{\mathrm{eff}}^T$.

Following the way essential boundary conditions are applied in static problems, the IFEM equations associated with the structural system are obtained by combining

the equilibrium equation $\mathbf{K}_{\text{eff}}\mathbf{u} + C^T\boldsymbol{\lambda} = \mathbf{f}$ and the constraint equation $C\mathbf{u} = 0$ (see Section 2.1.3.1 for detail), where C is the constraint matrix, and $\boldsymbol{\lambda}$ is the Lagrangian multiplier representing the internal forces and support reactions. When the structure is excited by external loads and $\mathbf{f} = F\boldsymbol{\delta}$, the governing equations are given by

$$\begin{Bmatrix} \mathbf{K}_{\text{eff}} & C^T \\ C & 0 \end{Bmatrix} \begin{Bmatrix} \mathbf{u} \\ \boldsymbol{\lambda} \end{Bmatrix} = \begin{Bmatrix} F \\ 0 \end{Bmatrix} \boldsymbol{\delta}. \tag{4.19}$$

Using the decompositions for $\mathbf{K}_{\text{eff}}$ in Eq. (4.17), the above equation is recast into

$$\left(\begin{Bmatrix} A_{\text{eff}} \\ 0 \end{Bmatrix} \text{diag}\left(\Lambda_{\text{eff}}\Delta\boldsymbol{\alpha}_{\text{eff}}\right) \begin{Bmatrix} B_{\text{eff}} & 0 \end{Bmatrix} \right. \tag{4.20}$$

$$\left. + \begin{Bmatrix} K_{\text{eff}0} & C^T \\ C & 0 \end{Bmatrix} \right) \begin{Bmatrix} \mathbf{u} \\ \boldsymbol{\lambda} \end{Bmatrix} = \begin{Bmatrix} F \\ 0 \end{Bmatrix} \boldsymbol{\delta},$$

where $\Delta\boldsymbol{\alpha}_{\text{eff}}$ is the difference between $\boldsymbol{\alpha}_{\text{eff}}$ and the reference vector $\alpha_{\text{eff}0}$, viz. $\Delta\boldsymbol{\alpha}_{\text{eff}} = \boldsymbol{\alpha}_{\text{eff}} - \alpha_{\text{eff}0}$, and $K_{\text{eff}0} = A_{\text{eff}}\text{diag}(\Lambda_{\text{eff}}\alpha_{\text{eff}0})B_{\text{eff}}$. Preferably, $\alpha_{\text{eff}0} = \text{mid } \boldsymbol{\alpha}_{\text{eff}}$, where mid denotes the midpoint value of an interval variable. By moving the first term in Eq. (4.20) to the right-hand side, the following equivalent form is obtained

$$\begin{Bmatrix} K_{\text{eff}0} & C^T \\ C & 0 \end{Bmatrix} \begin{Bmatrix} \mathbf{u} \\ \boldsymbol{\lambda} \end{Bmatrix} = \begin{Bmatrix} F \\ 0 \end{Bmatrix} \boldsymbol{\delta} - \begin{Bmatrix} A_{\text{eff}} \\ 0 \end{Bmatrix} \text{diag}\left(B_{\text{eff}}\mathbf{u}\right)\Lambda_{\text{eff}}\Delta\boldsymbol{\alpha}_{\text{eff}}, \tag{4.21}$$

where the following identity has been used

$$\text{diag}\left(\Lambda_{\text{eff}}\Delta\boldsymbol{\alpha}_{\text{eff}}\right)B_{\text{eff}}\mathbf{u} = \text{diag}\left(B_{\text{eff}}\mathbf{u}\right)\Lambda_{\text{eff}}\Delta\boldsymbol{\alpha}_{\text{eff}}. \tag{4.22}$$

When the structure is excited by ground acceleration, $\mathbf{f}$ is decomposed in accordance with Eq. (4.14), which can be rewritten into

$$\mathbf{f} = A_m\text{diag}\left(\Lambda_m\alpha_{m0}\right)B_f\boldsymbol{\delta} + A_m\text{diag}\left(\Lambda_m\Delta\boldsymbol{\alpha}_m\right)B_f\boldsymbol{\delta} \tag{4.23}$$

$$= F_0\boldsymbol{\delta} + A_m\text{diag}\left(B_f\boldsymbol{\delta}\right)\Lambda_m\Delta\boldsymbol{\alpha}_m,$$

where $\Delta\boldsymbol{\alpha}_m$ is the difference between $\boldsymbol{\alpha}_m$ and the reference vector α_{m0}, and the deterministic matrix $F_0 = A_f\text{diag}\left(\Lambda_m\alpha_{m0}\right)B_f$. Again, preferably, $\alpha_{m0} = \text{mid } \boldsymbol{\alpha}_m$.

116

By rewriting the generalized equivalent load of the system into

$$
\left\{ \begin{matrix} \mathbf{f} \\ 0 \end{matrix} \right\} = \left\{ \begin{matrix} F_0 \\ 0 \end{matrix} \right\} \boldsymbol{\delta} + \left\{ \begin{matrix} A_f \\ 0 \end{matrix} \right\} \operatorname{diag}\left(B_f \boldsymbol{\delta}\right) \Lambda_m \Delta \boldsymbol{\alpha}_m, \tag{4.24}
$$

and noting that $\Lambda_m \Delta \boldsymbol{\alpha}_m = \left\{ \begin{matrix} 0 & \Lambda_m \end{matrix} \right\} \Delta \boldsymbol{\alpha}_{\mathrm{eff}}$, the following equivalent governing equation is obtained

$$
\left\{ \begin{matrix} K_{\mathrm{eff}0} & C^T \\ C & 0 \end{matrix} \right\} \left\{ \begin{matrix} \mathbf{u} \\ \boldsymbol{\lambda} \end{matrix} \right\} = \left\{ \begin{matrix} F_0 \\ 0 \end{matrix} \right\} \boldsymbol{\delta} \tag{4.25}
$$

$$
- \left\{ \begin{matrix} A_{\mathrm{eff}} & A_m \\ 0 & 0 \end{matrix} \right\} \operatorname{diag}\left(\left\{ \begin{matrix} B_{\mathrm{eff}} \mathbf{u} \\ -B_f \boldsymbol{\delta} \end{matrix} \right\} \right) \left\{ \begin{matrix} \Lambda_{\mathrm{eff}} \\ 0 & \Lambda_m \end{matrix} \right\} \Delta \boldsymbol{\alpha}_{\mathrm{eff}}.
$$

To compute the derived quantities such as the strain vector $\boldsymbol{\varepsilon}$ and the stress vector $\boldsymbol{\sigma}$, the strain and stress equations $B\mathbf{u} - \boldsymbol{\varepsilon} = 0$ and $\mathbf{S}\mathbf{u} - \boldsymbol{\varepsilon} = 0$ are added to the governing equation. For instance, when the structure is excited by external loads and $\mathbf{f} = F\boldsymbol{\delta}$, the governing equation becomes

$$
\left\{ \begin{matrix} \mathbf{K}_{\mathrm{eff}} & C^T & 0 & 0 \\ C & 0 & 0 & 0 \\ B & 0 & -I & 0 \\ \mathbf{S} & 0 & 0 & -I \end{matrix} \right\} \left\{ \begin{matrix} \mathbf{u} \\ \boldsymbol{\lambda} \\ \boldsymbol{\varepsilon} \\ \boldsymbol{\sigma} \end{matrix} \right\} = \left\{ \begin{matrix} F \\ 0 \\ 0 \\ 0 \end{matrix} \right\} \boldsymbol{\delta}, \tag{4.26}
$$

which is equivalent to the following equation

$$
\left\{ \begin{matrix} K_{\mathrm{eff}0} & C^T & 0 & 0 \\ C & 0 & 0 & 0 \\ B & 0 & -I & 0 \\ S_0 & 0 & 0 & -I \end{matrix} \right\} \left\{ \begin{matrix} \mathbf{u} \\ \boldsymbol{\lambda} \\ \boldsymbol{\varepsilon} \\ \boldsymbol{\sigma} \end{matrix} \right\} = \left\{ \begin{matrix} F \\ 0 \\ 0 \\ 0 \end{matrix} \right\} \boldsymbol{\delta} \tag{4.27}
$$

$$
- \left\{ \begin{matrix} A_{\mathrm{eff}} & 0 \\ 0 & 0 \\ 0 & 0 \\ 0 & \Phi_s \end{matrix} \right\} \operatorname{diag}\left(\left\{ \begin{matrix} B_{\mathrm{eff}} \mathbf{u} \\ A_s^T \mathbf{u} \end{matrix} \right\} \right) \left\{ \begin{matrix} \Lambda_{\mathrm{eff}} \\ \Lambda_s & 0 \end{matrix} \right\} \Delta \boldsymbol{\alpha}_{\mathrm{eff}}.
$$

The above formulation can be extended to cases when the response is caused by ground acceleration.

In the previous discussions, the circular representation is used for the complex interval variables, in which each interval represents a circle in the complex plane (see Section 1.2.1.2 for detail). Alternatively, the rectangular representation can be used, in which the real and imaginary parts of the interval variables are modeled separately and each interval represents a rectangle in the complex plane. To implement the rectangular representation, all the complex interval variables are separately modeled by their real and imaginary parts, respectively. For instance, the nodal displacement vector $\mathbf{u}$ has the following two equivalent representations:

$$\mathbf{u} = \mathbf{u}^R + i\mathbf{u}^I, \quad \Rightarrow \quad \mathbf{u}^C = \left\{ \begin{array}{c} \mathbf{u}^R \\ \mathbf{u}^I \end{array} \right\}, \tag{4.28}$$

where superscripts ^{R} and ^{I} denote the real and imaginary parts of the interval variable, respectively, and superscript ^{C} denotes variables used in the realization. The decomposition of the nodal equivalent load $\mathbf{f}$ yields

$$\mathbf{f} = F^R \boldsymbol{\delta} + i F^I \boldsymbol{\delta}, \quad \Rightarrow \quad \mathbf{f}^C = F^C \boldsymbol{\delta} = \left\{ \begin{array}{c} F^R \\ F^I \end{array} \right\} \boldsymbol{\delta}. \tag{4.29}$$

For the constraint equation $C\mathbf{u} = 0$,

$$C\mathbf{u} = C\mathbf{u}^R + iC\mathbf{u}^I = 0, \quad \Rightarrow \quad C^C\mathbf{u}^C = \left\{ \begin{array}{cc} C & 0 \\ 0 & C \end{array} \right\} \left\{ \begin{array}{c} \mathbf{u}^R \\ \mathbf{u}^I \end{array} \right\} = \left\{ \begin{array}{c} 0 \\ 0 \end{array} \right\}. \tag{4.30}$$

Thus, the realized matrices F^C and C^C are defined as

$$F^C = \left\{ \begin{array}{c} F^R \\ F^I \end{array} \right\}, \quad C^C = \left\{ \begin{array}{cc} C & 0 \\ 0 & C \end{array} \right\}. \tag{4.31}$$

Similarly, the realized effective stiffness matrix $\mathbf{K}^C_{\text{eff}}$ is given by

$$\mathbf{K}^C_{\text{eff}} = \left\{ \begin{array}{cc} \mathbf{K} - \omega^2\mathbf{M} & -\omega(\alpha_d\mathbf{M} + \beta_d\mathbf{K}) \\ \omega(\alpha_d\mathbf{M} + \beta_d\mathbf{K}) & \mathbf{K} - \omega^2\mathbf{M} \end{array} \right\} \tag{4.32}$$

118

which can be decomposed into

$$\mathbf{K}_{\text{eff}}^C = A_{\text{eff}}^C \text{diag}(\Lambda_{\text{eff}}^C \boldsymbol{\alpha}_{\text{eff}}) B_{\text{eff}}^C, \tag{4.33}$$

with

$$A_{\text{eff}}^C = \left\{ \begin{array}{cccc} A & -(\beta_d \omega)A & -\omega^2 A_m & -(\alpha_d \omega)A_m \\ (\beta_d \omega)A & A & (\alpha_d \omega)A_m & -\omega^2 A_m \end{array} \right\};$$

$$\Lambda_{\text{eff}}^C = \left\{ \begin{array}{cc} \Lambda & 0 \\ \Lambda & 0 \\ 0 & \Lambda_m \\ 0 & \Lambda_m \end{array} \right\}, \quad B_{\text{eff}}^C = \left\{ \begin{array}{cc} A^T & 0 \\ 0 & A^T \\ A_m^T & 0 \\ 0 & A_m^T \end{array} \right\}. \tag{4.34}$$

Note that the realized effective stiffness matrix $\mathbf{K}_{\text{eff}}^C$ is not symmetric, and $B_{\text{eff}}^C \neq A_{\text{eff}}^{CT}$.
Then the governing equation is given by

$$\left\{ \begin{array}{cc} \mathbf{K}_{\text{eff}0}^C & C^{CT} \\ C^C & 0 \end{array} \right\} \left\{ \begin{array}{c} \mathbf{u}^C \\ \boldsymbol{\lambda}^C \end{array} \right\} = \left\{ \begin{array}{c} F^C \\ 0 \end{array} \right\} \boldsymbol{\delta}, \tag{4.35}$$

where $\boldsymbol{\lambda}^C$ contains the real and imaginary parts of the Lagrangian multiplier $\boldsymbol{\lambda}$. The corresponding decomposed form is given by

$$\left\{ \begin{array}{cc} K_{\text{eff}0}^C & C^{CT} \\ C^C & 0 \end{array} \right\} \left\{ \begin{array}{c} \mathbf{u}^C \\ \boldsymbol{\lambda}^C \end{array} \right\} = \left\{ \begin{array}{c} F^C \\ 0 \end{array} \right\} \boldsymbol{\delta} - \left\{ \begin{array}{c} A_{\text{eff}}^C \\ 0 \end{array} \right\} \text{diag}(B_{\text{eff}}^C \mathbf{u}^C) \Lambda_{\text{eff}} \Delta \boldsymbol{\alpha}_{\text{eff}}. \tag{4.36}$$

Apparently, the formulation can be extended to account for ground acceleration and derived quantity calculation.

4.1.3 Iterative enclosure method

To solve the interval linear systems Eqs. (4.21), (4.25), (4.27), and (4.36), they are recast into the following compact form

$$K_g \mathbf{u}_g = F_g \boldsymbol{\delta} - A_g \text{diag}(\mathbf{v}_g) \Lambda_g \Delta \boldsymbol{\alpha}_{\text{eff}}, \tag{4.37}$$

where K_g, F_g, A_g, Λ_g are given deterministic matrices, $\mathbf{u}_g$ is the unknown interval vector, $\boldsymbol{\delta}$ and $\Delta \boldsymbol{\alpha}_{\text{eff}}$ are given interval vectors, and $\mathbf{v}_g$ is linearly dependent on $\mathbf{u}_g$, viz.

119

$\mathbf{v}_g = \mathbf{v}_0 + B_g \mathbf{u}_g$. In the most general case, $\mathbf{u}_g$ includes all the primary and derived variables such as $\mathbf{u}$, $\boldsymbol{\lambda}$, $\boldsymbol{\varepsilon}$, and $\boldsymbol{\sigma}$, and $\mathbf{v}_g$ includes additional auxiliary variables $B_{\mathrm{eff}}\mathbf{u}$, $-B_f\boldsymbol{\delta}$, and $A_s^T\mathbf{u}$.

Now introduce $G = K_g^{-1}$ as the generalized flexibility matrix for the system. A fixed-point form for $\mathbf{v}_g$ is obtained as

$$\mathbf{v}_g = \mathbf{v}_0 + (B_g G F_g)\boldsymbol{\delta} - (B_g G A_g)\mathrm{diag}(\mathbf{v}_g)\Lambda_g\Delta\boldsymbol{\alpha}_{\mathrm{eff}}. \tag{4.38}$$

Following the general procedure of iterative enclosure method (see Section 2.2 for more details), a guaranteed outer enclosure for the fixed-point $\mathbf{v}_g$ is obtained using the following iterative scheme

$$\mathbf{v}_g^{j+1} = \mathbf{v}_0 + (B_g G F_g)\boldsymbol{\delta} - (B_g G A_g)\mathrm{diag}(\mathbf{v}_g^j)\Lambda_g\Delta\boldsymbol{\alpha}_{\mathrm{eff}}. \tag{4.39}$$

where subscripts ^{j} denote the j-th iteration. The trivial initial guess $\mathbf{v}_g^1 = \mathbf{v}_0 + (B_g G F_g)\boldsymbol{\delta}$ is used at the beginning. The iteration stops when no improvement in $\mathbf{v}_g^j$ is observed for two consecutive iterations, and the converged solution is denoted as $\mathbf{v}_g^n$. Then the outer solution

$$\mathbf{u}_g^{out} = (G F_g)\boldsymbol{\delta} - (G A_g)\mathrm{diag}(\mathbf{v}_g^n)\Lambda_g\Delta\boldsymbol{\alpha}_{\mathrm{eff}}. \tag{4.40}$$

Up to now, the discussion is restricted to the real and imaginary parts (the Cartesian form) of complex interval variables. However, magnitude and phase angle (the polar form) of a complex interval variable are also important. Here special algorithms are developed to compute a guaranteed enclosure of the magnitudes and phase angles of the solution vector $\mathbf{u}_g$ without unnecessary overestimation.

When the circular representation is adopted, the magnitudes and phase angles are computed after the outer solution is computed. For example, given the complex nodal displacement vector $\mathbf{u}$ in circular form, its magnitude is given by

$$|\mathbf{u}| = \big[|\mathrm{mid}\ \mathbf{u}| - \mathrm{rad}\ \mathbf{u}, \ |\mathrm{mid}\ \mathbf{u}| + \mathrm{rad}\ \mathbf{u}\big], \tag{4.41}$$

where | | denotes the magnitude of a complex variable, mid and rad denote the midpoint and radius of an interval, respectively. The associated phase angle

$$\arg(\mathbf{u}) = \begin{bmatrix} \arg(\text{mid } \mathbf{u}) - \sin^{-1}\left(\dfrac{\text{rad } \mathbf{u}}{|\text{mid } \mathbf{u}|}\right), \\ \arg(\text{mid } \mathbf{u}) + \sin^{-1}\left(\dfrac{\text{rad } \mathbf{u}}{|\text{mid } \mathbf{u}|}\right) \end{bmatrix}, \tag{4.42}$$

where $\arg(\ )$ is the phase angle of a complex variable.

When the rectangular representation is adopted, to reduce overestimation, Eq. (4.40) is reformulated to directly express the magnitudes and phase angles in terms of $\boldsymbol{\delta}$, $\Delta\boldsymbol{\alpha}_{\text{eff}}$, and $\mathbf{v}_g^n$. For example, to compute the magnitude of the nodal displacement $\mathbf{u}$, first compute

$$\begin{aligned}
|\mathbf{u}|^2 &= \left(\mathbf{u}^R\right)^2 + \left(\mathbf{u}^I\right)^2 \\
&= |u_0|^2 + \left(\mathbf{u}^R + u_0^R\right) \circ \Delta\mathbf{u}^R + \left(\mathbf{u}^I + u_0^I\right) \circ \Delta\mathbf{u}^I, \\
&= |u_0|^2 + \text{diag}\left(\mathbf{u}^R + u_0^R\right)\Delta\mathbf{u}^R + \text{diag}\left(\mathbf{u}^I + u_0^I\right)\Delta\mathbf{u}^I,
\end{aligned} \tag{4.43}$$

where superscripts ^{R} and ^{I} denote the real and imaginary parts of the interval variable, respectively, u_0 is a reference vector, and $\Delta\mathbf{u}$ is the difference between $\mathbf{u}$ and u_0, viz. $\Delta\mathbf{u} = \mathbf{u} - u_0$. Then the real and imaginary terms in Eq. (4.40) are separated,

$$\begin{cases} \mathbf{u}^R = (GF_g)^R\boldsymbol{\delta} - (GA_g)^R\text{diag}(\mathbf{v}_g)\Lambda_g\Delta\boldsymbol{\alpha}_{\text{eff}}; \\ \mathbf{u}^I = (GF_g)^I\boldsymbol{\delta} - (GA_g)^I\text{diag}(\mathbf{v}_g)\Lambda_g\Delta\boldsymbol{\alpha}_{\text{eff}}. \end{cases} \tag{4.44}$$

where the superscripts ^{R} and ^{I} denote the rows in GF_g and GA_g corresponding to $\mathbf{u}^R$ and $\mathbf{u}^I$, respectively. Inserting Eq. (4.44) into Eq. (4.43) yields

$$|\mathbf{u}|^2 = |u_0|^2 + \left\{ \begin{aligned} &\text{diag}(\mathbf{u}^R + u_0^R)(GF_g)^R \\ &+ \text{diag}(\mathbf{u}^I + u_0^I)(GF_g)^I \end{aligned} \right\}\Delta\boldsymbol{\delta} \tag{4.45}$$

$$- \left\{ \begin{aligned} &\text{diag}(\mathbf{u}^R + u_0^R)(GA_g)^R \\ &+ \text{diag}(\mathbf{u}^I + u_0^I)(GA_g)^I \end{aligned} \right\}\text{diag}(\mathbf{v})\Lambda_g\Delta\boldsymbol{\alpha}_{\text{eff}},$$

where $\Delta\boldsymbol{\delta} = \boldsymbol{\delta} - \delta_0$, and δ_0 is used to compute the reference vector u_0. Then $|\mathbf{u}|$ is obtained by taking the square root of $|\mathbf{u}|^2$.

Similarly, for the phase angle $\arg(\mathbf{u})$, by using the following guaranteed interval approximation

$$\arg(\mathbf{u}) = \arg(u_0) - \frac{u_0^I \circ \Delta \mathbf{u}^R}{|u_0| \circ |\mathbf{u}|} + \frac{u_0^R \circ \Delta \mathbf{u}^I}{|u_0| \circ |\mathbf{u}|}, \tag{4.46}$$

the interval phase angle $\arg(\mathbf{u})$ is obtained as

$$\arg(\mathbf{u}) = \arg(u_0) + \left\{ \begin{array}{l} -\mathrm{diag}\left\{ u_0^I / (|u_0| \circ |\mathbf{u}|) \right\} (GF_g)^R \\ + \mathrm{diag}\left\{ u_0^R / (|u_0| \circ |\mathbf{u}|) \right\} (GF_g)^I \end{array} \right\} \Delta \boldsymbol{\delta} \tag{4.47}$$
$$- \left\{ \begin{array}{l} -\mathrm{diag}\left\{ u_0^I / (|u_0| \circ |\mathbf{u}|) \right\} (GA_g)^R \\ + \mathrm{diag}\left\{ u_0^R / (|u_0| \circ |\mathbf{u}|) \right\} (GA_g)^I \end{array} \right\} \mathrm{diag}(\mathbf{v})\Lambda_g \Delta \boldsymbol{\alpha}_{\mathrm{eff}}.$$

The magnitudes and phase angles for other variables, such as the Lagrangian multiplier $\boldsymbol{\lambda}$, strain $\boldsymbol{\varepsilon}$, and stress $\boldsymbol{\sigma}$, are obtained in the same way as $\mathbf{u}$.

4.2 Natural Frequency and Modal Shape Analysis

In the interval-based modal analysis, interval enclosures of the natural frequencies and modal shapes of a given elastic structure with uncertain material properties are obtained by solving the Interval Generalized Eigenvalue Problem (IGEP) in Eq. (4.3). To reduce overestimation, the interval matrix decomposition is adopted, and a special version of iterative enclosure method is developed to solve the IGEP. In the following subsections, the proposed method is presented in detail.

4.2.1 Interval governing equations

In the proposed method, the stiffness matrix $\mathbf{K}$ and the mass matrix $\mathbf{M}$ are decomposed in accordance with Eqs. (4.5) and (4.6), viz.

$$\mathbf{K} = A\mathrm{diag}(\Lambda \boldsymbol{\alpha})A^T; \tag{4.48}$$
$$\mathbf{M} = A_m\mathrm{diag}(\Lambda_m \boldsymbol{\alpha}_m)A_m^T,$$

where interval parameter vectors $\boldsymbol{\alpha}$ and $\boldsymbol{\alpha}_m$ model uncertainties in the stiffness and mass of the structure, respectively.

To maintain the decomposition forms in Eq. (4.48), the compatibility conditions and essential boundary conditions are imposed by means of the constraint equation $C\mathbf{u} = 0$ (see Section 2.1.3.1 for detail). Thus the natural frequency $\boldsymbol{\omega}$ and the corresponding modal shape $\mathbf{u}$ of the structure satisfy

$$\left(\begin{Bmatrix} \mathbf{K} & C^T \\ C & 0 \end{Bmatrix} - \boldsymbol{\omega}^2 \begin{Bmatrix} \mathbf{M} & 0 \\ 0 & 0 \end{Bmatrix} \right) \begin{Bmatrix} \mathbf{u} \\ \boldsymbol{\lambda} \end{Bmatrix} = \begin{Bmatrix} 0 \\ 0 \end{Bmatrix}, \tag{4.49}$$

where $\boldsymbol{\lambda}$ is the Lagrangian multiplier associated with the constraint equation $C\mathbf{u} = 0$, which denotes internal forces and support reactions.

To solve the IGEP in Eq. (4.49), consider the deterministic system obtained by replacing $\mathbf{K}$ and $\mathbf{M}$ with their respective midpoint values. The corresponding deterministic solution ω_0, u_0, and λ_0 can be obtained from any generalized eigenvalue problem solver, which satisfy

$$\left(\begin{Bmatrix} K_0 & C^T \\ C & 0 \end{Bmatrix} - \omega_0^2 \begin{Bmatrix} M_0 & 0 \\ 0 & 0 \end{Bmatrix} \right) \begin{Bmatrix} u_0 \\ \lambda_0 \end{Bmatrix} = \begin{Bmatrix} 0 \\ 0 \end{Bmatrix}, \tag{4.50}$$

where $K_0 = A\mathrm{diag}(\Lambda\alpha_0)A^T$ and $M_0 = A_m\mathrm{diag}(\Lambda_m\alpha_{m0})A_m^T$, α_0 and α_{m0} are the midpoint of $\boldsymbol{\alpha}$ and $\boldsymbol{\alpha}_m$, respectively. To uniquely determine u_0, additional constraint $u_0^T M_0 u_0 = 1$ is imposed. Now define the auxiliary variables

$$\begin{aligned} \Delta\boldsymbol{\alpha} = \boldsymbol{\alpha} - \alpha_0, \qquad \Delta\boldsymbol{\alpha}_m = \boldsymbol{\alpha}_m - \alpha_{m0}; \\ \Delta\boldsymbol{\omega}^2 = \boldsymbol{\omega}^2 - \omega_0^2, \qquad \Delta\mathbf{u} = \mathbf{u} - u_0, \qquad \Delta\boldsymbol{\lambda} = \boldsymbol{\lambda} - \lambda_0 \end{aligned} \tag{4.51}$$

to represent the difference between the interval vectors and their respective reference solutions. Then the following equalities hold

$$\mathbf{Ku} = K_0 u_0 + K_0 \Delta\mathbf{u} + \Delta\mathbf{Ku};$$

$$\boldsymbol{\omega}^2 \mathbf{Mu} = \omega_0^2 M_0 u_0 + \omega_0^2 M_0 \Delta\mathbf{u} + \Delta\boldsymbol{\omega}^2 M_0 u_0 \tag{4.52}$$

$$+ \Delta\boldsymbol{\omega}^2 M_0 \Delta\mathbf{u} + \boldsymbol{\omega}^2 \Delta\mathbf{Mu}.$$

123

Then Eq. (4.49) is equivalent to

$$\begin{Bmatrix} -M_0 u_0 & K_0 - \omega_0^2 M_0 & C^T \\ 0 & C & 0 \end{Bmatrix} \begin{Bmatrix} \Delta\boldsymbol{\omega}^2 \\ \Delta\mathbf{u} \\ \Delta\boldsymbol{\lambda} \end{Bmatrix} = \begin{Bmatrix} M_0 \\ 0 \end{Bmatrix} \Delta\mathbf{u}\Delta\boldsymbol{\omega}^2 \qquad (4.53)$$

$$- \begin{Bmatrix} A & A_m \\ 0 & 0 \end{Bmatrix} \mathrm{diag}\left(\begin{Bmatrix} A^T\mathbf{u} \\ \omega^2 A_m^T\mathbf{u} \end{Bmatrix} \right) \begin{Bmatrix} \Lambda & 0 \\ 0 & \Lambda_m \end{Bmatrix} \begin{Bmatrix} \Delta\boldsymbol{\alpha} \\ \Delta\boldsymbol{\alpha}_m \end{Bmatrix}.$$

by using the following identities

$$\Delta\mathbf{K}\mathbf{u} - \boldsymbol{\omega}^2\Delta\mathbf{M}\mathbf{u} = A\mathrm{diag}(\Lambda\Delta\boldsymbol{\alpha})A^T\mathbf{u} - \boldsymbol{\omega}^2 A_m\mathrm{diag}(\Lambda_m\Delta\boldsymbol{\alpha}_m)A_m^T\mathbf{u}$$

$$= A\mathrm{diag}(A^T\mathbf{u})\Lambda\Delta\boldsymbol{\alpha} - A_m\mathrm{diag}(\boldsymbol{\omega}^2 A_m^T\mathbf{u})\Lambda_m\Delta\boldsymbol{\alpha}_m \qquad (4.54)$$

$$= \begin{Bmatrix} A & A_m \\ 0 & 0 \end{Bmatrix} \mathrm{diag}\left(\begin{Bmatrix} A^T\mathbf{u} \\ \omega^2 A_m^T\mathbf{u} \end{Bmatrix} \right) \begin{Bmatrix} \Lambda\Delta\boldsymbol{\alpha} \\ \Lambda_m\Delta\boldsymbol{\alpha}_m \end{Bmatrix},$$

and Eq. (4.50). Eq. (4.53) can be brought into the following compact form

$$\left\{ -M_b u_0 \quad K_b \right\} \begin{Bmatrix} \Delta\boldsymbol{\omega}^2 \\ \Delta\mathbf{u} \\ \Delta\boldsymbol{\lambda} \end{Bmatrix} = M_b\Delta\mathbf{u}\Delta\boldsymbol{\omega}^2 - A_b\mathrm{diag}\left(\begin{Bmatrix} A^T\mathbf{u} \\ \omega^2 A_m^T\mathbf{u} \end{Bmatrix} \right) \Lambda_{\mathrm{eff}}\Delta\boldsymbol{\alpha}_{\mathrm{eff}}, \quad (4.55)$$

by introducing the following block matrices

$$K_b = \begin{Bmatrix} K_0 - \omega_0^2 M_0 & C^T \\ C & 0 \end{Bmatrix}, \quad M_b = \begin{Bmatrix} M_0 \\ 0 \end{Bmatrix};$$

$$A_b = \begin{Bmatrix} A & A_m \\ 0 & 0 \end{Bmatrix}, \quad \Lambda_{\mathrm{eff}} = \begin{Bmatrix} \Lambda & 0 \\ 0 & \Lambda_m \end{Bmatrix}, \quad \Delta\boldsymbol{\alpha}_{\mathrm{eff}} = \begin{Bmatrix} \Delta\boldsymbol{\alpha} \\ \Delta\boldsymbol{\alpha}_m \end{Bmatrix}. \qquad (4.56)$$

Eq. (4.55) can be solved by the iterative enclosure method presented below.

4.2.2 Iterative enclosure method

To apply the iterative enclosure method to the interval nonlinear system Eq. (4.53), it must be transformed into a fixed-point form with respect to the unknown interval variables $\Delta\boldsymbol{\omega}^2$, $\Delta\mathbf{u}$, and $\Delta\boldsymbol{\lambda}$, which are given by

$$\Delta\boldsymbol{\omega}^2 = (G_\omega M_b)\Delta\mathbf{u}\Delta\boldsymbol{\omega}^2 - (G_\omega A_b)\mathrm{diag}\left(\begin{Bmatrix} A^T\mathbf{u} \\ \omega^2 A_m^T\mathbf{u} \end{Bmatrix} \right) \Lambda_{\mathrm{eff}}\Delta\boldsymbol{\alpha}_{\mathrm{eff}}, \qquad (4.57)$$

and

$$\left\{ \begin{array}{c} \Delta\mathbf{u} \\ \Delta\boldsymbol{\lambda} \end{array} \right\} = (G_u M_b)\Delta\mathbf{u}\Delta\boldsymbol{\omega}^2 - (G_u A_b)\mathrm{diag}\left(\left\{ \begin{array}{c} A^T\mathbf{u} \\ \boldsymbol{\omega}^2 A_m^T\mathbf{u} \end{array} \right\}\right)\Lambda_{\mathrm{eff}}\Delta\boldsymbol{\alpha}_{\mathrm{eff}}, \tag{4.58}$$

where $G_\omega = -\left\{ u_0^T \quad \lambda_0^T \right\}$, and G_u is defined as

$$G_u = \left(K_b + \gamma \left\{ \begin{array}{c} u_0 \\ \lambda_0 \end{array} \right\} u_0^T M_b^T \right)^{-1} \left(I - M_b u_0 \left\{ u_0^T \quad \lambda_0^T \right\} \right), \tag{4.59}$$

where the constant γ is used to adjust the conditioning number of the matrix to be inverted. The detailed derivation for Eqs. (4.57) and (4.58) is included in Appendix C. To further reduce overestimation, introduce the auxiliary variables

$$\left\{ \begin{array}{c} A^T\Delta\mathbf{u} \\ A_m^T\Delta\mathbf{u} \end{array} \right\} = \left\{ \begin{array}{cc} A^T & 0 \\ A_m^T & 0 \end{array} \right\} \left\{ \begin{array}{c} \Delta\mathbf{u} \\ \Delta\boldsymbol{\lambda} \end{array} \right\} = A_b^T \left\{ \begin{array}{c} \Delta\mathbf{u} \\ \Delta\boldsymbol{\lambda} \end{array} \right\}, \tag{4.60}$$

and from Eq. (4.58),

$$\left\{ \begin{array}{c} A^T\Delta\mathbf{u} \\ A_m^T\Delta\mathbf{u} \end{array} \right\} = (A_b^T G_u M_b)\Delta\mathbf{u}\Delta\boldsymbol{\omega}^2 - (A_b^T G_u A_b)\mathrm{diag}\left(\left\{ \begin{array}{c} A^T\mathbf{u} \\ \boldsymbol{\omega}^2 A_m^T\mathbf{u} \end{array} \right\}\right)\Lambda_{\mathrm{eff}}\Delta\boldsymbol{\alpha}_{\mathrm{eff}}. \tag{4.61}$$

As a result, the number of multiple occurrences of the same interval variables is minimized, the essential key step to reduce overestimation due to interval dependency [101]. From Eqs. (4.57), (4.58), and (4.61), the final fixed-point equations have the following compact form

$$\Delta\mathbf{u}_g = (GM_g)\Delta\mathbf{u}\Delta\boldsymbol{\omega}^2 - (GA_g)\mathrm{diag}\left(\left\{ \begin{array}{c} A^T\mathbf{u} \\ \boldsymbol{\omega}^2 A_m^T\mathbf{u} \end{array} \right\}\right)\Lambda_{\mathrm{eff}}\Delta\boldsymbol{\alpha}_{\mathrm{eff}}, \tag{4.62}$$

where

$$\Delta\mathbf{u}_g = \left\{ \begin{array}{c} \Delta\boldsymbol{\omega}^2 \\ \Delta\mathbf{u} \\ \Delta\boldsymbol{\lambda} \\ A^T\Delta\mathbf{u} \\ A_m^T\Delta\mathbf{u} \end{array} \right\}, \quad GM_g = \left\{ \begin{array}{c} G_\omega M_b \\ G_u M_b \\ A_b^T G_u M_b \end{array} \right\}, \quad GA_g = \left\{ \begin{array}{c} G_\omega A_b \\ G_u A_b \\ A_b^T G_u A_b \end{array} \right\}. \tag{4.63}$$

To solve Eq. (4.62), the following iterative scheme is used,

$$\Delta \mathbf{u}_g^{j+1} = (GM_g)\Delta \mathbf{u}^j (\Delta \boldsymbol{\omega}^2)^j - (GA_g)\mathrm{diag}\left(\left\{ \begin{array}{c} A^T \mathbf{u}^j \\ (\boldsymbol{\omega}^2)^j A_m^T \mathbf{u}^j \end{array} \right\}\right)\Lambda_{\mathrm{eff}}\Delta \boldsymbol{\alpha}_{\mathrm{eff}}, \qquad (4.64)$$

where $\Delta \mathbf{u}_g^{j+1}$ is the interval solution at the $(j+1)$-th iteration, and $\Delta \mathbf{u}^j$ and $(\Delta \boldsymbol{\omega}^2)^j$ are entries of $\Delta \mathbf{u}_g^j$ from the previous iteration. Moreover,

$$(\boldsymbol{\omega}^2)^j = \omega_0^2 + (\Delta \boldsymbol{\omega}^2)^j, \qquad \left\{ \begin{array}{c} A^T \mathbf{u}^j \\ A_m^T \mathbf{u}^j \end{array} \right\} = \left\{ \begin{array}{c} A^T u_0 \\ A_m^T u_0 \end{array} \right\} + \left\{ \begin{array}{c} A^T \Delta \mathbf{u}^j \\ A_m^T \Delta \mathbf{u}^j \end{array} \right\} \qquad (4.65)$$

The initial guess at $j = 1$ is set as

$$\Delta \mathbf{u}_g^1 = -(GA_g)\mathrm{diag}\left(\left\{ \begin{array}{c} A^T u_0 \\ \omega_0^2 A_m^T u_0 \end{array} \right\}\right)\Lambda_{\mathrm{eff}}\Delta \boldsymbol{\alpha}_{\mathrm{eff}}, \qquad (4.66)$$

and the iterations stop when there is no solution improvement after two consecutive steps, viz. when $\Delta \mathbf{u}_g^{n+1} = \Delta \mathbf{u}_g^n$. Now, denote the corresponding converged solution as $\Delta \mathbf{u}_g^n$. Then the outer solution $\mathbf{u}_g^{out} = u_{g0} + \Delta \mathbf{u}_g^n$ is obtained. The solution $\mathbf{u}_g^{out}$ includes the squared angular frequency $\boldsymbol{\omega}^2$ and the associated modal shape $\mathbf{u}$. The angular frequency $\boldsymbol{\omega}$ is obtained as the square root of $\boldsymbol{\omega}^2$, and can be transformed into the (temporal) frequency $\mathbf{f}$ measured in Hz, viz. $\mathbf{f} = \dfrac{1}{2\pi}\boldsymbol{\omega}$.

To further reduce overestimation in Eq. (4.64), the deterministic matrix GM_g and the interval matrix $(GA_g)\mathrm{diag}\left(\left\{ \begin{array}{c} A^T \mathbf{u}^j \\ (\boldsymbol{\omega}^2)^j A_m^T \mathbf{u}^j \end{array} \right\}\right)\Lambda_{\mathrm{eff}}$ have to be computed before multiplying each of them by the interval vectors $\Delta \mathbf{u}^j (\Delta \boldsymbol{\omega}^2)^j$ and $\Delta \boldsymbol{\alpha}_{\mathrm{eff}}$, respectively.

The aforementioned procedure can be repeated to obtain all interval natural frequencies and modal shapes, by choosing the corresponding deterministic frequency ω_0 and modal shape u_0 (and the Lagrangian multiplier λ_0) that satisfy Eq. (4.50).

4.3   Nonlinear Programming Approach

In the nonlinear programming approach, constrained optimization techniques are implemented to solve for the stationary responses under given frequencies, as well as

the natural frequencies and the corresponding modal shapes of the structure. The goal is to provide a reference solution to compare with the proposed method. In this section, real numbers are used exclusively, i.e. no interval or complex numbers are involved in the computation.

4.3.1 Frequency responses

In the frequency response analysis, the stationary responses under given frequency ω are computed. The solution vector x includes the load uncertainty vector δ, the parameter vector α_{eff}, the nodal displacement u, and the Lagrangian multiplier λ:

$$x = \left\{ \delta^T \quad \alpha_{\text{eff}}^T \quad u^{CT} \quad \lambda^{CT} \right\}^T, \tag{4.67}$$

where α_{eff} contains the stiffness and mass parameter vectors α and α_m, u^C contains the real and imaginary parts of the nodal displacement vector, and so does λ^C.

To compute the lower (or upper) bound of the real part of the j-th component of the nodal displacement vector u_j^R, the corresponding objective functional Ω has the following general form

$$\Omega = cu^R, \quad \text{or} \quad -cu^R, \tag{4.68}$$

where c is a row vector, whose only non-zero component is unity at the j-th component. For the j-th component of the stress or strain vector, the objective functional Ω has the same form as in Eq. (4.68), with $c = S_j$ or B_j being the j-th row of the stress- and strain-displacement matrices S and B, respectively. For the imaginary part of the unknown quantities, the real part u^R is substituted with the imaginary part u^I. For the magnitudes or the phase angles,

$$\|\Omega\| = \sqrt{(\Omega^R)^2 + (\Omega^I)^2}; \tag{4.69}$$

$$\text{or} \quad \arg(\Omega) = \text{atan2}\left(\Omega^I, \Omega^R \right),$$

where atan2( ) denotes the arctangent function with two arguments.

Equality constraints include equilibrium equations and essential boundary conditions, which are collectively given by

$$\begin{cases} K_{\text{eff}}^C u^C + C^{CT}\lambda^C = F^C\delta; \\ C^C u^C = 0. \end{cases} \tag{4.70}$$

where K_{eff}^C is the effective stiffness matrix parameterized by α_{eff}, as in Eq. (4.17). Further, the inequality constraints require that the load uncertainty vector δ and the parameter vectors α_{eff} vary within their respective interval bounds:

$$\begin{cases} \underline{\delta} \leq \delta \leq \overline{\delta}; \\ \underline{\alpha}_{\text{eff}} \leq \alpha_{\text{eff}} \leq \overline{\alpha}_{\text{eff}}, \end{cases} \tag{4.71}$$

where $\underline{a}$ and $\overline{a}$ denote the lower and upper bounds of an interval $\mathbf{a}$, respectively. Then standard MATLAB optimization toolbox is used to solve the problem, in which gradients are used to accelerate convergence. The method can be extended to cases when the structure is excited by ground motion.

4.3.2 Natural frequencies and modal shapes

To compute the natural frequencies and their respective modal shapes, the solution vector x includes the parameter vector α_{eff}, the natural frequency ω, the modal shape u, and the Lagrangian multiplier λ, viz.

$$x = \left\{ \alpha_{\text{eff}}^T \;\; \omega^2 \;\; u^T \;\; \lambda^T \right\}^T. \tag{4.72}$$

Note that the square of natural frequency ω^2 is treated as a single variable. To compute the lower (upper) bound of ω^2, u, or λ, the objective functional Ω to be minimized takes one of the following forms:

$$\Omega = cx, \quad \text{or} \quad -cx, \tag{4.73}$$

and c is a constant row vector. In particular, c is zero except for the j-th component, which can be either the squared natural frequency ω, or the modal shape u, or the Lagrangian multiplier λ.

128

The equality constraint requires: i) the structure is in equilibrium, ii) essential boundary conditions are satisfied, and iii) nodal displacement vector is normalized by the mass matrix M, viz.

$$\begin{cases} (K - \omega^2 M)u + (1 - \omega^2)C^T\lambda = 0; \\ Cu = 0; \\ u^T Mu - 1 = 0. \end{cases} \qquad (4.74)$$

In addition, the inequality constraints are given by

$$\underline{\alpha}_{\text{eff}} \leq \alpha_{\text{eff}} \leq \overline{\alpha}_{\text{eff}}, \qquad (4.75)$$

where $\underline{\alpha}_{\text{eff}}$ and $\overline{\alpha}_{\text{eff}}$ denote the lower and upper bounds of α_{eff}, respectively.

4.4 Numerical Examples

The proposed IFEM algorithm is coded in INTLAB [122], which is an interval arithmetic extension package developed in the MATLAB environment. To test the performance of the proposed method, the frequency responses, natural frequencies, and modal shapes are computed for several sample structures: i) a five story rigid frame, ii) a cantilever beam, iii) a plate with a circular cutoff, and iv) a gable frame. The Interval solutions (IS) obtained from the proposed method are compared against those obtained from: i) the endpoint combination method (EC [109]), ii) Monte Carlo predictions (MC) and iii) nonlinear programming approach (NLP). Material uncertainties in both stiffness and mass are considered. For the frequency response analysis, the excitation can be either external loading or ground motion. The computations are carried out on a PC with Intel Core2 Duo, CPU E8400, 3GHz with 4GB RAM under Windows 7. Numerical results show that IS guarantees to enclose the reference solution (NLP), and the corresponding computation time is negligible when compare with other available methods.

Table 4.1: Interval mass and stiffness for the five-story rigid frame of Figure 4.1, including 7%-11% uncertainties in mass, and 1%-3% uncertainties in stiffness.

Floor	Mass (kg)			Stiffness (N/m)		
	$\mathbf{m}_j$	mid $\mathbf{m}_j$	rad $\mathbf{m}_j$	$\mathbf{k}_j$	mid $\mathbf{k}_j$	rad $\mathbf{k}_j$
1	[29, 31]	30	1	[2000, 2020]	2010	10
2	[26, 28]	27	1	[1800, 1850]	1825	25
3	[26, 28]	27	1	[1600, 1630]	1615	15
4	[24, 26]	25	1	[1400, 1420]	1410	10
5	[17, 19]	18	1	[1200, 1210]	1205	5
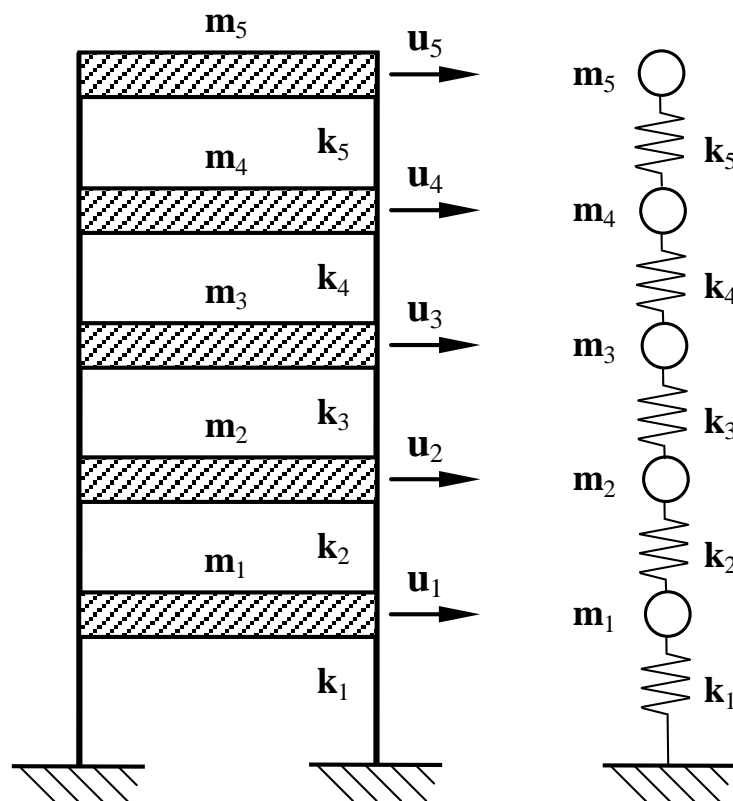
Figure 4.1: A five-story rigid frame and the equivalent spring-mass system.

4.4.1 Five-story rigid frame

In the first example, the five-story frame of Figure 4.1 is considered, adopted from the work of Sim, *et al.* [130]. The frame floors are assumed rigid enough to model the structure as an equivalent spring-mass system with 5 Degrees of Freedom (DOF) (see right-hand side of Figure 4.1). The mass $\mathbf{m}_j$ and shear stiffness $\mathbf{k}_j$ ($j = 1, \ldots, 5$) of each floor are modeled as independent interval variables (see Table 4.1).
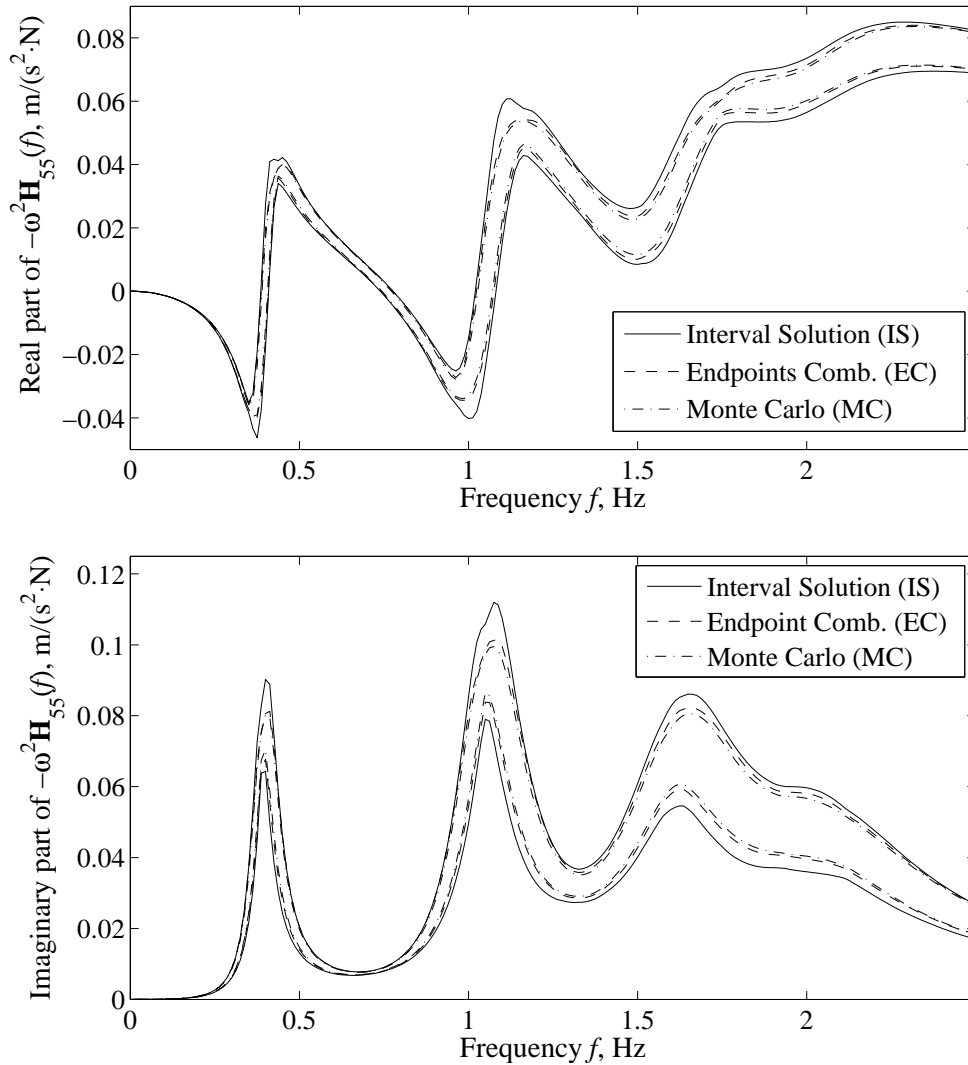
Figure 4.2: Real (top) and imaginary (bottom) parts of the frequency response function $-\omega^2 \mathbf{H}_{55}(f)$ for the five-story frame of Figure 4.1: IS (solid lines) from the proposed method, EC (dashed lines), and MC (dash-dotted lines) from an ensemble of 10,000 simulations. Material uncertainty is 7%-11% for mass, and 1%-3% for stiffness.

Table 4.2: Natural frequencies of the five-story frame of Figure 4.1. IS = Interval solution from the proposed method, MC = Monte Carlo solution from an ensemble of 10,000 simulations, and EC = endpoint combination reference solution. Material uncertainty is 7%-11% for mass, and 1%-3% for stiffness.

	1st-order frequency $\mathbf{f}_1$, (Hz)				2nd-order frequency $\mathbf{f}_2$, (Hz)			
	$\underline{f}_1$	Error (%)	$\bar{f}_1$	Error (%)	$\underline{f}_2$	Error (%)	$\bar{f}_2$	Error (%)
Simon *et al.* [130]	0.3420	-11.228	0.4454	9.741	1.0160	-1.528	1.0992	1.490
Proposed (IS)	0.3842	-0.275	0.4060	0.034	1.0281	-0.359	1.0845	0.129
Reference (EC)	0.3852	---	0.4058	---	1.0318	---	1.0831	---
Monte Carlo (MC)	0.3876	0.620	0.4038	-0.503	1.0364	0.446	1.0777	-0.499

	3rd-order frequency $\mathbf{f}_3$, (Hz)				4th-order frequency $\mathbf{f}_4$, (Hz)			
	$\underline{f}_3$	Error (%)	$\bar{f}_3$	Error (%)	$\underline{f}_4$	Error (%)	$\bar{f}_4$	Error (%)
Simon *et al.* [130]	1.5802	-0.142	1.6616	0.137	2.0060	0.254	2.0927	-0.256
Proposed (IS)	1.5743	-0.512	1.6639	0.277	1.9871	-0.690	2.1073	0.438
Reference (EC)	1.5824	---	1.6593	---	2.0009	---	2.0981	---
Monte Carlo (MC)	1.5902	0.493	1.6500	-0.560	2.0085	0.380	2.0890	-0.434

	5th-order frequency $\mathbf{f}_5$, (Hz)							
	$\underline{f}_5$	Error (%)	$\bar{f}_5$	Error (%)				
Simon *et al.* [130]	2.3146	0.473	2.4029	-0.463				
Proposed (IS)	2.2888	-0.647	2.4244	0.427				
Reference (EC)	2.3037	---	2.4141	---				
Monte Carlo (MC)	2.3146	0.473	2.4047	-0.389				

The structural frequency response within the range of $f = [0, 2.5]$ Hz is considered. In particular, the real and imaginary parts of the frequency response function $-\omega^2 \mathbf{H}_{55}(f)$ are computed, which denotes the nodal acceleration at node 5 due to a unit concentrated force at node 5. The damping matrix $\mathbf{C} = 0.4\mathbf{M} + 0.02\mathbf{K}$. Figure 4.2 compares IS (solid lines) with EC (dashed lines) and MC (dash-dotted lines)
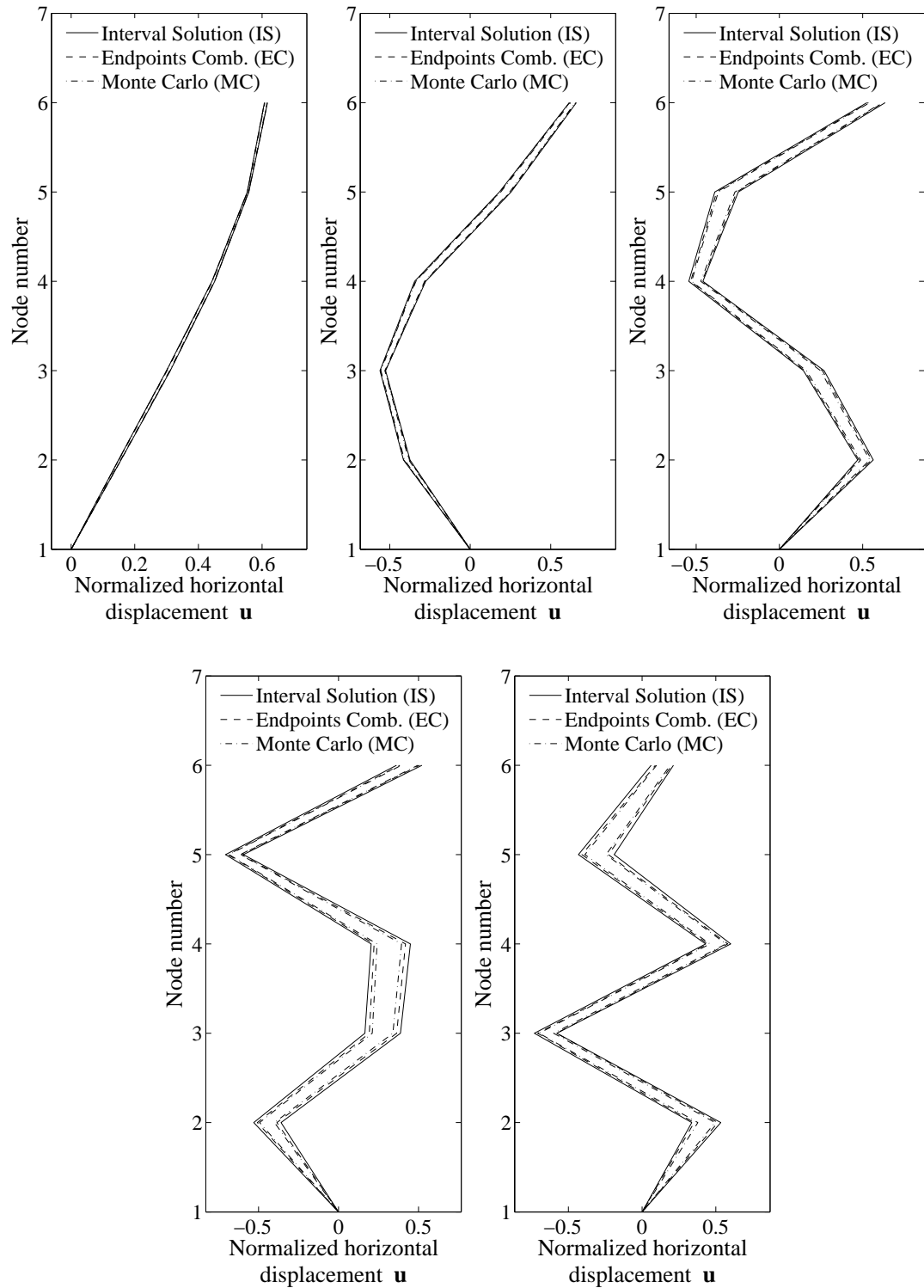
Figure 4.3: Modal shapes of the five natural frequencies of the five-story frame of Figure 4.1: IS = Interval solution (solid lines), EC = endpoint-combination reference solution (dashed lines), and MC = Monte Carlo solution from an ensemble of 10,000 simulations (dash-dotted lines). Material uncertainty is 7%-11% for mass, and 1%-3% for stiffness.

solutions obtained from 10,000 simulations. Observe that IS always contains EC, and EC always contains MC. In addition, IS has larger overestimation near the resonance frequencies $\approx$ 0.4, 1.1, and 1.6 Hz.

Table 4.2 compares the lower and upper bounds of the natural frequencies from IS against those from EC (used as the reference solution), MC (from an ensemble of 10,000 simulations), and Sim, *et al.* [130]. Observe that the overestimation for IS is the smallest for the lowest frequency ($\mathbf{f}_1$, about 0.3%), and it increases for higher frequencies ($\mathbf{f}_4$ and $\mathbf{f}_5$, about 1.1%).

The corresponding modal shapes are displayed in Figure 4.3. Here, IS (solid line) from the proposed method is displayed along with EC (dashed line) and MC (dash-dotted line). Observe that for the low-frequency modes, the uncertainty level is relatively small (0.8-5.0% for the 1st-order mode), and so is the overestimation level (0.05-0.25% for the 1st-order mode). As a result, the different solutions (IS, EC, and MC) are practically indistinguishable from each other. However, for the highest 5th-order mode, the uncertainty level is much higher (20-77%), and so is the overestimation level (3.4-52% for the 5th-order mode).
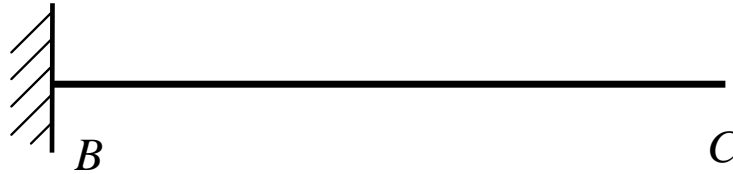
Figure 4.4: A cantilever beam subject vertical ground acceleration.

4.4.2 Cantilever beam

Consider now the cantilever beam shown in Figure 4.4 subject to ground acceleration. The beam has a length $L = 1$ m, and a constant rectangular cross section (with cross section area $A = 6 \times 10^{-4}$ m^2 and moment of inertia $I = 1.8 \times 10^{-7}$ m^4). Ten equal-length Bernoulli-Euler beam elements are used to model the beam. 5%

uncertainties in material are considered for each element, viz. mass density $\boldsymbol{\rho} = [7.605, 7.995] \times 10^3$ kg/m^3, and Young's modulus $\mathbf{E} = [195, 205]$ GPa. The damping matrix $\mathbf{C} = 50\mathbf{M} + 1 \times 10^{-4}\mathbf{K}$.

The nodal acceleration $\mathbf{a}_C$ of the free end of the beam are computed within in the range of $[0, 600]$ Hz. Unit vertical ground acceleration ($\boldsymbol{\delta} = 1$ m/s^2) is used as the excitation, and Figure 4.5 shows the real and imaginary parts of $\mathbf{a}_C$ as a function of
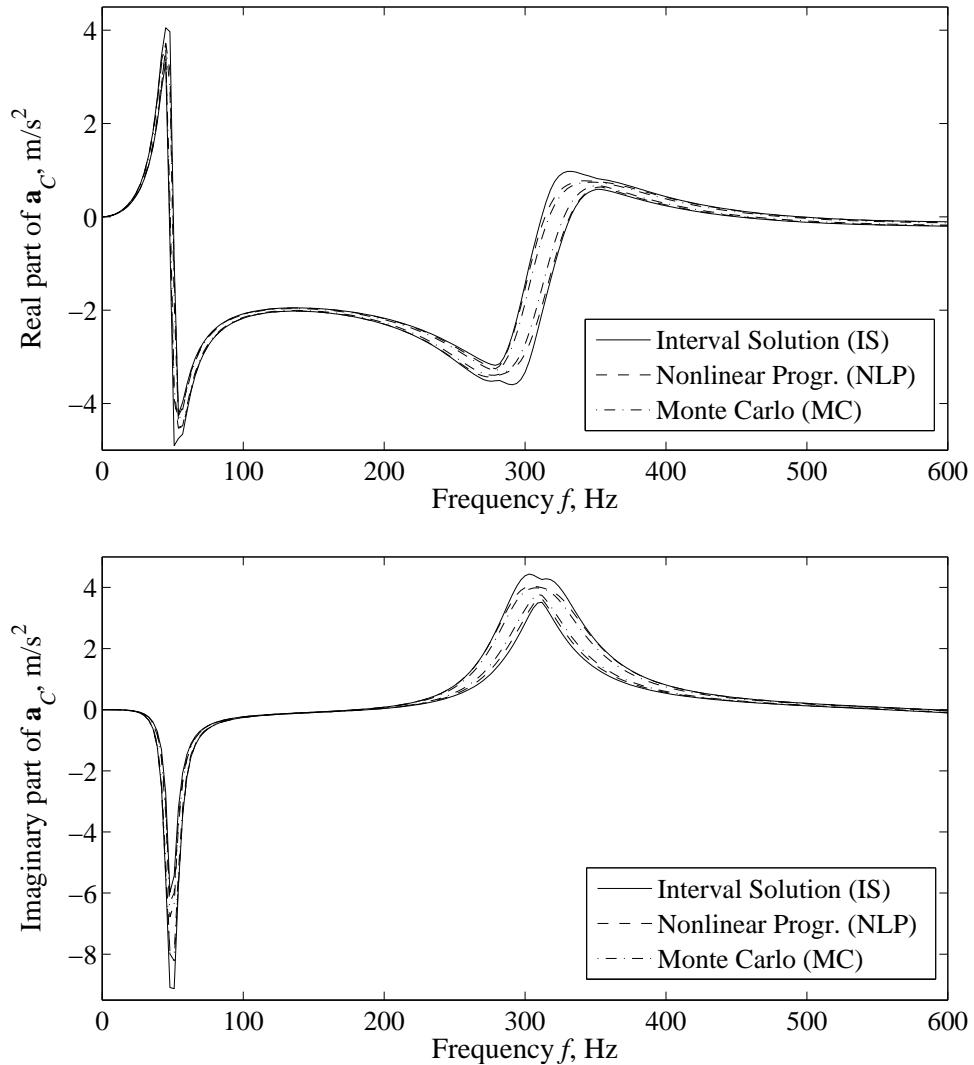
Figure 4.5: Real (top) and imaginary (bottom) parts of the free end acceleration $\mathbf{a}_C$ for the cantilever beam in Figure 4.4: IS (solid lines) from the proposed method, NLP (dashed lines), and MC (dash-dotted lines) from an ensemble of 10,000 simulations. Material uncertainty is 5% for both mass density and Young's modulus.
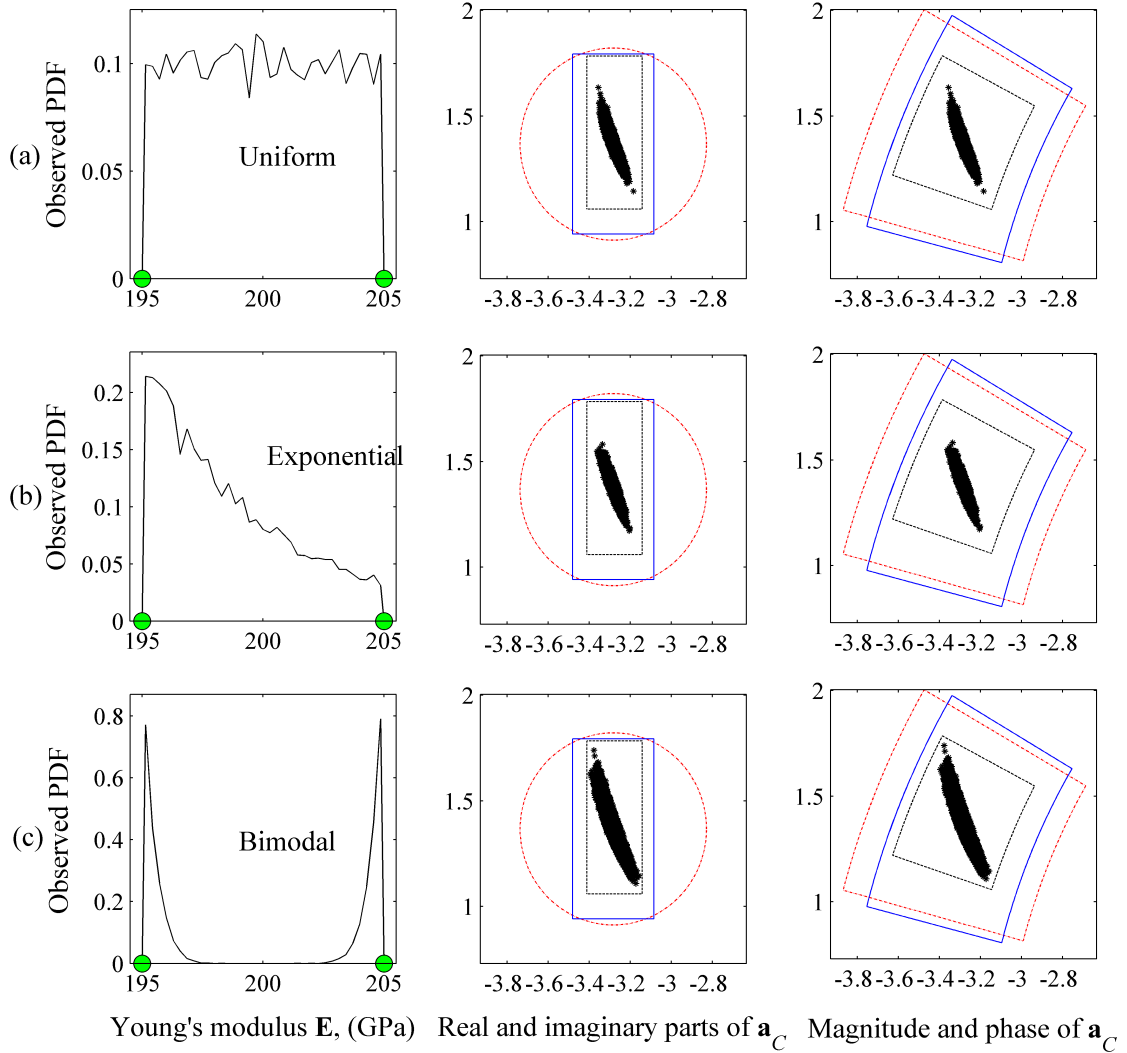
Figure 4.6: Comparisons between IS obtained from the proposed method, NLP, and MC of the free end acceleration $\mathbf{a}_C$ at $f = 300$ Hz of the cantilever beam of Figure 4.4 from an ensemble of 10,000 simulations: (left) observed probability density function (PDF) of the Young's modulus $\mathbf{E} = [195, 205]$ GPa (5% uncertainty) sampled from (a) uniform, (b) truncated exponential, and (c) bimodal probability distributions (interval endpoints denoted by circular markers); (middle) corresponding $\mathbf{a}_C$ in the complex plane: MC (dots), NLP (dashed box), IS from rectangular representation (solid box), IS from circular representation (dash-dotted box); (right) corresponding $\mathbf{a}_C$ in the complex plane, magnitude and phase angle: MC (dots), NLP (dashed curved box), IS from rectangular representation (solid curved box), IS from circular representation (dash-dotted curved box).
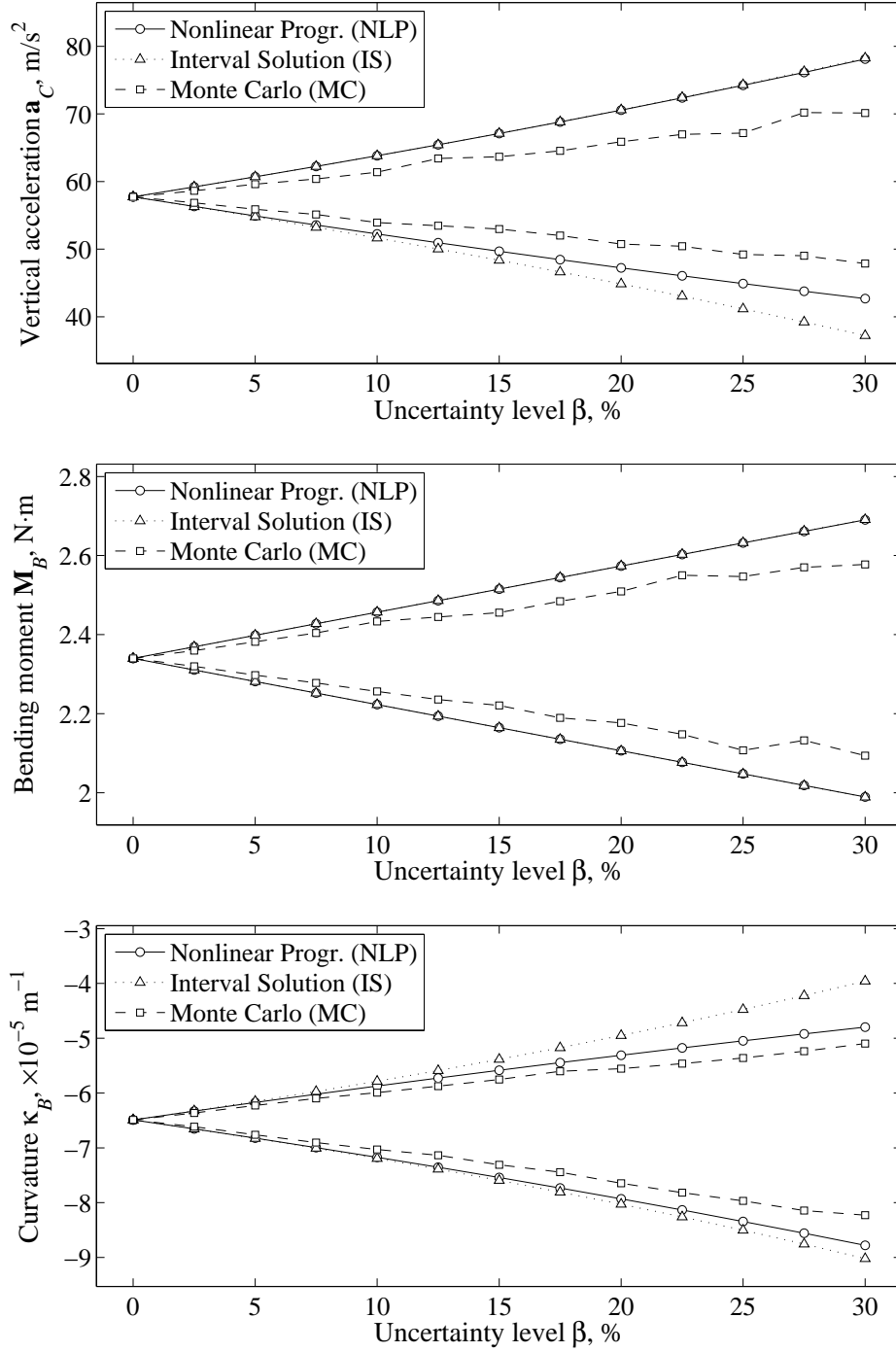
Figure 4.7: Selected results for the cantilever beam of Figure 4.4 under up to 30% uncertainties in material properties at given frequency $f = 300$ Hz: (top) real part of nodal acceleration $\mathbf{a}_C$ at the free end C, (middle) real part of bending moment $\mathbf{M}_B$ at the fixed end B, (bottom) real part of curvature $\boldsymbol{\kappa}_B$ at the fixed end B. IS (dotted lines with triangular markers) from the proposed method and MC (dashed lines with square markers) from an ensemble of 10,000 simulations are compared against reference solution NLP (solid lines with circular markers).

the frequency f. The EC solution is computationally unfeasible since it requires to solve for $2^{20} \approx 1.05 \times 10^6$ combinations (20 independent interval variables, i.e. $\boldsymbol{\rho}$ and $\mathbf{E}$ for each element). Thus the NLP solution is used as a reference. Figure 4.5 show that IS always contains NLP, and NLP contains MC. Again, observe the increased overestimation level for IS near the resonance frequencies ≈ 50, 310 Hz.

Figure 4.6 show IS guarantees to enclose both NLP and MC solutions, regardless of the type of probability distribution used to model the uncertainties. In addition, the rectangular representation for interval variables gives tighter enclosures than the circular representation, except for the phase angle.

Figure 4.7 shows that IS gives guaranteed enclosures up to 30% uncertainties in material properties for the nodal acceleration $\mathbf{a}_C$ at the free end C, as well as derived quantities such as the bending moment $\mathbf{M}_B$ and curvature $\boldsymbol{\kappa}_B$ at the fixed end B. Note that the IS and NLP solutions for MB are identical since the structure is statically determined. Overestimation on internal forces, such as $\mathbf{M}_B$, is completely eliminated if one solves for the Lagrangian multiplier $\boldsymbol{\lambda}$ [119]. Overestimation in the curvature $\boldsymbol{\kappa}_B$ is comparable to that in the nodal acceleration $\mathbf{a}_C$.
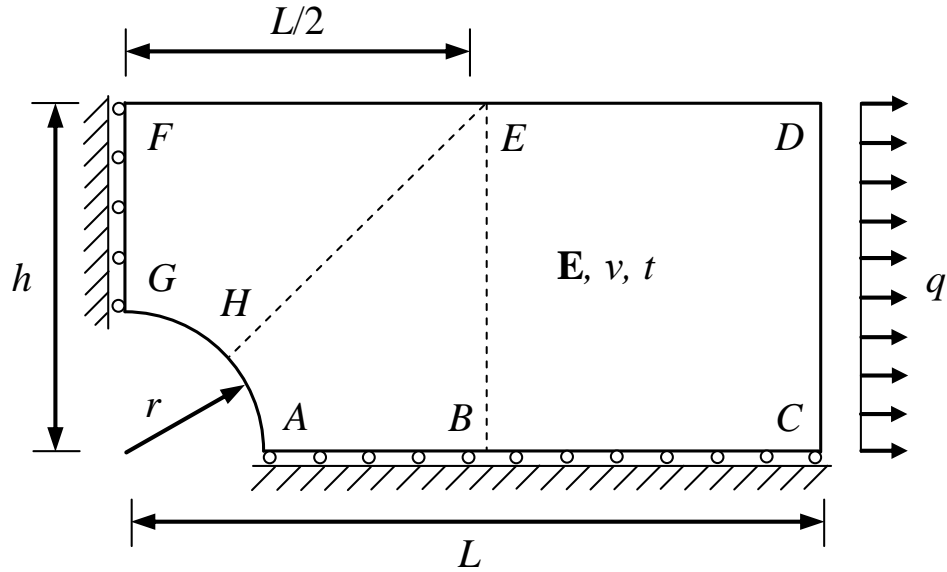
Figure 4.8: A plate with a circular cutoff subject to uniformly distributed line load.

4.4.3 Plate with a circular cutoff

The third example is a plate with a circular cutoff at its lower-left corner, subject to uniformly distributed load q on the right edge CD, as shown in Figure 4.8. The left and bottom edges (FG and AC) of the plate are restrained by rollers. The length, height, and thickness of the plate are respectively $L = 0.1$ m, $h = 0.05$ m, and $t = 0.005$ m. The radius of the circular cutoff is $r = 0.02$ m, and Poisson's ratio is $\nu = 0.3$. Here 2% uncertainties in material are considered, viz. $\boldsymbol{\rho} = [7.722, 7.878] \times 10^3$ kg/m^3 and $\mathbf{E} = [198, 202]$ GPa for each element. The damping matrix $\mathbf{C} = 2 \times 10^3 \mathbf{M} + 5 \times 10^{-7} \mathbf{K}$. For simplicity, $q = 10$ kN/m is assumed for all frequencies.

Figure 4.9 shows the finite element mesh used in the analysis. The mesh is generated as follows: first the plate is divided into three curvilinear quadrilaterals ($EFGH$, $ABEH$, and $BCDE$), as shown in Figure 4.8. Each quadrilateral macro element is further divided into $m \times n$ smaller curvilinear quadrilaterals, which are modeled by one 8-node quadrilateral isoparametric element. The generated mesh is characterized
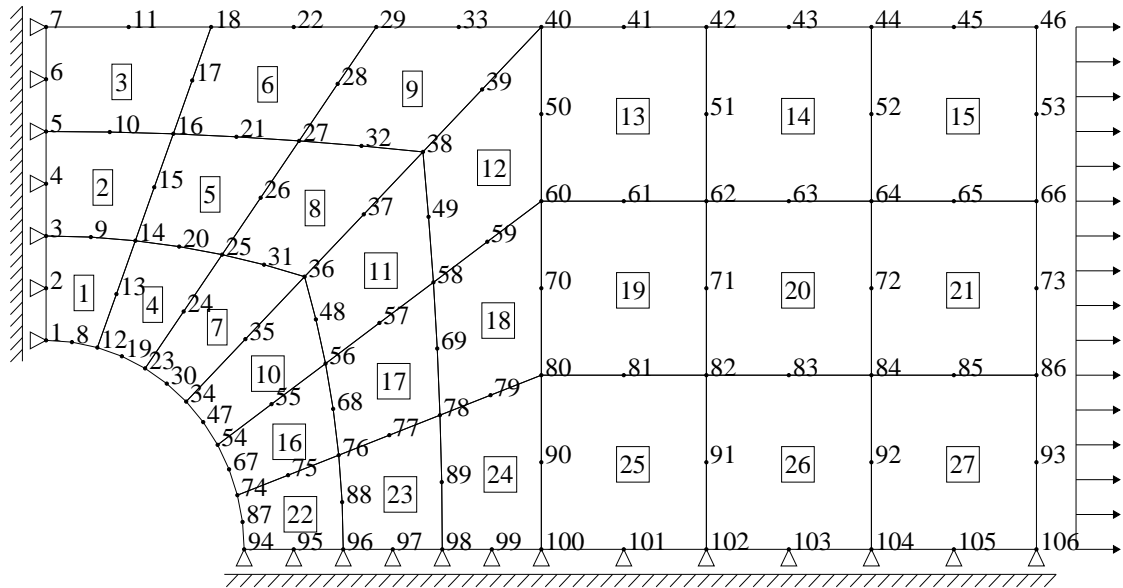
Figure 4.9: Finite element model used in the analysis of the plate with a circular cutoff of Figure 4.8 (8-node quadrilateral isoparametric elements are used).

by m and n. For instance, $m = n = 3$ for the mesh depicted in Figure 4.9.

Figure 4.10 plots the magnitude of the horizontal acceleration $\mathbf{a}_C$ at the corner C at different frequencies within the range $[0, 30]$ kHz, under distributed load $q = 10$ kN/m acting on the right edge CD. IS (solid lines) obtained from the proposed method is compared with NLP (dashed line) and MC (dash-dotted lines) obtained from an ensemble of 10,000 simulations. Observe that the overestimation level is low, except for points near the resonance frequencies $\approx$ 10, 17, and 25 kHz.

To study the performance of proposed method as function of the mesh size, a series of finite element meshes with coarse-to-fine discretization are considered. The corresponding horizontal acceleration $\mathbf{a}_C$ at the corner C at given frequency $f = 15$ kHz are computed, and plotted against the total DOF of the mesh in Figure 4.11. The corresponding DOF, number of elements, and computational time, if applicable, are listed in Table 4.3.
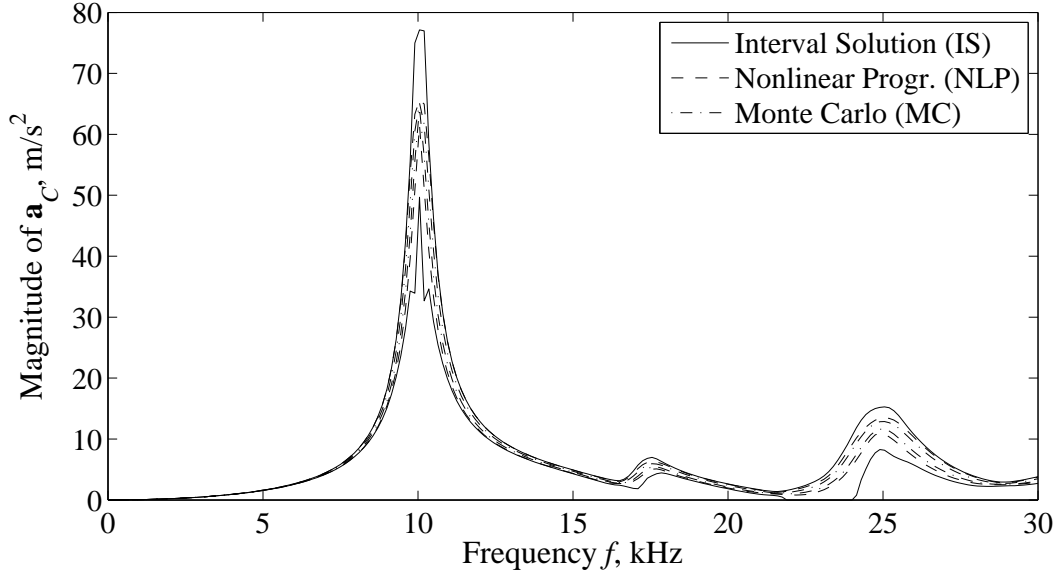
Figure 4.10: Magnitude of nodal acceleration $\mathbf{a}_C$ at the corner C for the plate of Figure 4.8 with 2% material uncertainties. IS (solid lines) from the proposed method, NLP (dashed lines), and MC (dash-dotted lines) from an ensemble of 10,000 simulations are included for comparison.

Table 4.3: Performance of proposed method under refinement of FE meshes of the plate of Figure 4.8. The number of total DOF and elements of different finite element meshes are listed, along with the corresponding computation time (in seconds) for different methods.

Mesh	Element Number	Number of DOF	Computational time (s)		
			NLP	MC	IS
1×1	3	36	2.046	16.623	0.137
2×2	12	106	18.676	63.496	0.582
3×3	27	212	2601.736	373.599	2.683
4×4	48	354	---	1467.872	11.957
5×5	75	532	---	3920.601	32.178
6×6	108	746	---	---	83.932
7×7	147	996	---	---	330.817
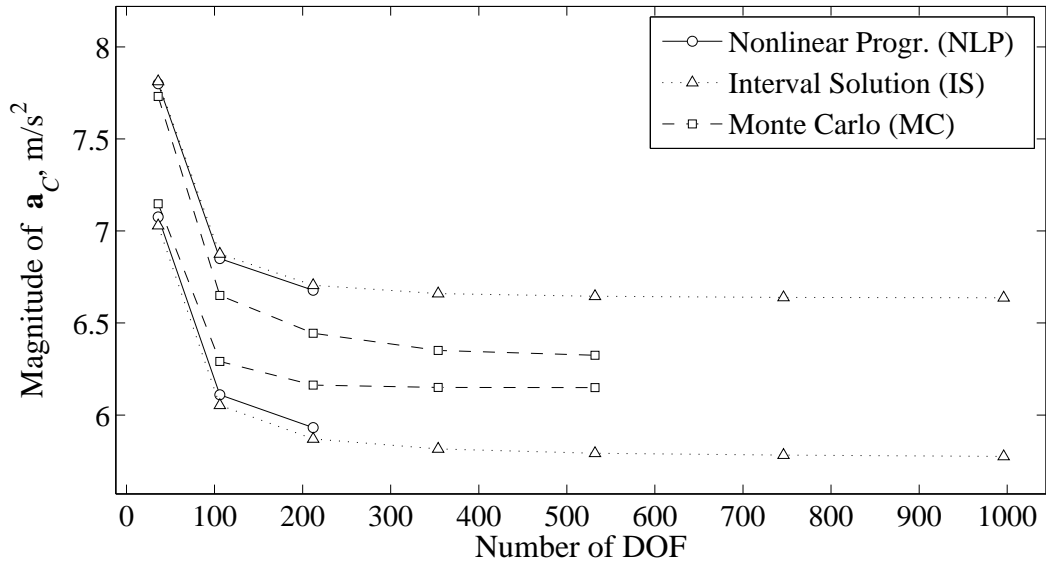
Figure 4.11: Magnitude of nodal acceleration $\mathbf{a}_C$ at the corner C for the plate of Figure 4.8 with 2% material uncertainties at given frequency $f = 15$ kHz, obtained from different finite element meshes. IS (solid lines) from the proposed method, NLP (dashed lines), and MC (dash-dotted lines) from an ensemble of 10,000 simulations are included for comparison.

From Table 4.3 and Figure 4.11, the following observations are made:

1) IS always contains NLP and MC. The difference between IS and NLP remains unchanged as the mesh refines. Thus the overestimation of the proposed method does not depend on the specific finite element mesh or problem scale (In other words, the level of overestimation is not increasing as a function of the number of uncertain parameters).

2) NLP and MC solutions are computationally expensive. Even when the mesh is quite coarse, the corresponding computational time is significantly longer than the proposed method.
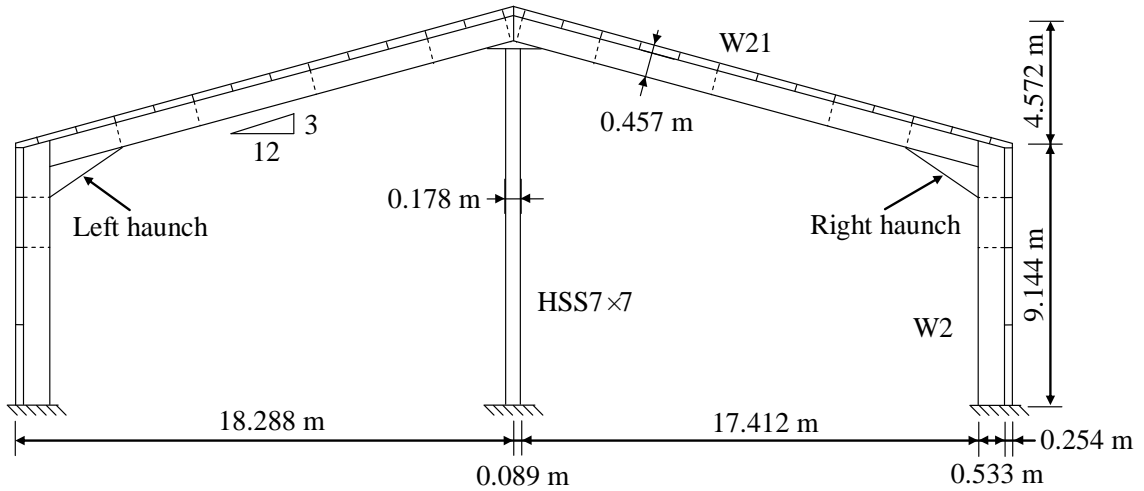
Figure 4.12: A symmetric gable frame with a hollow structural section (HSS) column at the midspan.

4.4.4 Gable frame

Consider the gable frame whose overall geometry is shown in Figure 4.12. Assume standard rolled steel sections are used (see AISC [89]). In particular, W21×44 is used for the rafters, W21×50 is used for the columns, and HSS7×7×1/4 is used for the Hollow Structural Section (HSS) column. Geometric and material properties, such as the cross section area A, moment of inertia I, mass density $\boldsymbol{\rho}$, and Young's modulus $\mathbf{E}$ are listed in Table 4.4. Here 5% uncertainty in $\boldsymbol{\rho}$ and 20% uncertainty in $\mathbf{E}$ are

Table 4.4: Geometric and material properties of the gable frame of Figure 4.12.

	A (10^{-3} m²)	I (10^{-4} m⁴)	ρ (10^3 kg/m³)	**E** (GPa)
Rafters	8.387	3.509	[7.605, 7.995]	[180, 220]
Columns	9.484	4.096	[7.605, 7.995]	[180, 220]
HSS column	3.980	0.193	[7.605, 7.995]	[180, 220]
Haunch 1	14.88	28.45	[7.605, 7.995]	[180, 220]
Haunch 2	10.55	8.573	[7.605, 7.995]	[180, 220]

considered. In addition, since two beam elements are used to model each haunch (four elements in total), two different cross section properties are listed for the haunches in Table 4.4.

The IFEM model for the gable frame consists of 37 two-node Euler-Bernoulli beam elements (labelled from $\underline{1}$ to $\underline{37}$), as shown in Figure 4.13. Moreover, 6 elements are used to model each column ($\underline{1}$ to $\underline{6}$ and $\underline{31}$ to $\underline{36}$), 12 elements for each rafter ($\underline{7}$ to $\underline{18}$ and $\underline{19}$ to $\underline{30}$), including the four used for the two haunches ($\underline{7}$ & $\underline{8}$, $\underline{29}$ & $\underline{30}$), and one element for the HSS column ($\underline{37}$). The gable frame is hinged to the ground, and
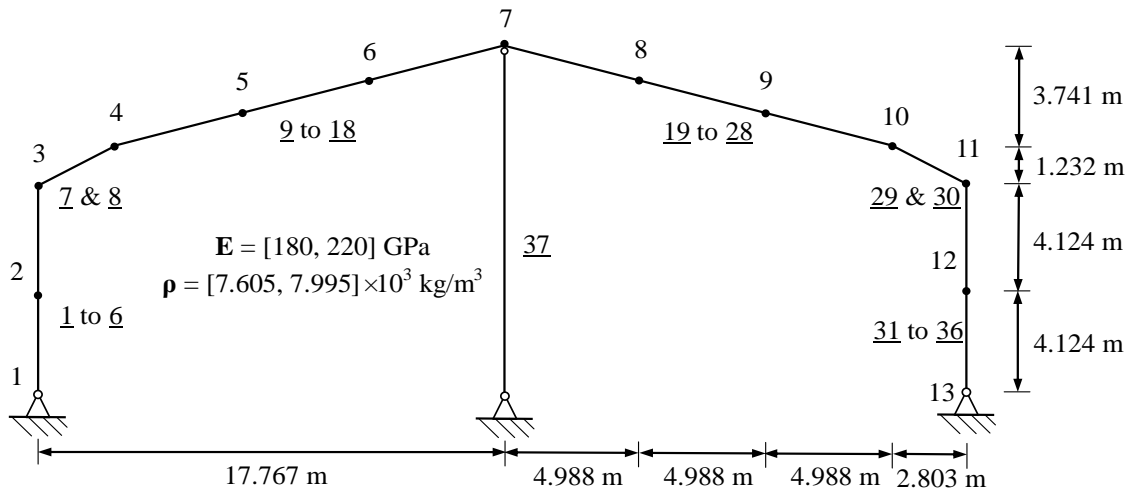
Figure 4.13: Finite element model used to model the gable frame of Figure 4.12.

the HSS column is subject to axial deformation only. For the columns and rafters (including the haunches), the corresponding mass densities and Young's moduli at the integration points are linearly interpolated from $\mathbf{E}_j$ and $\boldsymbol{\rho}_j$ ($j = 1, \ldots, 13$) at the material mesh nodes 1 to 13, as show in Figure 4.13. For the HSS column, the corresponding mass density and Young's modulus are denoted as $\mathbf{E}_{14}$ and $\boldsymbol{\rho}_{14}$, respectively. Note that the material mesh nodes do not coincide with the finite element mesh nodes.
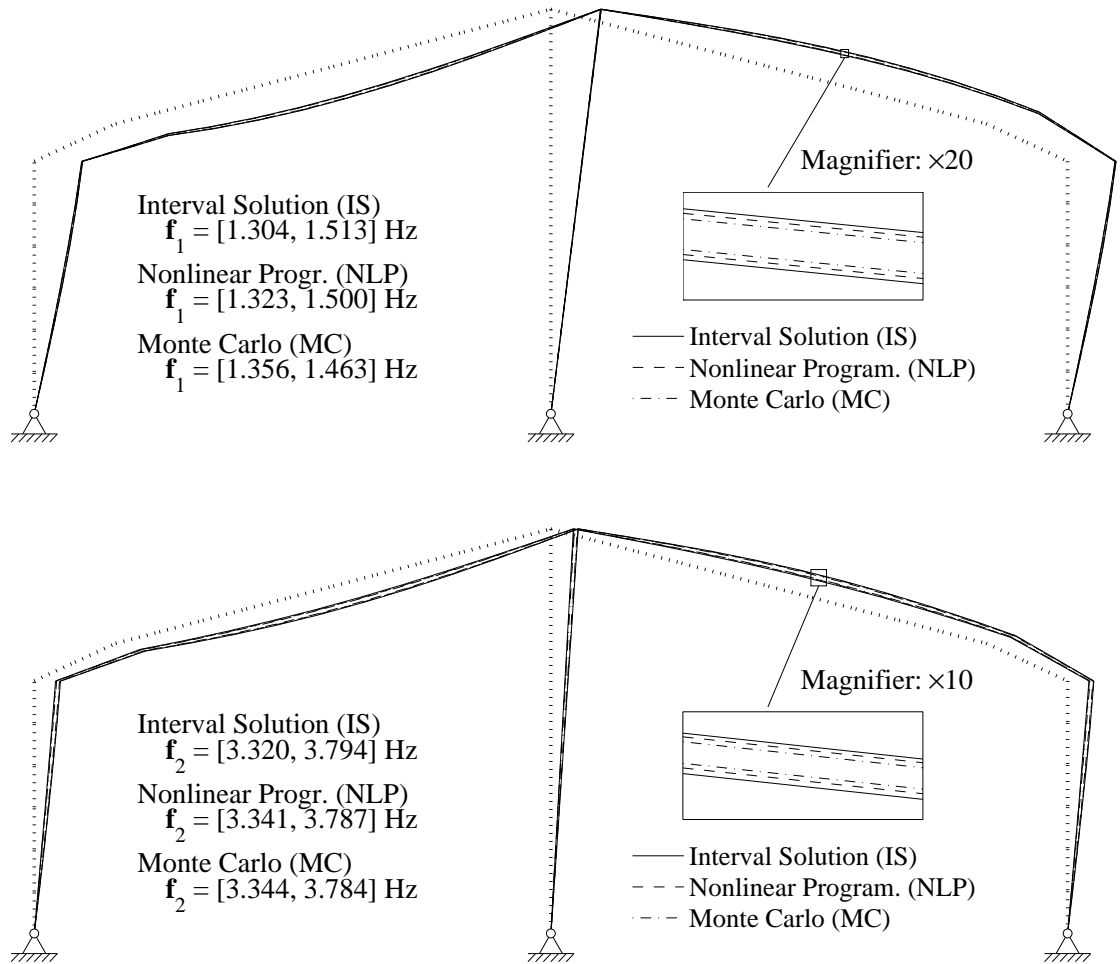
Figure 4.14: Enclosure of the natural frequencies $\mathbf{f}_1$, $\mathbf{f}_2$, $\mathbf{f}_3$, and $\mathbf{f}_4$, and corresponding modal shapes for the gable frame of Figure 4.12. Mass density $\boldsymbol{\rho}_j$ and Young's modulus $\mathbf{E}_j$ under 5% and 20% uncertainties, respectively. IS = Interval solution (solid line), NLP = nonlinear programming solution (dashed line) and MC = Monte Carlo prediction from an ensemble of 100,000 simulations (dash-dotted line).

The lowest four natural frequencies $\mathbf{f}_1$, $\mathbf{f}_2$, $\mathbf{f}_3$, and $\mathbf{f}_4$ are calculated, and the corresponding modal shapes of the gable frame are displayed in Figure 4.14. The undeformed frame configuration is also displayed (dotted lines). In the figure, the interval solution (IS, solid lines) from the proposed method is compared against solutions obtained from the nonlinear programming approach (NLP, dashed lines) and Monte Carlo predictions (MC, dash-dotted lines) from an ensemble of 100,000 simulations.
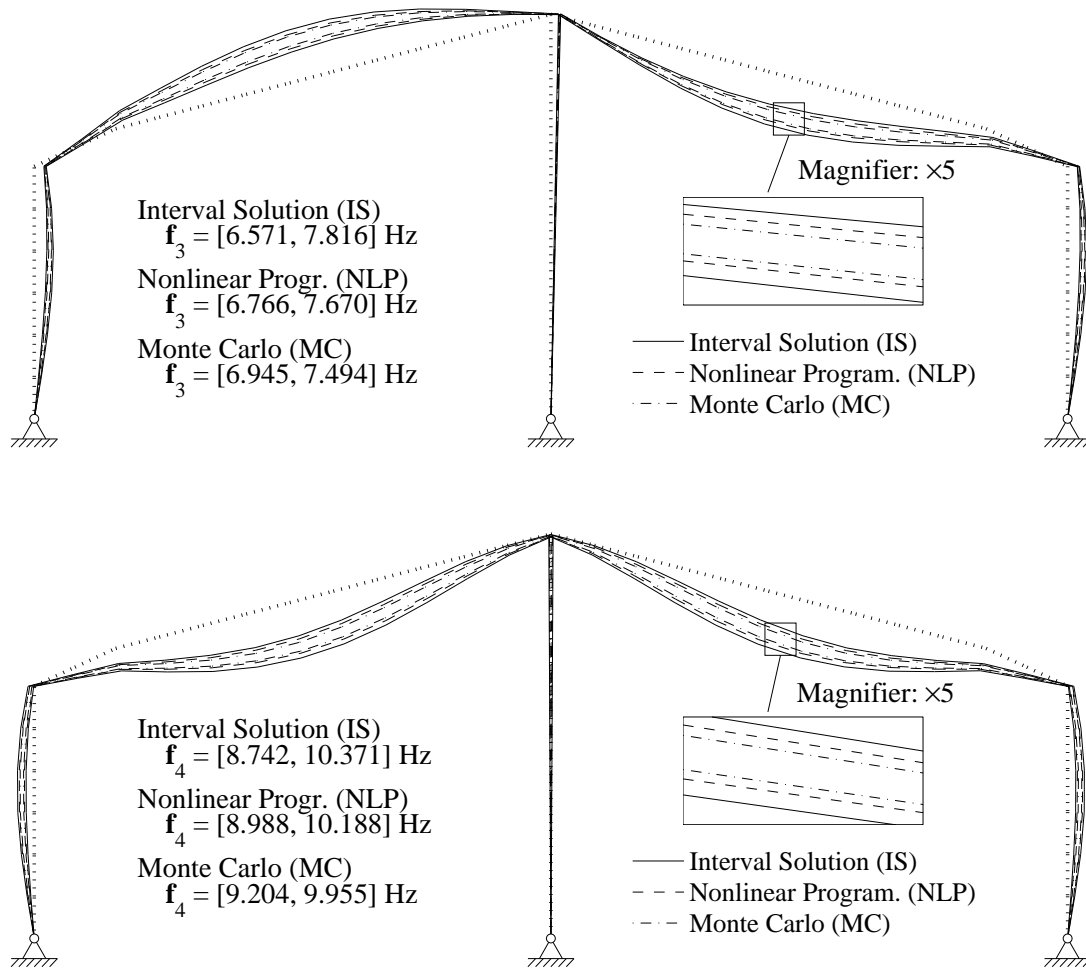
Figure 4.14: Enclosure of the natural frequencies $\mathbf{f}_1$, $\mathbf{f}_2$, $\mathbf{f}_3$, and $\mathbf{f}_4$, and corresponding modal shapes for the gable frame of Figure 4.12. Mass density $\boldsymbol{\rho}_j$ and Young's modulus $\mathbf{E}_j$ under 5% and 20% uncertainties, respectively. IS = Interval solution (solid line), NLP = nonlinear programming solution (dashed line) and MC = Monte Carlo prediction from an ensemble of 100,000 simulations (dash-dotted line).
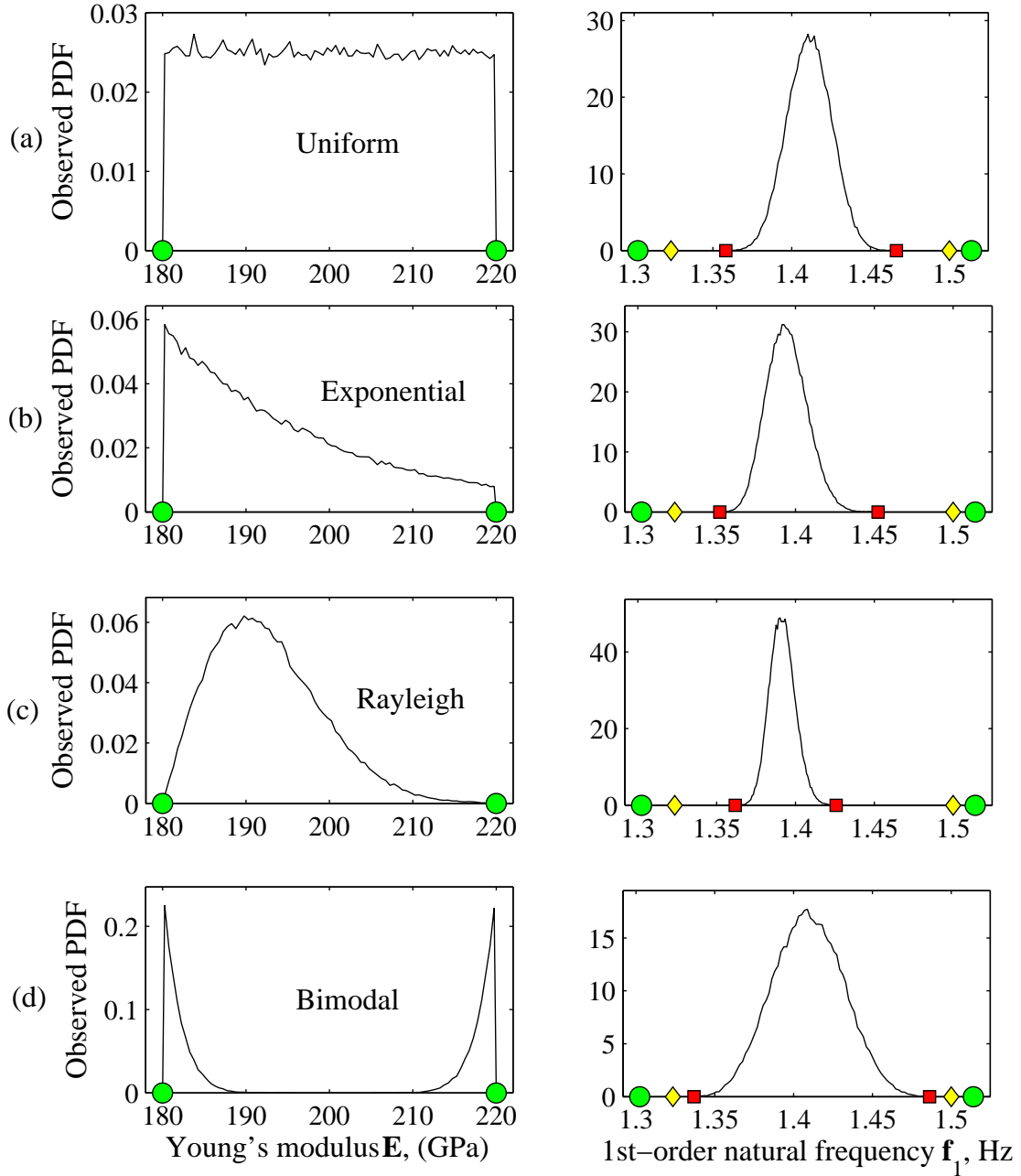
Figure 4.15: Comparisons between IS obtained from the proposed method, NLP, and MC of the first-order natural frequency $\mathbf{f}_1$ of the gable frame of Figure 4.12: (Left) observed probability density function (PDF) of the Young's modulus $\mathbf{E} = [180, 220]$ GPa (20% uncertainty) sampled from (a) uniform, (b) exponential, (c) Rayleigh, and (d) bimodal probability distributions (endpoints denoted by circular markers); (right) observed PDF of the first-order natural frequency $\mathbf{f}_1$ of the Interval solution (IS, endpoints denoted by circular markers), nonlinear programming approach (NLP, endpoints denoted by diamond markers) and Monte Carlo predicted interval $[\min(f_1), \max(f_1)]$ from an ensemble of 100,000 simulations (MC, square markers).

146

From the figure, observe that IS guarantees to enclose the exact solution NLP, which encloses MC. Further, the overestimation of IS is smaller than that of MC. Unfortunately, the NLP solution is not available at some nodes, because the MATLAB optimization solver did not always converge. In contrast, the proposed method works everywhere. In addition, note that the computational time for IS is 1.2 seconds, which is several order of magnitude less than that required by NLP (993 seconds) and MC methods (2889 seconds for an ensemble of 100,000 simulations).

Figure 4.15 shows that IS guarantees to enclose both NLP and MC predictions from an ensemble of 10,000 simulations, regardless of the type of probability distribution used to model uncertainties. Figure 4.16 reports the interval solutions for the lowest natural frequency $\mathbf{f}_1$ as function of the uncertainty level β (up to 30%) in mass density $\boldsymbol{\rho}_j$ and Young's modulus $\mathbf{E}_j$. The interval solution (IS) obtained from the proposed method always contains the reference NLP solution and MC predictions.
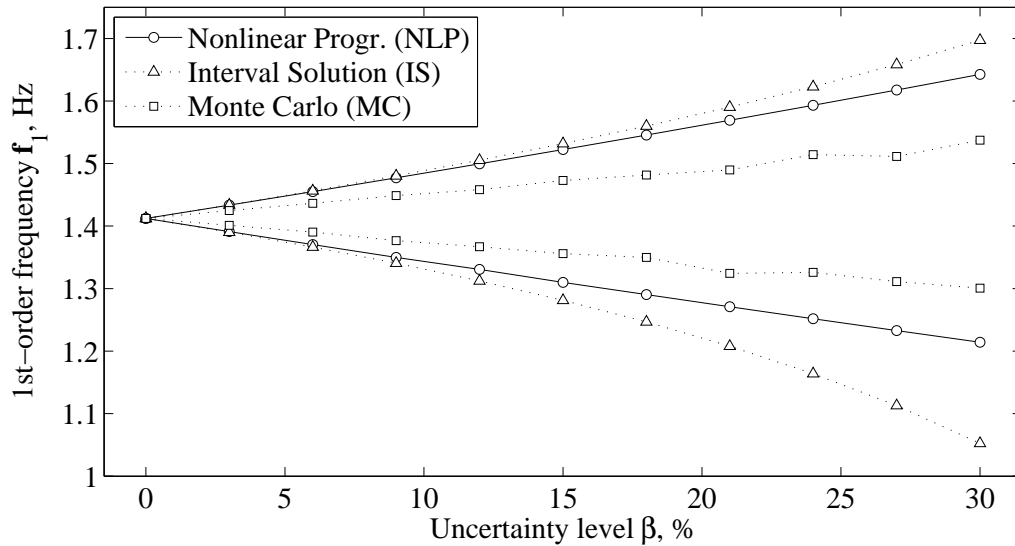
Figure 4.16: Enclosure of the lowest natural frequency $\mathbf{f}_1$ as a function of the uncertainty level β (up to 30%) in mass density $\boldsymbol{\rho}_j$ and Young's modulus $\mathbf{E}_j$: IS = Interval Solution (dotted line with triangular markers), MC = Monte Carlo solution from an ensemble of 10,000 simulations (dashed line with square markers) and NLP = Nonlinear programming reference solution (solid line with circular markers).

147

4.5 Summary

In this chapter, dynamics of structural systems under uncertainty are studied, and a new interval method is presented, which extends the application of the static forward solver discussed in Chapter 2. The presented method uses intervals to analyze the frequency responses, natural frequencies, and modal shapes of elastic structures with uncertain geometric and material properties. In the frequency response analysis, the structural responses at given frequencies are obtained by solving an complex interval linear system. In the modal analysis, the natural frequencies and corresponding modal shapes are obtained simultaneously by solving an Interval Generalized Eigen-value Problem (IGEP).

The proposed interval forward solver provides guaranteed enclosures of the exact reference solution with small overestimation, as shown in a number of numerical examples. The results prove that the new decomposition strategy for the IFEM matrices successfully reduces overestimation due to interval dependency. In addition, the efficiency of the proposed method is superior to other available methods in the literature.

CHAPTER V

TRANSIENT RESPONSE ANALYSIS OF STRUCTURAL DYNAMIC PROBLEMS BY INTERVALS

In this chapter, the time-domain dynamics of elastic structures with uncertain geometric and material properties are studied. Uncertain parameter of the structure are modeled by intervals, and Interval Finite Element Method (IFEM) is implemented [66, 118, 137, 150]. The structure is governed by the following interval differential equation in the time domain,

$$\mathbf{Ku} + \mathbf{C\dot{u}} + \mathbf{M\ddot{u}} = \mathbf{f}, \tag{5.1}$$

where $\mathbf{K}$, $\mathbf{C}$, and $\mathbf{M}$ are respectively the stiffness, damping, and mass matrix of the structure, $\mathbf{u}$ is the unknown nodal displacement vector, $\mathbf{\dot{u}}$ and $\mathbf{\ddot{u}}$ are the corresponding nodal velocity and acceleration vector, $\mathbf{f}$ is the time-varying nodal equivalent load. The initial conditions are expressed in an interval form, that is

$$\mathbf{u}(0) = \mathbf{u}_0, \qquad \mathbf{\dot{u}}(0) = \mathbf{v}_0, \tag{5.2}$$

where $\mathbf{u}_0$ and $\mathbf{v}_0$ are the initial nodal displacement and velocity vector, respectively. Besides the primary variables $\mathbf{u}$, $\mathbf{\dot{u}}$ and $\mathbf{\ddot{u}}$ at given time, derived variables such as the strain vector $\boldsymbol{\varepsilon}$ and the stress vector $\boldsymbol{\sigma}$ are also required, which are obtained from

$$\boldsymbol{\varepsilon} = B\mathbf{u}, \quad \boldsymbol{\sigma} = \mathbf{Su}, \tag{5.3}$$

where B and $\mathbf{S}$ are the strain- and stress-displacement matrix, respectively.

In practice, the differential Eq. (5.1) is solved at discrete time t_k, which are usually uniformly spaced in time. Conventional numerical integration approaches solve the above differential equations recursively, viz. the solution at the current

time t_k is obtained by using the solution in the previous time t_{k-1}. One notable example of the numerical integration method in structural analysis is the Newmark-β method [30, 40, 112]. However, such recursive approach is not applicable for IFEM implementation, because overestimation due to interval dependency accumulates, and the yielded interval enclosure quickly become excessively wide and practically useless after a few iterations in time.

Alternatively, the transformation approach can be used [11, 154]. In the proposed method, the Discrete Fourier Transform (DFT) approach is adopted. A brief introduction on the DFT can be found in [123] and Appendix D. The governing Eq. (5.1) is transformed into the frequency domain using DFT, and the computed response is expressed back into the time domain using the corresponding inverse transform (Inverse Discrete Fourier Transform, IDFT). As a result, the solution vector at all time steps are obtained simultaneously.

In the following sections, first the deterministic solver based on the DFT approach is presented. Then the proposed interval solver is introduced in detail. The governing Eq. (5.1) is reintroduced into a fixed-point form, and iterative enclosure method is implemented to obtain a sharp interval enclosure of the exact solution. Finally, the performance of the proposed method is compared with other available methods in a few numerical example.

5.1 Deterministic Dynamic Solver

In this section, the deterministic dynamic solver based on the DFT approach [140, 141] is presented. The dynamic response of a linearly elastic structure is studied, which, after FEM discretization, is governed by

$$Ku + C\dot{u} + M\ddot{u} = f, \tag{5.4}$$

where K, C, and M are the stiffness, damping, and mass matrices of the structure, respectively, u is the nodal displacement vector, $\dot{u}$ and $\ddot{u}$ are the first and second

derivatives of u with respect to the time (or, equivalently, nodal velocity and acceleration), and f is the nodal equivalent load. The initial condition is given by

$$u(0) = u_0, \qquad \dot{u}(0) = v_0. \tag{5.5}$$

In addition, the system is assumed discretized in time. The nodal equivalent load at discrete time t_k is given, and the goal is to solve for the nodal displacement vector u at t_k, as well as its derivatives $\dot{u}$ and $\ddot{u}$. That is,

$$f(t_k) = f_k, \qquad u(t_k) = u_k; \tag{5.6}$$

$$\dot{u}(t_k) = \dot{u}_k, \qquad \ddot{u}(t_k) = \ddot{u}_k.$$

Usually, the time steps are uniformly spaced, viz. $t_k = k\Delta t$. The sampling interval Δt must be small enough to prevent any potential aliasing [123]. Let T be the total time length of the signal and N the total number, then $T = N\Delta t$.

In the discrete Fourier transform approach, DFT is applied to the discrete version of the governing Eq. (5.4) and transform it into

$$\left(-\omega_j^2 M + i\omega_j C + K\right) \mathcal{F}_t(u)_j = \mathcal{F}_t(f)_j, \tag{5.7}$$

where $i = \sqrt{-1}$ is the imaginary unit, $\omega_j = j\Delta\omega$ with $\Delta\omega = 2\pi/T$ being the fundamental frequency, $\mathcal{F}_t(u)_j$ and $\mathcal{F}_t(f)_j$ are the Fourier transform of the nodal displacement u_k and equivalent load f_k, respectively. Then the nodal displacement vector in the time-domain is obtained by applying the IDFT to $\mathcal{F}_t(u)_j$, viz.

$$u_n = \frac{1}{N} \sum_{j=0}^{N-1} \mathcal{F}_t(u)_j e^{-i(2\pi/N)jn} \tag{5.8}$$

$$= \frac{1}{N} \sum_{j=0}^{N-1} G_j \mathcal{F}_t(f)_j e^{-i(2\pi/N)jn},$$

where G_j is the inverse of the effective stiffness matrix in Eq. (5.7). To ensure that the final solution u_n has zero imaginary part, G_j takes the following form,

$$G_j = \begin{cases} \left(-\omega_j^2 M + i\omega_j C + K\right)^{-1}, & 0 \leq j < N/2; \\ \text{conjugate of } G_{N-j}, & N/2 \leq j < N. \end{cases} \tag{5.9}$$

151

The above approach essentially solves for the stationary response of the structure caused by periodic loads with period T. The results are identical to the actual dynamic response with trivial initial conditions ($u_0 = v_0 = 0$) when enough zero-padding is attached. The length of the zero-padding, T_p, can be estimated from

$$e^{-\zeta\omega T_p} < \tau_{err}, \qquad \Rightarrow \qquad T_p > \frac{\ln \tau_{err}}{\zeta\omega}, \qquad (5.10)$$

where τ_{err} is the error tolerance, ω is the lowest natural frequency of the structure, and ζ is the corresponding effective damping ratio. Let T_0 be the length of the original signal, then $T = T_0 + T_p$.

Non-trivial initial conditions can be modeled by modifying the equivalent load [81, 85, 93]. For initial displacement u_0, it is equivalent to add a constant load

$$f_{u0} = Ku_0, \qquad (5.11)$$

which exist for the time interval $T_0 \leq t < T$. For initial velocity v_0, it is equivalent to add an impulse load

$$f_{v0} = \frac{M}{\Delta t}v_0, \qquad (5.12)$$

at time $t = 0$ for a duration of time Δt.

5.2 Interval Dynamic Solver

Assume the elastic structure under study contains uncertain parameters, which are modeled by intervals. The structural system is governed by Eqs. (5.1) and (5.2). For simplicity, the Rayleigh damping is adopted. The damping matrix

$$\mathbf{C} = \alpha_d\mathbf{M} + \beta_d\mathbf{K}, \qquad (5.13)$$

where α_d and β_d are the Rayleigh damping coefficients. To reduce overestimation due to interval dependency, the interval matrix decomposition outlined before is adopted. Then DFT is used to transform the governing equation into a fixed-point form, which is further solved by a new variant of iterative enclosure method. Details on the proposed method is presented as follows.

5.2.1 Interval matrix decomposition

The matrix decomposition strategy reduces overestimation due to interval dependency by avoiding multiple occurrences of the same interval variable in the formulation. As discussed before, the stiffness matrix $\mathbf{K}$, the mass matrix $\mathbf{M}$, and the stress-displacement matrix $\mathbf{S}$ are decomposed into

$$\mathbf{K} = A\mathrm{diag}(\Lambda\boldsymbol{\alpha})A^T;$$
$$\mathbf{M} = A_m\mathrm{diag}(\Lambda_m\boldsymbol{\alpha}_m)A_m^T; \qquad (5.14)$$
$$\mathbf{S} = \Phi_s\mathrm{diag}(\Lambda_s\boldsymbol{\alpha})A_s^T,$$

where A, Λ, A_m, Λ_m, Φ_s, Λ_s, and A_s are deterministic matrices, $\boldsymbol{\alpha}$ is the interval stiffness parameter vector that accounts for uncertainties in the stiffness matrix $\mathbf{K}$, and $\boldsymbol{\alpha}_m$ is the interval mass parameter vector that accounts for uncertainties in the mass matrix $\mathbf{M}$. Detailed discussions on the decomposition and assembly of $\mathbf{K}$, $\mathbf{M}$, and $\mathbf{S}$ can be found in Section 2.1 and 4.1.1.

By combining the nodal equivalent load vector $\mathbf{f}_k$ at different time steps t_k, the interval load matrix $\mathbf{f}$ is obtained, whose k-th column is $\mathbf{f}_k$. When the structure is subject to external loading and the M-$\boldsymbol{\delta}$ method is adopted [102], $\mathbf{f}$ is decomposed into

$$\mathbf{f} = F\boldsymbol{\delta}_t, \qquad (5.15)$$

where F is a deterministic matrix, and $\boldsymbol{\delta}_t$ is the time-varying load uncertainty matrix. Usually it is necessary to distinguish the uncertainty in the magnitude of the load and the uncertainty in the time-history of the load. Thus $\boldsymbol{\delta}_t$ is further decomposed into an interval column vector $\boldsymbol{\delta}$ and an interval row vector $\mathbf{d}_t$, viz. $\boldsymbol{\delta}_t = \boldsymbol{\delta}\mathbf{d}_t$, where $\boldsymbol{\delta}$ models the uncertainties in the load magnitude and $\mathbf{d}_t$ models the uncertainties in the load time-history. Finally, the nodal equivalent load $\mathbf{f}$ is decomposed into

$$\mathbf{f} = (F\boldsymbol{\delta})\mathbf{d}_t. \qquad (5.16)$$

Similarly, when the structure is subject to ground motion, $\mathbf{f}$ is decomposed into

$$\mathbf{f} = -\mathbf{Ma} = -\mathbf{M}q\boldsymbol{\delta}_t, \tag{5.17}$$

where $\boldsymbol{\delta}_t$ denotes the time-varying ground acceleration, $\mathbf{a}$ represents the resulting nodal acceleration of the structure, and q relates $\boldsymbol{\delta}_t$ to $\mathbf{a}$, viz. $\mathbf{a} = q\boldsymbol{\delta}_t$. By using the same decomposition for $\boldsymbol{\delta}_t$, and noting Eq. (5.14),

$$\mathbf{f} = -A_m \text{diag}(\Lambda_m \boldsymbol{\alpha}_m) A_m^T q \boldsymbol{\delta} \mathbf{d}_t \tag{5.18}$$

$$= A_m \left(\Lambda_m \boldsymbol{\alpha}_m \circ B_f \boldsymbol{\delta} \right) \mathbf{d}_t,$$

where $B_f = -A_m^T q$, and $a \circ b$ is the element-by-element Hadamard product of two vectors a and b.

When the initial conditions are non-trivial and modeled by intervals, as shown in Eq. (5.2), the corresponding nodal equivalent load $\mathbf{f}$ is given by

$$\mathbf{f} = \mathbf{K}\mathbf{u}_0 d_{u_0} + \mathbf{M}\mathbf{v}_0 d_{v_0}, \tag{5.19}$$

where d_{u_0} and d_{v_0} are two deterministic row vectors. d_{u_0} is zero for the time interval $0 \leq t_k < T_0$ and unity for the time interval $T_0 \leq t_k < T$, where T_0 and T are the length of the original and padded signal. d_{v_0} represents an impulse load which is $1/\Delta t$ at $t_k = 0$ and zero everywhere else. Noting the decomposition in Eq. (5.14),

$$\mathbf{f} = A \left(\Lambda \boldsymbol{\alpha} \circ A^T \mathbf{u}_0 \right) d_{u_0} \tag{5.20}$$

$$+ A_m \left(\Lambda_m \boldsymbol{\alpha}_m \circ A_m^T \mathbf{v}_0 \right) d_{v_0},$$

which has a similar matrix form as Eq. (5.18). Thus the non-trivial initial conditions are treated in the same manner as ground accelerations.

5.2.2 Interval governing equations

To solve the interval differential Eq. (5.1), following the DFT approach outlined in Section 5.1, the equation is transformed into the frequency domain, viz.

$$\left(-\omega_j^2 \mathbf{M} + i\omega_j \mathbf{C} + \mathbf{K} \right) \mathcal{F}_t(\mathbf{u})_j = \mathcal{F}_t(\mathbf{f})_j, \tag{5.21}$$

where $\mathcal{F}_t(\mathbf{u})_j$ and $\mathcal{F}_t(\mathbf{f})_j$ are the Fourier transform of the nodal displacement $\mathbf{u}_k$ and equivalent load $\mathbf{f}_k$, respectively.

To include compatibility requirements and essential boundary conditions in the governing equation, and to ensure that the final solution has zero imaginary part, Eq. (5.21) is brought into the following equivalent form,

$$\begin{Bmatrix} \mathbf{K}_{\text{eff},j} & C^T \\ C & 0 \end{Bmatrix} \begin{Bmatrix} \mathcal{F}_t(\mathbf{u})_j \\ \mathcal{F}_t(\boldsymbol{\lambda})_j \end{Bmatrix} = \begin{Bmatrix} \mathcal{F}_t(\mathbf{f})_j \\ 0 \end{Bmatrix}, \tag{5.22}$$

where $\mathbf{K}_{\text{eff},j}$ is the effective stiffness matrix corresponding to the j-th frequency ω_j, which is given by

$$\mathbf{K}_{\text{eff},j} = \begin{cases} -\omega_j^2 \mathbf{M} + i\omega_j \mathbf{C} + \mathbf{K}, & 0 \leq j < N/2; \\ \text{conjugate of } \mathbf{K}_{\text{eff},N-j}, & N/2 \leq j < N, \end{cases} \tag{5.23}$$

C is the constraint matrix that imposes compatibility requirements and essential boundary conditions, and $\boldsymbol{\lambda}_k$ is the Lagrangian multiplier representing the internal forces and support reactions at t_k. By adopting the Rayleigh damping and the decomposition of $\mathbf{K}$ and $\mathbf{M}$ in Eq. (5.14), $\mathbf{K}_{\text{eff},j}$ can be decomposed into

$$\mathbf{K}_{\text{eff},j} = A_{\text{eff},j} \text{diag} \left(\Lambda_{\text{eff}} \boldsymbol{\alpha}_{\text{eff}} \right) B_{\text{eff}}, \tag{5.24}$$

where $A_{\text{eff},j}$ is a deterministic matrix depending on the frequency ω_j,

$$A_{\text{eff},j} = \begin{cases} \{(1 + ib\omega_k)A \quad (-\omega_k^2 + ia\omega_k)A_m\}, & 0 \leq j < N/2; \\ \text{conjugate of } A_{\text{eff},N-j}, & N/2 \leq j < N, \end{cases} \tag{5.25}$$

and Λ_{eff}, B_{eff}, and $\boldsymbol{\alpha}_{\text{eff}}$ are time-invariant variables, previously given in Eq. (4.18)

$$\Lambda_{\text{eff}} = \begin{Bmatrix} \Lambda & 0 \\ 0 & \Lambda_m \end{Bmatrix}, \quad B_{\text{eff}} = \begin{Bmatrix} A^T \\ A_m^T \end{Bmatrix}, \quad \boldsymbol{\alpha}_{\text{eff}} = \begin{Bmatrix} \boldsymbol{\alpha} \\ \boldsymbol{\alpha}_m \end{Bmatrix}. \tag{5.26}$$

Suppose the structure is subject to external loading, then

$$\mathcal{F}_t(\mathbf{f})_j = \mathcal{F}_t(F\boldsymbol{\delta}\mathbf{d}_t)_j = F\boldsymbol{\delta}\mathcal{F}_t(\mathbf{d}_t)_j. \tag{5.27}$$

155

Then Eq. (5.22) is equivalent to the following decomposed form

$$
\left\{\begin{matrix} K_{\text{eff},j0} & C^T \\ C & 0 \end{matrix}\right\} \left\{\begin{matrix} \mathcal{F}_t(\mathbf{u})_j \\ \mathcal{F}_t(\boldsymbol{\lambda})_j \end{matrix}\right\} = \left\{\begin{matrix} F \\ 0 \end{matrix}\right\} \boldsymbol{\delta}\mathcal{F}_t(\mathbf{d}_t)_j \tag{5.28}
$$

$$
- \left\{\begin{matrix} A_{\text{eff},j} \\ 0 \end{matrix}\right\} \text{diag}\left(B_{\text{eff}}\mathcal{F}_t(\mathbf{u})_j\right)\Lambda_{\text{eff}}\Delta\boldsymbol{\alpha}_{\text{eff}},
$$

by using the decomposition in Eqs. (5.24) and (5.27) and the following identities

$$
A_{\text{eff},j}\text{diag}\left(\Lambda_{\text{eff}}\boldsymbol{\alpha}_{\text{eff}}\right)B_{\text{eff}}\mathcal{F}_t(\mathbf{u})_j
$$

$$
= A_{\text{eff},j}\left(\Lambda_{\text{eff}}\boldsymbol{\alpha}_{\text{eff}} \circ B_{\text{eff}}\mathcal{F}_t(\mathbf{u})_j\right) \tag{5.29}
$$

$$
= A_{\text{eff},j}\text{diag}\left(B_{\text{eff}}\mathcal{F}_t(\mathbf{u})_j\right)\Lambda_{\text{eff}}\boldsymbol{\alpha}_{\text{eff}},
$$

where $\Delta\boldsymbol{\alpha}_{\text{eff}}$ is the difference between $\boldsymbol{\alpha}_{\text{eff}}$ and the reference vector $\alpha_{\text{eff}0}$, viz. $\Delta\boldsymbol{\alpha}_{\text{eff}} = \boldsymbol{\alpha}_{\text{eff}} - \alpha_{\text{eff}0}$, and $K_{\text{eff},j0} = A_{\text{eff},j}\text{diag}(\Lambda_{\text{eff}}\alpha_{\text{eff}0})B_{\text{eff}}$.

When the structure is subject to ground motion, according to Eq. (5.18),

$$
\mathcal{F}_t(\mathbf{f})_j = A_f\left(\Lambda_m\boldsymbol{\alpha}_m \circ B_f\boldsymbol{\delta}\right)\mathcal{F}_t(\mathbf{d}_t)_j
$$

$$
= \left(A_f\left(\Lambda_m\alpha_{m0} \circ B_f\boldsymbol{\delta}\right) + A_f\left(\Lambda_m\Delta\boldsymbol{\alpha}_m \circ B_f\boldsymbol{\delta}\right)\right)\mathcal{F}_t(\mathbf{d}_t)_j \tag{5.30}
$$

$$
= F_0\boldsymbol{\delta}\mathcal{F}_t(\mathbf{d}_t)_j + A_f\text{diag}\left(B_f\boldsymbol{\delta}\mathcal{F}_t(\mathbf{d}_t)_j\right)\Lambda_m\Delta\boldsymbol{\alpha}_m,
$$

where $\Delta\boldsymbol{\alpha}_m$ is the difference between $\boldsymbol{\alpha}_m$ and the reference vector α_{m0}, viz. $\Delta\boldsymbol{\alpha}_m = \boldsymbol{\alpha}_m - \alpha_{m0}$, and $F_0 = A_f\text{diag}(\Lambda_m\alpha_{m0})B_f$. Then the generalized equivalent load in Eq. (5.22) is decomposed into

$$
\left\{\begin{matrix} \mathcal{F}_t(\mathbf{f})_j \\ 0 \end{matrix}\right\} = \left\{\begin{matrix} F_0 \\ 0 \end{matrix}\right\}\boldsymbol{\delta}\mathcal{F}_t(\mathbf{d}_t)_j + \left\{\begin{matrix} A_f \\ 0 \end{matrix}\right\}\text{diag}\left(B_f\boldsymbol{\delta}\mathcal{F}_t(\mathbf{d}_t)_j\right)\Lambda_m\Delta\boldsymbol{\alpha}_m, \tag{5.31}
$$

Eq. (5.22) is equivalent to the following decomposed form

$$
\left\{\begin{matrix} K_{\text{eff},j0} & C^T \\ C & 0 \end{matrix}\right\}\left\{\begin{matrix} \mathcal{F}_t(\mathbf{u})_j \\ \mathcal{F}_t(\boldsymbol{\lambda})_j \end{matrix}\right\} = \left\{\begin{matrix} F_0 \\ 0 \end{matrix}\right\}\boldsymbol{\delta}\mathcal{F}_t(\mathbf{d}_t)_j \tag{5.32}
$$

$$
- \left\{\begin{matrix} A_{\text{eff}} & A_f \\ 0 & 0 \end{matrix}\right\}\text{diag}\left(\left\{\begin{matrix} B_{\text{eff}}\mathcal{F}_t(\mathbf{u})_j \\ -B_f\boldsymbol{\delta}\mathcal{F}_t(\mathbf{d}_t)_j \end{matrix}\right\}\right)\left\{\begin{matrix} \Lambda_{\text{eff}} & \\ 0 & \Lambda_m \end{matrix}\right\}\Delta\boldsymbol{\alpha}_{\text{eff}}.
$$

156

Due to the similarities between the decomposition of the equivalent load in Eqs. (5.18) and (5.20), the above formulation can be extended to cases when the initial conditions are non-trivial, viz. either $\mathbf{u}_0 \neq 0$ or $\mathbf{v}_0 \neq 0$.

When derived quantities such as the strain vector $\boldsymbol{\varepsilon}$ and the stress vector $\boldsymbol{\sigma}$ are required, the strain and stress equations $B\mathbf{u} - \boldsymbol{\varepsilon} = 0$ and $\mathbf{S}\mathbf{u} - \boldsymbol{\varepsilon} = 0$ are added to the governing equation. Suppose the structure is subject to external loads and $\mathbf{f} = F\boldsymbol{\delta}\mathcal{F}_t(\mathbf{d}_t)_j$, the governing equations are given by

$$
\begin{Bmatrix}
\begin{bmatrix}
\mathbf{K}_{\text{eff},j} & C^T & 0 & 0 \\
C & 0 & 0 & 0 \\
B & 0 & -I & 0 \\
\mathbf{S} & 0 & 0 & -I
\end{bmatrix}
\end{Bmatrix}
\begin{Bmatrix}
\mathcal{F}_t(\mathbf{u})_j \\
\mathcal{F}_t(\boldsymbol{\lambda})_j \\
\mathcal{F}_t(\boldsymbol{\varepsilon})_j \\
\mathcal{F}_t(\boldsymbol{\sigma})_j
\end{Bmatrix}
=
\begin{Bmatrix}
F \\
0 \\
0 \\
0
\end{Bmatrix}
\boldsymbol{\delta}\mathcal{F}_t(\mathbf{d}_t)_j,
\tag{5.33}
$$

which is equivalent to the following decomposed form

$$
\begin{Bmatrix}
\begin{bmatrix}
K_{\text{eff},j0} & C^T & 0 & 0 \\
C & 0 & 0 & 0 \\
B & 0 & -I & 0 \\
S_0 & 0 & 0 & -I
\end{bmatrix}
\end{Bmatrix}
\begin{Bmatrix}
\mathcal{F}_t(\mathbf{u})_j \\
\mathcal{F}_t(\boldsymbol{\lambda})_j \\
\mathcal{F}_t(\boldsymbol{\varepsilon})_j \\
\mathcal{F}_t(\boldsymbol{\sigma})_j
\end{Bmatrix}
=
\begin{Bmatrix}
F \\
0 \\
0 \\
0
\end{Bmatrix}
\boldsymbol{\delta}\mathcal{F}_t(\mathbf{d}_t)_j
\tag{5.34}
$$

$$
- \begin{Bmatrix}
\begin{bmatrix}
A_{\text{eff},j} & 0 \\
0 & 0 \\
0 & 0 \\
0 & \Phi_s
\end{bmatrix}
\end{Bmatrix}
\text{diag}\left(\begin{Bmatrix} B_{\text{eff}}\mathcal{F}_t(\mathbf{u})_j \\ A_s^T \mathcal{F}_t(\mathbf{u})_j \end{Bmatrix}\right)
\begin{Bmatrix} \Lambda_{\text{eff}} \\ \Lambda_s \quad 0 \end{Bmatrix}
\Delta\boldsymbol{\alpha}_{\text{eff}}.
$$

Apparently, the formulation can be extended to account for ground motion and non-trivial initial conditions.

5.2.3 Iterative enclosure method

To solve the interval linear system Eqs. (5.28), (5.32), and (5.34), they are recast into the following compact form

$$
K_{g,j}\mathcal{F}_t(\mathbf{u}_g)_j = F_g\boldsymbol{\delta}\mathcal{F}_t(\mathbf{d}_t)_j - A_{g,j}\text{diag}\left(\mathcal{F}_t(\mathbf{v}_g)_j\right)\Lambda_g\Delta\boldsymbol{\alpha}_{\text{eff}},
\tag{5.35}
$$

157

where $K_{g,j}$, F_g, $A_{g,j}$, Λ_g are given deterministic matrices, $\mathbf{u}_g$ is the unknown interval vector, $\boldsymbol{\delta}$, $\mathbf{d}_t$, and $\Delta\boldsymbol{\alpha}_{\text{eff}}$ are given interval vectors, and $\mathbf{v}_g$ linearly depend on $\mathbf{u}_g$, viz. $\mathbf{v}_g = \mathbf{v}_0 + B_g\mathbf{u}_g$. Here subscripts $_j$ denotes variables associated with the j-th frequency ω_j. Note that matrices $K_{g,j}$ and $A_{g,j}$ are functions of the frequency ω_j. In the most general case, $\mathbf{u}_g$ includes all the primary and derived variables such as $\mathbf{u}$, $\boldsymbol{\lambda}$, $\boldsymbol{\varepsilon}$, and $\boldsymbol{\sigma}$, and the auxiliary variable $\mathbf{v}_g$ includes $B_{\text{eff}}\mathbf{u}$, $-B_f\boldsymbol{\delta}\mathbf{d}_t$, and $A_s^T\mathbf{u}$.

Now introduce $G_j = K_{g,j}^{-1}$. Multiplying both sides of Eq. (5.35) by G_j yields

$$\mathcal{F}_t(\mathbf{u}_g)_j = (G_jF_g)\boldsymbol{\delta}\mathcal{F}_t(\mathbf{d}_t)_j - (G_jA_{g,j})\mathrm{diag}\Big(\mathcal{F}_t(\mathbf{v}_g)_j\Big)\Lambda_g\Delta\boldsymbol{\alpha}_{\text{eff}}. \tag{5.36}$$

Then $\mathbf{u}_g$ is obtained by applying the IDFT to both side of (5.36),

$$\begin{aligned} \mathbf{u}_{g,k} &= \Big(\mathcal{F}_t^{-1}(G_jF_g) * \mathbf{d}_t\Big)_k\boldsymbol{\delta} \\ &- \Big(\mathcal{F}_t^{-1}(G_jA_{g,j}) * \mathrm{diag}(\mathbf{v}_g)\Big)_k\Lambda_g\Delta\boldsymbol{\alpha}_{\text{eff}}, \end{aligned} \tag{5.37}$$

where $(a * b)_k$ denotes the convolution between two discrete signals a_k and b_k (see Appendix D for detail). Eq. (5.37) can be recast into the following summation form,

$$\begin{aligned} \mathbf{u}_{g,k} &= \left(\sum_{l=0}^{N-1} \mathcal{F}_t^{-1}(G_jF_g)_{k-l}\mathbf{d}_{t,l}\right)\boldsymbol{\delta} \\ &- \left(\sum_{l=0}^{N-1} \mathcal{F}_t^{-1}(G_jA_{g,j})_{k-l}\mathrm{diag}(\mathbf{v}_{g,l})\right)\Lambda_g\Delta\boldsymbol{\alpha}_{\text{eff}}. \end{aligned} \tag{5.38}$$

Then a fixed-point form for $\mathbf{v}_{g,k}$ is obtained as

$$\begin{aligned} \mathbf{v}_{g,k} &= \mathbf{v}_{0,k} + B_g\Big(\mathcal{F}_t^{-1}(G_jF_g) * \mathbf{d}_t\Big)_k\boldsymbol{\delta} \\ &- B_g\Big(\mathcal{F}_t^{-1}(G_jA_{g,j}) * \mathrm{diag}(\mathbf{v}_g)\Big)_k\Lambda_g\Delta\boldsymbol{\alpha}_{\text{eff}}. \end{aligned} \tag{5.39}$$

A guaranteed outer enclosure for $\mathbf{v}_{g,k}$ is obtained by iteratively using Eq. (5.39), starting from the trivial initial guess $\mathbf{v}_{g,k}^1 = \mathbf{v}_{0,k} + \big(\mathcal{F}_t^{-1}(G_jF_g) * \mathbf{d}_t\big)_k\boldsymbol{\delta}$. The iteration stops when no improvement in $\mathbf{v}_{g,k}^j$ is observed for two consecutive iterations, and the converged solution is denoted as $\mathbf{v}_{g,k}^n$. Then the outer solution $\mathbf{u}_{g,k}^{out}$ is obtained by substituting $\mathbf{v}_{g,k}$ in Eq. (5.37) with the converged solution $\mathbf{v}_{g,k}^n$.

5.2.4 Fast enclosure of convolution

In the iterative enclosure method, the convolution between two signals are computed multiple times, as shown in Eqs. (5.37) and (5.39). To increase the computational efficiency and reduce overestimation in the final solution, the fast interval convolution algorithm, proposed by Liu and Kreinovich [86], is adopted. For a deterministic signal a_k and an interval signal $\mathbf{b}_k$, the convolution

$$(a * \mathbf{b})_k = \sum_{l=0}^{N-1} a_{k-l}\mathbf{b}_l. \tag{5.40}$$

Using the midpoint-radius form for intervals, Eq. (5.40) is equivalent to

$$\begin{cases} \text{mid}\,(a * \mathbf{b})_k = \sum_{l=0}^{N-1} a_{k-l}\,\text{mid}\,(\mathbf{b}_l); \\ \text{rad}\,(a * \mathbf{b})_k = \sum_{l=0}^{N-1} |a_{k-l}|\,\text{rad}\,(\mathbf{b}_l). \end{cases} \tag{5.41}$$

In other words, the midpoint of $(a * \mathbf{b})_k$ is the convolution of two deterministic signals a_k and mid $\mathbf{b}_k$; the radius of $(a * \mathbf{b})_k$ is the convolution of another two non-negative deterministic signals $|a_k|$ and rad $\mathbf{b}_k$. They can be computed efficiently using the DFT (see Eqs. (D.6), (D.7), and (D.8) in Appendix D. For instance,

$$\text{mid}\,(a * \mathbf{b})_k = \mathcal{F}_t^{-1}\big\{\mathcal{F}_t(a)\mathcal{F}_t(\text{mid}\,\mathbf{b})\big\}_k, \tag{5.42}$$

where the superscript * denotes the conjugate of a complex variable.

In particular, consider the first convolution in Eq. (5.37), the midpoint

$$\text{mid}\left(\mathcal{F}_t^{-1}(G_j F_g) * \mathbf{d}_t\right)_k \tag{5.43}$$
$$= \mathcal{F}_t^{-1}\big\{(G_j F_g)\mathcal{F}_t(\text{mid}\,\mathbf{d}_t)^*\big\}_k,$$

and the corresponding radius

$$\text{rad}\left(\mathcal{F}_t^{-1}(G_j F_g) * \mathbf{d}_t\right)_k \tag{5.44}$$
$$= \mathcal{F}_t^{-1}\big\{\mathcal{F}_t\big(|\mathcal{F}_t^{-1}(G_j F_g)|\big)\mathcal{F}_t(\text{rad}\,\mathbf{d}_t)^*\big\}_k.$$

For the second convolution in Eq. (5.37), the midpoint

$$\text{mid}\left(\mathcal{F}_t^{-1}(G_j A_{g,j}) * \text{diag}(\mathbf{v}_g)\right)_k \tag{5.45}$$
$$= \mathcal{F}_t^{-1}\left\{(G_j A_{g,j})\text{diag}\mathcal{F}_t(\text{mid } \mathbf{v}_g)^*\right\}_k,$$

and the corresponding radius

$$\text{rad}\left(\mathcal{F}_t^{-1}(G_j A_{g,j}) * \text{diag}(\mathbf{v}_g)\right)_k \tag{5.46}$$
$$= \mathcal{F}_t^{-1}\left\{\mathcal{F}_t(|\mathcal{F}_t^{-1}(G_j A_{g,j})|)\text{diag}\mathcal{F}_t(\text{rad } \mathbf{v}_g)^*\right\}_k.$$

During the iteration in Eq. (5.39), only the radius of $\mathbf{v}_g$ is updated. All other vectors and matrices do not change after the first iteration. In other words, Eqs. (5.43), (5.44), and (5.45) are used once before the iteration starts, and Eq. (5.46) is used once per iteration.

5.3   Numerical Examples

The proposed IFEM algorithm is implemented using the interval MATLAB toolbox INTLAB [122]. Interval enclosures of the structural responses of the following sample problems are calculated: i) a four-story rigid frame and ii) a simply supported truss. The performance of the proposed method is compared against other available methods in the literature: i) the endpoint combination method (EC) and ii) the Monte Carlo (MC) simulation. The results shows that the proposed method is applicable to the transient analysis of structural dynamic problems with uncertain parameters. Guaranteed interval enclosures of the exact structural responses in the time domain are obtained with small overestimations. In addition, the computational time is negligible when compared with other competing methods.

5.3.1   Four-story rigid frame

The first example is a four-story frame shown in Figure 5.1. The floors of the frame are assumed to be rigid enough to model the structure as an equivalent spring-mass
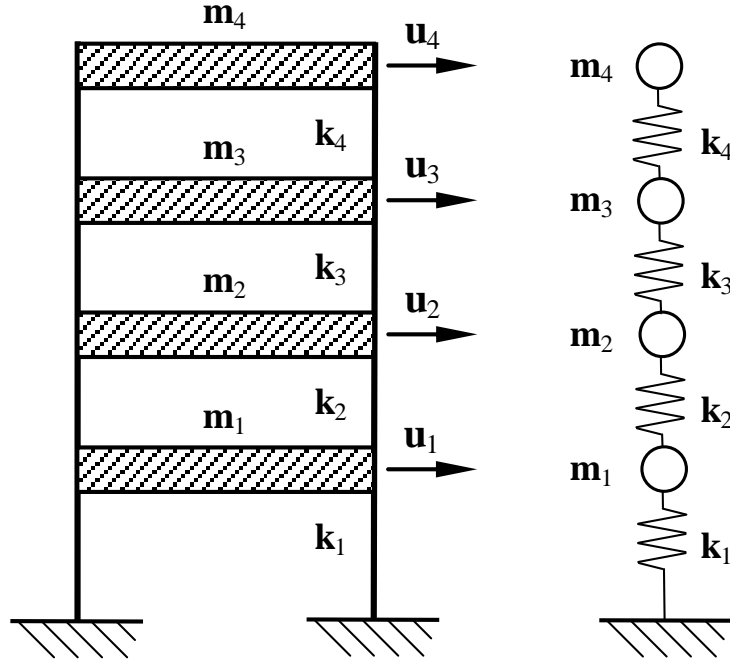
Figure 5.1: A four-story rigid frame and the equivalent spring-mass system.

system (shown in the right-hand side of Figure 5.1). The mass $\mathbf{m}_j$ and the inter-story shear stiffness $\mathbf{k}_j$ of each floor ($j = 1, \ldots, 4$) are modeled by independent interval variables, and given in Table 5.1.

Consider the structural response of the frame under a concentrated impact force acting on the top floor. The force has a duration of 4 s, and its variation during that time is deterministic, viz.

$$\mathbf{f}(t) = \begin{cases} \mathbf{P}\sin(\pi t/2), & 0 \le t \le 4 \text{ s}; \\ 0, & t > 4 \text{ s}, \end{cases} \tag{5.47}$$

where $\mathbf{P} = [0.99, 1.01]$ kN (2% uncertainty in the magnitude of the load). The damping matrix $\mathbf{C} = 0.5\mathbf{M} + 5 \times 10^{-3}\mathbf{K}$. The sampling rate is 100 Hz, so the sampling interval $\Delta t = 0.01$ s.

To compare the recursive Newmark-β method and the Discrete Fourier Transform (DFT) approach in Section 5.1, the nodal displacement $\mathbf{u}_4$ at the top floor for the first 10 s is displayed in Figure 5.2. Midpoint values are taken for all interval variables,

Table 5.1: Interval mass and stiffness for the five-story rigid frame of Figure 5.1, including 1% uncertainties in mass, and 5% uncertainties in stiffness.

Floor	Mass (kg)			Stiffness (kN/m)		
	$\mathbf{m}_j$	mid $\mathbf{m}_j$	rad $\mathbf{m}_j$	$\mathbf{k}_j$	mid $\mathbf{k}_j$	rad $\mathbf{k}_j$
1	[5.416, 5.470]	5.443	0.027	[1.180, 1.240]	1.210	0.030
2	[5.416, 5.470]	5.443	0.027	[1.677, 1.763]	1.720	0.043
3	[5.416, 5.470]	5.443	0.027	[1.862, 1.958]	1.910	0.048
4	[5.416, 5.470]	5.443	0.027	[1.775, 1.865]	1.820	0.045

viz. $m_j = $ mid $\mathbf{m}_j$, $k_j = $ mid $\mathbf{k}_j$, and $P = $ mid $\mathbf{P}$. Observe these two solutions are indistinguishable. Their maximal difference is 1.89×10^{-6} m, which is less than 0.1%.

Figure 5.3 compares the lower and upper bounds of $\mathbf{u}_4$ for the first 10 s, obtained from the proposed method (IS, solid lines), Monte Carlo predictions (MC, dashed
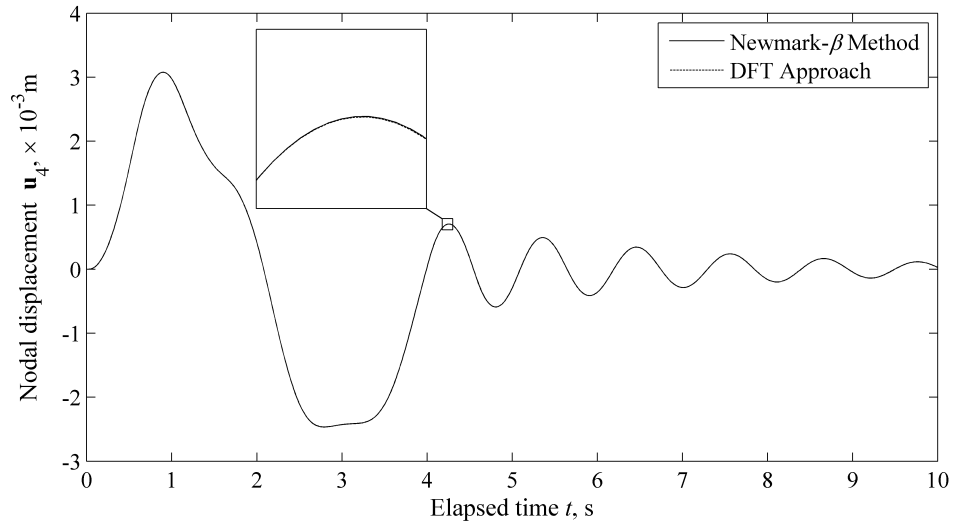
Figure 5.2: Deterministic time history of the nodal displacement $\mathbf{u}_4$ for the four-story frame of Figure 5.1 under a sinusoidal impact force: solutions obtained from the recursive Newmark-β method (solid line) and the DFT approach (dashed line). Midpoint values are taken for the interval variables.

lines) from an ensemble of 10,000 simulations, the reference solution obtained from endpoint combination (EC, dash-dotted lines), and the deterministic solution (DS, dotted line). Note that IS always contains the reference solution EC, and MC is always contained by EC. In addition, the overestimation level of the proposed method slightly increases as the time increases. In the figure, MC solution is obtained using the DFT approach, which indistinguishable from the solution obtained from a recursive Newmark-β method.

Then the concentrated force $\mathbf{f}(t)$ is removed, and the structure is subject to non-trivial initial conditions. Figure 5.4 shows the nodal displacement $\mathbf{u}_4$ at the top floor for the first 10 s with non-trivial initial nodal displacement $\mathbf{u}_0$ (top) and nodal velocity $\mathbf{v}_0$ (bottom), respectively. Here 2% uncertainty is considered for $\mathbf{u}_0$ and $\mathbf{v}_0$, viz.

$$\mathbf{u}_0 = \left\{ 0 \ \ 0 \ \ 0 \ \ 0 \ \ [0.99, \ 1.01] \right\}^T \times 10^{-3} \text{ m}; \tag{5.48}$$

$$\mathbf{v}_0 = \left\{ 0 \ \ 0 \ \ 0 \ \ 0 \ \ [0.99, \ 1.01] \right\}^T \times 10^{-2} \text{ m/s}.$$
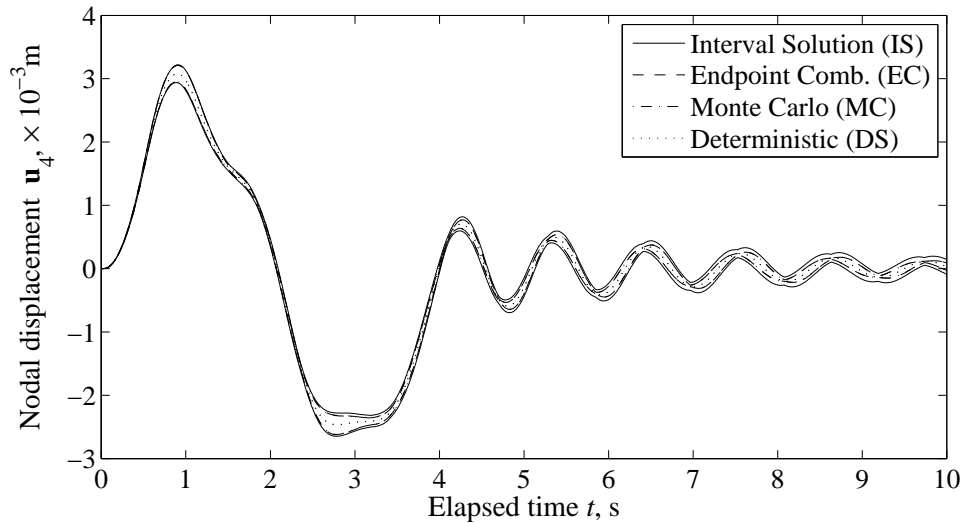
Figure 5.3: Lower and upper bounds of the nodal displacement $\mathbf{u}_4$ for the four-story frame of Figure 5.1 under a sinusoidal impact force: IS (solid lines) from the proposed method, NLP (dashed lines), and MC (dash-dotted lines) from an ensemble of 10,000 simulations. Material uncertainty is 1% for mass, and 5% for stiffness. Load uncertainty is 2% for the magnitude.

Figure 5.4 shows that the high frequency components dissipate quickly. After about 3 s, the response of the structure is dominated by the lowest frequency vibration. Observe that the performance of the proposed method is the same as in the previous case. The obtained interval solution guarantees to enclose the reference solution (endpoint combination, EC), and the overestimation level increases slightly as the time increases. Thus non-trivial initial conditions are handled successfully.
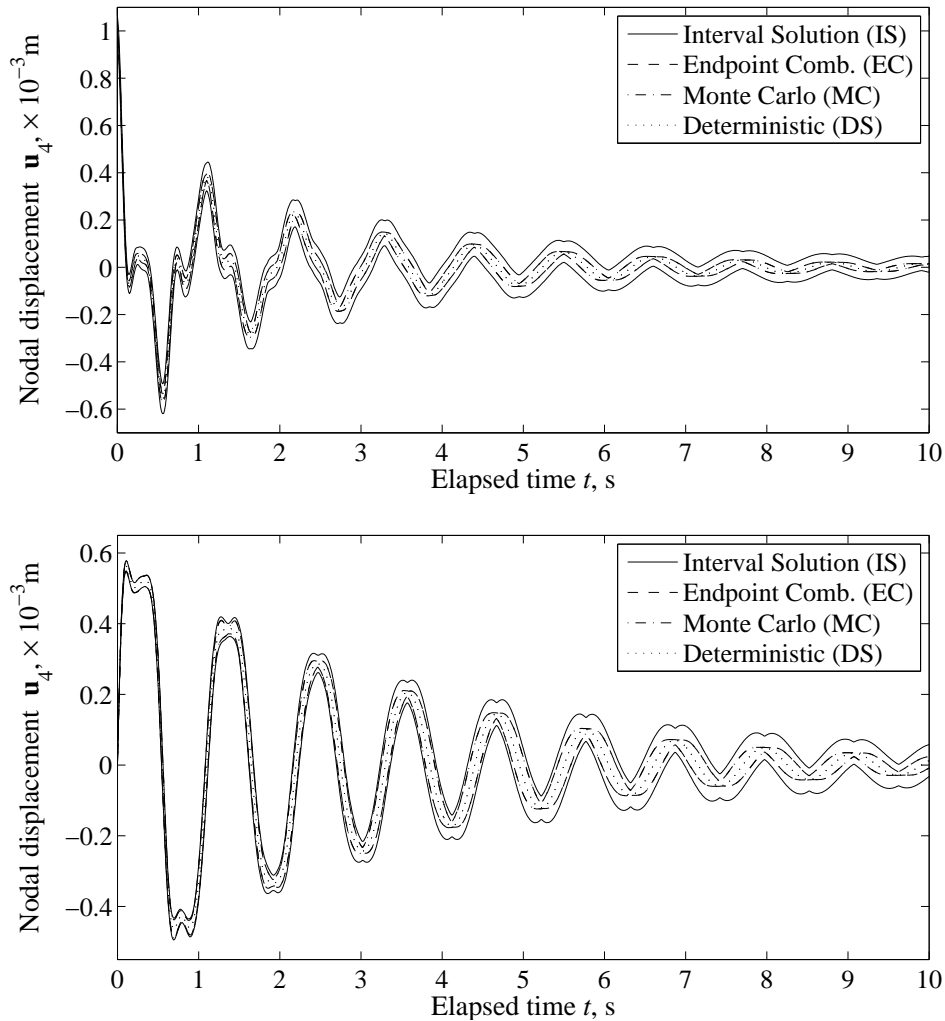
Figure 5.4: Lower and upper bounds of the nodal displacement $\mathbf{u}_4$ for the four-story frame of Figure 5.1 under non-trivial initial conditions: (top) non-trivial initial displacement $\mathbf{u}_0$, (bottom) non-trivial initial velocity $\mathbf{v}_0$. IS (solid lines) from the proposed method, EC (dashed lines), and MC (dash-dotted lines) from an ensemble of 10,000 simulations. Material uncertainty is 1% for mass, and 5% for stiffness. Uncertainty in the initial condition is 2%.
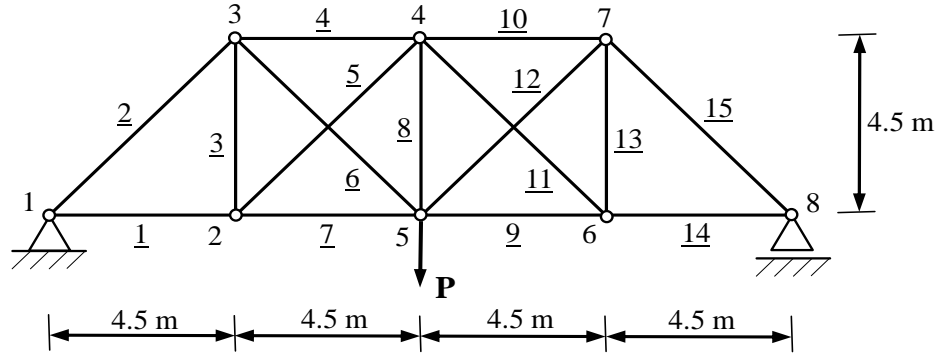
Figure 5.5: A simply supported symmetric truss subject to concentrated force.

5.3.2 Simply supported truss

The second example is a simply supported symmetric truss composed of 15 bars, as shown in Figure 5.5. The joints are labeled from 1 to 8, and the bars are labeled from $\underline{1}$ to $\underline{15}$. Time-varying concentrated load $\mathbf{P}$ acts at joint 5. Bars $\underline{1}$ to $\underline{3}$, $\underline{13}$ to $\underline{15}$ have the same cross section area $A = 1.0 \times 10^{-3}$ m^2, and all other bars, viz. bars $\underline{4}$ to $\underline{12}$, have smaller cross section area $A = 6.0 \times 10^{-4}$ m^2. All the bars are made of steel. They have the interval mass density $\boldsymbol{\rho}$ with midpoint value $\rho = 7.8 \times 10^3$ kg/m^3, and the interval Young's modulus $\mathbf{E}$ with midpoint value $E = 200$ GPa.

Fifteen bar elements are used to model the truss in Figure 5.5. Element mass density $\boldsymbol{\rho}$ and Young's modulus $\mathbf{E}$ are assumed independent, and they are modeled by 30 interval variables. The midpoint value of the concentrated load $\mathbf{P}$ is a sinusoid with a frequency of 50 Hz and an amplitude of 200 kN, viz.

$$P = 200 \sin(100\pi t) \text{ kN.} \tag{5.49}$$

The damping matrix $\mathbf{C} = 20\mathbf{M} + 3 \times 10^{-5}\mathbf{K}$. The sampling rate is 10 kHz, so the sampling interval $\Delta t = 1 \times 10^{-4}$ s.

Then vertical displacement $\mathbf{v}_5$ at joint 5 and axial strain $\boldsymbol{\varepsilon}_8$ in bar $\underline{8}$ are selected for comparison among the various methods mentioned previously. Consider 1% uncertainty for the magnitude and time-history of the load, as well as Young's modulus and

165

mass density of each bar. Figure 5.6 plots the lower and upper bounds of $\mathbf{v}_5$ and ε_8 for the first 0.1 s obtained from the proposed method (IS, solid lines) and the Monte Carlo predictions (MC, dashed lines from the Newmark-β approach, and dash-dotted lines from the DFT approach) from an ensemble of 100,000 simulations. Observe that the proposed method obtains guaranteed enclosures of the MC prediction for both the primary and derived quantities.
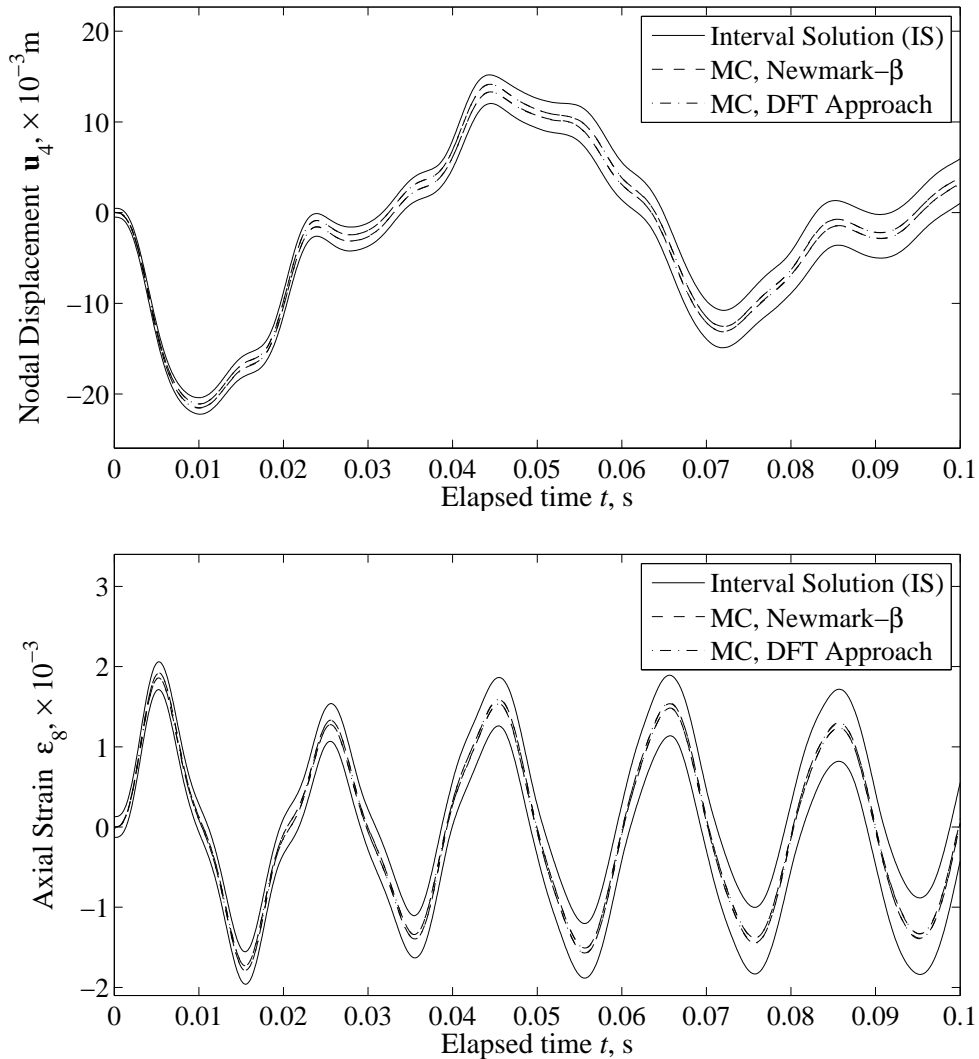
Figure 5.6: Lower and upper bounds of the nodal displacement $\mathbf{v}_5$ at joint 5 (top) and axial strain ε_8 in bar $\underline{8}$ (bottom) for the four-story frame of Figure 5.5 under external loads: IS (solid lines) from the proposed method and MC predictions (dashed lines and dash-dotted lines) from an ensemble of 100,000 simulations. Parameter uncertainties are 1% for load magnitude, load history, Young's modulus, and mass density.

To compares the impact of different types uncertainties, Figure 5.7 and Figure 5.8 respectively plot the vertical displacement $\mathbf{v}_5$ at joint 5 with 2% uncertainties in material and load. In Figure 5.7, 2% uncertainty is assigned to the Young's modulus (top subplot) and mass density (bottom subplot) of the structure, respectively. Observe that the uncertainties in the structural responses are almost identical. In addition, the uncertainties do not increase over time. In Figure 5.8, 2% uncertainty
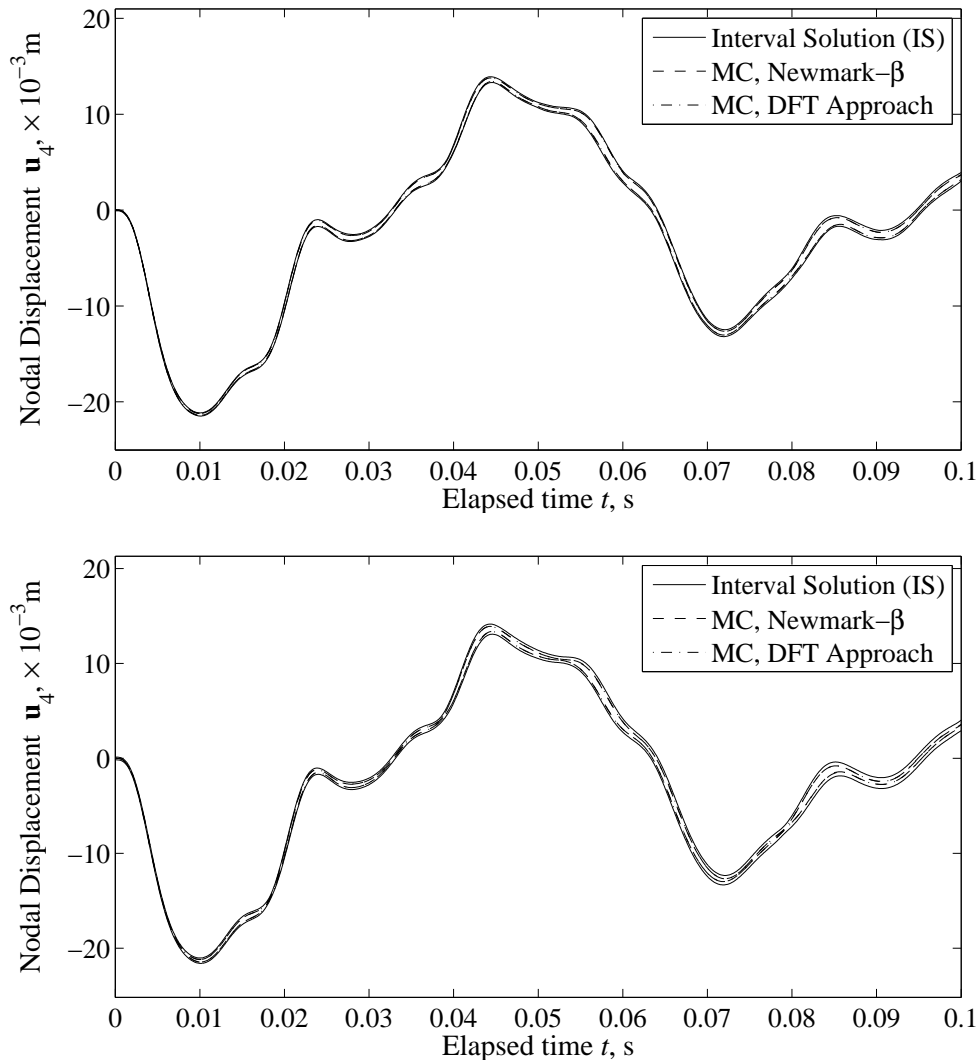
Figure 5.7: Lower and upper bounds of the nodal displacement $\mathbf{v}_5$ at joint 5 for the four-story frame of Figure 5.5 with only material uncertainties: (top) 2% uncertainty only in Young's modulus; (bottom) 2% uncertainty only in mass density. IS (solid lines) from the proposed method and MC predictions (dashed lines and dash-dotted lines) from an ensemble of 100,000 simulations.

is assigned to the load magnitude (top subplot) and load time-history (bottom subplot), respectively. Apparently, the uncertainties in the structural responses increase significantly when the load time-history uncertainty is considered.

This behavior is due to the fact that the load history uncertainties are modeled by independently varied intervals at different time steps. In the current example, this means 0.1 s × 10 kHz = 1,000 independent interval variables. As a result, the
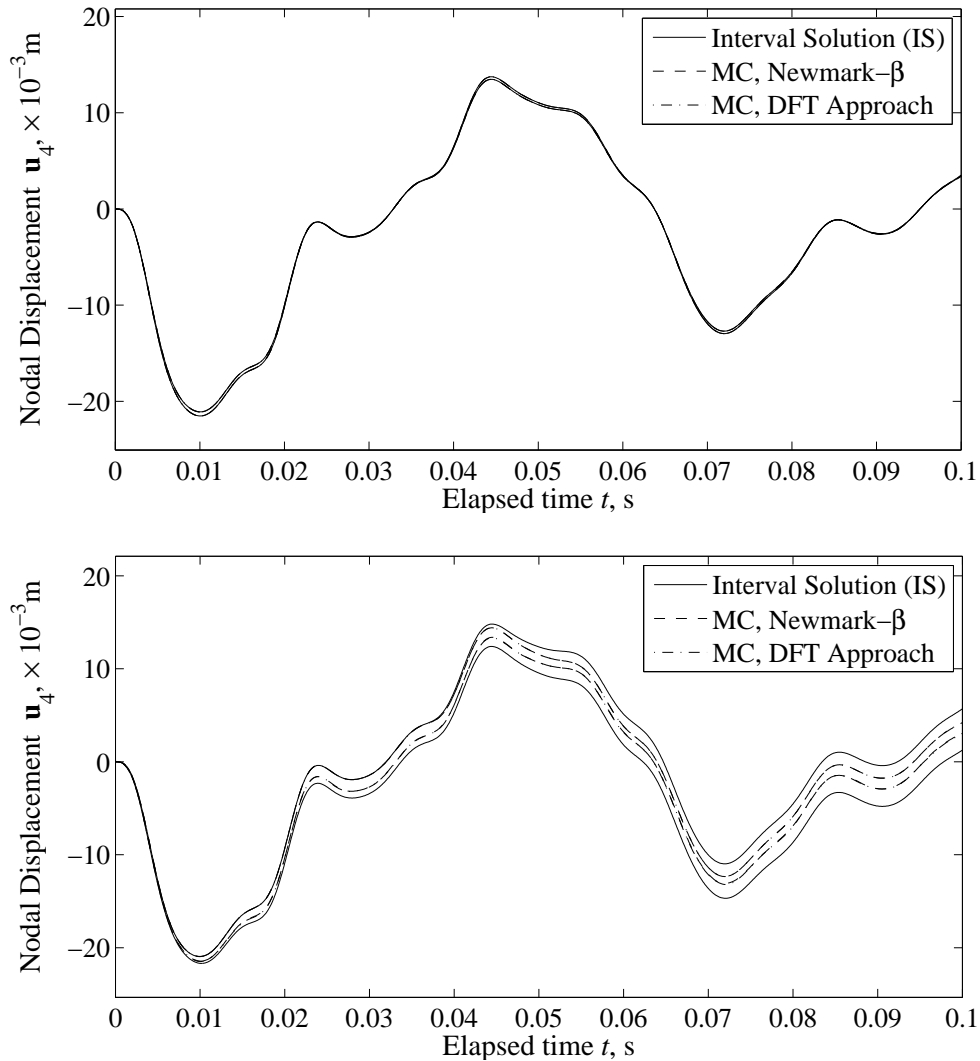
Figure 5.8: Lower and upper bounds of the nodal displacement $\mathbf{v}_5$ at joint 5 for the four-story frame of Figure 5.5 with load uncertainties: (top) 2% uncertainty only in load magnitude; (bottom) 2% uncertainty only in load history. IS (solid lines) from the proposed method and MC predictions (dashed lines and dash-dotted lines) from an ensemble of 100,000 simulations.

overall uncertainty level is much higher than 2%. This also explains the growing differences between IS and MC predictions over time. Figure 5.9 plots the vertical displacement $\mathbf{v}_5$ at joint 5 with 2% uncertainties in load magnitude, Young's modulus, and mass density. Observe that the uncertainties now do not increase over time, and the difference between IS and MC is much smaller than previous cases in Figure 5.8. So it is indeed the increased number of interval variables that caused the increased uncertainty and the difference between IS and MC.
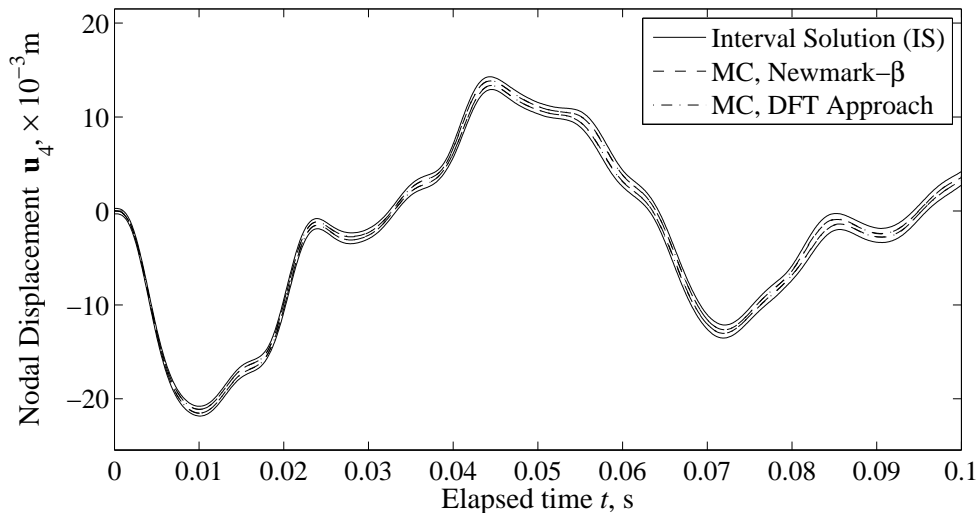
Figure 5.9: Lower and upper bounds of the nodal displacement $\mathbf{v}_5$ at joint 5 for the four-story frame of Figure 5.5 with load and material uncertainties: 2% uncertainties in load magnitude, Young's modulus, and mass density. IS (solid lines) from the proposed method and MC predictions (dashed lines and dash-dotted lines) from an ensemble of 100,000 simulations.

5.4   Summary

In this chapter, an interval finite element formulation is presented for the time-domain dynamic analysis of elastic structures with uncertain geometric and material properties. By using the Discrete Fourier Transform (DFT) and the Inverse Discrete Fourier Transform (IDFT), the given equivalent load and the final obtained structural responses are both given in the time domain, but the matrix inversion process

169

is performed in the frequency domain. Ground motion and non-trivial initial conditions are successfully handled via the introduction of the corresponding equivalent nodal forces. The resulting method is both efficient and widely applicable.

Uncertain parameters of the structure are modeled as intervals. The obtained interval enclosures guarantee to enclose the exact solution set, and the corresponding overestimation is small, even for large uncertainty levels. Numerical examples show that the presented method gives guaranteed sharp bounds on the dynamic responses of the structure, even in cases when a large number of interval variables are present and other available methods give over-optimistic prediction on the lower and upper bounds.

CHAPTER VI

INTERVAL PARAMETER IDENTIFICATION OF STRUCTURAL DYNAMIC PROBLEMS

In this chapter, the interval-based parameter identification algorithms are extended to structural dynamic problems with uncertainties in load, geometry, and material of the structure [55, 113, 152]. The proposed interval inverse solver models the uncertainties of the structure as intervals, and the formulation is based on the Interval Finite Element Method (IFEM). The goal is to predict the material properties of the structure (such as Young's modulus) based on measured structural responses in the frequency domain [14, 84, 129]. Other uncertain parameters, such as the corresponding external excitations, the mass and damping properties of the structure, are known in prior. In particular, the structure is governed by the following complex interval linear system

$$\left(\mathbf{K} + i\omega \mathbf{C} - \omega^2 \mathbf{M} \right) \mathbf{u} = \mathbf{f}, \tag{6.1}$$

where $i = \sqrt{-1}$ is the imaginary unit, ω is the given angular frequency (measured in rad/s), $\mathbf{K}$, $\mathbf{C}$, and $\mathbf{M}$ are respectively the interval stiffness, damping, and mass matrix for the system, $\mathbf{u}$ is the interval nodal displacement vector, and $\mathbf{f}$ is the interval nodal equivalent load. Measurement data includes acceleration and strain signals collected at prescribed locations of the structure, which are transformed into the frequency domain and brought into the following general matrix form,

$$\boldsymbol{\eta} = H\mathbf{u}, \tag{6.2}$$

where H is a deterministic matrix, and $\boldsymbol{\eta}$ is the measurement vector.

171

In the current study, the Rayleigh damping is adopted, and the damping matrix

$$\mathbf{C} = \alpha_d \mathbf{M} + \beta_d \mathbf{K}, \tag{6.3}$$

where α_d and β_d are the Rayleigh damping coefficients. To reduce overestimation due to interval dependency, the interval matrix decomposition is used, avoiding multiple occurrences of the same interval variables as much as possible. In particular, the stiffness matrix $\mathbf{K}$ and the mass matrix $\mathbf{M}$ are decomposed into

$$\mathbf{K} = A\mathrm{diag}(\Lambda\boldsymbol{\alpha})A^T; \tag{6.4}$$

$$\mathbf{M} = A_m\mathrm{diag}(\Lambda_m\boldsymbol{\alpha}_m)A_m^T,$$

where A, Λ, A_m, and Λ_m are deterministic matrices, $\boldsymbol{\alpha}$ is the unknown interval stiffness parameter vector that accounts for uncertainties in the stiffness matrix $\mathbf{K}$, and $\boldsymbol{\alpha}_m$ is the given interval mass parameter vector that accounts for uncertainties in the mass matrix $\mathbf{M}$. When the structure is subject to external loading, the nodal equivalent load vector $\mathbf{f}$ is decomposed into

$$\mathbf{f} = F\boldsymbol{\delta}, \tag{6.5}$$

where F is a deterministic matrix, and $\boldsymbol{\delta}$ is the load uncertainty vector. When the excitation is caused by ground motion, the nodal equivalent load

$$\mathbf{f} = -\mathbf{M}\mathbf{a} = -\mathbf{M}q\boldsymbol{\delta}, \tag{6.6}$$

where $\boldsymbol{\delta}$ denotes the ground acceleration at given frequency, $\mathbf{a}$ represents the nodal acceleration of the structure caused by the ground motion, and deterministic column vector q relates $\boldsymbol{\delta}$ to $\mathbf{a}$, viz. $\mathbf{a} = q\boldsymbol{\delta}$.

In the proposed method, the unknown parameters of the structure are solved by adjoint-based constrained optimization techniques. For convenience, all the complex variables are replaced by their respective real and imaginary parts. For instance, the

governing Eq. (6.1) is replaced by its realized form

$$\left(\mathbf{K}^C + \mathbf{M}^C\right)\mathbf{u}^C = \mathbf{f}^C, \tag{6.7}$$

where the superscripts ^{C} emphasize that these variables contains the real and imaginary parts of the corresponding complex variables. In particular, $\mathbf{u}^C$ and $\mathbf{f}^C$ contain their respective real and imaginary parts, viz.

$$\mathbf{u}^C = \left\{\begin{matrix} \mathbf{u}^R \\ \mathbf{u}^I \end{matrix}\right\}, \qquad \mathbf{f}^C = \left\{\begin{matrix} \mathbf{f}^R \\ \mathbf{f}^I \end{matrix}\right\}, \tag{6.8}$$

in which superscripts ^{R} and ^{I} denote the real and imaginary parts of complex variables, respectively. $\mathbf{K}^C$ is the part of the effective stiffness matrix that is directly related to the unknown stiffness parameter $\boldsymbol{\alpha}$, which can be decomposed into

$$\mathbf{K}^C = \left\{\begin{matrix} \mathbf{K} & -\beta_d\omega\mathbf{K} \\ \beta_d\omega\mathbf{K} & \mathbf{K} \end{matrix}\right\} = A^C\text{diag}(\Lambda^C\boldsymbol{\alpha})B^C, \tag{6.9}$$

where deterministic matrices A^C, Λ^C, and B^C are given by

$$A^C = \left\{\begin{matrix} A & 0 \\ 0 & A \end{matrix}\right\}, \qquad \Lambda^C = \left\{\begin{matrix} \Lambda \\ \Lambda \end{matrix}\right\}, \qquad B^C = \left\{\begin{matrix} A^T & -(\beta_d\omega)A^T \\ (\beta_d\omega)A^T & A^T \end{matrix}\right\}. \tag{6.10}$$

Note that $B^C \neq A^{CT}$, because $\mathbf{K}^C$ is not a symmetric matrix. Similarly, $\mathbf{M}^C$ is the part of the effective stiffness matrix that is directly related to the given mass parameter vector $\boldsymbol{\alpha}_m$, which can be decomposed into

$$\mathbf{M}^C = \left\{\begin{matrix} -\omega^2\mathbf{M} & -\alpha_d\omega\mathbf{M} \\ \alpha_d\omega\mathbf{M} & -\omega^2\mathbf{M} \end{matrix}\right\} = A_m^C\text{diag}(\Lambda_m^C\boldsymbol{\alpha}_m)B_m^C, \tag{6.11}$$

where the corresponding deterministic A_m^C, Λ_m^C, and B_m^C are given by

$$A_m^C = \left\{\begin{matrix} A_m & 0 \\ 0 & A_m \end{matrix}\right\}, \qquad \Lambda_m^C = \left\{\begin{matrix} \Lambda_m \\ \Lambda_m \end{matrix}\right\}, \qquad B_m^C = \left\{\begin{matrix} -\omega^2 A_m^T & -(\alpha_d\omega)A_m^T \\ (\alpha_d\omega)A_m^T & -\omega^2 A_m^T \end{matrix}\right\}. \tag{6.12}$$

173

Note that $B_m^C \neq A_m^{CT}$ as well. When the structure is subject to external loading, $\mathbf{f}^C$ is decomposed into the following matrix form,

$$\mathbf{f}^C = \begin{Bmatrix} F\boldsymbol{\delta}^R \\ F\boldsymbol{\delta}^I \end{Bmatrix} = \begin{Bmatrix} F & 0 \\ 0 & F \end{Bmatrix} \begin{Bmatrix} \boldsymbol{\delta}^R \\ \boldsymbol{\delta}^I \end{Bmatrix} = F^C \boldsymbol{\delta}^C, \tag{6.13}$$

where $\boldsymbol{\delta}^R$ and $\boldsymbol{\delta}^I$ are the uncertainties in the real and imaginary parts of the load, respectively. When the excitation is caused by ground motion, $\mathbf{f}^C$ is decomposed into

$$\mathbf{f}^C = \begin{Bmatrix} -\mathbf{M}q\boldsymbol{\delta}^R \\ -\mathbf{M}q\boldsymbol{\delta}^I \end{Bmatrix} = \begin{Bmatrix} -\mathbf{M}q & 0 \\ 0 & -\mathbf{M}q \end{Bmatrix} \begin{Bmatrix} \boldsymbol{\delta}^R \\ \boldsymbol{\delta}^I \end{Bmatrix} \tag{6.14}$$

$$= A_m^C \mathrm{diag}(\Lambda_m^C \boldsymbol{\alpha}_m) B_f^C \boldsymbol{\delta}^C,$$

where A_m^C and Λ_m^C are the same as in Eq. (6.12), and B_f^C is given by

$$B_f^C = \begin{Bmatrix} -A_m^T q & 0 \\ 0 & -A_m^T q \end{Bmatrix}. \tag{6.15}$$

The corresponding measurement Eq. (6.2) is replaced by

$$\boldsymbol{\eta}^C = H^C \mathbf{u}^C, \tag{6.16}$$

where $\boldsymbol{\eta}^C$ and H^C are given by

$$\boldsymbol{\eta}^C = \begin{Bmatrix} \boldsymbol{\eta}^R \\ \boldsymbol{\eta}^I \end{Bmatrix}, \qquad H^C = \begin{Bmatrix} H & 0 \\ 0 & H \end{Bmatrix}. \tag{6.17}$$

In the above discussion, the measurements are assumed to be the real and imaginary parts (Cartesian form) of the structural responses in the frequency domain. However, such complete information is not always available. For instance, when only the magnitude information is available, the measurement vector

$$\boldsymbol{\eta}_\rho = |H\mathbf{u}| = \sqrt{(H\mathbf{u}^R)^2 + (H\mathbf{u}^I)^2}, \tag{6.18}$$

where $|\ |$ denotes the norm of a complex variable. When only the phase information is available, the measurement vector contains the phase angles, viz.

$$\boldsymbol{\eta}_\varphi = \arg(H\mathbf{u}) = \mathrm{atan2}\left(H\mathbf{u}^I, H\mathbf{u}^R\right). \tag{6.19}$$

where arg( ) is the argument of a complex variable, and atan2( ) is the arctangent function with two arguments.

In the following sections, the proposed interval inverse solver for structural dynamic problems is presented in detail. The solver is based on the adjoint optimization, and contains a deterministic stage and an interval stage. The structural excitation can be external loads or ground motion. The measurement data contains the real and imaginary parts (Cartesian form) of the frequency response, or the magnitudes and the phase angles (polar form), which can be obtained via the Discrete Fourier Transform (DFT) of the original measurement data in the time domain. In both cases, the measurements are modeled by intervals. The goal is to provide a reliable prediction of the stiffness of the structure, which guarantees to enclose the exact solution. Several numerical examples validate the performance of the proposed method.

6.1   *Deterministic Inverse Solver*

In the deterministic stage of the proposed inverse solver, a deterministic solution of the unknown stiffness parameter vector α is sought, using the midpoint values for all the given interval variables in the system, such as the load uncertainty vector $\boldsymbol{\delta}$, the mass parameter vector $\boldsymbol{\alpha}_m$, and the measurement vector $\boldsymbol{\eta}$. The algorithm is derived using the adjoint-based constrained optimization, and conjugate gradient or Newton-Raphson type methods are exploited to find the optimal estimate of the unknown parameters. In the first subsection, the measurement data contains both the real and imaginary parts of the frequency response. Then in the second subsection, the solver is extended to cases when only the magnitudes or phase angles are measured.

6.1.1   Adjoint-based constrained optimization

The proposed inverse solver aims at minimizing the differences between the predicted structural response and the midpoint measurement vector, under the equilibrium

constraint. The objective functional to be minimized is given by

$$\Gamma = \frac{1}{2}(H^C u^C - \eta^C)^T W^C (H^C u^C - \eta^C) \tag{6.20}$$
$$+ w^{CT}(K_{\text{eff}}^C u^C - f^C) + \frac{1}{2}\alpha^T(\gamma R)\alpha,$$

where $H^C u^C$ is the predicted structural response, η^C is the midpoint of the measurement vector $\boldsymbol{\eta}^C$, viz. $\eta^C = \text{mid}\,\boldsymbol{\eta}^C$, W^C is a diagonal matrix containing the measurement weights, w^C is the Lagrangian multiplier introduced to enforce the equilibrium condition $K_{\text{eff}}^C u^C = f^C$, $K_{\text{eff}}^C = K^C + M^C$ is the effective stiffness matrix of the structure, γ and R are the regularization weight and regularization matrix, respectively.

From the decomposition of K^C in Eq. (6.9), the first variation of Γ

$$\delta\Gamma = \delta u^{CT} H^{CT} W^C (H^C u^C - \eta^C) + \delta w^{CT}(K_{\text{eff}}^C u^C - f^C) \tag{6.21}$$
$$+ \delta u^{CT} K_{\text{eff}}^{CT} w^C + w^{CT}\delta K^C u^C + \delta\alpha^T(\gamma R)\alpha,$$

leads to the following optimization conditions:

$$\begin{cases} K_{\text{eff}}^C u^C - f^C = 0; \\ K_{\text{eff}}^{CT} w^C - H^{CT} W^C (\eta^C - H^C u^C) = 0; \\ \Lambda^{CT}(A^{CT} w^C \circ B^C u^C) + (\gamma R)\alpha = 0, \end{cases} \tag{6.22}$$

where $a \circ b$ denotes the element-by-element (Hadamard) product of two vectors a and b. To obtain Eq. (6.22) from Eq. (6.21), the following identity

$$w^T A^C \text{diag}(\Lambda^C \delta\alpha) B^C u = \delta\alpha^T \Lambda^{CT}(B^C u \circ A^{CT} w) \tag{6.23}$$

have been exploited. The three equations in Eq. (6.22) can be interpreted as: *i)* equilibrium condition of the original system with equivalent load f^C, *ii)* equilibrium condition for the adjoint system with equivalent load $H^{CT} W^C (\eta^C - H^C u^C)$, and *iii)* optimal condition that the gradient g of Γ with respect to α is zero.

In the conjugate gradient approach, the gradient of the objective functional is computed as follows. The equilibrium conditions for the original and adjoint systems

176

are recast into a block matrix form

$$
\left\{ \begin{matrix} W_\eta^C & K_{\text{eff}}^{CT} \\ K_{\text{eff}}^C & 0 \end{matrix} \right\} \left\{ \begin{matrix} u^C \\ w^C \end{matrix} \right\} = \left\{ \begin{matrix} P_\eta^C \eta^C \\ f^C \end{matrix} \right\}, \tag{6.24}
$$

where $W_\eta^C = H^{CT} W^C H^C$ and $P_\eta^C = H^{CT} W^C$. Then the solution vectors u^C and w^C follow as

$$
\left\{ \begin{matrix} u^C \\ w^C \end{matrix} \right\} = \left\{ \begin{matrix} 0 & K_{\text{eff}}^{-C} \\ K_{\text{eff}}^{-CT} & T_w^C \end{matrix} \right\} \left\{ \begin{matrix} P_\eta^C \eta^C \\ f^C \end{matrix} \right\}, \tag{6.25}
$$

where $T_w^C = -K_{\text{eff}}^{-CT} W_\eta^C K_{\text{eff}}^{-C}$. Then the corresponding objective functional and its gradient are expressed in terms of u^C, w^C and α as

$$
\Gamma = \frac{1}{2}(H^C u^C - \eta^C)^T W^C (H^C u^C - \eta^C) + \frac{1}{2}\alpha^T (\gamma R)\alpha; \tag{6.26}
$$

$$
g = \frac{\partial \Gamma}{\partial \alpha} = \Lambda^{CT} \left(A^{CT} w^C \circ B^C u^C \right) + (\gamma R)\alpha.
$$

Then the conjugate gradient method can be implemented, using the same descending direction updating strategy, inexact line search method, and stopping criteria as discussed before.

When the Newton-Raphson approach is adopted, the linearization of the governing Eq. (6.22) leads to

$$
\left\{ \begin{matrix} W_\eta^C & K_{\text{eff}}^{CT} & T^B \langle A^{CT} w^C \rangle^T \\ K_{\text{eff}}^C & 0 & T^A \langle B^C u^C \rangle^T \\ T^B \langle A^{CT} w^C \rangle & T^A \langle B^C u^C \rangle & \gamma R \end{matrix} \right\} \left\{ \begin{matrix} \Delta u^C \\ \Delta w^C \\ \Delta \alpha \end{matrix} \right\} = \left\{ \begin{matrix} 0 \\ 0 \\ -g \end{matrix} \right\}, \tag{6.27}
$$

where $T^A \langle x \rangle$ and $T^B \langle x \rangle$ maps a vector x into the following matrices

$$
T^A \langle x \rangle = \Lambda^{CT} \text{diag}(x) A^{CT}; \tag{6.28}
$$

$$
T^B \langle x \rangle = \Lambda^{CT} \text{diag}(x) B^C,
$$

respectively. When one is only interested in the update of the stiffness parameter $\Delta \alpha$, by defining the following block matrices

$$
K_b = \left\{ \begin{matrix} W_\eta^C & K_{\text{eff}}^{CT} \\ K_{\text{eff}}^C & 0 \end{matrix} \right\}, \qquad T_b = \left\{ T^B \langle A^{CT} w^C \rangle \quad T^A \langle B^C u^C \rangle \right\}, \tag{6.29}
$$

the inverse of the generalized stiffness matrix in Eq. (6.27) is given by

$$
\begin{Bmatrix} K_b & T_b^T \\ T_b & \gamma R \end{Bmatrix}^{-1} = \begin{Bmatrix} K_b^{-1} + K_b^{-1}T_b^T G_\alpha T_b K_b^{-1} & -K_b^{-1}T_b^T G_\alpha \\ -G_\alpha T_b K_b^{-1} & G_\alpha \end{Bmatrix},
\tag{6.30}
$$

where $G_\alpha = \left(\gamma R - T_b K_b^{-1} T_b^T\right)^{-1}$. Then the update $\Delta\alpha$ is obtained from

$$
\Delta\alpha = -G_\alpha g.
\tag{6.31}
$$

Then the same inexact line search method and stopping criteria, combined with conjugate gradient method, can be implemented in the algorithm.

The structure can be excited by either external forces or ground motion, and appropriate decomposition form the equivalent load $\mathbf{f}^C$ should be chosen accordingly.

6.1.2 Measuring the magnitude and phase

When the measurement data contains only the magnitude information, the corresponding objective functional Ω to be minimized is given by

$$
\begin{aligned}
\Gamma = &\frac{1}{2} \left(|Hu| - \eta_\rho\right)^T W \left(|Hu| - \eta_\rho\right) \\
&+ w^{CT}\left(K_{\text{eff}}^C u^C - f^C\right) + \frac{1}{2}\alpha^T(\gamma R)\alpha,
\end{aligned}
\tag{6.32}
$$

where η_ρ is the midpoint of the measurement vector $\boldsymbol{\eta}_\rho^C$, viz. $\eta_\rho^C = \text{mid } \boldsymbol{\eta}_\rho^C$. By noting the equality

$$
\begin{aligned}
\delta\left(|Hu|\right) &= \frac{Hu^R}{|Hu|} \circ \left(H\delta u^R\right) + \frac{Hu^I}{|Hu|} \circ \left(H\delta u^I\right) \\
&= \left\{\text{diag}\left(\frac{Hu^R}{|Hu|}\right) \quad \text{diag}\left(\frac{Hu^I}{|Hu|}\right)\right\} H^C \delta u^C,
\end{aligned}
\tag{6.33}
$$

the governing equations for the system are obtained as

$$
\begin{cases}
K_{\text{eff}}^C u^C - f^C = 0; \\
K_{\text{eff}}^{CT} w^C - \left(P_{\eta\rho}^C \eta_\rho - H^{CT} W^C H^C u^C\right) = 0; \\
\Lambda^{CT}\left(A^{CT} w^C \circ B^C u^C\right) + (\gamma R)\alpha = 0,
\end{cases}
\tag{6.34}
$$

where the deterministic matrix $P_{\eta\rho}^C$ is defined as

$$P_{\eta\rho}^C = H^{CT}W^C \left\{ \begin{array}{c} \text{diag}\left(Hu^R/|Hu|\right) \\ \text{diag}\left(Hu^I/|Hu|\right) \end{array} \right\}. \tag{6.35}$$

Note that the only difference between Eqs. (6.22) and (6.34) is the equivalent load term for the adjoint system: $H^{CT}W^C\left(\eta^C - H^C u^C\right)$ in Eq. (6.22) is replaced by $\left(P_{\eta\rho}^C\eta_\rho - H^{CT}W^C H^C u^C\right)$ in Eq. (6.34). Thus the rest of the derivation is exactly the same as before. The only modifications are replacing P_η^C in Eqs. (6.24) and (6.25) by $P_{\eta\rho}^C$ in Eq. (6.35), and replacing W_η^C in Eq. (6.27) by

$$W_{\eta\rho}^C = H^{CT}W^C \left\{ \begin{array}{cc} D_{\eta\rho}^{11} & D_{\eta\rho}^{12} \\ D_{\eta\rho}^{12} & D_{\eta\rho}^{22} \end{array} \right\} H^C. \tag{6.36}$$

where $D_{\eta\rho}^{11}$, $D_{\eta\rho}^{12}$, and $D_{\eta\rho}^{22}$ are diagonal matrices given by

$$D_{\eta\rho}^{11} = \text{diag}\left\{ 1 - \frac{\eta_\rho}{|Hu|} \circ \frac{(Hu^I)^2}{|Hu|^2} \right\};$$

$$D_{\eta\rho}^{12} = \text{diag}\left(\frac{\eta_\rho}{|Hu|} \circ \frac{Hu^R}{|Hu|} \circ \frac{Hu^I}{|Hu|} \right); \tag{6.37}$$

$$D_{\eta\rho}^{22} = \text{diag}\left\{ 1 - \frac{\eta_\rho}{|Hu|} \circ \frac{(Hu^R)^2}{|Hu|^2} \right\}.$$

Alternatively, when the measurement data contains only the phase angles,

$$\Gamma = \frac{1}{2}\left(\arg\left(Hu\right) - \eta_\varphi \right)^T W\left(\arg\left(Hu\right) - \eta_\varphi \right) \tag{6.38}$$
$$+ w^{CT}\left(K_{\text{eff}}^C u^C - f^C \right) + \frac{1}{2}\alpha^T(\gamma R)\alpha.$$

where η_φ is the midpoint of the measurement vector $\boldsymbol{\eta}_\varphi^C$, viz. $\eta_\varphi^C = \text{mid}\,\boldsymbol{\eta}_\varphi^C$. By noting the equality

$$\delta \arg\left(Hu\right) = -\frac{Hu^I}{|Hu|^2} \circ \left(H\delta u^R\right) + \frac{Hu^R}{|Hu|^2} \circ \left(H\delta u^I\right) \tag{6.39}$$
$$= \left\{ -\text{diag}\left(\frac{Hu^I}{|Hu|^2} \right) \quad \text{diag}\left(\frac{Hu^R}{|Hu|^2} \right) \right\} H^C \delta u^C,$$

the governing equations for the system are obtained as

$$
\begin{cases}
K_{\text{eff}}^C u^C - f^C = 0; \\
K_{\text{eff}}^{CT} w^C - P_{\eta\varphi}^C\big(\eta_\rho - \arg(H^C u^C)\big) = 0; \\
\Lambda^{CT}\big(A^{CT} w^C \circ B^C u^C\big) + (\gamma R)\alpha = 0,
\end{cases}
\tag{6.40}
$$

where the deterministic matrix $P_{\eta\varphi}^C$ is defined as

$$
P_{\eta\varphi}^C = H^{CT} W^C
\begin{Bmatrix}
-\operatorname{diag}\big(Hu^I/|Hu|^2\big) \\
\operatorname{diag}\big(Hu^R/|Hu|^2\big)
\end{Bmatrix}.
\tag{6.41}
$$

The subsequent derivation is the same as before. One only needs to replace P_η^C in Eqs. (6.24) and (6.25) by $P_{\eta\varphi}^C$ in Eq. (6.41), and W_η^C in Eq. (6.27) by

$$
W_{\eta\varphi}^C = H^{CT} W^C
\begin{Bmatrix}
D_{\eta\varphi}^{11} & D_{\eta\varphi}^{12} \\
D_{\eta\varphi}^{12} & D_{\eta\varphi}^{22}
\end{Bmatrix} H^C,
\tag{6.42}
$$

where $D_{\eta\varphi}^{11}$, $D_{\eta\varphi}^{12}$, and $D_{\eta\varphi}^{22}$ are diagonal matrices given by

$$
D_{\eta\varphi}^{11} = \operatorname{diag}\left\{2\Big(\eta_\varphi - \arg(Hu)\Big)\circ\frac{Hu^R}{|Hu|}\circ\frac{Hu^I}{|Hu|} + \frac{(Hu^I)^2}{|Hu|^2}\right\};
$$

$$
D_{\eta\varphi}^{12} = \operatorname{diag}\left\{\Big(\eta_\varphi - \arg(Hu)\Big)\circ\left(\frac{(Hu^I)^2}{|Hu|^2} - \frac{(Hu^R)^2}{|Hu|^2}\right) - \frac{Hu^R}{|Hu|}\circ\frac{Hu^I}{|Hu|}\right\};
\tag{6.43}
$$

$$
D_{\eta\varphi}^{22} = \operatorname{diag}\left\{2\Big(\eta_\varphi - \arg(Hu)\Big)\circ\frac{Hu^R}{|Hu|}\circ\frac{Hu^I}{|Hu|} + \frac{(Hu^R)^2}{|Hu|^2}\right\}.
$$

Then either the conjugate gradient method or the Newton-Raphson method can be implemented to solve the governing Eqs. (6.34) and (6.40). The yielded result is the optimal prediction of the system properties that minimize the difference between the measured and predicted responses of the structure.

6.2   Interval Inverse Solver

The deterministic solution u_0^C, w_0^C, and α_0 obtained from the deterministic solver outlined in the previous section now serves as the reference solution in the interval stage. The corresponding interval governing equations are transformed into a fixed-point form, and a guaranteed interval enclosure of the unknown stiffness parameter

vector $\boldsymbol{\alpha}$ is obtained by using the iterative enclosure method. The proposed method is also extended to account for magnitude and phase angle measurements.

6.2.1 Iterative enclosure method

When the structure response is caused by external loads, the interval extension of Eq. (6.22) yields

$$
\begin{cases}
\mathbf{K}_{\text{eff}}^C \mathbf{u}^C - F^C \boldsymbol{\delta}^C = 0; \\
\mathbf{K}_{\text{eff}}^{CT} \mathbf{w}^C - H^{CT} W^C \left(\boldsymbol{\eta}^C - H^C \mathbf{u}^C \right) = 0; \\
\Lambda^{CT} (A^{CT} \mathbf{w}^C \circ B^C \mathbf{u}^C) + (\gamma R)\boldsymbol{\alpha} = 0,
\end{cases}
\tag{6.44}
$$

where $\mathbf{K}_{\text{eff}}^C = \mathbf{K}^C + \mathbf{M}^C$, and $\boldsymbol{\eta}^C$ includes both the real and imaginary parts of the measured response. Note that the decomposition $\mathbf{f}^C = F^C \boldsymbol{\delta}^C$ has been used above.

To transform Eq. (6.44) into a fixed-point form, let δ_0^C, η_0^C, and α_{m0} be the midpoint values of $\boldsymbol{\delta}^C$, $\boldsymbol{\eta}^C$, and $\boldsymbol{\alpha}_m$, respectively. Now, introduce the auxiliary variables

$$
\begin{aligned}
\Delta\boldsymbol{\delta}^C = \boldsymbol{\delta}^C - \delta_0^C, \quad \Delta\boldsymbol{\eta}^C = \boldsymbol{\eta}^C - \eta_0^C, \quad \Delta\boldsymbol{\alpha}_m = \boldsymbol{\alpha}_m - \alpha_{m0}; \\
\Delta\mathbf{u}^C = \mathbf{u}^C - u_0^C, \quad \Delta\mathbf{w}^C = \mathbf{w}^C - w_0^C, \quad \Delta\boldsymbol{\alpha} = \boldsymbol{\alpha} - \alpha_0
\end{aligned}
\tag{6.45}
$$

to denote the difference between the interval vectors and their respective deterministic reference vectors. Then the following equalities hold

$$
\begin{aligned}
\mathbf{K}^C \mathbf{x} &= K_0^C x_0 + K_0^C \Delta\mathbf{x} + \Delta\mathbf{K}^C x_0 + \Delta\mathbf{K}^C \Delta\mathbf{x}; \\
\mathbf{M}^C \mathbf{x} &= M_0^C x_0 + M_0^C \Delta\mathbf{x} + \Delta\mathbf{M}^C x_0 + \Delta\mathbf{M}^C \Delta\mathbf{x}; \\
A^{CT} \mathbf{w}^C \circ B^C \mathbf{u}^C &= A^{CT} w_0^C \circ B^C u_0^C + A^{CT} w_0^C \circ B^C \Delta\mathbf{u}^C \\
&\quad + A^{CT} \Delta\mathbf{w}^C \circ B^C u_0^C + A^{CT} \Delta\mathbf{w}^C \circ B^C \Delta\mathbf{u}^C,
\end{aligned}
\tag{6.46}
$$

where $\mathbf{x}$ can be either $\mathbf{u}^C$ or $\mathbf{w}^C$. Eq. (6.44) is equivalent to

$$
\begin{cases}
\begin{bmatrix}
W_\eta^C & K_{\text{eff}0}^{CT} & T^B \langle A^{CT} w_0^C \rangle^T \\
K_{\text{eff}0}^C & 0 & T^A \langle B^C u_0^C \rangle^T \\
T^B \langle A^{CT} w_0^C \rangle & T^A \langle B^C u_0^C \rangle & \gamma R
\end{bmatrix}
\begin{Bmatrix}
\Delta\mathbf{u}^C \\
\Delta\mathbf{w}^C \\
\Delta\boldsymbol{\alpha}
\end{Bmatrix}
\end{cases}
$$

$$= \left\{ \begin{array}{ccc} 0 & P_\eta^C & -T_m^B \langle A_m^{CT} \mathbf{w}^C \rangle^T \\ F^C & 0 & -T_m^A \langle B_m^C \mathbf{u}^C \rangle^T \\ 0 & 0 & 0 \end{array} \right\} \left\{ \begin{array}{c} \Delta \boldsymbol{\delta}^C \\ \Delta \boldsymbol{\eta}^C \\ \Delta \boldsymbol{\alpha}_m \end{array} \right\} \tag{6.47}$$

$$- \left\{ \begin{array}{ccc} B^{CT} & 0 & 0 \\ 0 & A^C & 0 \\ 0 & 0 & \Lambda^{CT} \end{array} \right\} \left\{ \begin{array}{c} A^{CT} \Delta \mathbf{w}^C \circ \Lambda^C \Delta \boldsymbol{\alpha} \\ B^C \Delta \mathbf{u}^C \circ \Lambda^C \Delta \boldsymbol{\alpha} \\ B^C \Delta \mathbf{u}^C \circ A^{CT} \Delta \mathbf{w}^C \end{array} \right\},$$

by repeatedly using Eq. (6.46) and the following identities

$$\Delta \mathbf{K}^C \mathbf{x} = A^C \mathrm{diag}(\Lambda^C \Delta \boldsymbol{\alpha}) B^C \mathbf{x} = A^C \mathrm{diag}(B^C \mathbf{x}) \Lambda^C \Delta \boldsymbol{\alpha};$$

$$\Delta \mathbf{M}^C \mathbf{x} = A_m^C \mathrm{diag}(\Lambda_m^C \Delta \boldsymbol{\alpha}_m) B_m^C \mathbf{x} = A_m^C \mathrm{diag}(B_m^C \mathbf{x}) \Lambda_m^C \Delta \boldsymbol{\alpha}_m; \tag{6.48}$$

$$\mathbf{x} \circ \mathbf{y} = \mathrm{diag}(\mathbf{x}) \mathbf{y} = \mathrm{diag}(\mathbf{y}) \mathbf{x},$$

where $W_\eta^C = H^{CT} W^C H^C$, $P_\eta^C = H^{CT} W^C$, $K_{\mathrm{eff}\,0}^C$ denotes the effective stiffness matrix parameterized by α_0 and α_{m0}, $T^A \langle x \rangle$ and $T^B \langle x \rangle$ are defined earlier in Eq. (6.28), $T_m^A \langle x \rangle$ and $T_m^B \langle x \rangle$ are given by

$$T_m^A \langle x \rangle = \Lambda_m^{CT} \mathrm{diag}(x) A_m^{CT}; \tag{6.49}$$

$$T_m^B \langle x \rangle = \Lambda_m^{CT} \mathrm{diag}(x) B_m^C.$$

To further separate the deterministic and interval terms, the following interval matrix in Eq. (6.47) can be decomposed into

$$\mathbf{F}_g = \left\{ \begin{array}{ccc} 0 & P_\eta^C & -T_m^B \langle A_m^{CT} \mathbf{w}^C \rangle^T \\ F^C & 0 & -T_m^A \langle B_m^C \mathbf{u}^C \rangle^T \\ 0 & 0 & 0 \end{array} \right\} = F_{g0} + A_g^F \mathrm{diag}\left(\mathbf{v}_g^F\right) B_g^F, \tag{6.50}$$

where

$$F_{g0} = \left\{ \begin{array}{ccc} 0 & H^{CT} W^C & 0 \\ F_0^C & 0 & 0 \\ 0 & 0 & 0 \end{array} \right\}, \qquad A_g^F = \left\{ \begin{array}{ccc} 0 & -B_m^{CT} \\ -A_m^C & 0 \\ 0 & 0 \end{array} \right\};$$

$$\mathbf{v}_g^F = \left\{ \begin{array}{c} B_m^C \mathbf{u}^C \\ A_m^{CT} \mathbf{w}^C \end{array} \right\}, \qquad B_g^F = \left\{ \begin{array}{ccc} 0 & 0 & \Lambda_m^C \\ 0 & 0 & \Lambda_m^C \end{array} \right\}. \tag{6.51}$$

Thus the governing Eq. (6.47) can be recast into the following compact form

$$K_g \Delta \mathbf{u}_g = \left\{ F_{g0} + A_g^F \text{diag}\left(\mathbf{v}_g^F\right) B_g^F \right\} \Delta \boldsymbol{\delta}_g - A_g \boldsymbol{\Theta}(B_g \Delta \mathbf{u}_g), \qquad (6.52)$$

where K_g, A_g, F_{g0}, A_g^F, and B_g^F are known deterministic matrices, and $\Delta \mathbf{u}_g$ depends upon the unknown interval vectors $\Delta \mathbf{u}^C$, $\Delta \mathbf{w}^C$, and $\Delta \boldsymbol{\alpha}$. Further, $\Delta \boldsymbol{\delta}_g$ depends upon the known interval vectors $\Delta \boldsymbol{\delta}^C$, $\Delta \boldsymbol{\eta}^C$, and $\Delta \boldsymbol{\alpha}_m$. $\mathbf{v}_g^F$ is composed of the interval vectors $B_m^C \mathbf{u}^C$, and $A_m^{CT} \mathbf{w}^C$. $B_g \Delta \mathbf{u}_g$ is composed of the secondary unknown vectors $B^C \Delta \mathbf{u}^C$, $A^{CT} \Delta \mathbf{w}^C$, and $\Lambda^C \Delta \boldsymbol{\alpha}$. The function $\boldsymbol{\Theta}(B_g \Delta \mathbf{u}_g)$ in Eq. (6.52) maps $B_g \Delta \mathbf{u}_g$ into the following interval vector

$$\boldsymbol{\Theta}(B_g \Delta \mathbf{u}_g) = \boldsymbol{\Theta} \left(\left\{ \begin{array}{c} B^C \Delta \mathbf{u}^C \\ A^{CT} \Delta \mathbf{w}^C \\ \Lambda^C \Delta \boldsymbol{\alpha} \end{array} \right\} \right) = \left\{ \begin{array}{c} A^{CT} \Delta \mathbf{w}^C \circ \Lambda^C \Delta \boldsymbol{\alpha} \\ B^C \Delta \mathbf{u}^C \circ \Lambda^C \Delta \boldsymbol{\alpha} \\ B^C \Delta \mathbf{u}^C \circ A^{CT} \Delta \mathbf{w}^C \end{array} \right\}. \qquad (6.53)$$

Eq. (6.52) emphasizes the direct relationship between uncertainties of the given data $\Delta \boldsymbol{\delta}^C$, $\Delta \boldsymbol{\eta}^C$, $\Delta \boldsymbol{\alpha}_m$ (collectively denoted by $\Delta \boldsymbol{\delta}_g$) and those of the unknown vectors $\Delta \mathbf{u}^C$, $\Delta \mathbf{w}^C$, $\Delta \boldsymbol{\alpha}$ (collectively denoted by $\Delta \mathbf{u}_g$).

By introducing $G = K_g^{-1}$, Eq. (6.52) is equivalent to

$$\Delta \mathbf{u}_g = \left\{ (GF_{g0}) + (GA_g^F)\text{diag}(\mathbf{v}_g^F)B_g^F \right\} \Delta \boldsymbol{\delta}_g - (GA_g)\boldsymbol{\Theta}(B_g \Delta \mathbf{u}_g). \qquad (6.54)$$

Then iterative enclosure method can be implemented to obtain a guaranteed outer enclosure for the exact solution $\mathbf{u}_g$ (see Section 3.2.2 for reference). To avoid unnecessary overestimation during the computation, instead of directly iterating on $\Delta \mathbf{u}_g$, the following auxiliary variable is introduced

$$\mathbf{v}_g = \left\{ \left(B_m^C \Delta \mathbf{u}^C\right)^T \left(A_m^{CT} \Delta \mathbf{w}^C\right)^T \left(B^C \Delta \mathbf{u}^C\right)^T \left(A^{CT} \Delta \mathbf{w}^C\right)^T \left(\Lambda^C \Delta \boldsymbol{\alpha}\right)^T \right\}^T. \qquad (6.55)$$

which contains all the secondary uknown vectors.

When the structure is subject to ground motion, $\mathbf{f}^C = A_m^C \text{diag}(\Lambda_m^C \boldsymbol{\alpha}_m) B_f^C \boldsymbol{\delta}^C$, the

nodal equivalent load $\mathbf{f}^C$ can be rewritten into

$$\mathbf{f}^C = A_m^C \text{diag}(\Lambda_m^C \alpha_{m0}) B_f^C \boldsymbol{\delta}^C + A_m^C \text{diag}(\Lambda_m^C \Delta\boldsymbol{\alpha}_m) B_f^C \boldsymbol{\delta}^C \tag{6.56}$$

$$= F_0^C \boldsymbol{\delta}^C + A_m^C \text{diag}(B_f^C \boldsymbol{\delta}^C)\Lambda_m^C \Delta\boldsymbol{\alpha}_m,$$

where $F_0^C = A_m^C \text{diag}(\Lambda_m^C \alpha_{m0}) B_f^C$. Then the governing equation is the same as in Eq. (6.47), except for the interval matrix $\mathbf{F}_g$, which has the following form

$$\mathbf{F}_g = \left\{ \begin{array}{ccc} 0 & P_\eta^C & -T_m^B \langle A_m^{CT} \mathbf{w}^C \rangle^T \\ F_0^C & 0 & -T_m^A \langle B_m^C \mathbf{u}^C - B_f^C \boldsymbol{\delta}^C \rangle^T \\ 0 & 0 & 0 \end{array} \right\}. \tag{6.57}$$

Thus the formulation remains mostly unchanged, and the only modification is to substitute $B_m^C \mathbf{u}^C$ with $B_m^C \mathbf{u}^C - B_f^C \boldsymbol{\delta}^C$.

6.2.2 Measuring the magnitude and phase

When the measurement data contains only the magnitudes, the interval extension of the governing Eq. (6.34) yields

$$\left\{ \begin{array}{l} \mathbf{K}_{\text{eff}}^C \mathbf{u}^C - F^C \boldsymbol{\delta}^C = 0; \\ \mathbf{K}_{\text{eff}}^{CT} \mathbf{w}^C - \left(\mathbf{P}_{\eta\rho}^C \boldsymbol{\eta}_\rho - H^{CT} W^C H^C \mathbf{u}^C \right) = 0; \\ \Lambda^{CT} (A^{CT} \mathbf{w}^C \circ B^C \mathbf{u}^C) + (\gamma R)\boldsymbol{\alpha} = 0, \end{array} \right. \tag{6.58}$$

where $\boldsymbol{\eta}_\rho$ is the measurement vector, and the interval matrix $\mathbf{P}_{\eta\rho}^C$ is defined as

$$\mathbf{P}_{\eta\rho}^C = H^{CT} W^C \left\{ \begin{array}{l} \text{diag} \left(H\mathbf{u}^R / |H\mathbf{u}| \right) \\ \text{diag} \left(H\mathbf{u}^I / |H\mathbf{u}| \right) \end{array} \right\}, \tag{6.59}$$

By using the following guaranteed interval approximation,

$$\Delta \left(\mathbf{P}_{\eta\rho}^C \boldsymbol{\eta}_\rho - H^{CT} W^C H^C \mathbf{u}^C \right) = \mathbf{P}_{\eta\rho}^C \Delta\boldsymbol{\eta}_\rho - W_{\eta\rho}^C \Delta\mathbf{u}^C, \tag{6.60}$$

Eq. (6.58) can be transformed into a similar equivalent matrix form as Eq. (6.47). One only needs to replace W_η^C in Eq. (6.47) with $W_{\eta\rho}^C$, and P_η^C in Eq. (6.47) with

184

$\mathbf{P}^C_{\eta\rho}$. Here $W^C_{\eta\rho}$ has been introduced earlier in Eq. (6.36). Noting the following decomposition of $\mathbf{P}^C_{\eta\rho}$,

$$\mathbf{P}^C_{\eta\rho} = H^{CT}W^C\text{diag}\left(\left\{\begin{matrix} H\mathbf{u}^R/|H\mathbf{u}| \\ H\mathbf{u}^I/|H\mathbf{u}| \end{matrix}\right\}\right)\left\{\begin{matrix} I \\ I \end{matrix}\right\}, \tag{6.61}$$

the interval matrix $\mathbf{F}_g$ can be decomposed into a similar form as before.

When the measurement data contains only the phase angles, the interval extension of the governing Eq. (6.40) yields

$$\begin{cases} \mathbf{K}^C_{\text{eff}}\mathbf{u}^C - F^C\boldsymbol{\delta}^C = 0; \\ \mathbf{K}^{CT}_{\text{eff}}\mathbf{w}^C - \mathbf{P}^C_{\eta\varphi}\big(\boldsymbol{\eta}_\varphi - \arg(H^C\mathbf{u}^C)\big) = 0; \\ \Lambda^{CT}(A^{CT}\mathbf{w}^C \circ B^C\mathbf{u}^C) + (\gamma R)\boldsymbol{\alpha} = 0, \end{cases} \tag{6.62}$$

where $\boldsymbol{\eta}_\varphi$ is the measurement vector, and the interval matrix $\mathbf{P}^C_{\eta\varphi}$ is defined as

$$\mathbf{P}^C_{\eta\varphi} = H^{CT}W^C\left\{\begin{matrix} -\text{diag}\left(H\mathbf{u}^I/|H\mathbf{u}|^2\right) \\ \text{diag}\left(H\mathbf{u}^R/|H\mathbf{u}|^2\right) \end{matrix}\right\}, \tag{6.63}$$

By using the following guaranteed interval approximation,

$$\Delta\left\{\mathbf{P}^C_{\eta\varphi}\big(\boldsymbol{\eta}_\varphi - \arg(H\mathbf{u})\big)\right\} = \mathbf{P}^C_{\eta\varphi}\Delta\boldsymbol{\eta}_\varphi - W^C_{\eta\varphi}\Delta\mathbf{u}^C, \tag{6.64}$$

Eq. (6.62) can be transformed into a similar equivalent matrix form as Eq. (6.47). One only needs to replace W^C_η in Eq. (6.47) with $W^C_{\eta\varphi}$, and P^C_η in Eq. (6.47) with $\mathbf{P}^C_{\eta\varphi}$. Here $W^C_{\eta\varphi}$ has been introduced earlier in Eq. (6.42). Noting the following decomposition of $\mathbf{P}^C_{\eta\varphi}$,

$$\mathbf{P}^C_{\eta\varphi} = H^{CT}W^C\text{diag}\left(\left\{\begin{matrix} -H\mathbf{u}^I/|H\mathbf{u}|^2 \\ H\mathbf{u}^R/|H\mathbf{u}|^2 \end{matrix}\right\}\right)\left\{\begin{matrix} I \\ I \end{matrix}\right\}, \tag{6.65}$$

the interval matrix $\mathbf{F}_g$ can be decomposed into a similar form as before.

6.3 Nonlinear Programming Approach

In this section, nonlinear programming (NLP) techniques are implemented to solve the uncertain parameter identification problem. Similar to the static case, depending

on how the solution vector x and the equality constraints f_{eq} are constructed, the NLP methods are classified into: i) the direct approach, ii) the explicit adjoint approach, and iii) the implicit adjoint approach. These approaches are presented as follows.

6.3.1   The direct approach

In the direct approach, the solution vector x includes the load uncertainty vector δ^C, the measurement vector η^C, the mass parameter vector α_m, the nodal displacement vector u^C, the Lagrangian multiplier λ^C, and the stiffness parameter vector α:

$$x = \left\{ \delta^{CT} \quad \eta^{CT} \quad \alpha_m^T \quad u^{CT} \quad \lambda^{CT} \quad \alpha^T \right\}^T. \tag{6.66}$$

When the lower (or upper) bound of the j-th component of the stiffness parameter vector α is required, the objective functional Ω has the following general form

$$\Omega = c\alpha, \quad \text{or} \quad -c\alpha, \tag{6.67}$$

where c is a row vector whose only non-zero component is unity at the j-th entry.

Equality constraints include equilibrium conditions, compatibility requirements, essential boundary conditions, and measurement equation, collectively given by

$$\begin{cases} K_{\text{eff}}^C u^C + C^{CT}\lambda^C - F^C \delta^C = 0; \\ C^C u^C = 0; \\ H^C u^C = \eta^C. \end{cases} \tag{6.68}$$

And the inequality constraints require that the load uncertainty vector δ, the measurement vector η, and the mass parameter vector α_m vary within their respective interval bounds:

$$\begin{cases} \underline{\delta}^C \leq \delta^C \leq \overline{\delta}^C; \\ \underline{\eta}^C \leq \eta^C \leq \overline{\eta}^C; \\ \underline{\alpha}_m \leq \alpha_m \leq \overline{\alpha}_m. \end{cases} \tag{6.69}$$

To accelerate the convergence, the gradient of the objective functional

$$\frac{\partial \Omega}{\partial x} = \left\{ 0 \quad 0 \quad 0 \quad 0 \quad 0 \quad c \right\}, \tag{6.70}$$

and the gradient of the equality constraint equations

$$\frac{\partial f_{eq}}{\partial x} = \left\{ \begin{array}{cccccc} -F^C & 0 & T_m^A \langle B_m^C u^C \rangle^T & K_{\text{eff}}^C & C^{CT} & T^A \langle B^C u^C \rangle^T \\ 0 & 0 & 0 & C^C & 0 & 0 \\ 0 & -I & 0 & H^C & 0 & 0 \end{array} \right\}. \tag{6.71}$$

are computed, where $T^A \langle x \rangle = \Lambda^{CT} \text{diag}(x) A^{CT}$ and $T_m^A \langle x \rangle = \Lambda_m^{CT} \text{diag}(x) A_m^{CT}$, as defined earlier in Eqs. (6.28) and (6.49).

6.3.2 Explicit adjoint optimization

The adjoint approach does not directly use the measurement equation $\eta^C = H^C u^C$. Instead, the governing Eq. (6.22) is used, either explicitly or implicitly. In the explicit adjoint approach, the solution vector x includes the load uncertainty vector δ^C, the measurement vector η^C, the mass parameter vector α_m, the nodal displacement vector u^C, its Lagrangian multiplier λ^C, the adjoint solution w^C, its Lagrangian multiplier λ_w^C, and the stiffness parameter vector α:

$$x = \left\{ \delta^{CT} \quad \eta^{CT} \quad \alpha_m^T \quad u^{CT} \quad \lambda^{CT} \quad w^{CT} \quad \lambda_w^{CT} \quad \alpha^T \right\}^T. \tag{6.72}$$

Then the objective functional Ω, its gradient $\partial \Omega / \partial x$, and the inequality constraints are the same as in the direct approach.

However, the equality constraints are given by

$$\left\{ \begin{array}{l} K_{\text{eff}}^{CT} w^C + C^{CT} \lambda_w^C + (H^{CT} W^C H^C) u^C - (H^{CT} W^C) \eta^C = 0; \\ K_{\text{eff}}^C u^C + C^{CT} \lambda^C - F^C \delta^C = 0; \\ C^C u^C = 0, \quad C^C w^C = 0; \\ \Lambda^{CT} (B^C u^C \circ A^{CT} w^C) + \gamma R \alpha = 0. \end{array} \right. \tag{6.73}$$

The corresponding gradient is

$$
\frac{\partial f_{eq}}{\partial x} = \left\{
\begin{array}{ccccc}
0 & 0 & -F^{CT} & 0 & 0 \\
-W^C H^C & 0 & 0 & 0 & 0 \\
T_m^B \langle A_m^{CT} w^C \rangle & 0 & T_m^A \langle B_m^C u^C \rangle & 0 & 0 \\
H^{CT} W^C H^C & 0 & K_{\text{eff}}^{CT} & C^{CT} & T^B \langle A^{CT} w^C \rangle^T \\
0 & 0 & C^C & 0 & 0 \\
K_{\text{eff}}^C & C^{CT} & 0 & 0 & T^A \langle B^C u^C \rangle^T \\
C^C & 0 & 0 & 0 & 0 \\
T^B \langle A^{CT} w^C \rangle & 0 & T^A \langle B^C u^C \rangle & 0 & \gamma R
\end{array}
\right\}^T ,
\tag{6.74}
$$

where deterministic matrices $T^A\langle x \rangle$, $T^B\langle x \rangle$, $T_m^A\langle x \rangle$, and $T_m^B\langle x \rangle$ have been defined earlier in Eqs. (6.28) and (6.49).

6.3.3 Implicit adjoint optimization

In the implicit adjoint approach, the adjoint equations are no longer explicitly included in the equality constraints. Instead, they are implicitly satisfied in the optimization process. In particular, the solution vector

$$
x = \left\{ \delta^{CT} \quad \eta^{CT} \quad \alpha_m^T \quad \alpha^T \right\}^T ,
\tag{6.75}
$$

and the equality constraint is just

$$
\Lambda^{CT} (B^C u^C \circ A^{CT} w^C) + \gamma R \alpha = 0,
\tag{6.76}
$$

where u^C and w^C are the solution vectors to the original and adjoint systems, viz.

$$
\left\{
\begin{array}{cc}
W_\eta^C & K_{\text{eff}}^{CT} \\
K_{\text{eff}}^C & 0
\end{array}
\right\}
\left\{
\begin{array}{c}
u^C \\
w^C
\end{array}
\right\}
=
\left\{
\begin{array}{c}
P_\eta^C \eta^C \\
F^C \delta^C
\end{array}
\right\} ,
\tag{6.77}
$$

where $W_\eta^C = H^{CT} W^C H^C$ and $P_\eta^C = H^{CT} W^C$, and u^C and w^C implicitly depend on the unknown stiffness parameter vector α. The corresponding gradient of the equality constraints is given by

$$
\frac{\partial f_{eq}}{\partial x} = \left\{ T_b K_b^{-1} F_b \quad - T_b K_b^{-1} T_{mb} \quad \gamma R - T_b K_b^{-1} T_b^T \right\} ,
\tag{6.78}
$$

188

where K_b and T_b are introduced earlier in Eq. (6.29), and the other two block matrices F_b and T_{mb} are given by

$$F_b = \left\{ \begin{matrix} 0 & W_\eta^C \\ F^C & 0 \end{matrix} \right\}, \quad T_{mb} = \left\{ \begin{matrix} T_m^B \langle A_m^{CT} w^C \rangle^T \\ T_m^A \langle B_m^C u^C \rangle^T \end{matrix} \right\} \tag{6.79}$$

Finally, note that the formulation outlined in this section can be extended to account for magnitude and phase angle measurements.

6.4 Numerical Examples

The proposed interval inverse algorithm for structural dynamic analysis in the frequency domain is implemented using the interval MATLAB toolbox INTLAB developed by Rump [122]. The performance of the proposed method is illustrated by solving: i) a pin-roller bar and ii) a simply supported beam. Displacements at given locations on the structure are collected as measurement data, which are transformed into the frequency domain prior to the analysis. By assigning appropriate measurement noises, interval measurement vector models the frequency response of the structure of i) both the real and imaginary parts, or ii) only the magnitudes. The yielded lower and upper bounds from the proposed method are compared against solutions obtained from the nonlinear programming (NLP) approach and the Monte Carlo prediction (MC). The results show that the proposed method gives guaranteed enclosure of the exact solution, and its computational time is negligible when compared with other methods.

6.4.1 Pin-roller bar

Consider a straight bar of length $L = 5$ m, as shown in Figure 6.1. The pin-roller bar is subject to concentrated force $P = 100$ kN at one end C. The cross section of the bar is uniform, with an area $A = 0.005$ m². Only axial deformations are allowed, and the bar is modeled by 10 equal-length planar truss elements with uniform material
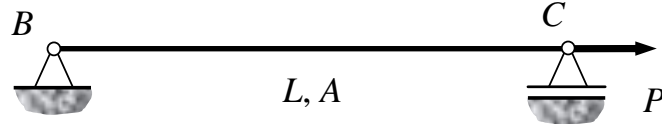
Figure 6.1: A pin-roller bar subject to concentrated traction at the other end.

properties. For each element, the Young' modulus

$$E = 115 + 10 \sin\left(\frac{x}{L}\right) - 5 \cos\left(\frac{x}{L}\right) \text{ GPa}, \tag{6.80}$$

where x is the coordinate of element centroid, and the values of E are given up to four significant digits. The mass density $\rho = 8.3 \times 10^3$ kg/m^3.

The same 10-element model is also used to generate measurement data. Axial displacements at 10 equally distributed nodes along the bar are collected into the exact measurement vector η_{ex}. The measurement data is obtained within the frequency range [0.1, 1] kHz, and the fundamental frequency $\Delta f = 25$ Hz. Thus the measurement data $\boldsymbol{\eta}$ contains axial displacements at 36 different frequencies. The uncertainties in $\boldsymbol{\eta}$ range from 0.1% to 2%, and material uncertainty in $\boldsymbol{\rho}$ is 1%.

For each frequency point, there are 10 measurements and 10 unknown element Young's moduli E_j. The problem is well-posed, so no regularization is required. The initial guess $E = 60$ GPa for all the elements. Figure 6.2 shows the obtained deterministic solution as a function of the frequency f. In the figure, the solid lines are the obtained deterministic solutions corresponding different frequencies, starting from 0.1 kHz to 1 kHz at every 25 Hz. Observe that the solutions at lower frequencies oscillate, while the solutions at higher frequencies are more stable. This is due to the additional stabilization introduced by the increased influence of the mass matrix $\mathbf{M}$, which improves the conditioning number of the problem.

Then the proposed interval inverse solver is applied. The obtained lower and upper bounds of the the estimated Young's modulus $\mathbf{E}_4$ for the fourth element are plotted
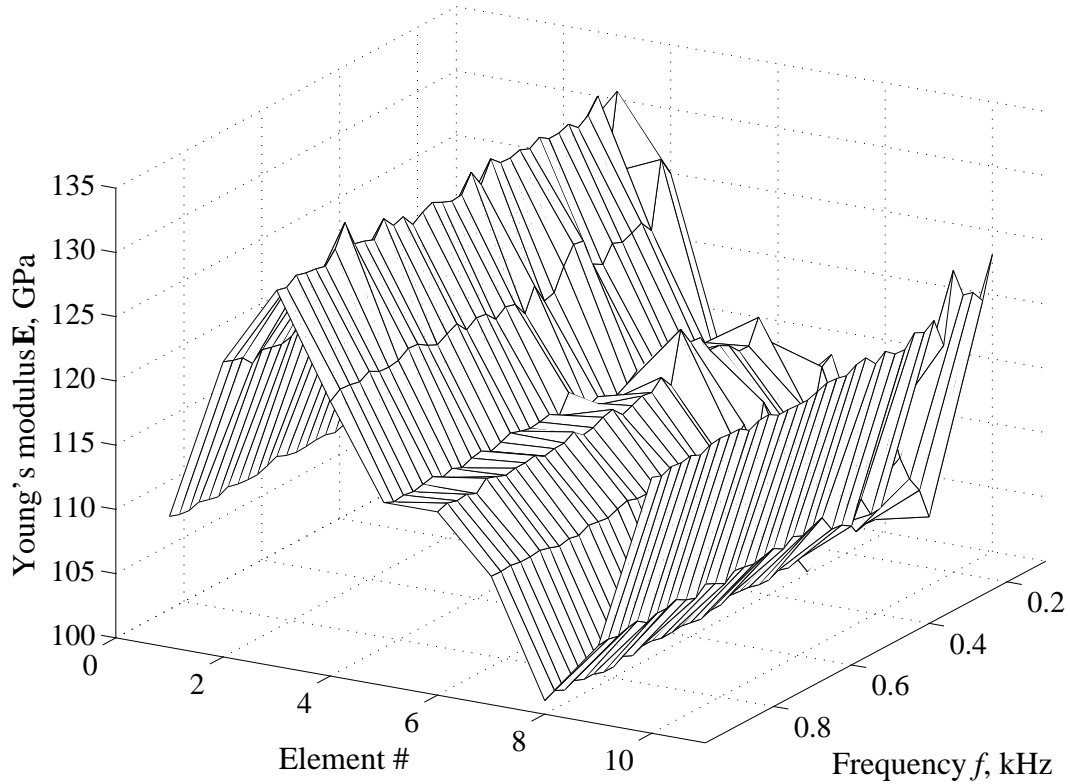
Figure 6.2: Deterministic solution of the Young's modulus **E** for the pin-roller bar in Figure 6.1 at different frequencies: from 0.1 kHz to 1 kHz with 25 Hz intervals. Measurement uncertainty is 0.1-2% and material uncertainty is 1% in mass.

in Figure 6.3. Observe that the low-frequency solutions are missing, because the measurement uncertainty is too large and the corresponding fixed-point iteration does not converge. However, when the proposed method converges, the yielded interval solutions (IS, solid lines with circular markers) guarantee to enclose the reference solutions obtained from the nonlinear programming solution (NLP, dashed lines with rectangular markers) and Monte Carlo predictions (MC, dotted lines with triangular markers). All these solutions contain the exact Young's modulus (solid line).

By intersecting these interval solutions, the final enclosure of the Young's moduli is obtained. The results are plotted in Figure 6.4, following the same guidelines as in 6.3. Apparently, the proposed method provides guaranteed interval enclosures of the exact solution set, for all the unknown parameters of the structure.
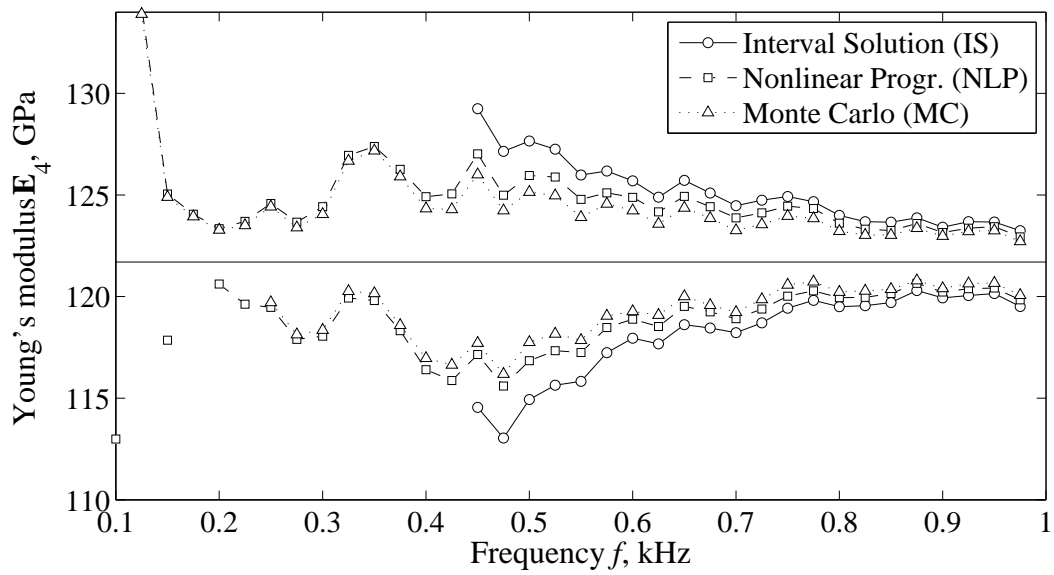
Figure 6.3: Lower and upper bounds of the Young's modulus $\mathbf{E}_4$ for the pin-roller bar in Figure 6.1 at different frequencies: exact value (solid line), interval solution (IS), nonlinear programming solution (NLP), and Monte Carlo prediction (MC) obtained from an ensemble of 10,000 simulations. Measurement uncertainty is 0.1-2% and material uncertainty is 1% in mass.
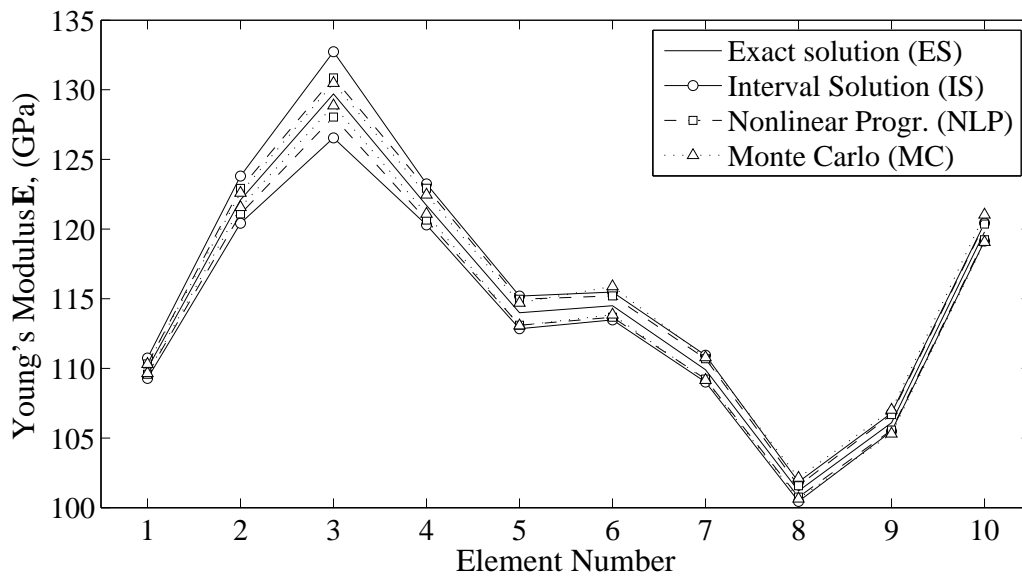
Figure 6.4: Interval-based identification of Young's moduli of the pin-roller bar of Figure 6.1: exact values (ES), interval solution (IS), nonlinear programming solution (NLP), and Monte Carlo prediction (MC) from an ensemble of 10,000 simulations. Measurement uncertainty is 0.1-2% and material uncertainty is 1% in mass.

Figure 6.5: A simply supported beam subject to vertical ground motion.

6.4.2 Simply supported beam

The second example is a simply supported beam subject to vertical ground motion, as shown in Figure 6.5. The beam has a length $L = 2$ m, and a 5 cm × 3 cm rectangular cross section (cross section area $A = 0.015$ m^2 and moment of inertia $I = 1.125 \times 10^{-4}$ m^4). The beam is subject to lateral deformation, and 20 two-node Euler-Bernoulli beam elements are used in the finite element mesh. The stiffness matrix and the mass matrix are obtained using the three-node Gaussian quadrature rule. In order to generated a continuous material field, Young's moduli at the quadrature nodes are linearly interpolated from those at the material mesh nodes

$$E = 220 + 10 \sin\left(\frac{6x}{L}\right) - 5 \cos\left(\frac{13x}{L}\right) \text{ GPa}, \tag{6.81}$$

where x is the nodal coordinate, and the values are given up to four significant digits. The mass density $\rho = 7.8 \times 10^3$ kg/m^3 is interpolated from the same material mesh as **E**. Thus the stiffness parameter vector $\boldsymbol{\alpha}$ and mass parameter vector $\boldsymbol{\alpha}_m$ both have 21 components, one for each mesh node.

A finer 80-element finite element model is used to generate the measurement data. Further, the magnitude of nine lateral deflections at equidistant points along the beam are collected as measurements. The measurement vector $\boldsymbol{\eta}_j$ at different frequencies, which has 9 components, is obtained with a constant device tolerance $\pm 2 \times 10^{-4}$ m. The sampling frequency ranges from 50 Hz to 750 Hz at a 25 Hz increment. The resulting interval measurement vector $\boldsymbol{\eta}$ has uncertainties ranging from 0.1% to 1%, and contains the exact measurement data.
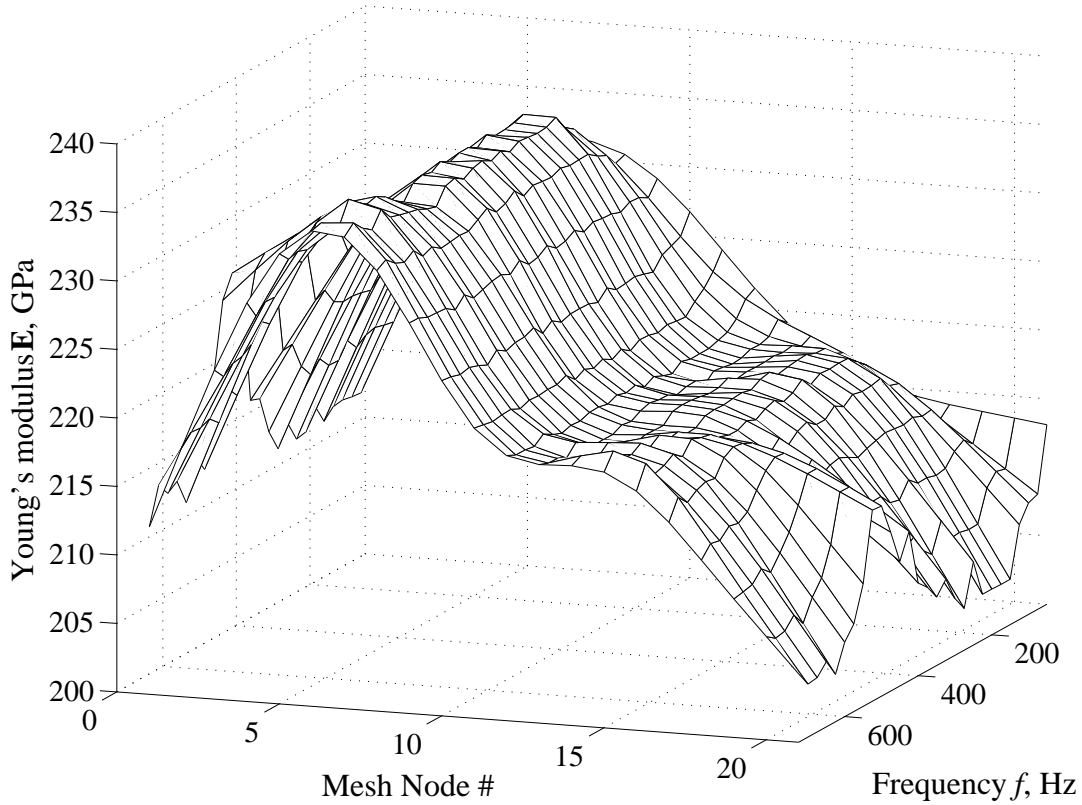
Figure 6.6: Deterministic solution of the Young's modulus **E** of the simply supported beam of Figure 6.5 at different frequencies: from 50 Hz to 750 Hz with 25 Hz intervals (measurement uncertainty level 0.1-1%).

The problem is ill-posed, and the measurement data at each frequency is not enough to uniquely determine the 21 unknown parameters. Thus regularization is required. Here, a second-order regularization matrix R is used. The regularizer weight γ is cautiously chosen [62]: the famous L-curve method is used, and $\gamma = 2 \times 10^{-4}$ is chosen as the optimal regularization weight.

Then for the proposed method, the initial guess $E = 160$ GPa for all elements. Figure 6.6 displays the deterministic solutions obtained from the proposed method. Observe that the deterministic solution is more stable near the mid-span of the beam, where more effective measurements are available, than those near both ends. Figure 6.7 compares the corresponding lower and upper bounds of the Young's modulus $\mathbf{E}_9$ as a function of the sampling frequency f. Observe that the Monte Carlo prediction
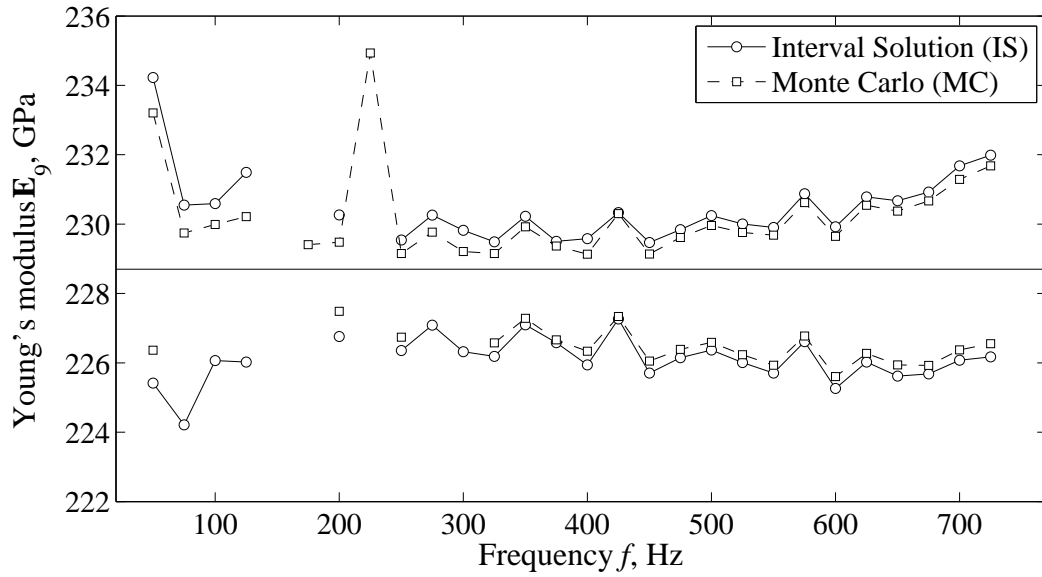
Figure 6.7: Lower and upper bounds of the Young's modulus $\mathbf{E}_9$ of the simply supported beam of Figure 6.5: exact values (solid line), interval solution (IS), and Monte Carlo prediction (MC) obtained from an ensemble of 10,000 simulations (measurement uncertainty level 0.1-1%).
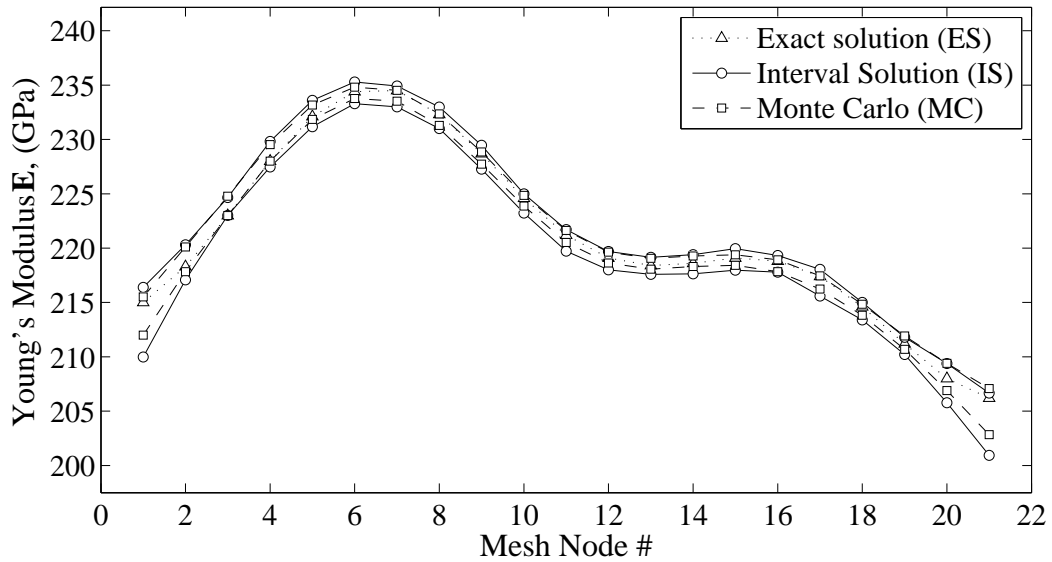
Figure 6.8: Interval-based identification of Young's moduli of the simply supported beam of Figure 6.5: exact values (ES), interval solution (IS), nonlinear programming solution (NLP), and Monte Carlo prediction (MC) from an ensemble of 10,000 simulations (measurement uncertainty level 0.1-1%).

obtained from an ensemble of 10,000 simulations is always contained by the interval solution (IS). Both methods fail to provide reliable estimates on the Young's modulus near the resonance frequency (≈ 200 Hz), even where the measurement uncertainty level is uniform. As a result, it is better to avoid resonance frequencies in the measurement data aquisition process.

The final interval enclosure of the exact solution set is obtained by intersecting the obtained interval enclosures at all frequencies. Figure 6.8 compares the proposed method with the MC predictions. Observe that containment is guaranteed and the overestimation is very small. Thus the proposed method works well, even for ill-conditioned problems.

6.5   *Summary*

In this chapter, the proposed interval parameter identification algorithm is extended to dynamic problems. The measurement data is processed and transformed into the frequency domain prior to the analysis, and the goal is to predict material properties of the structure based on noisy measurement data modeled by intervals. Other parameters of the structure, such as external loads and inertial properties, are also modeled by intervals.

The algorithm is composed of the deterministic stage and the interval stage. In the deterministic stage, a deterministic prediction is obtained by minimizing the difference between the predicted and measured responses of the structure, using the adjoint-based optimization technique. In the interval stage, the interval enclosure of the unknown parameter is obtained, which guarantees to enclose the exact solution set. In addition, a new variant of the iterative enclosure method is used in the algorithm. Numerical examples show that the current method is reliable and efficient.

CHAPTER VII

CONCLUSION

In this dissertation, for the first time structural inverse problems under uncertainty are successfully solved using an interval finite element approach. Inverse problems in structural analysis include some important applications that have drawn the attention of numerous researchers in recent years, such as structure health monitoring [1, 22, 57, 111, 149] and structure damage detection [14, 35, 39, 84, 142, 156, 163]. In these problems, internal properties of the structure are predicted based on measurement data collected from measuring devices deployed on the structure. Inevitably, measurements contain noise and the prediction contains uncertainties. The main source of uncertainty is due to the accuracy of measuring devices; these are designed to operate within specific allowable tolerances, as defined by National Institute of Standards and Technology (NIST). Tolerances are performance requirements that fix the limit of allowable error or departure from true performance or value. Thus closed intervals are the most realistic way to model uncertainty in measurements. In this dissertation, intervals are adopted as a basis for the analysis of the uncertainty modeling and propagation [28, 37, 69, 104]. The results are reliable and computationally inexpensive.

The presented work studies elastic structures that can be modeled as trusses, frames, and plane stress/strain problems. Interval Finite Element Method (IFEM) [32, 90, 102, 103, 105, 110, 119] is used as a cornerstone of the formulation. Efficient and accurate interval forward and inverse solutions in static and dynamic domains have been developed. The static forward solver solves for structural response under given load, geometry, and material uncertainties. The static inverse solver predicts

material properties of the structure (e.g. Young's modulus), based on the displacement or strain measurements at prescribed locations. The dynamic forward solver yields the interval enclosure of the frequency responses, natural frequencies, modal shapes, and transient responses of elastic structures with uncertain parameters. The dynamic inverse solver obtains interval predictions on the structural material properties using dynamic measurement data, which are collected and transformed into the frequency domain.

In the implementation of the current method, the first challenge encountered is caused by the ill-conditioning nature of inverse problems. The ill-conditioning basically means that the problem might have no solution, or have multiple solutions, or show significant changes in the solution when there is only small perturbations in the data. Thus various regularization techniques are exploited to stabilize the inverse algorithm and improve the conditioning of the problem. The second challenge is the inherent high computational cost that the uncertainty analysis possesses. In order to reliably estimate the accuracy of the solution, the computational resources required are immense when compared with those in a deterministic analysis. However, due to the adoption of interval arithmetic, the interval-based uncertainty analysis is performed similarly to the conventional deterministic analysis. In addition, the obtained interval enclosures guarantee to contain the exact solution set, regardless of the actual nature of the uncertainty under consideration. However, due to the conservative nature of interval arithmetic, which yields guaranteed results in the calculation, there are overestimations in the final solution when dependency exists among interval variables. If not handled properly, this detrimental effect can quickly accumulate and render the final solution excessively wide and practically useless. Thus the third challenge is to develop interval algorithms that reduce this overestimation due to interval dependency to a minimum.

The current work successfully handles these challenges. For the inverse problem

solving, the adjoint-based optimization technique is incorporated into the formulation, which provides a computational efficient approach to calculate the gradient of a given function under given constraint. By combining the adjoint method with other optimization techniques such as conjugate gradient method, Newton-Raphson method, and inexact line search, the current method is applicable to structural inverse problems both in the static and dynamic cases. For the reduction of overestimation due to interval dependency, the following innovative approaches are adopted: *i*) new decomposition strategies for the interval variables in IFEM formulation, *ii*) an element-by-element assembly strategy followed by the Lagrangian multiplier approach in enforcing compatibility requirements and essential boundary conditions, and *iii*) new variants of iterative enclosure method. The key idea is to reduce multiple occurrences of the same interval variables and delay interval operations.

To illustate the performance of the current method, a variety of numerical examples are presented. The examples include plane trusses, space trusses, plane beams, plane frames, and plane stress/strain problems. Besides simple finite elements such as two-node truss elements and two-node Euler-Bernoulli beam elements, isoparametric elements such as 8-node rectangular plane elements and 6-node triangular plane elements are included. The examples include simple illustrative ones that have only a few elements, as well as more complex ones that require several hundreds. The problems can be either linear in the mathematical sense, such as the static forward problems and the frequency response analysis and the transient response analysis of dynamic problems, or nonlinear, such as the natural frequency and modal shape analysis of dynamic problems and inverse problems (both static and dynamic). In all the examples, the current method yields guaranteed interval enclosure of the exact solution set with small overestimation, regardless of the conditioning of the problem, the source of the external excitation, or the level of uncertainty. The obtained interval enclosures are sharp and the corresponding overestimation is small when compared

with other competing methods, such as endpoint combination method [109], the sensitivity analysis [77], the Monte Carlo simulation [110], the nonlinear programming approach [16, 91], and other interval-based methods proposed by other researchers. The computational time of the current method is negligible when compared with other competing methods in the literature, such as endpoint combination, Monte Carlo simulation, and nonlinear programming approach.

In summary, the presented method works well for a wide spectrum of structural forward and inverse problems. Interval arithmetic has been proven a useful tool in the uncertainty analysis of elastic structures with load, geometry, and material uncertainties. The obtained interval enclosure guarantees to enclose the exact solution set with very small overestimation, and the corresponding computational time is negligible when compared with other conventional approaches in uncertainty analysis of structural problems. The current method can be extended in different directions. For instance, currently it is assumed that no information other than the bounds are known for the uncertainties under study. In reality, it is plausible to know partial information about the nature of the uncertainty, and to model them as random variables with interval parameters. Also it is future work to extend the current work to other types of finite elements, such as space frames, solid elements, plate elements, and shell elements, and other types of analysis, such as buckling analysis. Finally it is worth mentioning that the current method only assumes a linear constitutive law, and considers elastic structures. It is plausible to extend to include nonlinearity in geometry, material, and boundary condition, and beyond the range of elasticity.

APPENDIX A

DERIVED QUANTITY CALCULATION

For displacement-based finite element method as in the current study, the primary variable in the formulation is the nodal displacement vector u. All other quantities, such as element displacements, strains, internal forces, and stresses, are calculated after nodal displacement vector u has been obtained. Thus they are referred to as derived quantities. For linear problems, these derived quantities can be expressed linearly in terms of the primary variable u.

Consider the displacement d_ξ at given point ξ inside an element. It is interpolated from the element nodal displacement vector u_e via the shape function matrix N_e,

$$d_\xi = N_e(\xi)u_e = N_e(\xi)T_e u. \tag{A.1}$$

where T_e is the transformation matrix that relates between the element and global displacement vector, viz. $u_e = T_e u$. For the strain component ε_ξ at given location ξ,

$$\varepsilon_\xi = B_e(\xi)u_e = B_e(\xi)T_e u, \tag{A.2}$$

where B_e is the element strain-displacement vector. Eqs. (A.1) and (A.2) show that the calculation of d_ξ and ε_ξ has the following generalized form

$$\varepsilon = Bu, \tag{A.3}$$

where ε is the generalized strain vector, and B depends on the assumed displacement field, geometry and orientation of the element. Note that B is not influenced by the material properties of the structure.

The internal forces between elements are obtained from the element nodal force

201

r_e due to element deformation, which is further given by

$$r_e = K_e u_e = K_e T_e u. \tag{A.4}$$

For the stress component σ_ξ at given location ξ, the simplest approach is to multiply the strain ε_ξ in Eq. (A.2) with the constitutive matrix $E_e(\xi)$ at the given location,

$$\sigma_\xi = E_e(\xi)\varepsilon_\xi = E_e(\xi)B_e(\xi)T_e u. \tag{A.5}$$

If the stress σ_ξ is extrapolated from stresses at Gaussian integration points inside the same element, or even averaged from stresses obtained from different elements, the calculation is very similar to Eq. (A.5). Alternatively, σ_ξ can be obtained from the direct interpolation of the stress field [?]. As the stress field must generate the same element nodal force as in Eq. (A.4), σ_ξ is related to the element nodal force r_e. Thus

$$\sigma_\xi = P_e(\xi)r_e = P_e(\xi)K_e T_e u, \tag{A.6}$$

where the matrix $P_e(\xi)$ is determined by the assumed stress field and geometry of the element. Eqs. (A.4), (A.5), and (A.6) show that the calculation of r_e and σ_ξ has the following generalized form

$$\sigma = Su, \tag{A.7}$$

where σ is the generalized stress vector, and S is influenced by the structural material properties and is linearly dependent on the stiffness of the element.

APPENDIX B

RAYLEIGH DAMPING

Structural systems in real life possess energy dissipation mechanisms, which are referred to as damping. The Rayleigh damping assumes that the damping matrix C is a linear combination of the stiffness and mass matrix, viz.

$$C = \alpha_d M + \beta_d K, \tag{B.1}$$

where α_d and β_d are the Rayleigh damping coefficients, with units 1/sec and sec, respectively. The Rayleigh damping model is especially useful for the modal analysis of structural dynamic systems, as the resulting governing equations are uncoupled [6, 25]. Although real life structures usually have non-proportional damping, it is a common practice to adopt the Rayleigh damping in both experimental and theoretical studies [107, 154].

The Rayleigh damping has different effective damping ratio for different frequencies. At given frequency ω, the corresponding damping ratio ζ is given by

$$\zeta = \frac{1}{2} \left(\frac{\alpha_d}{\omega} + \beta_d \omega \right). \tag{B.2}$$

Figure B.1 plots the effective damping ratio ζ against the frequency ω for differnet sets of Rayleigh damping coefficients. It is observed that ζ is very large for low frequencies, remains relatively unchanged for middle frequencies, and increases slowly for high frequencies.

According to Hall [60], to obtain a desired damping ratio that lies within an interval $[\zeta - \alpha_c,\ \zeta + \alpha_c]$ for frequencies ranging from ω to $\beta_c \omega$, the damping coefficients α_d and β_d should be chosen as

$$\alpha_d = 2\zeta\omega \frac{2\beta_c}{1 + 2\sqrt{\beta_c} + \beta_c}, \qquad \beta_d = \frac{2\zeta}{\omega} \frac{2}{1 + 2\sqrt{\beta_c} + \beta_c}. \tag{B.3}$$
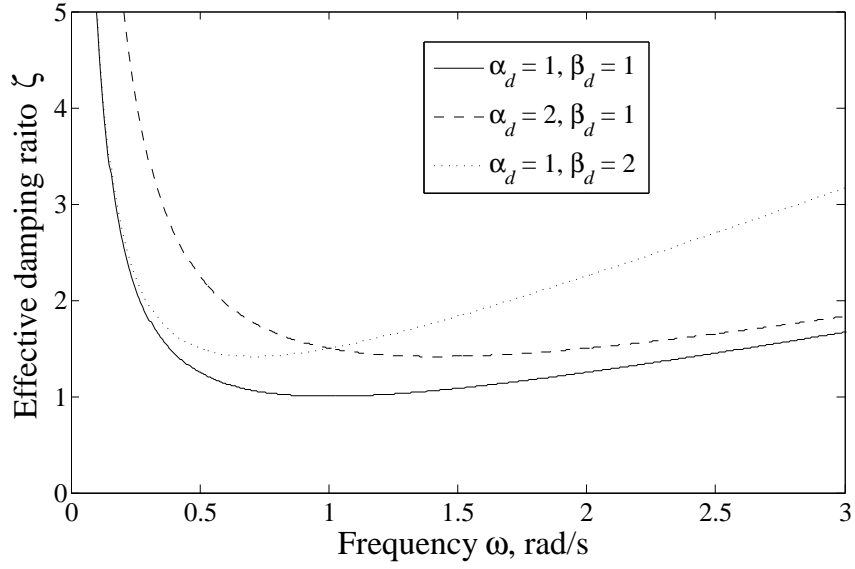
Figure B.1: Effective damping ratio as a function of frequency for Rayleigh damping with different damping coefficients.

The corresponding α_c is also determined by the range ratio β_c,

$$\alpha_c = \zeta \frac{1 - 2\sqrt{\beta_c} + \beta_c}{1 + 2\sqrt{\beta_c} + \beta_c}. \tag{B.4}$$

Apparently, α_c increases as the desired range ratio β_c increases.

APPENDIX C

FIXED-POINT FORM DERIVATION

The goal of this section is to transform the following interval nonlinear system into a fixed-point form with respect to the unknown interval variables $\Delta\boldsymbol{\omega}^2$, $\Delta\mathbf{u}$, and $\Delta\boldsymbol{\lambda}$,

$$\left\{ -M_b u_0 \quad K_b \right\} \begin{Bmatrix} \Delta\boldsymbol{\omega}^2 \\ \Delta\mathbf{u} \\ \Delta\boldsymbol{\lambda} \end{Bmatrix} = M_b \Delta\mathbf{u}\Delta\boldsymbol{\omega}^2 - A_b \mathrm{diag}\left(\begin{Bmatrix} A^T\mathbf{u} \\ \boldsymbol{\omega}^2 A_m^T\mathbf{u} \end{Bmatrix} \right) \Lambda_{\mathrm{eff}} \Delta\boldsymbol{\alpha}_{\mathrm{eff}}, \quad (\mathrm{C}.1)$$

where K_b, M_b, and A_b are given by

$$K_b = \begin{Bmatrix} K_0 - \omega_0^2 M_0 & C^T \\ C & 0 \end{Bmatrix}, \quad M_b = \begin{Bmatrix} M_0 \\ 0 \end{Bmatrix}, \quad A_b = \begin{Bmatrix} A & A_m \\ 0 & 0 \end{Bmatrix}, \quad (\mathrm{C}.2)$$

ω_0, u_0, and λ_0 are deterministic reference solution that satisfies

$$\begin{Bmatrix} K_0 - \omega_0^2 M_0 & C^T \\ C & 0 \end{Bmatrix} \begin{Bmatrix} u_0 \\ \lambda_0 \end{Bmatrix} = \begin{Bmatrix} 0 \\ 0 \end{Bmatrix}, \quad u_0^T M_0 u_0 = 1, \quad (\mathrm{C}.3)$$

and $\Delta\boldsymbol{\omega}^2$, $\Delta\mathbf{u}$, and $\Delta\boldsymbol{\lambda}$ are the difference between the interval variables and their respective reference points,

$$\Delta\boldsymbol{\omega}^2 = \boldsymbol{\omega}^2 - \omega_0^2, \qquad \Delta\mathbf{u} = \mathbf{u} - u_0, \qquad \Delta\boldsymbol{\lambda} = \boldsymbol{\lambda} - \lambda_0. \quad (\mathrm{C}.4)$$

To solve for $\Delta\boldsymbol{\omega}^2$, both sides of Eq. (C.1) are multiplied by $G_\omega = -\left\{ u_0^T \quad \lambda_0^T \right\}$. According to Eq. (C.3),

$$G_\omega K_b = -\left\{ u_0^T \quad \lambda_0^T \right\}\left\{ -M_b u_0 \quad K_b \right\} = \left\{ u_0^T M_0 u_0 \quad 0 \right\} = \left\{ 1 \quad 0 \right\}, \quad (\mathrm{C}.5)$$

$\Delta\boldsymbol{\omega}^2$ is obtained from

$$\Delta\boldsymbol{\omega}^2 = (G_\omega M_b)\Delta\mathbf{u}\Delta\boldsymbol{\omega}^2 - (G_\omega A_b)\mathrm{diag}\left(\begin{Bmatrix} A^T\mathbf{u} \\ \boldsymbol{\omega}^2 A_m^T\mathbf{u} \end{Bmatrix} \right) \Lambda_{\mathrm{eff}} \Delta\boldsymbol{\alpha}_{\mathrm{eff}}. \quad (\mathrm{C}.6)$$

To solve for $\Delta\mathbf{u}$ and $\Delta\boldsymbol{\lambda}$, both sides of Eq. (C.1) are multiplied by

$$G_u = \left(K_b + \gamma \begin{Bmatrix} u_0 \\ \lambda_0 \end{Bmatrix} u_0^T M_b^T \right)^{-1} \left(I - M_b u_0 \{ u_0^T \quad \lambda_0^T \} \right), \tag{C.7}$$

where the constant γ is used to adjust the conditioning number of the matrix to be inverted. For the deterministic matrix $-M_b u_0$, multiplication with $\left(I - M_b u_0 \{ u_0^T \quad \lambda_0^T \}\right)$ yields

$$\left(I - M_b u_0 \{ u_0^T \quad \lambda_0^T \}\right)(-M_b u_0)$$
$$= -M_b u_0 + M_b u_0 \{ u_0^T \quad \lambda_0^T \} M_b u_0 \tag{C.8}$$
$$= -M_b u_0 + M_b u_0 \left(u_0^T M_0 u_0 \right) = 0.$$

For the block stiffness matrix K_b, observe that

$$\left(I - M_b u_0 \{ u_0^T \quad \lambda_0^T \}\right) K_b = K_b - M_b u_0 \{ u_0^T \quad \lambda_0^T \} K_b = K_b. \tag{C.9}$$

and

$$\left(K_b + \gamma \begin{Bmatrix} u_0 \\ \lambda_0 \end{Bmatrix} u_0^T M_b^T \right) \left(I - \begin{Bmatrix} u_0 \\ \lambda_0 \end{Bmatrix} u_0^T M_b^T \right)$$
$$= K_b + \gamma \begin{Bmatrix} u_0 \\ \lambda_0 \end{Bmatrix} u_0^T M_b^T - K_b \begin{Bmatrix} u_0 \\ \lambda_0 \end{Bmatrix} u_0^T M_b^T \tag{C.10}$$
$$- \gamma \begin{Bmatrix} u_0 \\ \lambda_0 \end{Bmatrix} \left(u_0^T M_b^T \begin{Bmatrix} u_0 \\ \lambda_0 \end{Bmatrix} \right) u_0^T M_b^T = K_b.$$

According to Eqs. (C.8) and (C.9),

$$\left(I - M_b u_0 \{ u_0^T \quad \lambda_0^T \}\right) \{ -M_b u_0 \quad K_b \} = \{ 0 \quad K_b \}. \tag{C.11}$$

According to Eq. (C.8),

$$\left(K_b + \gamma \begin{Bmatrix} u_0 \\ \lambda_0 \end{Bmatrix} u_0^T M_b^T \right)^{-1} \{ 0 \quad K_b \} = \left\{ 0 \quad I - \begin{Bmatrix} u_0 \\ \lambda_0 \end{Bmatrix} u_0^T M_b^T \right\}. \tag{C.12}$$

206

Combining Eqs. (C.11) and (C.12) yields

$$
G_u \left\{ -M_b u_0 \quad K_b \right\} = \left\{ 0 \quad I - \left\{ \begin{matrix} u_0 \\ \lambda_0 \end{matrix} \right\} u_0^T M_b^T \right\} = \left\{ \begin{matrix} 0 & I - u_0 u_0^T M_0 & 0 \\ 0 & -\lambda_0 u_0^T M_0 & I \end{matrix} \right\}. \quad (C.13)
$$

Finally, by assuming $\Delta \mathbf{u}$ is perpendicular to the deterministic vector $M_0 u_0$, viz. $u_0^T M_0 \Delta \mathbf{u} = \Delta \mathbf{u}^T M_0 u_0 = 0$, $\Delta \mathbf{u}$ and $\Delta \boldsymbol{\lambda}$ are obtained from

$$
\left\{ \begin{matrix} \Delta \mathbf{u} \\ \Delta \boldsymbol{\lambda} \end{matrix} \right\} = (G_u M_b) \Delta \mathbf{u} \Delta \boldsymbol{\omega}^2 - (G_u A_b) \mathrm{diag} \left(\left\{ \begin{matrix} A^T \mathbf{u} \\ \boldsymbol{\omega}^2 A_m^T \mathbf{u} \end{matrix} \right\} \right) \Lambda_{\mathrm{eff}} \Delta \boldsymbol{\alpha}_{\mathrm{eff}}. \quad (C.14)
$$

APPENDIX D

DISCRETE FOURIER TRANSFORM

Discrete time signals can be decomposed into a series of sines and cosines. This representation is called the Discrete Fourier Transform (DFT) of the signal. The process is reversible and the inverse transform is called the Inverse Discrete Fourier Transform (IDFT). The DFT and IDFT are widely used in the analysis of discrete time signals [123].

Suppose a discrete time signal x_k is given at time t_k. The *sampling interval* Δt is the distance between two contiguous time steps, and it is usually a constant for a specific problem. Then the k-th time is

$$t_k = k\Delta t. \tag{D.1}$$

The DFT of the signal x_k yields a series of complex coefficients $X_j = \mathcal{F}_t(x_k)_j$. The real and imaginary parts of the coefficients, viz. $\text{Re}(X_j)$ and $\text{Im}(X_j)$, denote the amplitude of the cosine and sine with frequency ω_j that is required to form the signal x_k, respectively, where ω_j is given by

$$\omega_j = j\frac{2\pi}{T}. \tag{D.2}$$

Here the *fundamental period* $T = N\Delta t$ is the duration of the N-component signal x_k, and $\Delta\omega = 2\pi/T$ is the *fundamental frequency*.

In practice, the Fourier coefficients X_j are computed from the signal x_k according to the following *analysis equation*:

$$X_j = \mathcal{F}_t(x)_j = \sum_{k=0}^{N-1} x_k e^{-i(2\pi/N)kj}, \tag{D.3}$$

in which $i = \sqrt{-1}$ is the imaginary unit, and the Euler's formula $e^{i\theta} = \cos\theta + i\sin\theta$ has been used. The inverse procedure computes the time signal x_k from the Fourier coefficients X_j according to the following *synthesis equation*:

$$x_k = \mathcal{F}_t^{-1}(X)_k = \frac{1}{N}\sum_{j=0}^{N-1} X_j e^{i(2\pi/N)kj}.$$
(D.4)

Eqs. (D.3) and (D.4) together form a "Fourier pair". For a real-valued signal x_k, its Fourier coefficients X_j is conjugate symmetric, viz.

$$X_j = X_{N-j}^*,$$
(D.5)

where superscript * denotes complex conjugate.

Due to the development of the Fast Fourier Transform (FFT) algorithm [27, 139], DFT is widely applied in engineering, science, and mathematics. One application of DFT is the calculation of the convolution z_k of two discrete signals x_k and y_k,

$$z_k = \sum_{j=0}^{N-1} x_{k-j} y_j,$$
(D.6)

where the head of the signal y_k is filled with zeros such that $y_{-1} = y_{-2} = \ldots = 0$. Eq. (D.6) is especially useful in the analysis of dynamic systems, in which x_k is the system excitation, y_k is the impulse response signal, and z_k is the system response. The DFT-based approach first compute the DFT of x_k and y_k,

$$X_j = \mathcal{F}_t(x)_j, \qquad Y_j = \mathcal{F}_t(y)_j.$$
(D.7)

Then the convolution z_k is obtained by applying the IDFT to the product of the Fourier coefficients X_j and Y_j, viz.

$$z_k = \mathcal{F}_t^{-1}(XY)_k.$$
(D.8)

Due to the high-efficiency of the FFT algorithm, the DFT-based approach is much faster than the direct formula in Eq. (D.6).

The DFT implicitly assumes periodicity over the duration T of the finite length signal x_k, as the base functions in Eqs. (D.3) and (D.4) have the common period T. Thus truncated signals cause discontinuities at both ends, and yield highe-frequency components in the Fourier coefficients. Figure D.1 illustrates this phenomenon in detail. Subplot (a) shows a sinusoid signal with 6 complete cycles. Its auto spectrum (or equivalently, the norm of its Fourier coefficients) is shown in (b), which is an impulse in the frequency domain. Subplot (c) shows a truncated sinusoid signal with 5.5 cycles, and its auto-spectrum in (d) shows a significant energy leakage to the neighboring frequencies. To reduce the leakage, the original signal x_k is multiplied with a gradually varying window w_k. Then the "windowed" signal x'_k is obtained as

$$x'_k = x_k \cdot w_k. \tag{D.9}$$
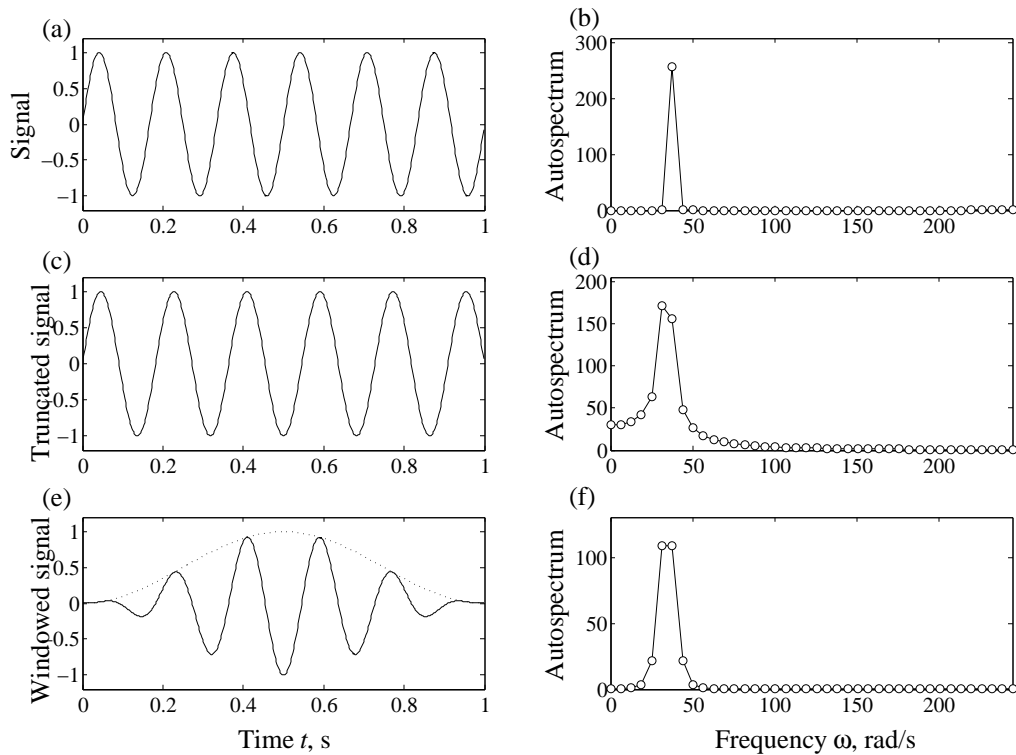
Figure D.1: Effects of truncation and windowing in Discrete Fourier Transform: (a,b) A single-frequency sinusoid with complete number of cycles and its auto-spectrum; (c,d) The same sinusoid with incomplete number of cycles and its auto-spectrum; (e,f) Windowed signal and its auto-spectrum.

The Hanning and Hamming windows are two commonly used windowing functions:

$$Hanning \qquad w_k = \frac{1}{2} - \frac{1}{2}\cos\left(\frac{2\pi}{N}k\right); \qquad\qquad (D.10)$$

$$Hamming \qquad w_k = 0.54 - 0.46\cos\left(\frac{2\pi}{N}k\right).$$

In Figure D.1, the signal in subplot (e) is obtained from applying the Hanning window to the truncated signal in (c). Its auto-spectrum in (f) shows a significant reduction in leakage. Also it is observed that windowing reduces the energy of the signal.

In DFT, the frequency resolution $\Delta\omega = 2\pi/T$ can be increased by expanding the original signal for a longer duration T. The most common extension strategy just appends zeros to the signal. Figure D.2 considers a simple example. A truncated sinusoid signal with $N = 32$ is displayed in subplot (a), as well as its auto-spectrum in (b). The corresponding zero-padded signal in subplot (c) doubles the duration, and the corresponding auto-spectrum in (d) shows a doubled frequency resolution.
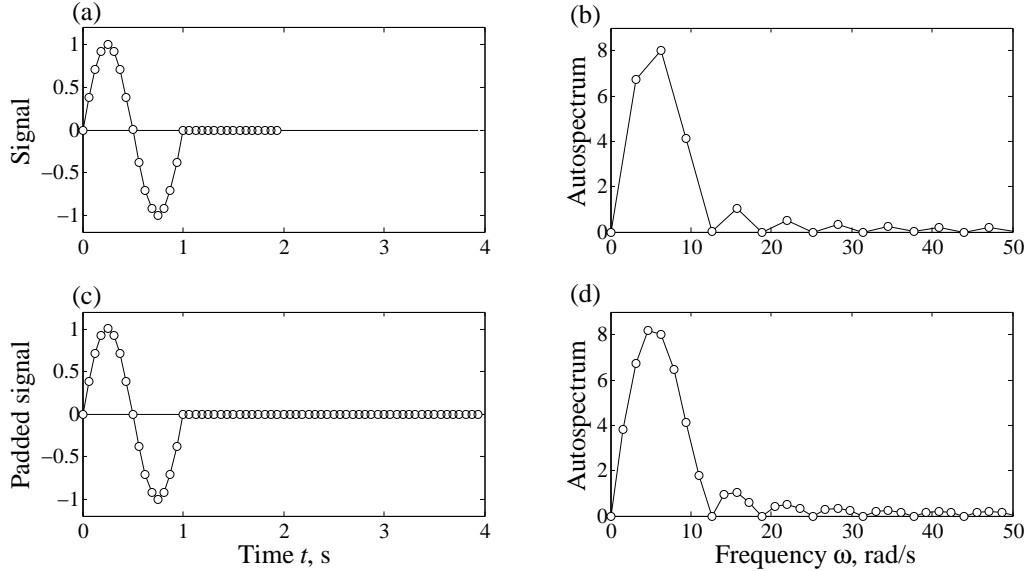
Figure D.2: Effects of zero-padding in Discrete Fourier Transform: (a,b) A truncated sinusoid signal with $N = 32$ and its auto-spectrum; (c,d) The zero-padded signal with $N = 64$ and its auto-spectrum. Note the doubled frequency resolution for the padded signal in (d).

REFERENCES

[1] ABBIATI, G., CERAVOLO, R., and SURACE, C., "Time-dependent estimators for on-line monitoring of full-scale structures under ambient excitation," *Mechanical Systems and Signal Processing*, 2015.

[2] ADHIKARI, S. and KHODAPARAST, H. H., "A spectral approach for fuzzy uncertainty propagation in finite element analysis," *Fuzzy Sets and Systems*, vol. 243, pp. 1–24, 2014.

[3] AKASHI, H., IMAI, H., and MOUSTAFA, K. A., "Parameter identification technique for multivariate stochastic systems," *Automatica*, vol. 15, no. 2, pp. 217–221, 1979.

[4] AKÇAY, H. and HJALMARSON, H., "The least-squares identification of fir systems subject to worst-case noise," *Systems & control letters*, vol. 23, no. 5, pp. 329–338, 1994.

[5] ALEFELD, G. and HERZBERGER, J., *Introduction to interval computation*. Academic press, 1984.

[6] ALIPOUR, A. and ZAREIAN, F., "Study rayleigh damping in structures; unceratinties and treatments," in *Proceedings of 14th World Conference on Earthquake Engineering, Beijing, China*, 2008.

[7] ANDREI, N., "Acceleration of conjugate gradient algorithms for unconstrained optimization," *Applied Mathematics and Computation*, vol. 213, no. 2, pp. 361–369, 2009.

[8] ARMENAKIS, A., GAREY, L., and GUPTA, R., "An adaptation of a root finding method to searching ordered disk files," *BIT Numerical Mathematics*, vol. 25, no. 4, pp. 561–568, 1985.

[9] ARMIJO, L. and OTHERS, "Minimization of functions having lipschitz continuous first partial derivatives," *Pacific Journal of mathematics*, vol. 16, no. 1, pp. 1–3, 1966.

[10] AVRIEL, M. and WILDE, D. J., "Optimality proof for the symmetric fibonacci search technique," *Fibonacci Quarterly*, vol. 4, pp. 265–269, 1966.

[11] BAE, S., CHO, J., BAE, S., and JEONG, W., "A discrete convolutional hilbert transform with the consistent imaginary initial conditions for the time-domain analysis of five-layered viscoelastic sandwich beam," *Computer Methods in Applied Mechanics and Engineering*, vol. 268, pp. 245–263, 2014.

[12] BAI, E.-W., TEMPO, R., and NAGPAL, K., "Recursive system identification in the presence of noise and model uncertainties," *Systems & control letters*, vol. 32, no. 1, pp. 57–62, 1997.

[13] BAI, Y., JIANG, C., HAN, X., and HU, D., "Evidence-theory-based structural static and dynamic response analysis under epistemic uncertainties," *Finite Elements in Analysis and Design*, vol. 68, pp. 52–62, 2013.

[14] BANDARA, R. P., CHAN, T. H., and THAMBIRATNAM, D. P., "Frequency response function based damage identification using principal component analysis and pattern recognition technique," *Engineering Structures*, vol. 66, pp. 116–128, 2014.

[15] BELFORTE, G., "Parameter identification for models with bounded errors in all variables," *Systems & control letters*, vol. 19, no. 6, pp. 425–428, 1992.

[16] BERTSEKAS, D. P., *Nonlinear programming*. Athena scientific Belmont, 1999.

[17] BOCHE, R. E., "Complex interval arithmetic with some applications.," Master's thesis, San Jose State College, 1966.

[18] BONET, J. and WOOD, R., "Nonlinear continuum mechanics for finite element analysis. 1997."

[19] BUONOPANE, S. G., SCHAFER, B. W., and IGUSA, T., "Reliability implications of advanced analysis in design of steel frames," in *Proc. ASSCCA-03*, 2003.

[20] BURDEN, R. L. and FAIRES, J. D., "2.1 the bisection algorithm," *Numerical Analysis. Prindle, Weber & Schmidt, Boston, MA., pp. x*, 1985.

[21] CAMPI, M. C., CALAFIORE, G., and GARATTI, S., "Interval predictor models: Identification and reliability," *Automatica*, vol. 45, no. 2, pp. 382–392, 2009.

[22] CHANG, P. C., FLATAU, A., and LIU, S. C., "Review paper: health monitoring of civil infrastructure," *Structural Health Monitoring*, vol. 2, no. 3, pp. 257–267, 2003.

[23] CHEN, S. H. and WU, J., "Interval optimization of dynamic response for structures with interval parameters," *Computers & structures*, vol. 82, no. 1, pp. 1–11, 2004.

[24] CHEN, S.-H. and YANG, X.-W., "Interval finite element method for beam structures," *Finite elements in analysis and design*, vol. 34, no. 1, pp. 75–88, 2000.

[25] CLOUGH, R. W. and PENZIEN, J., *Dynamics of structures*. McGraw-Hill Companies, 1975.

[26] Cook, D. A., Fedele, F., and Yezzi, A. J., "Detection of spherical inclusions using active surfaces," in *Proc., Int. Conf. on Synthetic Aperture Sonar and Synthetic Aperture Radar*, vol. 32, pp. 43–50, Institute of Acoustics St. Albans, Hertfordshire, UK, 2010.

[27] Cooley, J. W. and Tukey, J. W., "An algorithm for the machine calculation of complex fourier series," *Mathematics of computation*, vol. 19, no. 90, pp. 297–301, 1965.

[28] Corliss, G., Foley, C., and Kearfott, R. B., "Formulation for reliable analysis of structural frames," *Reliable Computing*, vol. 13, no. 2, pp. 125–147, 2007.

[29] Dai, Y.-H. and Yuan, Y., "A nonlinear conjugate gradient method with a strong global convergence property," *SIAM Journal on Optimization*, vol. 10, no. 1, pp. 177–182, 1999.

[30] De Borst, R., Crisfield, M. A., Remmers, J. J., and Verhoosel, C. V., *Nonlinear finite element analysis of solids and structures.* John Wiley & Sons, 2012.

[31] De Munck, M., Moens, D., Desmet, W., and Vandepitte, D., "A response surface based optimisation algorithm for the calculation of fuzzy envelope frfs of models with uncertain properties," *Computers & Structures*, vol. 86, no. 10, pp. 1080–1092, 2008.

[32] Degrauwe, D., Lombaert, G., and De Roeck, G., "Improving interval analysis in finite element calculations by means of affine arithmetic," *Computers & structures*, vol. 88, no. 3, pp. 247–254, 2010.

[33] Dehghan, M., Hashemi, B., and Ghatee, M., "Computational methods for solving fully fuzzy linear systems," *Applied Mathematics and Computation*, vol. 179, no. 1, pp. 328–343, 2006.

[34] Dempster, A. P., "Upper and lower probabilities induced by a muilti-valued mapping," *Ann. Math. Stat.*, vol. 38, pp. 325–339, 1967.

[35] Dessi, D. and Camerlengo, G., "Damage identification techniques via modal curvature analysis: Overview and comparison," *Mechanical Systems and Signal Processing*, vol. 52-53, pp. 181–205, 2015.

[36] Dessombz, O., Thouverez, F., Laîné, J.-P., and Jézéquel, L., "Analysis of mechanical systems using interval computations applied to finite element methods," *Journal of Sound and Vibration*, vol. 239, no. 5, pp. 949–968, 2001.

[37] Do, D. M., Gao, W., Song, C., and Tangaramvong, S., "Dynamic analysis and reliability assessment of structures with uncertain-but-bounded parameters under stochastic process excitations," *Reliability Engineering & System Safety*, vol. 132, pp. 46–59, 2014.

[38] DÖHLER, M., HILLE, F., MEVEL, L., and RÜCKER, W., "Structural health monitoring with statistical methods during progressive damage test of s101 bridge," *Engineering Structures*, vol. 69, pp. 183–193, 2014.

[39] DÖHLERA, M., MEVEL, L., and HILLE, F., "Subspace-based damage detection under changes in the ambient excitation statistics," *Mechanical Systems and Signal Processing*, vol. 45, pp. 207–224, 2014.

[40] DOKAINISH, M. and SUBBARAJ, K., "A survey of direct time-integration methods in computational structural dynamics?i. explicit methods," *Computers & Structures*, vol. 32, no. 6, pp. 1371–1386, 1989.

[41] DONALD, E. K., "The art of computer programming," *Sorting and searching*, vol. 3, pp. 426–458, 1999.

[42] EPPSTEIN, M. J., FEDELE, F., LAIBLE, J., ZHANG, C., GODAVARTY, A., and SEVICK-MURACA, E. M., "A comparison of exact and approximate adjoint sensitivities in fluorescence tomography," *Medical Imaging, IEEE Transactions on*, vol. 22, no. 10, pp. 1215–1223, 2003.

[43] ERDOGAN, Y. S. and BAKIR, P. G., "Inverse propagation of uncertainties in finite element model updating through use of fuzzy arithmetic," *Engineering Applications of Artificial Intelligence*, vol. 26, no. 1, pp. 357–367, 2013.

[44] ERDOGAN, Y. S., GUL, M., CATBAS, F. N., and BAKIR, P. G., "Quantification of parametric model uncertainties in finite element model updating problem via fuzzy numbers," in *Topics in Model Validation and Uncertainty Quantification, Volume 5*, pp. 67–74, Springer, 2013.

[45] FEDELE, F., LAIBLE, J., and EPPSTEIN, M., "Coupled complex adjoint sensitivities for frequency-domain fluorescence tomography: theory and vectorized implementation," *Journal of Computational Physics*, vol. 187, no. 2, pp. 597–619, 2003.

[46] FEDELE, F., MUHANNA, R. L., XIAO, N., and MULLEN, R. L., "Interval-based approach for uncertainty propagation in inverse problems," *Journal of Engineering Mechanics*, vol. 141, no. 1, 2014.

[47] FERNÁNDEZ-MARTÍNEZ, J., PALLERO, J., FERNÁNDEZ-MUÑIZ, Z., and PEDRUELO-GONZÁLEZ, L., "The effect of noise and Tikhonov's regularization in inverse problems. Part I: The linear case," *Journal of Applied Geophysics*, 2014.

[48] FERNÁNDEZ-MARTÍNEZ, J. L., FERNÁNDEZ-MUÑIZ, Z., PALLERO, J., and PEDRUELO-GONZÁLEZ, L. M., "From bayes to tarantola: new insights to understand uncertainty in inverse problems," *Journal of Applied Geophysics*, vol. 98, pp. 62–72, 2013.

[49] FLETCHER, R. and REEVES, C. M., "Function minimization by conjugate gradients," *The computer journal*, vol. 7, no. 2, pp. 149–154, 1964.

[50] FLETCHER, R., "Conjugate gradient methods for indefinite systems," in *Numerical analysis*, pp. 73–89, Springer, 1976.

[51] FRICKER, T. E., OAKLEY, J. E., SIMS, N. D., and WORDEN, K., "Probabilistic uncertainty analysis of an frf of a structure using a gaussian process emulator," *Mechanical Systems and Signal Processing*, vol. 25, no. 8, pp. 2962–2975, 2011.

[52] FRISWELL, M. I., "Damage identification using inverse methods," *Philosophical Transactions of the Royal Society A: Mathematical, Physical and Engineering Sciences*, vol. 365, no. 1851, pp. 393–410, 2007.

[53] GAO, W., "Natural frequency and mode shape analysis of structures with uncertainty," *Mechanical Systems and Signal Processing*, vol. 21, no. 1, pp. 24–39, 2007.

[54] GAO, W., SONG, C., and TIN-LOI, F., "Probabilistic interval analysis for structures with uncertainty," *Structural Safety*, vol. 32, no. 3, pp. 191–199, 2010.

[55] GHERLONE, M., CERRACCHIO, P., MATTONE, M., DI SCIUVA, M., and TESSLER, A., "Shape sensing of 3d frame structures using an inverse finite element method," *International Journal of Solids and Structures*, vol. 49, no. 22, pp. 3100–3112, 2012.

[56] GILES, M. B. and PIERCE, N. A., "An introduction to the adjoint approach to design," *Flow, turbulence and combustion*, vol. 65, no. 3-4, pp. 393–415, 2000.

[57] GLASER, S. D., LI, H., WANG, M. L., OU, J., and LYNCH, J., "Sensor technology innovation for the advancement of structural health monitoring: a strategic program of us-china research for the next decade," *Smart Structures and Systems*, vol. 3, no. 2, pp. 221–244, 2007.

[58] GURARI, E., "Cis 680: Data structures: Chapter 19: Backtracking algorithms," 1999.

[59] HAAG, T., HERRMANN, J., and HANSS, M., "Identification procedure for epistemic uncertainties using inverse fuzzy arithmetic," *Mechanical Systems and Signal Processing*, vol. 24, no. 7, pp. 2021–2034, 2010.

[60] HALL, J. F., "Problems encountered from the use (or misuse) of rayleigh damping," *Earthquake engineering & structural dynamics*, vol. 35, no. 5, pp. 525–545, 2006.

[61] HAN, X., SUN, W., and DANG, C., "Nonmonotone second-order wolfe?s line search method for unconstrained optimization problems," *Computers & Mathematics with Applications*, vol. 60, no. 9, pp. 2517–2525, 2010.

[62] HANSEN, P. C., *Discrete Inverse Problems : Insight and Algorithms*. Technical University of Denmark, Lyngby, Denmark: Society for Industrial and Applied Mathematics, Philadelphia, Copyright 2010 by the Society for Industrial and Applied Mathematics.

[63] HARGREAVES, G. I., "Interval analysis in matlab," 2002.

[64] HESTENES, M. R. and STIEFEL, E., "Methods of conjugate gradients for solving linear systems," 1952.

[65] HLADÍK, M., DANEY, D., and TSIGARIDAS, E. P., "An algorithm for addressing the real interval eigenvalue problem," *Journal of computational and applied mathematics*, vol. 235, no. 8, pp. 2715–2730, 2011.

[66] HU, J. and QIU, Z., "Non-probabilistic convex models and interval analysis method for dynamic response of a beam with bounded uncertainty," *Applied Mathematical Modelling*, vol. 34, no. 3, pp. 725–734, 2010.

[67] IGUSA, T., BUONOPANE, S., and ELLINGWOOD, B., "Bayesian analysis of uncertainty for structural engineering applications," *Structural Safety*, vol. 24, no. 2, pp. 165–186, 2002.

[68] IMPOLLONIA, N., "A method to derive approximate explicit solutions for structural mechanics problems," *International journal of solids and structures*, vol. 43, no. 22, pp. 7082–7098, 2006.

[69] IMPOLLONIA, N. and MUSCOLINO, G., "Interval analysis of structures with uncertain-but-bounded axial stiffness," *Computer Methods in Applied Mechanics and Engineering*, vol. 200, no. 21, pp. 1945–1962, 2011.

[70] JIANG, C., ZHANG, Z., HAN, X., and LIU, J., "A novel evidence-theory-based reliability analysis method for structures with epistemic uncertainty," *Computers & Structures*, vol. 129, pp. 1–12, 2013.

[71] KALMAN, R., "A new approach to linear filtering and prediction problems," *Transactions of the ASME-Journal of Basic Engineering*, vol. 82, no. D, pp. 35–45, 1960.

[72] KEARFOTT, R. B., "Complete search in continuous global optimization and constraint satisfaction," *Nonconvex Optimization and Its Applications 13*, 2004.

[73] KHOO, S., ISMAIL, Z., KONG, K., ONG, Z., NOROOZI, S., CHONG, W., and RAHMAN, A., "Impact force identification with pseudo-inverse method on a lightweight structure for under-determined, even-determined and over-determined cases," *International Journal of Impact Engineering*, vol. 63, pp. 52–62, 2014.

[74] KIEFER, J., "Sequential minimax search for a maximum," *Proceedings of the American Mathematical Society*, vol. 4, no. 3, pp. 502–506, 1953.

[75] KLIR, G. J. and WIERMAN, M. J., *Uncertainty-based information - Elements of generalized information theory*. Physica-Verlag, Heidelberg, 1999.

[76] KOBAYASHI, M., NARUSHIMA, Y., and YABE, H., "Nonlinear conjugate gradient methods with structured secant condition for nonlinear least squares problems," *Journal of computational and applied mathematics*, vol. 234, no. 2, pp. 375–397, 2010.

[77] KREINOVICH, V., BECK, J., FERREGUT, C., SANCHEZ, A., KELLER, G., AVERILL, M., and STARKS, S., "Monte-carlo-type techniques for processing interval uncertainty, and their engineering applications," in *Proc. NSF workshop on reliable engineering computing*, Savannah, GA. http://www. gtsav. gatech. edu/rec/recworkshop/index. html, 2004.

[78] KREINOVICH, V., LAKEYEV, A., ROHN, J.-., and KLUWER, P. K., "Computational complexity and feasibility of data processing and interval computations," *Computers and Mathematics with Applications*, vol. 36, no. 8, 1998.

[79] KULISCH, U. W. and MIRANKER, W. L., *Computer Arithmetic in Theory and Practice*. Academic press, New York, 1981.

[80] LAURO, F., BENNANI, B., CROIX, P., and OUDIN, J., "Identification of the damage parameters for anisotropic materials by inverse technique: application to an aluminium," *Journal of Materials Processing Technology*, vol. 118, no. 1, pp. 472–477, 2001.

[81] LEE, U., KIM, S., and CHO, J., "Dynamic analysis of the linear discrete dynamic systems subjected to the initial conditions by using an fft-based spectral analysis method," *Journal of sound and vibration*, vol. 288, no. 1, pp. 293–306, 2005.

[82] LENG, H., "Real eigenvalue bounds of standard and generalized real interval eigenvalue problems," *Applied Mathematics and Computation*, vol. 232, pp. 164–171, 2014.

[83] LENG, H. and HE, Z., "Computing eigenvalue bounds of structures with uncertain-but-non-random parameters by a method based on perturbation theory," *Communications in Numerical Methods in Engineering*, vol. 23, no. 11, pp. 973–982, 2007.

[84] LI, J., LAW, S., and DING, Y., "Substructure damage identification based on response reconstruction in frequency domain and model updating," *Engineering Structures*, vol. 41, pp. 270–284, 2012.

[85] LIU, F., LI, H., WANG, W., and LIANG, B., "Initial-condition consideration by transferring and loading reconstruction for the dynamic analysis of linear structures in the frequency domain," *Journal of Sound and Vibration*, vol. 336, pp. 164–178, 2015.

[86] LIU, G. and KREINOVICH, V., "Fast convolution and fast fourier transform under interval and fuzzy uncertainty," *Journal of Computer and System Sciences*, vol. 76, no. 1, pp. 63–76, 2010.

[87] LIU, W. and WU, C., "A predictor-corrector iterated Tikhonov regularization for linear ill-posed inverse problems," *Applied Mathematics and Computation*, vol. 221, pp. 802–818, 2013.

[88] LOW, Y., "Prediction of extreme responses of floating structures using a hybrid time/frequency domain coupled analysis approach," *Ocean Engineering*, vol. 35, no. 14, pp. 1416–1428, 2008.

[89] LRFD, A., "Manual of steel construction, load and resistance factor design," *Chicago: American Institute of Steel Construction*, 1994.

[90] LU, Z., LIU, J., LIU, Y., DING, R., and YANG, F., "The interval sensitivity analysis and optimization of the distribution network parameters considering the load uncertainty," *International Journal of Electrical Power & Energy Systems*, vol. 64, pp. 931–936, 2015.

[91] LUENBERGER, D. G. and YE, Y., *Linear and nonlinear programming*, vol. 116. Springer Science & Business Media, 2008.

[92] LUTES, L. D. and SARKANI, S., *Random vibrations: analysis of structural and mechanical systems*. Butterworth-Heinemann, 2004.

[93] MANSUR, W. J., CARRER, J. A. M., FERREIRA, W. G., AM CLARET, D. G., and VENANCIO-FILHO, F., "Time-segmented frequency-domain analysis for non-linear multi-degree-of-freedom structural systems," *Journal of sound and vibration*, vol. 237, no. 3, pp. 457–475, 2000.

[94] MARCHUK, G., SHUTYAEV, V., and BOCHAROV, G., "Adjoint equations and analysis of complex systems: Application to virus infection modelling," *Journal of computational and applied mathematics*, vol. 184, no. 1, pp. 177–204, 2005.

[95] MIYAJIMA, S., "Fast enclosure for all eigenvalues in generalized eigenvalue problems," *Journal of computational and applied mathematics*, vol. 233, no. 11, pp. 2994–3004, 2010.

[96] MIYAJIMA, S., "Numerical enclosure for each eigenvalue in generalized eigenvalue problem," *Journal of Computational and Applied Mathematics*, vol. 236, no. 9, pp. 2545–2552, 2012.

[97] MODARES, M. and VENKITARAMAN, S., "Reliable condition assessment of structures using hybrid structural measurements and structural uncertainty analyses," *Structural Safety*, vol. 52, pp. 202–208, 2015.

[98] MOENS, D. and HANSS, M., "Non-probabilistic finite element analysis for parametric uncertainty treatment in applied mechanics: Recent advances," *Finite Elements in Analysis and Design*, vol. 47, no. 1, pp. 4–16, 2011.

[99] MOENS, D. and VANDEPITTE, D., "Interval sensitivity theory and its application to frequency response envelope analysis of uncertain structures," *Computer methods in applied mechanics and engineering*, vol. 196, no. 21, pp. 2486–2496, 2007.

[100] MOORE, E. H., "On the reciprocal of the general algebraic matrix," *Bulletin of the American Mathematical Society*, vol. 26, no. 9, pp. 394–395, 1920.

[101] MOORE, R. E., KEARFOTT, R. B., and CLOUD, M. J., *Introduction to interval analysis*. Society for Industrial and Applied Mathematics, 2009.

[102] MUHANNA, R. L. and MULLEN, R. L., "Uncertainty in mechanics problems-interval-based approach," *Journal of Engineering Mechanics*, vol. 127, no. 6, pp. 557–566, 2001.

[103] MUHANNA, R. L. and ZHANG, H., "Interval finite elements as a basis for generalized models of uncertainty in engineering mechanics," *Reliable computing*, vol. 13, pp. 173–194, 2007.

[104] MUHANNA, R. L., ZHANG, H., and MULLEN, R. L., "Combined axial and bending stiffness in interval finite-element methods," *Journal of Structural Engineering*, vol. 133, no. 12, pp. 1700–1709, 2007.

[105] MULLEN, R. L. and MUHANNA, R. L., "Bounds of structural response for all possible loading combinations," *Journal of Structural Engineering*, vol. 125, no. 1, pp. 98–106, 1999.

[106] MUSCOLINO, G., RICCIARDI, G., and IMPOLLONIA, N., "Improved dynamic analysis of structures with mechanical uncertainties under deterministic input," *Probabilistic Engineering Mechanics*, vol. 15, no. 2, pp. 199–212, 2000.

[107] MUSCOLINO, G., SANTORO, R., and SOFI, A., "Explicit frequency response functions of discretized structures with uncertain parameters," *Computers and Structures*, vol. 133, pp. 64–78, 2014.

[108] MUSCOLINO, G. and SOFI, A., "Bounds for the stationary stochastic response of truss structures with uncertain-but-bounded parameters," *Mechanical Systems and Signal Processing*, vol. 37, no. 1, pp. 163–181, 2013.

[109] NEUMAIER, A., *Interval methods for systems of equations*, vol. 37. Cambridge university press, 1990.

[110] NEUMAIER, A. and POWNUK, A., "Linear systems with large uncertainties, with applications to truss structures," *Reliable Computing*, vol. 13, no. 2, pp. 149–172, 2007.

[111] PARK, S., PARK, H., KIM, J., and ADELI, H., "3d displacement measurement model for health monitoring of structures using a motion capture system," *Measurement*, vol. 59, pp. 352–362, 2015.

[112] PAZ, M., *Structural dynamics: theory and computation.* Springer Science & Business Media, 1997.

[113] PEI, Q. and LI, L., "Modal parameter identification of civil engineering structures under seismic excitations," *Advanced Materials Research*, vol. 859, pp. 163–166, 2014.

[114] PENROSE, R., "A generalized inverse for matrices," in *Mathematical proceedings of the Cambridge philosophical society*, vol. 51, pp. 406–413, Cambridge Univ Press, 1955.

[115] PETKOVIĆ, M. S. and PETKOVIĆ, L. D., "Complex interval arithmetic and its applications," *Mathematical Research*, 1998.

[116] POLAK, E. and RIBIÈRE, G., "Note sur la convergence de directions conjugèes," *Rev. Francaise Informat Recherche Operationelle*, vol. 16, pp. 35–43, 1969.

[117] POLYAK, B. T., "The conjugate gradient method in extreme problems," *USSR Computational Mathematics and Mathematical Physics*, vol. 9, pp. 94–112, 1969.

[118] QIU, Z. and NI, Z., "An inequality model for solving interval dynamic response of structures with uncertain-but-bounded parameters," *Applied Mathematical Modelling*, vol. 34, no. 8, pp. 2166–2177, 2010.

[119] RAO, M. R., MULLEN, R. L., and MUHANNA, R. L., "A new interval finite element formulation with the same accuracy in primary and derived variables," *International Journal of Reliability and Safety*, vol. 5, no. 3, pp. 336–357, 2011.

[120] RIBEIRO, M. I., "Kalman and extended kalman filters: Concept, derivation and properties," *Institute for Systems and Robotics*, p. 43, 2004.

[121] RONG, T.-Y. and LÜ, A.-Q., "Theory and method of structural variations of finite element systems," *AIAA journal*, vol. 32, no. 9, pp. 1911–1919, 1994.

[122] RUMP, S. M., *INTLAB - INTerval LABoratory.* Kluwer Academic Publishers, 1999.

[123] SANTAMARINA, J. C. and FRATTA, D., *Discrete signals and inverse problems: an introduction for engineers and scientists.* John Wiley & Sons, 2005.

[124] Sarkar, A. and Ghanem, R., "Mid-frequency structural dynamics with parameter uncertainty," *Computer Methods in Applied Mechanics and Engineering*, vol. 191, no. 47, pp. 5499–5513, 2002.

[125] Schultz, T., Sheplak, M., and Cattafesta, L. N., "Application of multivariate uncertainty analysis to frequency response function estimates," *Journal of sound and vibration*, vol. 305, no. 1, pp. 116–133, 2007.

[126] Shafer, G., *A mathematical theory of evidence.* Princeton University Press, Princeton, 1968.

[127] Shi, Z.-J. and Shen, J., "A gradient-related algorithm with inexact line searches," *Journal of computational and applied mathematics*, vol. 170, no. 2, pp. 349–370, 2004.

[128] Shi, Z.-J., Wang, S., and Xu, Z., "The convergence of conjugate gradient method with nonmonotone line search," *Applied Mathematics and Computation*, vol. 217, no. 5, pp. 1921–1932, 2010.

[129] Shye, K. and Richardson, M., "Mass, stiffness, and damping matrix estimates from structural measurements," in *Proceedings of the Fifth International Modal Analysis Conference*, vol. 1, pp. 756–761, 1987.

[130] Sim, J., Qiu, Z., and Wang, X., "Modal analysis of structures with uncertain-but-bounded parameters via interval analysis," *Journal of Sound and Vibration*, vol. 303, no. 1, pp. 29–45, 2007.

[131] Simon, D., *Optimal state estimation: Kalman, H_∞, and nonlinear approaches.* John Wiley & Sons, Inc.

[132] Soize, C., "Bayesian posteriors of uncertainty quantification in computational structural dynamics for low-and medium-frequency ranges," *Computers & Structures*, vol. 126, pp. 41–55, 2013.

[133] Stull, C. J., Nichols, J. M., and Earls, C. J., "Stochastic inverse identification of geometric imperfections in shell structures," *Computer Methods in Applied Mechanics and Engineering*, vol. 200, no. 25-28, pp. 2256–2267, 2011.

[134] Sun, X., Liu, J., Han, X., Jiang, C., and Chen, R., "A new improved regularization method for dynamic load identification," *Inverse Problems in Science and Engineering*, vol. 22, no. 7, pp. 1062–1076, 2014.

[135] Terejanu, G. A., "Unscented kalman filter tutorial," *University at Buffalo, Buffalo*, 2011.

[136] Tipireddy, R., Nasrellah, H., and Manohar, C., "A kalman filter based strategy for linear structural system identification based on multiple static and dynamic test data," *Probabilistic Engineering Mechanics*, vol. 24, no. 1, pp. 60–74, 2009.

[137] TO, C. W. S., "Response analysis of nonlinear multi-degree-of-freedom systems with uncertain properties to non-gaussian random excitations," *Probabilistic Engineering Mechanics*, vol. 27, no. 1, pp. 75 – 81, 2012. The {IUTAM} Symposium on Nonlinear Stochastic Dynamics and Control.

[138] UNGER, J. F. and KÖNKE, C., "An inverse parameter identification procedure assessing the quality of the estimates using bayesian neural networks," *Applied Soft Computing*, vol. 11, no. 4, pp. 3357–3367, 2011.

[139] VAN LOAN, C., *Computational frameworks for the fast Fourier transform*, vol. 10. SIAM, 1992.

[140] VELETSOS, A. S. and KUMAR, A., "Steady-state and transient responses of linear structures," *Journal of Engineering Mechanics*, vol. 109, no. 5, pp. 1215–1230, 1983.

[141] VELETSOS, A. S. and VENTURA, C. E., "Dynamic analysis of structures by the dft method," *Journal of structural engineering*, vol. 111, no. 12, pp. 2625–2642, 1985.

[142] VESTRONI, F. and CAPECCHI, D., "Damage detection in beam structures based on frequency measurements," *Journal of Engineering Mechanics*, vol. 126, no. 7, pp. 761–768, 2000.

[143] WANG, C.-J., "Some remarks on conjugate gradient methods without line search," *Applied mathematics and computation*, vol. 181, no. 1, pp. 370–379, 2006.

[144] WANG, L., XU, Y., and LI, L., "Parameter identification of chaotic systems by hybrid nelder-mead simplex search and differential evolution algorithm," *Expert Systems with Applications*, vol. 38, pp. 3238–3245, 2011.

[145] WANG, X., YANG, C., WANG, L., and QIU, Z., "Probabilistic damage identification of structures with uncertainty based on dynamic responses," *Acta Mechanica Solida Sinica*, vol. 27, no. 2, pp. 172–180, 2014.

[146] WEISS, M. A. and HARTMAN, S., *Data structures and problem solving using Java*, vol. 204. Addison-Wesley Reading, 1998.

[147] WOLFE, P., "Convergence conditions for ascent methods," *SIAM review*, vol. 11, no. 2, pp. 226–235, 1969.

[148] WOLFE, P., "Convergence conditions for ascent methods. ii: Some corrections," *SIAM review*, vol. 13, no. 2, pp. 185–188, 1971.

[149] XIA, Y., ZHANG, P., NI, Y., and ZHU, H., "Deformation monitoring of a super-tall structure using real-time strain data," *Engineering Structures*, vol. 67, pp. 29–38, 2014.

[150] Xia, Y., Qiu, Z., and Friswell, M. I., "The time response of structures with bounded parameters and interval initial conditions," *Journal of Sound and Vibration*, vol. 329, no. 3, pp. 353–365, 2010.

[151] Xie, Z. and Feng, J., "Real-time nonlinear structural system identification via iterated unscented kalman filter," *Mechanical Systems and Signal Processing*, vol. 28, pp. 309–322, 2012.

[152] Xu, B., He, J., Rovekamp, R., and Dyke, S. J., "Structural parameters and dynamic loading identification from incomplete measurements: approach and validation," *Mechanical systems and signal processing*, vol. 28, pp. 244–257, 2012.

[153] Yan, Y., Cheng, L., Wu, Z., and Yam, L., "Development in vibration-based structural damage detection technique," *Mechanical Systems and Signal Processing*, vol. 21, no. 5, pp. 2198–2211, 2007.

[154] Yang, Y., Cai, Z., and Liu, Y., "Interval analysis of dynamic response of structures using laplace transform," *Probabilistic Engineering Mechanics*, vol. 29, pp. 32–39, 2012.

[155] Yang, Y., Cai, Z., and Liu, Y., "Interval analysis of frequency response functions of structures with uncertain parameters," *Mechanics Research Communications*, vol. 47, pp. 24–31, 2013.

[156] Yang, Y. and Nagarajaiah, S., "Structural damage identification via a combination of blind feature extraction and sparse representation classification," *Mechanical Systems and Signal Processing*, vol. 45, no. 1, pp. 1–23, 2014.

[157] Yu, G., Guan, L., and Wei, Z., "Globally convergent polak–ribière–polyak conjugate gradient methods under a modified wolfe line search," *Applied Mathematics and Computation*, vol. 215, no. 8, pp. 3082–3090, 2009.

[158] Yu, G., Zhao, Y., and Wei, Z., "A descent nonlinear conjugate gradient method for large-scale unconstrained optimization," *Applied mathematics and computation*, vol. 187, no. 2, pp. 636–643, 2007.

[159] Zaman, K., Rangavajhala, S., McDonald, M. P., and Mahadevan, S., "A probabilistic approach for representation of interval uncertainty," *Reliability Engineering & System Safety*, vol. 96, no. 1, pp. 117–130, 2011.

[160] Zhang, H., *Nondeterministic linear static finite element analysis: an interval approach.* PhD thesis, Georgia Institute of Technology, 2005.

[161] Zhang, K., Li, H., Duan, Z., and Law, S., "A probabilistic damage identification approach for structures with uncertainties under unknown input," *Mechanical Systems and Signal Processing*, vol. 25, no. 4, pp. 1126–1145, 2011.

[162] ZHANG, L. and LI, J., "A new globalization technique for nonlinear conjugate gradient methods for nonconvex minimization," *Applied Mathematics and Computation*, vol. 217, no. 24, pp. 10295–10304, 2011.

[163] ZHANG, Q., DUAN, Z., and OTHERS, "Simultaneous identification of excitation time histories and parametrized structural damages," *Mechanical Systems and Signal Processing*, vol. 33, pp. 56–68, 2012.

VITA

Naijia Xiao was born in Shaoyang, Hunan, China on August 24, 1987. He received his Bachelor of Engineering degree and Master of Engineering degree in Civil Engineering in 2009 and 2011, respectively, from Department of Civil Engineering of Tsinghua University, Beijing, China. He began his PhD studies at the Georgia Institute of Technology in the fall of 2011. During his doctoral studies, he worked under the guidance of Dr. Francesco Fedele and Dr. Rafi L. Muhanna.